Towards plastic electronic sensing devices with TTF-based molecular conductors as active components

Victor Lebedev

Tesi doctoral

Programa de Doctorat de Ciència de Materials

Directors:
Jaume Veciana Miró **i** ***Elena Laukhina***
Tutora:
Rosa Maria Sebastián Pérez

Departament de Química Facultat de Ciències

2014

Memòria presentada per aspirar al Grau de Doctor per:

Victor Lebedev

Vist i plau,
Els directors:

Prof. Jaume Veciana Miró

Dr. Elena Laukhina

La tutora:

Prof. Rosa Maria Sebastián Pérez

a Bellaterra, 25 de Setembre del 2014

JAUME VECIANA MIRÓ, Research Professor and **ELENA LAUKHINA** Researcher, of the Spanish Council of Research at the Materials Science Institute of Barcelona (ICMAB-CSIC)

CERTIFY

That **Victor Lebedev**, Chemical Engineer, has performed, under their supervision, the research work entitled **"Towards plastic electronic sensing devices with TTF-based molecular conductors as active components".** This work has been carried out under the framework of the Materials Science Ph. D. program of the Chemistry Department of the Autonomous University of Barcelona.

In witness whereof this is signed by

Supervisors:

Dr. Elena Laukhina

Prof. Jaume Veciana Miró

”The opposite of a fact is falsehood, but the opposite of one profound truth may very well be another profound truth.”

Niels Bohr

Acknowledgments

Here, I would like to thank many people who made this thesis possible. I owe my gratitude to Prof. Jaume Veciana and Prof. Concepció Rovira for giving me a chance to work in the Nanomol group.

First and foremost I thank my supervisors Prof. Jaume Veciana and Dr. Elena Laukhina, for their help and inspiration. Their valuable comments and constructive criticism, expressed in a straight-forward but friendly manner, not only helped me gain new insights, but also motivated me time and time again. I doubt that I would have been able to overcome all difficulties without them.

I am very thankful also to Prof. Jaume Veciana for the careful reading of the Thesis, his critical remarks and help in improving the contents of the dissertation. My special gratitude goes to Dr. Elena Laukhina for opening to me the fascinating field of molecular conductors; her moral support, patience and understanding during the whole period of my PhD study and writing this Thesis. Without her guidance as a great mentor, this work would not have been possible.

I am very thankful to Prof. Vladimir Laukhin, who introduced me to physics and was never afraid to ask difficult questions, for his great help with all experiments and prototypes designs, and for his tireless efforts in the physics laws explanations in the simple understandable manner enabled great progress in my PhD studies.

I am also very grateful to Prof. James S. Brooks and Dr. Steven Eden from the National High Magnetic Field Laboratory (HMFL), for their activity and great collaboration both in Barcelona and in Tallahassee.

I especially would like to mention Dr. Silvia Milita, Dr. Fabiola Liscio, Laura Ferlauto from the Consiglio Nazionale delle Ricerche (CNR) as well as Prof Aldo Brillante and Dr. Ivano Bilatti from the Università di Bologna for the enjoyable collaborative work during my short stay in Bologna and fruitful results.

I would like to thank Prof. Francisco Rivadulla from Universidad de Santiago de Compostela as well as both Prof. Ryszard C Jachwicz and Dr. Jerzy Weremczuk from Warsaw University of Technology for the nice results they obtained for me.

I would like to acknowledge Dr. Gerard Oncins from Parc Científic de Barcelona for his numerous experiments on the Young´s moduli measurements using the AFM as well as for interesting discussions of obtained results. Additionally I would like to thank Xavier Fontrodona from Servies Tècnics de Reserca de la Universitat de Girona for his help in performing X-ray measurements and analysis of single crystals. Special thanks to CIBER-BBN for the initial contract, which my PhD was starting from, and not only for financial support but also for collaborative work with Dr. Estefanía Peña de la Universidad de Zaragoza who helped us with a mechanical properties testing of BL films. Prof. Majid Ebrahim-Zadeh, Prof. Gerasimos Konstantatos, Dr. Suddapalli Chaitanya Kumar, Dr. Francisco Pelayo García de Arquer, Badarla Venkata Ramaiah from The Institute of Photonic Science (ICFO) are acknowledged for all help concerning the bolometer prototype examination. My thanks are also directed to Prof. Valery Traven who was a first person on my road to the PhD Thesis. I would like to recognize the Generalitat de Catalunya for the FI fellowship that helped me to perform this Thesis.

Also I would like to mention Dr. Raphael Pfattner for his help with measurements and introduction to a programming as well as for the insightful discussions that we had together both professional and personal. Many thanks to Dr. Evelyn Moreno for her enormous help in X-ray diffraction interpretations as well as to Lourdes Ferreras and Elena Marchante, who were helping me a lot during these years with a films preparation and electrocrystallization of the single crystals. My respect to all people from the Nanomol group as well as from whole ICMAB who were my family during these 5 years.

Last but not least I would like to thank my family, specially my parents and sister, for their love and support during all these years that made possible a completing of this Thesis.

Thank you all so much!!!!

Table of content

List of Abbreviations and Symbols

1D	one-dimensional
2D	two-dimensional
AC	alternating current
AFM	Atomic Force Microscopy
BEDT-TTF = ET	bis(ethylenedithio)tetrathiafulvalene
BEDO-TTF	bis(ethylenedioxo)tetrathiafulvalene
BL	bi-layer
CAP	Cellulose acetate propionate
CS-AFM	current sensing AFM
CT	charge transfer
CTA	Cellulose triacetate
DC	direct current
E_a	activation energy
E	Young´s modulus
EDX	Energy-Dispersive X-ray spectroscopy
EPR	Electronic Paramagnetic Resonance
F	force
GF	gauge-factor
Hal	halogen
IOP	intraocular pressure
IR	Infrared spectroscopy

IRS	ion-radical salt
L	length
nBu_4N	tetrabutylammonia
P	pressure
PC	poly(bisphenol-A carbonate)
PXRD	powder X-ray diffraction
R	electrical resistance
R□	sheet resistance
R_{yield}	resistance elastic limit
RY	relative mass yield
r	radius
S	Seebeck coefficient
SEM	scanning electron microscopy
sq. or □	square (in the units of sheet electrical resistance)
T	temperature
TAA	tetraalkylammonium salt
TCNQ	tetracyanoquinodimethane
TCR	temperature coefficient of resistance
tpdt	2,3-thiophenedithiolate
TTF	tetrathiafulvalene
UV-Vis	ultraviolet-visible spectra
UTS	ultimate tensile strength
Z	thermoelectric figure of merit

ε	relative strain
ε_{yield}	strain yield
σ	electrical conductivity
κ	thermal conductivity
ρ	electrical resistivity

Chapter 1

Introduction to organic molecular conductors and their applications as sensing materials for flexible electronics. Motivation and Objectives

Motivation

It is a matter of a general knowledge that the major innovations in sensors come from the development of new materials and new fabrication techniques.[1, 2] For example, metallized plastics, that have been developed in order to replace heavy-weight metal-based devices in traditional technologies, have permitted scientists to develop the lightweight world of conducting sensing materials. The application of metallized plastics in electronics is a key point in the development of high-tech applications. Indeed thin-metal coatings on plastics can give large-scale lightweight antennas, surface conductive flexible tapes, or cheap materials for the construction of flexible and weightless electronic devices.[3, 4] Many reported methods[5-10] for preparation of thin inorganic conductive films on different substrates have shown that physical processes are powerful methods for the deposition of thermally stable materials, like metals and semiconductors, but they are not always available for either fragile or nonvolatile substances, like organic molecules. It is also well known that a high temperature sintering process is crucial to achieve better electrical contacts between inorganic conducting grains forming a conductive layer. [6-8] However, flexible transparent substrates, such as plastics and indium tin oxides-polyethylene terephthalate (ITO-PET), are not able to withstand high temperatures. [11] The major problems of metallized plastics are: i) poor adhesion of conventional metals to chemically inert polymers[3, 12] and ii) a significant difference in the Young's moduli of soft plastics and the rigid inorganic metallic compounds. These disadvantages result in a low binding between metallic and plastic layers.[3, 5, 12] Such disadvantages can be overcome by the metallization of plastics with "soft" organic molecular metals [13-16] due to the high similarity of the mechanical properties between the molecular metal layer and plastic one.

The discovery of organic molecular conductors as materials of low dimensionality with exotic electronic properties[17-19] has opened several promising research venues. First, the physics of one- and two-dimensional metals derived from anisotropic organic materials provides several advantages to these materials.[15, 20-23] Second, the capability to perform a molecular and crystal design of organic conductive materials, which are fundamental to the progress of electronics, incorporate additional benefits. [16, 24-27] Third, the engineering of novel high-tech materials with organic molecular metals as active components also provides another advantage to the field. [28-30]

A simple single- or two-stage "self-metallization" procedure has been developed for the fabrication of conducting bi-layer (BL) films composed of a thin layer of an organic

molecular conductor on a polymeric one. [29, 31-33] The method (Figure 1-1) consists in switching on a redox reaction with an halogen in the swollen surface of a solid solution of a polymer and a redox active molecule, casted as a thin film, that provokes the nucleation of small clusters of the molecular conductor, which are able to growth into a conductive polycrystalline layer on the surface of the polymeric thin film.

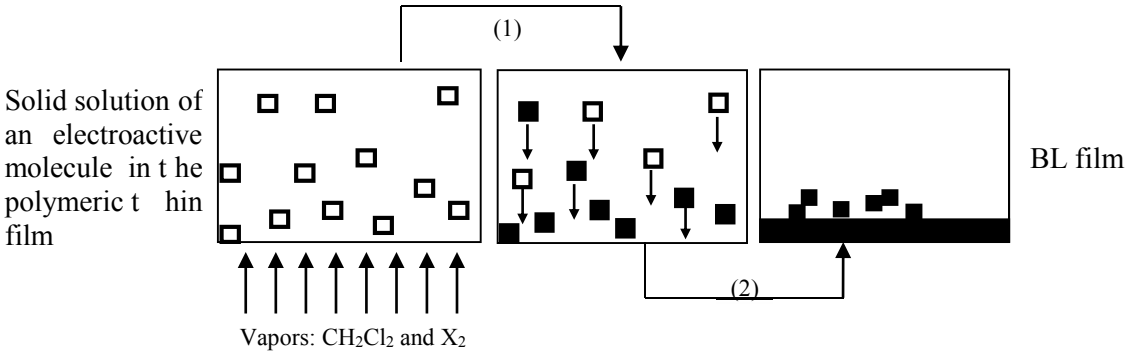

Figure 1-1. Scheme of process leading to the conductive BL film formation with a layer of crystals of an organic molecular conductor as an active component. The halogen/solvent annealing involves two consecutive processes: (1) an internal oxidation of neutral molecules of the electroactive organic molecule (□) and (2) the nucleation of small clusters of a molecular conductor (■) that form the conductive layer.

Such conductive covering layers reveal a long-term stability and robustness as well as attractive electrical and mechanical properties to the BL films providing them unprecedented properties as flexible and robust deformation sensors. [33, 34] Such flexible all-organic sensing composite materials work with an electrical detection principle leading therefore to great opportunities for high-tech applications. [1, 2, 35] An electric output from the sensor is highly desirable because of the advantages it gives in further signal processing. It permits to simplify the sensor design since it can be incorporated directly into electrical circuits. Flexible sensors that can be easily located at the tissues of our body, or on synthetic and natural textiles, on artificial skins, and inside of catheters, etc. are raising a large interest in many industries. [36, 37] These sensors have special interest for biomedical applications specially for health care monitoring since there is a big problem all around the world to provide quality care to a large numbers of individuals through remote patient monitoring products and medical devices (Figure 1-2).

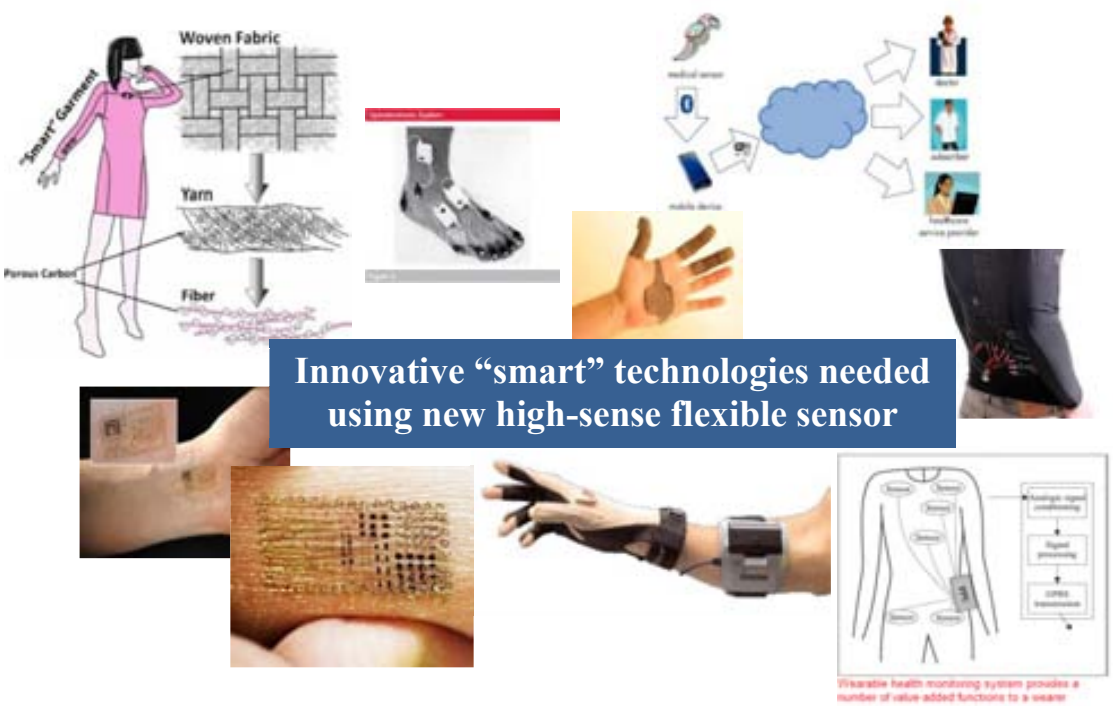

Figure 1-2. Potential applications for innovative flexible lightweight sensors.

Objectives

The two main goals of this Thesis are: (1) developing lightweight, flexible, and all-organic sensing materials that use electrical detection principles and (2) engineering simple prototypes that may use such sensing materials for pressure, temperature and relative humidity monitoring.

When this Thesis was started, the preparation and properties of highly piezoresistive BL films composed of a polycarbonate (PC) matrix "self-metallized" with a polycrystalline layer of the organic molecular metal β-(BEDT-TTF)$_2$I$_3$ (were BEDT-TTF = bis(ethylenedithio)tetrathiafulvalene) had been reported (Figure 1-3). [38] This BL film shows ability to sense tiny uniaxial deformations down to a minimum relative strain value of 10^{-4} %. This value was well below those of many conventional metal foil strain gauges.[39] **In this context, covering polymeric films with organic molecular conductors different from β-(BEDT-TTF)$_2$I$_3$ was used as one of the key approach to achieve the first goal of this research project: the development of lightweight, flexible, and all-organic sensing materials with an electrical detection principle.**

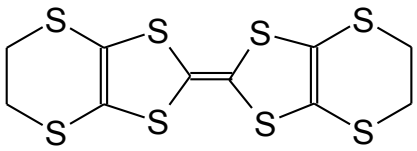

Figure 1-3. Formula of BEDT-TTF.

To accomplish such a main goal we proposed the following six steps.

Step 1. Improve the preparation and sensing properties of the BL films. It should be noted that the discovery of the sensor properties of BL films does not result automatically in their applications, since many other accompanying properties are required. To demonstrate the capability of the BL films to be used as active components for flexible sensing devices it is necessary to perform an in-depth study of both the synthetic procedure of BL films and their response to external stimuli.

Step 2. Study of the electromechanical properties of the BL films. Despite of a lot of crystalline organic molecular conductors have been synthesized and the physics of low dimensional conducting systems have been deeply studied over the years, there is a scant information about their mechanical properties which are of great importance for their processing and engineering. In addition, there are no data on the mechanical behavior of polymeric films covered with organic molecular conductors and its relationship with their conducting properties. Therefore the characterization of electromechanical properties of such materials was a matter of a large interest.

Step 3. Understand the formation of the BL films. Although numerous articles on all-organic conducting BL films were published during last years,[29, 40-44] the formation of sensing layers of molecular conductors was little understood. To get insight through this point and to engineer properly the BL films (Figure 1-4) with the desired electrical properties, the processing parameters, such as temperature and time of halogen/solvent annealing of the conductive layer formation, needed a deeper study.

Step 4. Develop humidity and temperature sensors based on the BL films. Until recent times the response of the electrical resistance of BL films to humidity was rarely studied. The importance of this study is obvious on the light of their applications at different ambient conditions. One cannot but infer that the advanced combination of the physical properties of the developed BL films may give a momentum to engineering novel flexible humidity and strain sensors for innovative hi-tech biomedical applications. In this context,

we set out an objective to achieve the obtaining of new BL films that may be used as either humidity and/or temperature sensors.

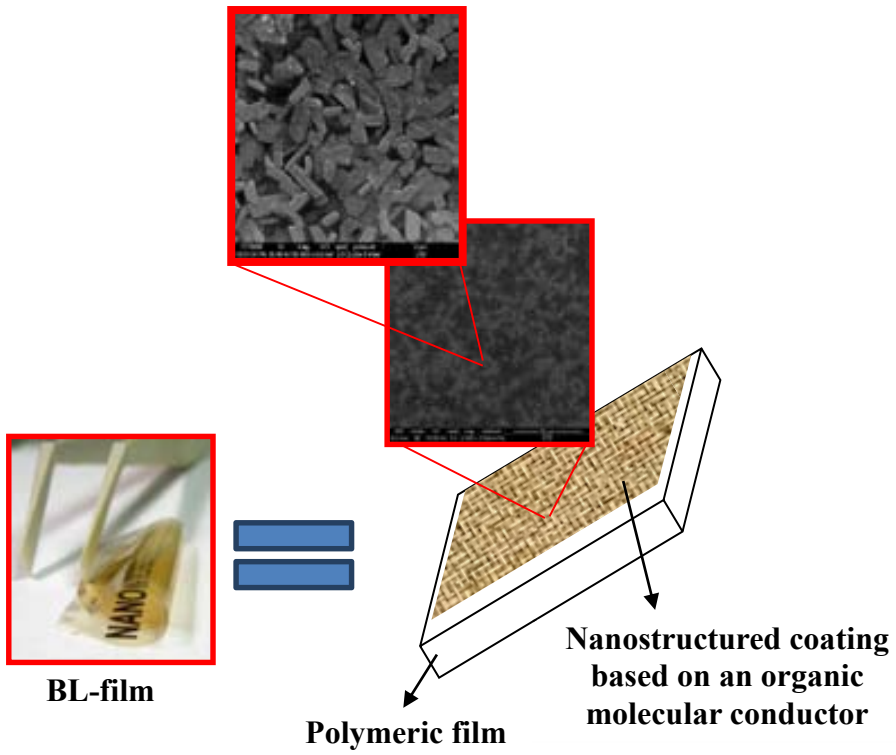

Figure 1-4. Schematic view and photo images (top and bottom-left) of a typical BL film.

Step 5. Develop of cheap sensors based on the BL films. Design and preparation of novel BL films with lower costs is also another big challenge in the field. From the commercial point of view, the use of TTF (TTF= tetrathiafulvalene) (Figure 1-5) instead of BEDT-TTF may significantly reduce the costs of sensing films because the gram-scale production of TTF is much less expensive than that of BEDT-TTF. The development of BL films with an active conducting layer formed by conductive charge transfer salts based on TTF was another important aspect of the Thesis. Taking into account that TTF charge transfer salts have one-dimensional (1D) electronic state, the study of electromechanical properties of the BL films formed by 1D molecular conductor may have also a special interest for understanding some of the physics of low dimensional conductors.

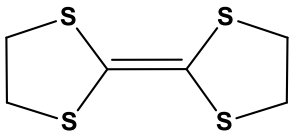

Figure 1-5. Formula of TTF.

Step 6. Increase of sensitivity of sensors based on the BL films. BL films with a conducting layer based on an amorphous molecular material is also an important goal because an amorphous material will be able to keep conductive covering layers free from problems associated with polymorphism and grain boundaries since there will be no preferred orientation for the crystals to allow conductivity. According to this the BL film covered with single component organic molecular conductors, which is depicted in Figure 1-6 became also a goal of the Thesis since they could increase the sensitivity of the BL films.

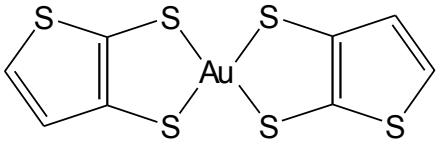

Figure 1-6. Formula of $[Au(\alpha\text{-tpdt})_2]^0$.

The development of various sensor architectures allowing the use of different operated principles as a holistic approach to achieve the second main objective of the Thesis: the engineering of simple prototypes using the BL films for sensing pressure, temperature and relative humidity.

It is obvious that for a proper response of the sensing devices not only a high sensitive material is required, but also the engineering of the prototype and sensor itself should be optimized to achieve a better detection of the external stimuli. Numerous factors should be taken into account to construct sensing prototypes. Among the most important we may mention: (i) optimum size of the sensing active element; (ii) the increase of both the sensitivity and repeatability of BL film-based devices; (iii) the decrease of their response time to strain, temperature and humidity changes; (iv) to improve of the electrical contacts that communicate the sensing element with a device; (v) the transfer the sensing BL films into different supports, like textile, plastics, glass, metals; and (vi) the transfer a conducting layer of a BL film from its parent polymeric matrix to other supports maintaining their sensing behavior.

The structure of this Thesis is divided into eight chapters. A general introduction of the Thesis and the motivation and objectives of the research are given in Chapter 1. Chapter 2 presents a complete analysis of the mechanical and electro-mechanical properties of thin layers of α-, and β_H-$(BEDT\text{-}TTF)_2I_3$ molecular conductors and their engineering to prepare

strain sensing materials. Chapters 3 and 4 provide the results on the formation, the structure determination and sensitivity to strain of BL films covered with $(TTF)I_{0.7\pm\delta}$ salt and the single component organic molecular conductor $[Au(\alpha\text{-tpdt})_2]^{0,}$ where tpdt=2,3-thiophenedithiolate complex. Chapter 5 discusses the different attempts to use the BL films covered with α'-$(BEDT\text{-}TTF)_2I_xBr_{(3-x)}$ as a temperature sensing material for a precise temperature monitoring. Chapter 6 shows the results obtained for the BL films covered with $(BEDT\text{-}TTF)_xBr_y(H_2O)_n$ and their sensitivity to humidity. The possibility to cover scalped surfaces by a polycrystalline layer of organic molecular conductors is discussed in Chapter 7. Materials and experimental techniques used for the growth and characterization of BL films and single crystals are presented in Chapter 8. The Thesis concludes with a Annex getting the results for obtaining single crystals of conducting $(TTF)I_{0.7+\delta}$ and $(BEDT\text{-}TTF)_2Br(H_2O)_3$ salts.

Bibliography

1. N. V. K. Sergey Y. Yurish, Igor L. Myshkin, World sensors and MEMS markets: analysis and trends, Sensors & Transducers Magazine (S&T e-Digest), 2005, 62, 456-461.

2. F. Axisa, P. M. Schmitt, C. Gehin, G. Delhomme, E. McAdams and A. Dittmar, Flexible technologies and smart clothing for citizen medicine, home healthcare, and disease prevention, Ieee Transactions on Information Technology in Biomedicine, 2005, 9, 325-336.

3. J. Sungchul and F. B. Daniel, Adhesion mechanisms of nanoparticle silver to substrate materials: identification, Nanotechnology, 2010, 21, 055204.

4. M. Leonardi, P. Leuenberger, D. Bertrand, A. Bertsch and P. Renaud, First steps toward noninvasive intraocular pressure monitoring with a sensing contact lens, Invest Ophthalmol Vis Sci, 2004, 45, 3113-3117.

5. R. E. Southward and D. W. Thompson, Inverse CVD: A novel synthetic approach to metallized polymeric films, Advanced Materials, 1999, 11, 1043-1047.

6. T. Oekermann, T. Yoshida, H. Minoura, K. G. U. Wijayantha and L. M. Peter, Electron transport and back reaction in electrochemically self-assembled nanoporous ZnO/dye hybrid films, Journal of Physical Chemistry B, 2004, 108, 8364-8370.

7. M. Durr, A. Schmid, M. Obermaier, S. Rosselli, A. Yasuda and G. Nelles, Low-temperature fabrication of dye-sensitized solar cells by transfer of composite porous layers, Nature Materials, 2005, 4, 607-611.

8. T. Yamaguchi, N. Tobe, D. Matsumoto and H. Arakawa, Highly efficient plastic substrate dye-sensitized solar cells using a compression method for preparation of TiO2 photoelectrodes, Chemical Communications, 2007, 4767-4769.

9. T. Miyasaka, M. Ikegami and Y. Kijitori, Photovoltaic performance of plastic dye-sensitized electrodes prepared by low-temperature binder-free coating of mesoscopic titania, Journal of the Electrochemical Society, 2007, 154, A455-A461.

10. H. C. Weerasinghe, P. M. Sirimanne, G. V. Franks, G. P. Simon and Y. B. Cheng, Low temperature chemically sintered nano-crystalline TiO_2 electrodes for flexible dye-sensitized solar cells, Journal of Photochemistry and Photobiology a-Chemistry, 2010, 213, 30-36.

11. A. R. Madaria, A. Kumar, F. N. Ishikawa and C. W. Zhou, Uniform, highly conductive, and patterned transparent films of a percolating silver nanowire network on rigid and flexible substrates using a dry transfer technique, Nano Research, 2010, 3, 564-573.

12. S. Pimanpang, P. I. Wang, G. C. Wang and T. M. Lu, Self-assembled monolayer growth on chemically modified polymer surfaces, Applied Surface Science, 2006, 252, 3532-3540.

13. J. M. Williams, Organic Superconductors (including Fullerenes): Synthesis, Structure, Properties, and Theory, Prentice Hall, 1992.

14. R. P. Shibaeva and E. B. Yagubskii, Molecular conductors and superconductors based on trihalides of BEDT-TTF and some of its analogues, Chemical Reviews, 2004, 104, 5347-5378.

15. D. Jerome, Organic conductors: From charge density wave TTF-TCNQ to superconducting $(TMTSF)_2PF_6$, Chemical Reviews, 2004, 104, 5565-5591.

16. G. Saito, in Organic Molecular Solids: Properties and Applications, CRC Press, 1997.

17. H. Akamatu, H. Inokuchi and Y. Matsunaga, Electrical conductivity of the perylene-bromine complex, Nature, 1954, 173, 168-169.

18. J. Ferraris, V. Walatka, Perlstei.Jh and D. O. Cowan, Electron transfer in a new highly conducting donor-aceptor complex, Journal of the American Chemical Society, 1973, 95, 948-949.

19. S. S. P. Parkin, E. M. Engler, R. R. Schumaker, R. Lagier, V. Y. Lee, J. C. Scott and R. L. Greene, Superconductivity in a new family of organic conductors, Physical Review Letters, 1983, 50, 270-273.

20. P. M. Chaikin, J. F. Kwak, T. E. Jones, A. F. Garito and A. J. Heeger, Thermoelectric power of tetrathiofulvalinium tetracyanoquinodimethane, Physical Review Letters, 1973, 31, 601-604.

21. E. B. Yagubskii, I. F. Shchegolev, V. N. Laukhin, R. P. Shibaeva, E. E. Kostyuchenko, A. G. Khomenko, Y. V. Sushko and A. V. Zvarykina, Supercinducting transition in the dielectric alpha-phase of iodine-doped $(BEDT-TTF)_2I_3$ compound, Jetp Letters, 1984, 40, 1201-1204.

22. X. Yan, M. J. Naughton, R. V. Chamberlin, S. Y. Hsu, L. Y. Chiang, J. S. Brooks and P. M. Chaikin, Rapid magnetic oscillations in an organic conductor - possibility of a new type of quantum oscillation, Physical Review B, 1987, 36, 1799-1802.

23. M. Tokumoto, H. Anzai, H. Bando, G. Saito, N. Kinoshita, K. Kajimura and T. Ishiguro, Critical field anisotropy in an organic superconductor beta-$(BEDT-TTF)_2IBr_2$, Journal of the Physical Society of Japan, 1985, 54, 1669-1672.

24. K. Bechgaard, C. S. Jacobsen, K. Mortensen, H. J. Pedersen and N. Thorup, Properties of 5 highly conducting salts - $(TMTSF)_2X$,X=PF_6-,ASF_6-,BF_4- AND NO_3^-, derived from tetramethyltetraselenafulvalene (TMTSF), Solid State Communications, 1980, 33, 1119-1125.

25. R. P. Shibaeva and E. B. Yagubskii, Molecular conductors and superconductors based on trihalides of BEDT-TTF and some of its analogues, Chem Rev, 2004, 104, 5347-5378.

26. E. Coronado and P. Day, Magnetic molecular conductors, Chemical Reviews, 2004, 104, 5419-5448.

27. G. Saito and Y. Yoshida, Development of conductive organic molecular assemblies: Organic metals, superconductors, and exotic functional materials, Bulletin of the Chemical Society of Japan, 2007, 80, 1-137.

28. J. K. Jeszka and A. Tracz, A new method of growing crystalline networks in polymer matrices by simultaneous CT complex formation and in situ crystallization, Polymers for Advanced Technologies, 1992, 3, 139-142.

29. E. Laukhina, C. Rovira and J. Ulanski, Organic metals as active components in surface conducting semi-transparent films, Synthetic Metals, 2001, 121, 1407-1408.

30. T. Haneda, A. Tracz, G. Saito and H. Yamochi, Continuous and discontinuous water release/intake of (BEDO-TTF)$_2$Br(H_2O)$_3$ micro-crystals embedded in polymer film, Journal of Materials Chemistry, 2011, 21, 1621-1626.

31. E. Laukhina, V. Tkacheva, I. Chuev, R. Wojciechowski, J. Ulanski, J. Vidal-Gancedo, J. Veciana, V. Laukhin and C. Rovira, Harnessing ICI reduction processes for synthesis of different BEDT-TTF-based molecular conductors, Journal of Physical Chemistry B, 2005, 109, 16705-16710.

32. A. Tracz, J. K. Jeszka, A. Sroczynska, J. Ulanski, J. Plocharski, H. Yamochi, S. Horiuchi and G. Saito, New transparent, colorless, metallically conductive polymer films and their electrochemical transformations, Synthetic Metals, 1997, 86, 2173-2174.

33. E. Laukhina, R. Pfattner, L. R. Ferreras, S. Galli, M. Mas-Torrent, N. Masciocchi, V. Laukhin, C. Rovira and J. Veciana, Ultrasensitive piezoresistive all-organic flexible thin films, Advanced Materials, 2010, 22, 977-+.

34. E. Laukhina, R. Pfattner, M. Mas-Torrent, C. Rovira, J. Veciana and V. Laukhin, Film-based sensors with piezoresistive molecular conductors as active components: Strain damage and thermal regeneration, Sensors and Transducers, 2011, 10, 1-12.

35. E. Laukhina, V. Lebedev, V. Laukhin, G. Oncins, R. Pfattner, C. Rovira and J. Veciana, in Solid-State Sensors, Actuators and Microsystems Conference (TRANSDUCERS), 2011 16th International 2011, pp. 1978 - 1981.

36. L. R. Ferreras, R. Pfattner, M. Mas-Torrent, E. Laukhina, L. Lopez, V. Laukhin, C. Rovira and J. Veciana, Highly piezoresistive textiles based on a soft conducting charge transfer salt, Journal of Materials Chemistry, 2011, 21, 637-640.

37. V. Laukhin, I. Sanchez, A. Moya, E. Laukhina, R. Martin, F. Ussa, C. Rovira, A. Guimera, R. Villa, J. Aguilo, J.-C. Pastor and J. Veciana, Non-invasive intraocular pressure monitoring with a contact lens engineered with a nanostructured polymeric sensing film, Sensors and Actuators a-Physical, 2011, 170, 36-43.

38. E. Laukhina, R. Pfattner, L. R. Ferreras, S. Galli, M. Mas-Torrent, N. Masciocchi, V. Laukhin, C. Rovira and J. Veciana, Ultrasensitive piezoresistive all-organic flexible thin films, Adv Mater, 2010, 22, 977-981.

39. Y. Nagase and Y. Nakamura, Fatigue gauge utilizing slip deformation of aluminium foil - (effect of material factor on the evolution of roughness), Jsme International Journal Series I-Solid Mechanics Strength of Materials, 1992, 35, 247-252.

40. J. K. Jeszka, A. Tracz, M. Kryszewski and J. Ulanski, Conducting organic composites - properties of melecular metals crystallized under diffusion-limited condituins, Synthetic Metals, 1988, 27, B115-B122.

41. J. K. Jeszka, A. Tracz, J. Ulanski and M. Kryszewski, Surface conductive polymer films by reticulate doping with organic metals, Journal of Physics D-Applied Physics, 1985, 18, L167-L170.

42. E. Laukhina, J. Ulanski, A. Khomenko, S. Pesotskii, V. Tkachev, L. Atovmyan, E. Yagubskii, C. Rovira, J. Veciana, J. Vidal-Gancedo and V. Laukhin, Systematic study of the $(ET)_2I_3$ reticulate doped polycarbonate film: Structure, ESR, transport properties and superconductivity, Journal De Physique I, 1997, 7, 1665-1675.

43. J. Moldenhauer, U. Niebling, T. Ludwig, B. Thoma, D. Schweitzer, W. Strunz, H. J. Keller, P. Bele and H. Brunner, Thin films of BEDT-TTF and BEDO-TTF radical cation salts, Molecular Crystals and Liquid Crystals Science and Technology Section a-Molecular Crystals and Liquid Crystals, 1996, 284, 161-182.

44. U. Niebling, J. Steinl, D. Schweitzer and W. Strunz, Preparation of superconducting alpha-$(BEDT\text{-}TTF)_2I_3$ thin films by structural transformation of $(BEDT\text{-}TTF)_2I_3$ in an I_2 atmosphere, Solid State Communications, 1998, 106, 505-507.

Chapter 2

Developing piezoresistive bi-layer materials based on α- and β-(BEDT-TTF)$_2$I$_3$ molecular conductors for pressure and strain sensors

2.1. Introduction

This Chapter focuses on the study and engineering of BL films able to be used as flexible highly piezoresistive elements for strain/pressure sensing devices.

It should be noted that the design and manufacture of reliable and robust strain/pressure sensors is one of the more challenging tasks in the field of sensors, because of the growing demand for new applications. [1-3] Thus, there is a continuing need to lower the cost of sensors utilized for cheap strain and pressure sensing applications. To lower the cost without decreasing the efficiency of sensors, few components, less expensive materials and fewer manufacturing-processing steps are needed. For some other applications, size and weight constraints may be also an important, even more, than their cost. For example, in biomedicine, sensors for catheters must occupy a small volume or they cannot be used at all. [4-6] In addition, for biomedical applications sensors must be biocompatible and for this reason sensors made of organic materials look very promising. Most of organic pressure sensors reported up to now are composed of a polymeric material surfaced with a conducting polymeric layer. [7-10] The conducting polymeric layers of such composite materials are preferably grown electrochemically. [11, 12] Therefore, making sensitive covering layers based on conductive polymers requires the use of a specific electrochemical equipment as well as the deposition of conventional metallic conductors on the surface of the sensor. [7] These preparations have certain internal problems that must be worked out. Therefore, the adhesion between conducting layers, substrates, and electrodes, the growth of conductive polymer should be performed in a reproducible manner. Moreover, the conductive polymers tend to degrade rapidly at ambient conditions, resulting in sensors having only a relative short lifespan.

As it was mentioned in Chapter 1, covering a plastic substrate with crystals of organic molecular conductors,[13, 14] like the β_H-(BEDT-TTF)$_2$I$_3$, has opened a new strategy for preparing all-organic strain/pressure sensors. Over the years a lot of organic molecular conductors have been synthesized as single crystals and their physics was studied. [15-20] It could be noted that such organic conducting crystals have deformable molecular and crystal structures with a strong electron–phonon coupling. Due to the soft nature of such crystals their anisotropic electronic structures show many fascinating electronic and structural phase transitions caused by lattice deformations, which can be controlled by external stimuli such as light, temperature, pressure, humidity, etc.[21-33] These characteristics open the possibility to use them as strain/pressure sensors.

Young's moduli, as well as other elastic constants, determine the response of any material and crystal to external forces providing important information on their mechanical properties. Therefore, a detailed study of the relationship between the anisotropy of Young's modulus of $(BEDT\text{-}TTF)_2I_3$ crystals and their crystalline structures is essential to understand their influence on a sensing capability of materials as well as on electromechanical properties of these crystals and BL films.

In this Chapter the study of electromechanical properties of α- and β_H- $(BEDT\text{-}TTF)_2I_3$ molecular conductors, which were prepared as single crystals and as covering layers of BL films, are presented. The relationship between anisotropy of Young's modulus of both α- and β_H-$(BEDT\text{-}TTF)_2I_3$ crystals and their molecular and crystalline structures are discussed. Moreover the development of BL films with desirable elastic, electronic transport properties based on both crystalline phases is also presented. Several approaches to design prototypes of strain sensors with the BL films as an active component are also reported.

2.2. Mechanical properties of α- and β_H-$(BEDT\text{-}TTF)_2I_3$ crystals

Taking into account that the nanoindentation[34-36] is the most realistic tool at the present time to determine the elastic constants for small single crystals, we applied this method for measuring the Young's moduli of α- and β-$(BEDT\text{-}TTF)_2I_3$ single crystals along different crystallographic planes. For the measurements we used an Atomic Force Microscopy (AFM) tip as a nanoindentor operating in the force spectroscopic mode.

In line with a reported synthetic procedure, [37] a mixture of single crystals of both α- and β-phases of $(BEDT\text{-}TTF)_2I_3$ was prepared via oxidation of neutral BEDT-TTF with iodine in 1,1,2-trichloroethane (yield ≅ 80 %). Crystals with two different shapes – elongated and hexagonal plates – were obtained which were identified using X-ray diffraction technique (Table 2-1). X-ray data collected for the elongated plates (Figure 2-1, left) revealed the crystallographic parameters of the α-$(BEDT\text{-}TTF)_2I_3$ phase (Figure 2-1, right and Table 2-1), while the hexagonal plates (Figure 2-2, left) showed the typical parameters of the β-$(BEDT\text{-}TTF)_2I_3$ phase (Figure 2-2, right and Table 2-1).[38]

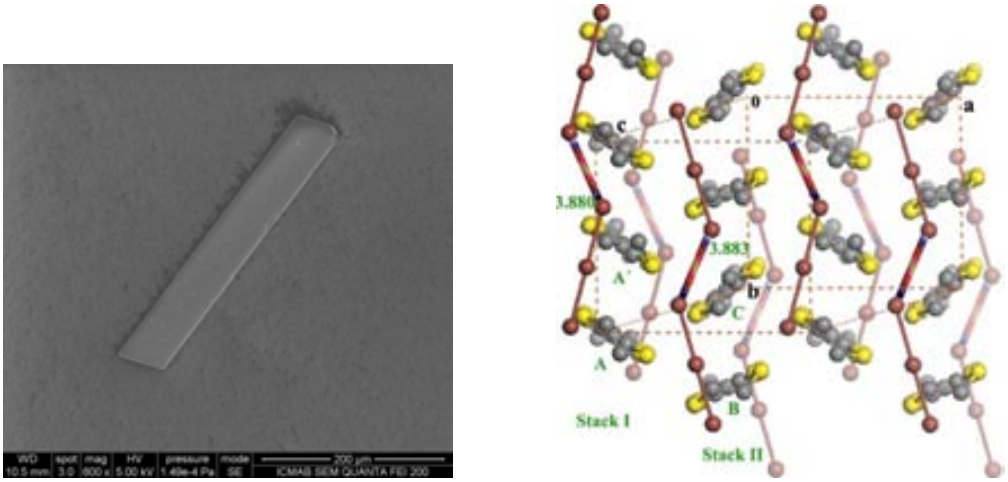

Figure 2-1. SEM image of an elongated plate crystal (left) and the view of the crystal structure of α-(BEDT-TTF)$_2$I$_3$ along the c*-axes where different molecules, stacks and chains, important for the mechano-structured analysis, are labeled (Data obtained from the CSD, code: CILHIO14). C, S, and I atoms are in grey, yellow, and red, respectively, H atoms are not shown.

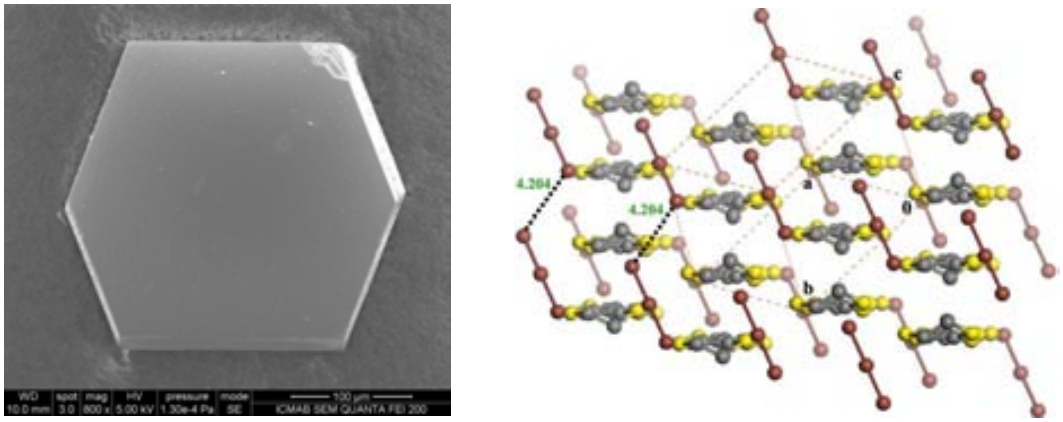

Figure 2-2. SEM image of a hexagon plate crystal (left) and the view of the crystal structure of β-(BEDT-TTF)$_2$I$_3$ along the c*-axes where different molecules, stacks and chains, important for the mechano-structured analysis, are labeled (Data obtained from the CSD, code: DATREV01). C, S, and I atoms are grey, yellow, and red, respectively, H atoms are not shown.

Concerning the macroscopic shape of the crystals, it should be noted, that under the surface-energy minimization criterion, the crystallographic planes (*001*) of α- and β-phases (Figure 2-3 andFigure 2-4) are parallel to their largest crystal faces. [39-41] Thus, the largest crystal faces of both phases coincide with their conductive *ab* planes while the thinner dimensions of crystals coincide with their crystallographic *c*-axes. [16, 42-44]

Table 2-1. Crystallographic parameters determined by X-ray of different single crystals of (BEDT-TTF)$_2$I$_3$ along the reported values for α- and β-phases.

	elongated plates	α-(BEDT-TTF)$_2$I$_3$[45, 46]	hexagonal plates	β-(BEDT-TTF)$_2$I$_3$[40, 47-49]
Lattice parameters				
a, Å	10.832(3)	10.785	6.603(3)	6.609
b, Å	9.202(3)	9.172	9.081(4)	9.083
c, Å	17.442(5)	17.389	15.251(6)	15.286
α, º	82.107(6)	82.02	85.68(1)	85.63
β, º	97.031(6)	96.92	95.60(1)	95.62
γ, º	89.039(7)	89.13	70.23(1)	70.22
V, Å	1708(1)	1690.3	852(1)	852.2

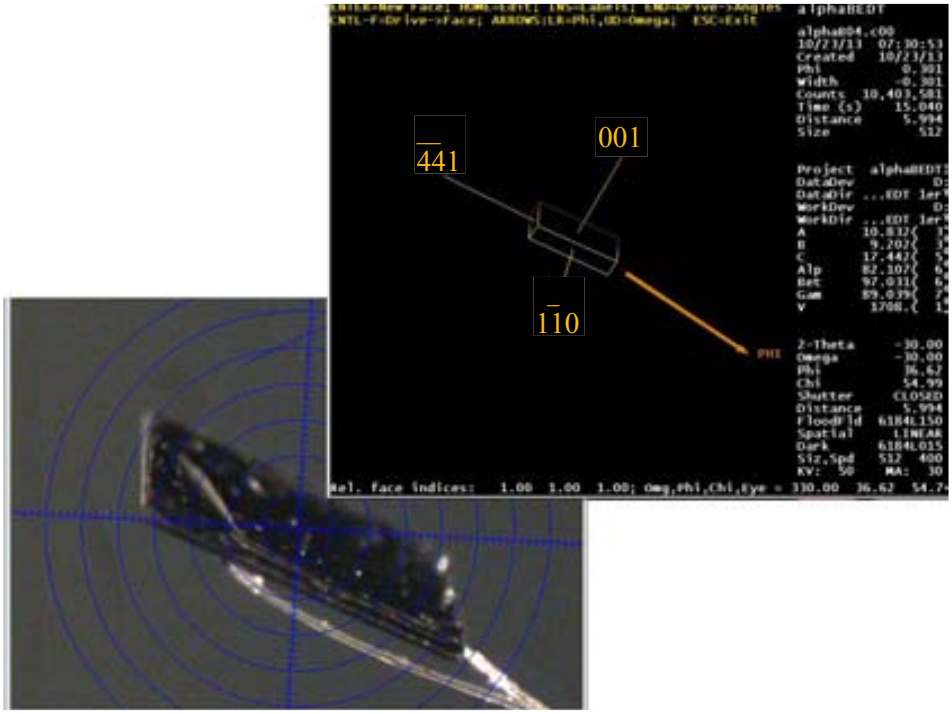

Figure 2-3. Images and crystallographic planes of α-(BEDT-TTF)$_2$I$_3$ single.

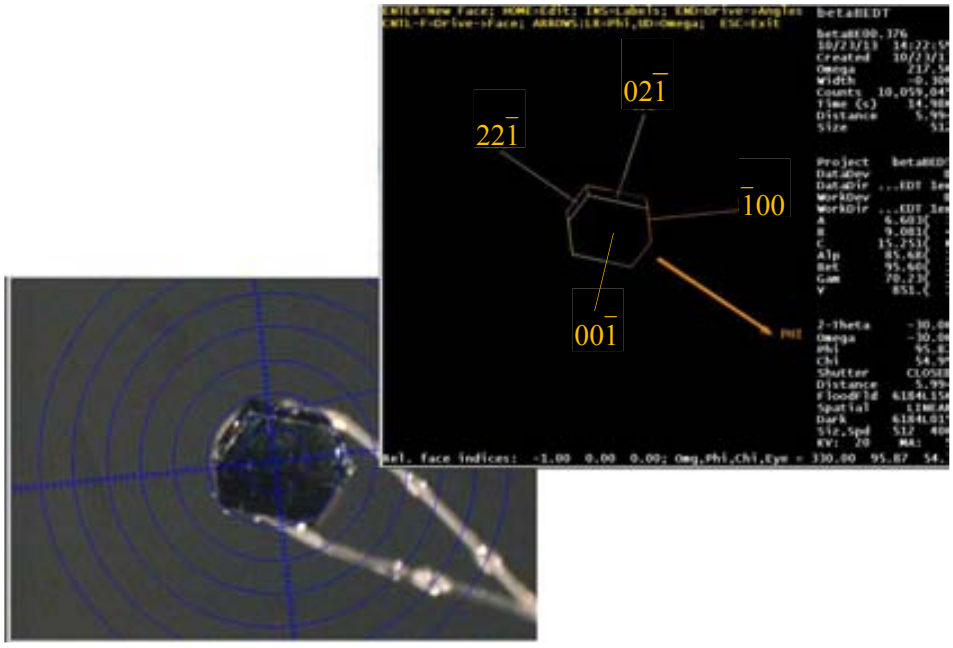

Figure 2-4. Images and crystallographic planes of β-(BEDT-TTF)$_2$I$_3$ single crystals.

To measure the Young´s moduli crystallographically oriented single crystals of both phases of (BEDT-TTF)$_2$I$_3$ were positioned in two different orientations with respect to the AFM tip; as it is schematically shown in Figure 2-5 and Figure 2-6. Orientations 1 and 2 are those where the AFM tip is perpendicular and parallel to the largest crystal face, respectively.

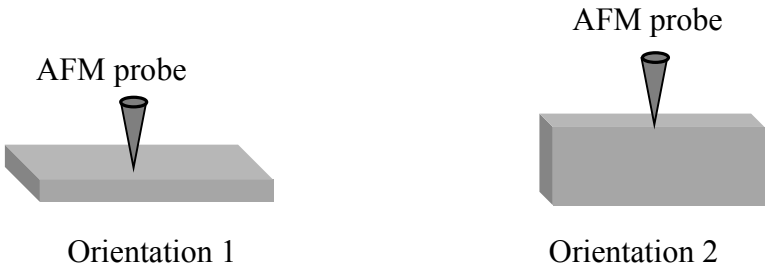

Figure 2-5. Schematic representation of two different orientations of the elongated plate-like crystal of α-(BEDT-TTF)$_2$I$_3$ used f or nanoindentation measurements. Left, (orientation 1) AF M pro be is perpendicular to the crystallographic (*001*) plane. Right, (orientation 2) AFM probe is parallel to the crystallographic (*001*) plane and perpendicular to the (*1-10*) plane.

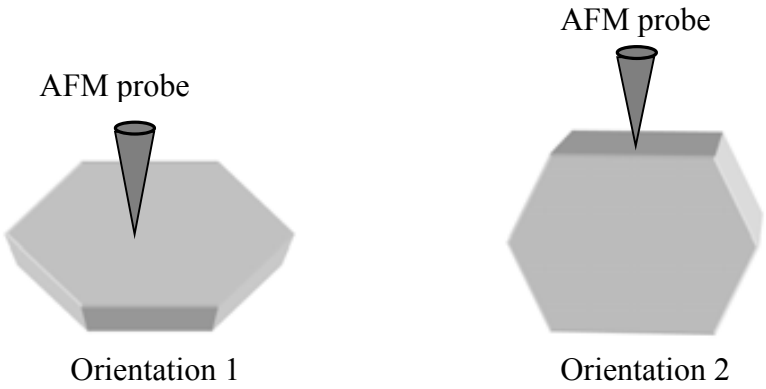

Figure 2-6. Schematic representation of two different orientations of the hexagonal plate-like crystal of β-(BEDT-TTF)$_2$I$_3$ used for the nanoindentation measurements. Left, (orientation 1) AFM probe is perpendicular to the crystallographic (*00-1*) plane. Right, (orientation 2) AFM probe is parallel to the crystallographic (*00-1*) and perpendicular to the (*02-1*) plane.

The nanomechanical characterization of soft crystalline materials requires the simultaneous measurement of the applied forces, ranging from 10^{-11} to 10^{-8} N, and of the resulting deformation of the crystal with a sub-nanometric accuracy. For each sample, force values necessary to provoke a plastic deformation (permanent deformation) was experimentally assessed and topographically detected as a resulting hole in the crystal sample surface. Then, the applied force (F) value for the mechanical measurements were set to be 70% of this plastic-onset F value to ensure that all the mechanical measurements are fully inside the elastic deformation region. In all cases applied F values of 250 nN were chosen. In order to obtain statistically representative results, one force curve was performed in each sample location so as to ensure that the previous mechanical tests did not change the local mechanical response of the sample and then a minimum of 200 individual experiments were performed for each crystal sample. In order to extract the Young's moduli (E) value from each extension force curve, the Hertz model that considers a spherical tip of radius *r* was applied. When a sample is indented, if the resulting deformations are sufficiently large but not so large as to cause plastic deformation, the results from classical continuum elasticity theory may be applied. In the Hertz model [50-52] it is assumed a spherical tip indenting a homogeneous and isotropic elastic material as

$$F = \frac{4E^* R^{0.5} \delta^{1.5}}{3} \qquad \text{eq (2.1)}$$

where F is the force applied to cause an elastic indentation depth, δ. R is the radius of the spherical indenter and E^* is the complex or reduced modulus. E* is a function of both Young's moduli of the sample and the tip, E_{sample} and E_{tip}, and Poisson's ratios, ν_{sample} and ν_{tip}, respectively, where

$$\frac{1}{E^*} = \frac{1-\nu_{sample}^2}{E_{sample}} + \frac{1-\nu_{tip}^2}{E_{tip}} \qquad \text{eq (2.2)}$$

Reported values of Young's moduli are extracted from the force-displacement curves collected during the nanoindentation, as follows. Force-indentation data were collected on three different single crystals of α- and β_H-$(BEDT\text{-}TTF)_2I_3$ phases prepared under identical conditions. The data collected for three crystals of both phases, shown in Figure 2-7, where obtained at two different orientations: one perpendicular to the conducting *ab* plane and another parallel to it.

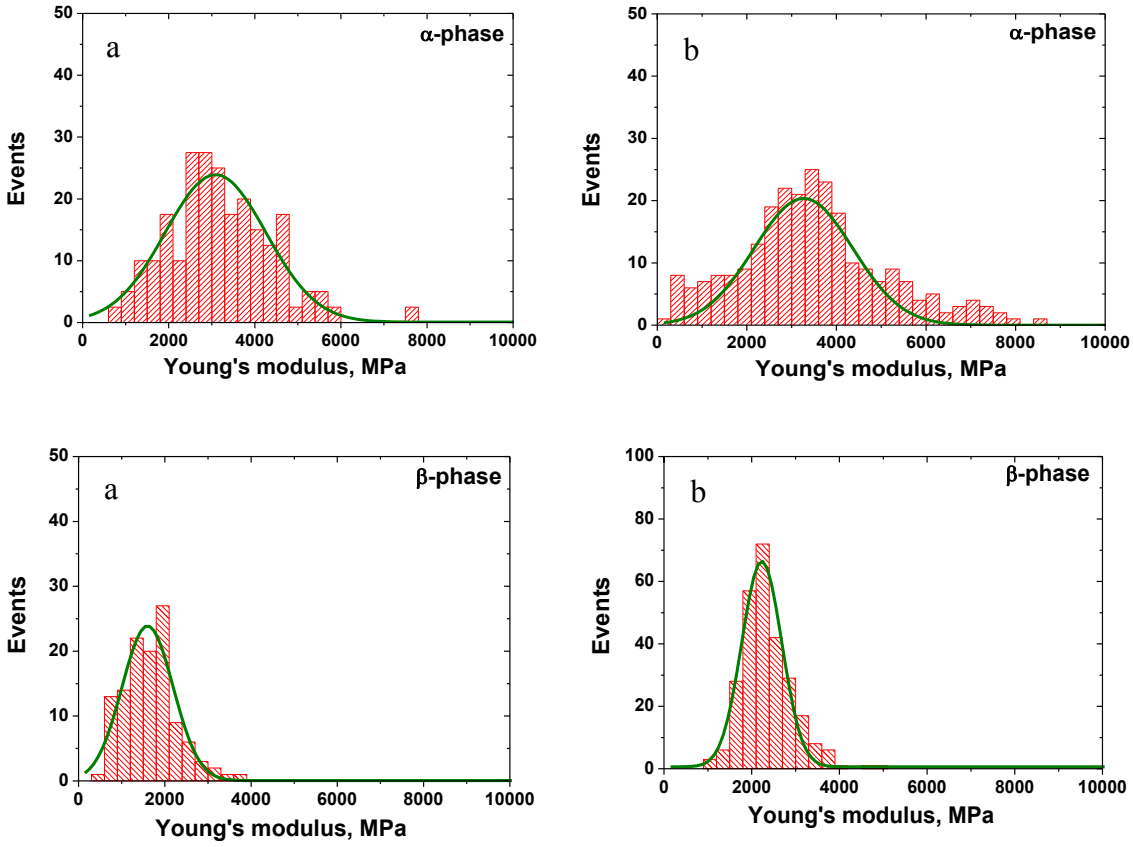

Figure 2-7. Distribution of Young´s modulus values and Gaussian fits for α-$(BEDT\text{-}TTF)_2I_3$ (top) and β-$(BEDT\text{-}TTF)_2I_3$ (bottom) crystals measured perpendicular to the conducting *ab*-plane (a) and along to it (b).

Experimental results, summarized in Table 2-2 clearly demonstrated that the β-phase exhibits highly anisotropic mechanical properties since the elastic modulus in the direction perpendicular to the conducting *ab* plane [or the crystallographic plane (00-1)] is 30 % smaller than that parallel to it. In contrast, the α-phase did not show any remarkable anisotropy of the mechanical properties along the two studied directions since the difference between elastic modulus measured perpendicular to conducting *ab* plane and along it is only of 6 %. The mechanical difference observed for two phases of (BEDT-TTF)$_2$I$_3$ may be rationalized in light of the various specific intermolecular interactions present in the crystals which are unique for each phase. Here it should be noted that many researchers pointed out the key role of C-H···I hydrogen bonds in dictating the structural and physical behaviors of both α and β crystal phases of (BEDT-TTF)$_2$I$_3$. [16, 53, 54]

Table 2-2. Mean values of Young's moduli of the single crystals of α-and β$_H$-(BEDT-TTF)$_2$I$_3$ along two different crystal directions.

Phase of (BEDT-TTF)$_2$I$_3$	Young´s modulus, GPa	
	position 1: (⊥ conducting *ab* plane)	**position 2**: (∥ conducting *ab* plane)
α	3.09±1.10	3.27±1.10
β$_H$	1.60±0.59	2.23±0.45

To analyze correctly the relationship between the measured elastic constants of α- and β-phases and their structural characteristics, a consideration must be given to possible structural changes that may occur locally under nanoindentation. We estimate that during the nanoindentation experiments the pressure applied by the AFM probe is of 1.2 GPa. As for α-(BEDT-TTF)$_2$I$_3$, it has been showed that up to a 1.8 GPa isostatic pressure no structural phase transition occurs; based on the pressure dependence of lattice parameters presented by I. Tamura et al.[30] Indeed, there is no large distortions in the BEDT-TTF molecules and two crystallographically independent I-I bond lengths decrease rather monotonically with increasing pressure. Therefore, it is reasonable to assume that the pressure applied by the AFM probe (1.2 GPa) does not result in any structural phase transition. The Young's modulus of α-(BEDT-TTF)$_2$I$_3$ (Table 2-2), which is a measure of how soft the crystal lattice is toward deformation along and perpendicular to the conducting

ab plane, clearly shows that the stiffness produced by a set of short hydrogen bonds C-H···I forming the donor-anion interface[53] is comparable with that of a set of short contacts (C-H···C, S···S, I···I) in the donor-donor interface. [22, 53, 54] Therefore, the short hydrogen bonds involving anions are enough strong to provide a crystalline structure that exhibit a small anisotropy in its mechanical properties.

When looking at a pressure diagram of single crystal of β-(BEDT-TTF)$_2$I$_3$ under isostatic conditions,[23] it is easily to see that the β-phase is transformed into the β$_H$-phase above a pressure of 0.05 GPa (≅500 bars). Additionally it was showed that defects of crystals that can be introduced in different ways also provoke the formation of β$_H$-phase.[39] Considering these points, we assumed that the elastic constants measured using nanoindentation correspond to the β$_H$-phase rather that to the β-one. In the following, we will examine the structural features of β$_H$-phase in order to relate them with the softness of their crystalline lattice. In this connection it should be noted that under a pressure greater than 0.05 GPa, each eclipsed BEDT-TTF molecule of the β-(BEDT-TTF)$_2$I$_3$ phase undergoes a conformational flipping at one of the two ethylene groups, so that all BEDT-TTF molecules forming the donor-donor interface of β$_H$-phase have staggered conformations.[18 55] The reported data[55] also demonstrate that, although BEDT-TTF molecules in the BEDT-TTF network change very little under pressure, the short hydrogen bonds C-H···I, which form the donor-anion interface and which are responsible for the lattice softness in the direction perpendicular to the conducting *ab* plane, become significantly longer (softer) when BEDT-TTF molecules adopted the staggered conformation (Table 2-4).

Table 2-3. Short contacts in α-(BEDT-TTF)$_2$I$_3$ crystal structure.

along *ab*-plane, Å					perpendicular to *ab*-plane, Å
donor-donor				anion-anion	donor-anion
C-H···H	C-H···C	C-H···S	S···S	I···I	C-H···I
<2.4	<2.9	<3.0	(3.5-3.7)x6	3.88 3.89	2.85; 2.93 2.91; 2.91

The observed anisotropy of Young's moduli for the β$_H$-(BEDT-TTF)$_2$I$_3$ phase (Table 2-2) pointed out that the stiffness of these shortest C-H···I bonds is remarkable less comparable

with that of the short contacts (C-H···C and S···S) in the donor-donor interface that in turn contributes to the formation of the lattice with highly anisotropic mechanical properties. As illustrated Table 2-3 and Table 2-4, the C-H···I bonds of β_H-(BEDT-TTF)$_2$I$_3$ are also remarkably longer in comparison with those of α-phase. Moreover, the latter phase has shorter C-H···C bonds and additional I···I interunit contacts. These structural peculiarities of α-(BEDT-TTF)$_2$I$_3$ are mainly responsible for the higher stiffness of its lattice in comparison with that of the β_H-phase. Thus, elastic modulus of α-phase in the direction perpendicular to conducting *ab* plane, were the hydrogen C-H···I bonds construct the donor-anion interface, is almost twice higher than that of β_H-phase (Table 2-2).

Table 2-4. Short contacts in β_H-(BEDT-TTF)$_2$I$_3$ crystal structure.

along *ab*-plane, Å					perpendicular to *ab*-plane, Å
donor-donor				anion-anion	donor-anion
C-H···H	C-H···C	C-H···S	S···S	I···I	C-H···I
<2.4	<2.9	<3.0	(3.5-3.6)x6	–	2.83 3.00 3.05

The difference between Young's moduli of α- and β_H-phases along the conducting *ab* planes is significantly large. Indeed the value of Young's modulus of β_H-phase is about 45 % smaller than that determined for α-phase. Therefore, our experimental data confirm numerous previous suggestions given by E.Laukhina at el. [37, 56, 57] Then, the longitude of the short C-H···I$^-$ contacts drastically affects the softness and anisotropy of the lattice of (BEDT-TTF)$_2$I$_3$-based molecular conductors. The elastic constants of the two phases of the (BEDT-TTF)$_2$I$_3$ salt are remarkable because its values of ca. 1.6-3.3 GPa are similar to these of many commercial polymers such as polycarbonate (2.3 GPa), polyimide (2.5 GPa), polystyrene (3.5 GPa) and poly(methylmethacrylate) (1.8-3.1 GPa). This result is interesting since the similarity of the elastic properties of layered components is one of the key requirements for allowing highly robust electronic layered composites. Consequently, covering polymeric films with thin layers of (BEDT-TTF)$_2$I$_3$ has to result in flexible conducting materials whose robustness should be significantly higher than that of polymeric films metalized with conventional metals, such as copper (117 GPa,), gold (80 GPa) and platinum (168 GPa), which commonly used in flexible electronics.[58, 59]

2.3. Mechanical properties of bi-layer films based on α- or β_H-(BEDT-TTF)$_2$I$_3$ molecular conductors

It is known that the mechanical properties of bulk materials and thin layers can be different. For instance, for Au, Pt and Pd films, the elastic moduli (E) are about 12%, 12% and 7 %, respectively, lower than the respective bulk elastic moduli.[60] For this reason we addressed to measure the mechanical properties of BL films with α- and β_H-(BEDT-TTF)$_2$I$_3$ crystallites.

Preparation and characterization of BL films. To determine such mechanical properties we first prepared three representative BL film samples using polycarbonate (PC) as a polymeric component of BL films with a polycrystalline layer of β_H-(BEDT-TTF)$_2$I$_3$ and two others with a polycrystalline layer of α-(BEDT-TTF)$_2$I$_3$ that differ in their textures and thickness. The two latter BL films were prepared with a single-stage procedure,[37, 61] using a casted thin film (20 μm in thickness) of a solid solution of 2 % of neutral BEDT-TTF completely dispersed in polycarbonate. The film surfaces of such casted films were vapor annealed with a saturated solution of iodine in CH_2Cl_2 at two different temperatures – 7 and 33 °C – leading to the formation of two BL films with different thicknesses of the active conducting layers. The BL film with a layer of the β-(BEDT-TTF)$_2$I$_3$ was prepared by a thermal annealing at 150 °C during an hour of a BL film with the α-phase prepared at 33 °C. This thermal annealing leads to the well-known structural phase transition of crystals of the α–phase to the β-one[37] forming a BL film with submicron sized crystallites of the β_H-(BEDT-TTF)$_2$I$_3$ phase.

The BL films were characterized by scanning electron microscopy (SEM) and powder X-ray diffraction (PXRD) techniques. SEM images (Figure 2-8) revealed the presence in all cases of networks of well-connected crystals with different sizes. So, the BL film prepared at 7 °C shows nanoscale crystallites of 50-200 nm, while the BL film prepared at 33 °C exhibits well-shaped submicron crystals with sizes of 200-600 μm. The powder X ray diffraction data presented in Figure 2-8 exhibit only the presence of very sharp (*00l*) reflections of either α-(BEDT-TTF)$_2$I$_3$ or β_H-(BEDT-TTF)$_2$I$_3$ crystals showing that the conductive layers have a high degree of a structural orientation and are formed exclusively by c^*-oriented α- and β_H-(BEDT-TTF)$_2$I$_3$ crystals, in agreement with previously reported data.[37] With this orientation the molecular conducting *ab* planes of the α- and β_H-(BEDT-TTF)$_2$I$_3$ crystallites are parallel to the film planes.

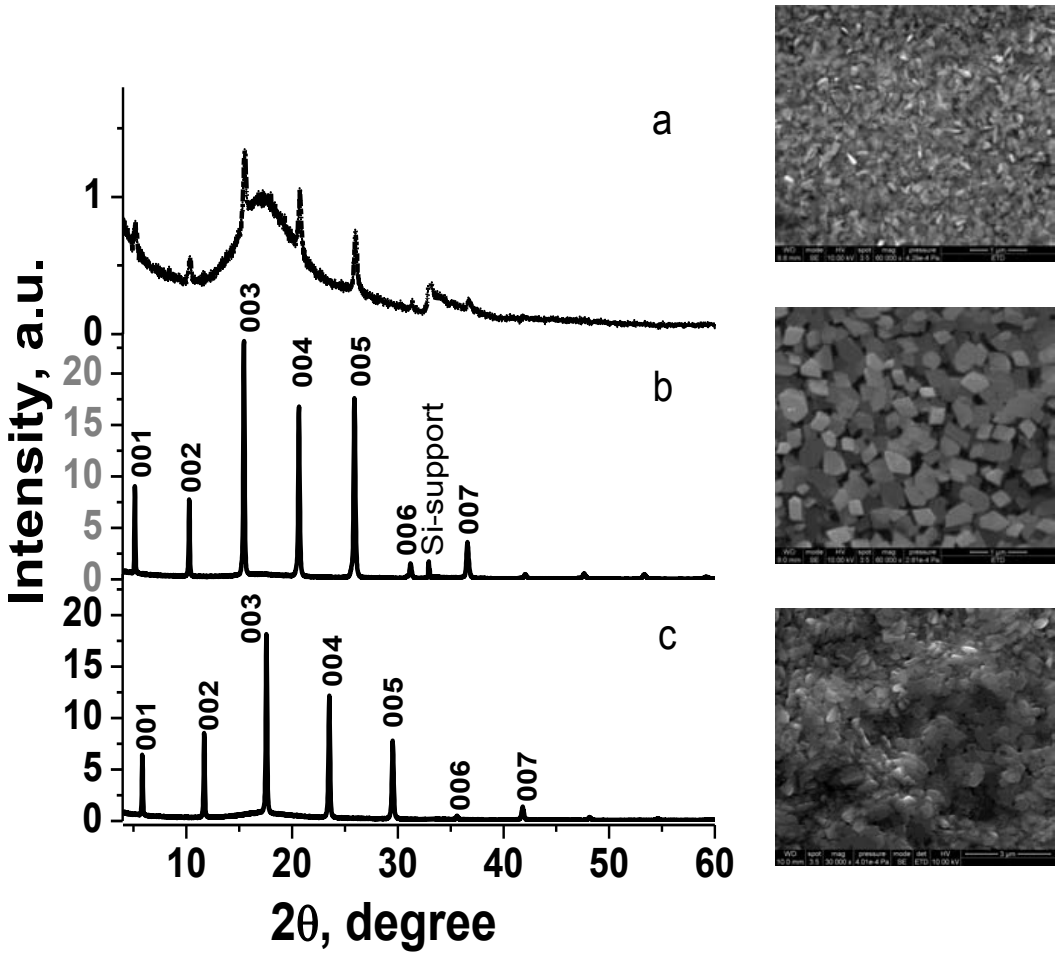

Figure 2-8. X-ray diffraction patterns (left) and SEM images (right) of BL films with α-(BEDT-TTF)$_2$I$_3$ prepared at the different temperatures of the iodine/solvent annealing: at 7 ºC (a), at 33 ºC (b) and of the BL film covered with β$_H$-(BEDT-TTF)$_2$I$_3$(c).

For a qualitative comparison purposes the PXRD data of all BL films were also collected using samples with the same area and with identical scan rates. Thereby, the intensity of X-ray reflections for such BL film samples are proportional to the mass of oriented crystals on the surface of the polycarbonate films. This fact permitted to estimate the relative thickness of the crystalline layer of the two prepared BL films with the α-phase. Then, a comparison of the intensity of (*005*) reflections observed in the BL films suggests that the thickness of the conducting layer prepared at low temperature is about 25 times less than that formed at 33 ºC.

The actual thickness of the conductive covering layers is quite more difficult to determine by direct measurements. Nevertheless it is possible to estimate an upper thickness limit of the crystalline layers of BL films[62] by making two assumptions: (1) all

the amount of BEDT-TTF, molecularly dispersed in a 20 μm thick polycarbonate film, participates in the crystal formation of the α-phase and (2) such α-$(BEDT\text{-}TTF)_2I_3$ crystals grows forming a single component crystalline layer only on the top of the polymer film. Assuming such points and in line with the chemical reaction for the formation of the salt – $4BEDT\text{-}TTF+3I_2=2(BEDT\text{-}TTF)_2I_3$, – a 2 % in weight of BEDT-TTF embedded in a polycarbonate film must form a 3 wt.% of the salt α-$(BEDT\text{-}TTF)_2I_3$ with a density 2.2 g/cm^3. [62] Taking into account that the polycarbonate density is 1.2 g/cm^3, [63] and the total density of the composite BL film is additive, the maximum mass of the conducting layer for a BL film sample with a 15×15 mm^2 size is estimated to be 0.165 mg. Therefore, the upper thickness limit for the layer of crystals, based on a geometric factor, is estimated to be about 330 nm. Based on these estimations and on the PXRD data one may suggest that the upper thickness limit (h) of the conductive layer of α-$(BEDT\text{-}TTF)_2I_3$ prepared at 33 and 7 °C are less than 330 and 13 nm, respectively. A similar estimation for conducting layer of the BL film with the β_H-$(BEDT\text{-}TTF)_2I_3$ salt gives upper thickness limit of ca. 330 nm.

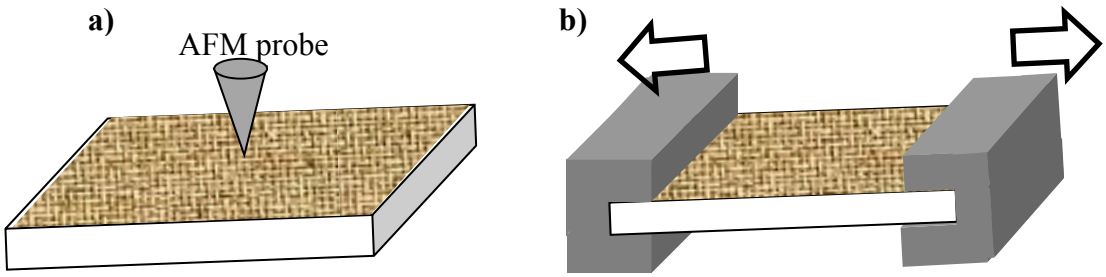

Figure 2-9. Schematic representations of the orientations of the BL films used for the mechanical testing with: a) the nanoindentation method, where the AFM probe is perpendicular to crystallographic plane (*001*) of the crystals in the conducting layer of the BL films and b) the tensile stress method.

2.3.1. Elastic constants of the BL films using the nanoindentation method

Once the three prepared BL films were morphologically and structurally characterized we proceeded to determine their elastic constants using two methods: a) the nanoindentation method with an AFM tip as a nanoindentor employing the force spectroscopic mode and b) the tensile strength method. Both methods are complementary since they provide the elastic constant of the BL films in two orthogonal directions, the nanoindentation method perpendicular to the surface of the BL film and the tensile strength method parallel to the surface (see Figure 2-9). According with the relative orientation of the crystals with respect

the surface of the BL film, the elastic constant given by nanoindentation will be along the crystallographic *c**-axis of the crystallites of the BL films while the other method will provide averaged data along the crystallographic *ab* plane of the crystals being therefore comparable with the data obtained for the single crystals of α- and β-phases.

Results of the mechanical measurements made with nanoindentation method on the three BL films and on a pure polycarbonate film with a similar thickness are depicted in Figure 2-10. Table 2-5 shows the average values of the Young's moduli for the four measured film samples together with the standard deviation as well as the corresponding Young's moduli for the single crystals along the crystallographic *c**-axis.

If one exclude the result obtained for the BL film with the α-phase prepared at 7 ºC, the rest of data are in agreement with the expectations for composite films composed by two layers of different nature. So, Young's moduli of the BL films with α- and β-phases are between those shown by PC and single crystals of such phases similarly oriented. Furthermore, the value of the elastic constant of the BL film with α-phase is higher than that with β-one as it was also observed for the single crystals. Surprisingly the elastic constant obtained for the BL film with α-phase prepared at 7 ºC deviates from such expectations since it exceeds that the single crystal of the α-phase similarly oriented. Although this result must be taken with care because of the large dispersion of data obtained during the measurements, it could be also related to the nanoscopic size of the crystallites and the small thickness of the crystalline layer in the BL film. Indeed, similar enhancements in the mechanical properties of materials when they are thinned have been reported for other nanocomposite materials.

Table 2-5. Young's moduli and physical dimensions of studied BL films and crystals.

Films	Crystallite sizes, µm	Young's modulus, GPa	Upper thickness limit, µm
α-(BEDT-TTF)$_2$I$_3$ (7 ºC)	0.05-0.20	3.8±0.8	0.013
α-(BEDT-TTF)$_2$I$_3$ (33 ºC)	0.20-0.20	1.9±0.8	0.33
β-(BEDT-TTF)$_2$I$_3$	0.40-0.60	1.0±0.5	0.33
PC film	–	0.8±0.2	20
Single crystals	dimensions, µm	Young's modulus, GPa	experimental thickness, µm
α-(BEDT-TTF)$_2$I$_3$	500x70	3.1±1.1	20
β-(BEDT-TTF)$_2$I$_3$	300x300	1.6±0.6	30

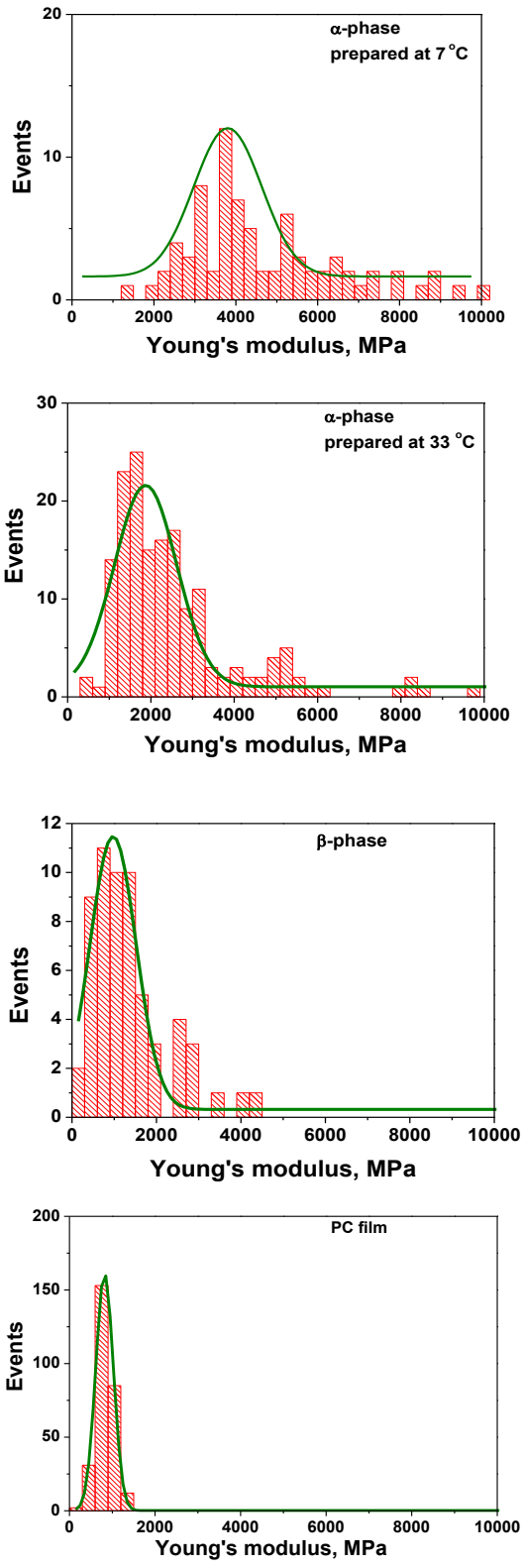

Figure 2-10. Young´s moduli values distribution and Gaussian fits for BL films covered with α-(BEDT-TTF)$_2$I$_3$ prepared at different temperatures 7 ºC (a) and 33 ºC (b) and with β-(BEDT-TTF)$_2$I$_3$ (c). The data for PC film are shown for comparison (d).

Indeed, Angadi et al.[64] also observed the increase in Young's modulus of MnTe and MnSe films with decreasing thickness when their thickness was less than 60 nm. Moreover, Torrent et al. recently reported[65] that there is a 70 % increase in elastic properties of the tris(8-hydroxyquinolinato)aluminium-based film when its thickness decrease from 20 to 10 nm. The authors attributed the increase in modulus of such thin films to variations in molecular packing of tris(8-hydroxy-quinolinato)aluminium as a function of the film thickness.

2.3.2. Elastic constants of the BL films using the tensile stress method

As already mentioned, the mechanical properties of the BL films were also studied using an equipment for tensile strength testing, equipped with a 1 kg load cell (5848 MicroTester, Instron). For such measurements, strips of the films with dimensions of ca. 28x2 mm^2 and free from physical imperfections were held between two clamps positioned at a distance of ca. 18 mm (Figure 2-11).

During the measurements, the strips were pulled by the top clamp with a constant velocity of 2.0 μm/s. The applied force and the resulting elongation were monitored up to the film samples were broken. Measurements were run with two replicates for each film. The stress-strain dependences of polycarbonate films covered with polycrystalline layers of α- and β_H-$(BEDT\text{-}TTF)_2I_3$, as well as of that of the pure polycarbonate film the same thickness (25 μm), are plotted in Figure 2-12. All three films showed the classical behavior of rigid plastic materials with values of the elastic limits (ε_{Yield}) well over 0.02%; a typical value observed for conventional metals.[66] Other interesting characteristic obtained from these measurements were the Young's moduli (E) and the ultimate tensile strength (UTS) values, which are summarized in Table 2-6.

Table 2-6. Characteristic mechanical parameters of the studied BL films.

Sample	Conducting layer	Young's modulus GPa		ε_{yield}, %	UTS, $N \cdot m^{-2}$ x10^7
		BL Films	Single crystals		
BL film	α-$(BEDT\text{-}TTF)_2I_3$ (33 °C)	1.90±0.20	3.27±1.10	1.2	3.33
BL film	β_H-$(BEDT\text{-}TTF)_2I_3$	1.46±0.20	2.23±0.49	1.2	3.42
PC	-	2.05±0.20	-	1.4	4.65

[a] Values obtained from measurements with single crystals at a direction parallel to the crystallographic *ab* plane by the nanoindentation method using the Atomic Force Microscopy.

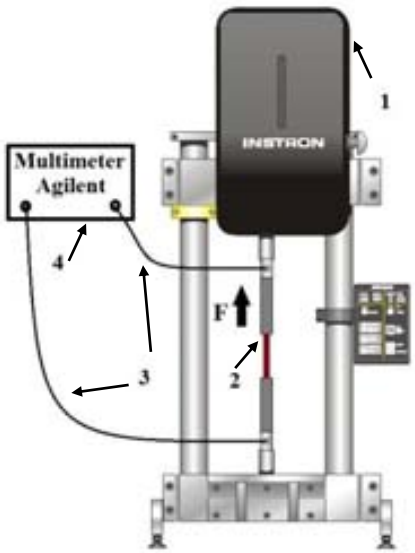

Figure 2-11. Schematic view of the used setup, equipped with electrical cables for carrying out tensile test with a simultaneous resistance monitoring: 1) Micro-tester (Instron 5848, 2); 2) BL film sample; 3) electrical connections and 4) the multimeter (Agilent 34401A).

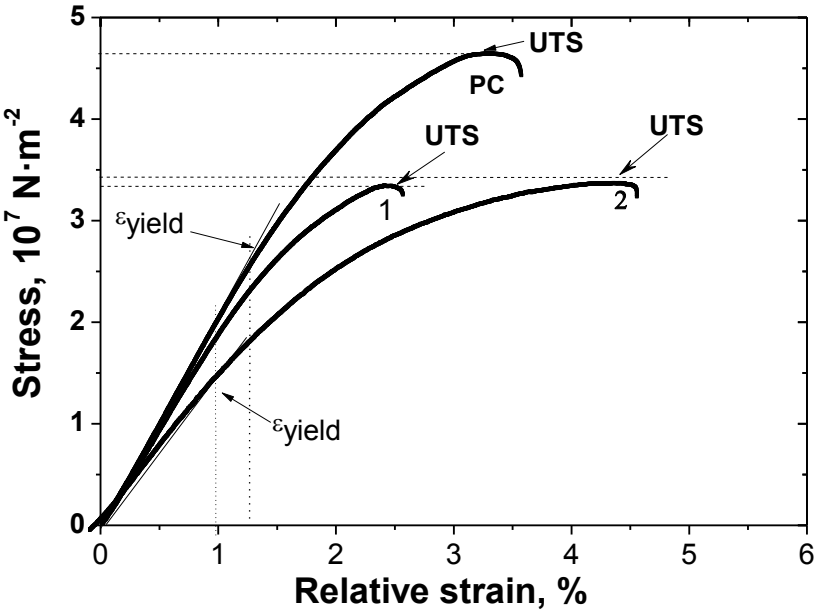

Figure 2-12. Full stress-strain curves of BL films with α- and β_H-$(BEDT\text{-}TTF)_2I_3$ (curves 1 and 2, respectively) as well as of a polycarbonate film (curve PC).

The Young's moduli of the two BL films were lower than that of the PC film being somewhat higher that of the BL film containing the α-$(BEDT\text{-}TTF)_2I_3$ crystals. This result is reasonable since the presence of crystals increases the softness of the film being such increase higher for the BL film with β-phase. The two BL films exhibit very similar values

of ε_{Yield} and of UTS being lower than the values observed for the PC film. In spite of the above mentioned differences, all important mechanical characteristics of BL films are close to those of PC-films. Therefore, the self-metallization of PC films with organic molecular metals did not affect adversely mechanical properties of polycarbonate films. [63]

2.4. Electromechanical properties of BL films based on α- and β_H-(BEDT-TTF)$_2$I$_3$ molecular conductors

To complete the characterization of the piezoresistive BL films the influence on the deformations on the electrical properties was studied. For such study the tensile strength measurements were coupled with direct resistance measurements with two electrical contacts. With this set up (Figure 2-11) the resistance changes under tensile testing were monitored in the elastic region of the material, using a multimeter connected via LAN bus to a computer.

Figure 2-13 shows that resistance changes versus strain for both BL films deviate from a linear trend at similar values of relative strain; *i.e.* ε = 0.60 and 0.65 %, for α- and β_H-(BEDT-TTF)$_2$I$_3$, respectively. By analogy with the elastic limit point, this point has been termed as the resistance elastic limit (R_{yield}). The appearance of the nonlinearity region at higher relative strain was associated with the formation of numerous nanocracks, as experimentally confirmed by appearance of the nanocracks with width of 60-100 nm perpendicular to the elongation direction at relative strain of 0.5 % (see Figure 2-13). [14] Interestingly, the resistance elastic limit value for both BL films were half of the values of the elastic limits (ε_{yield} =1.2%) indicating that the elastic limit of the network of crystals is smaller than that of the PC.

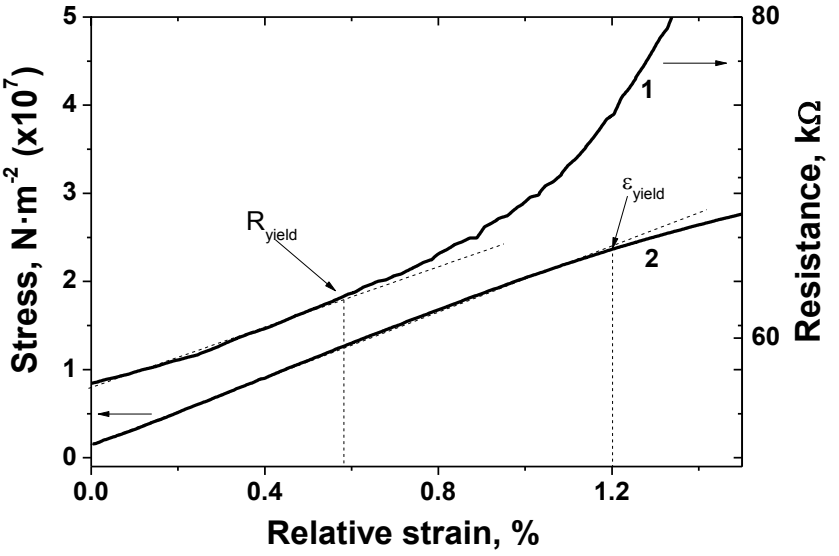

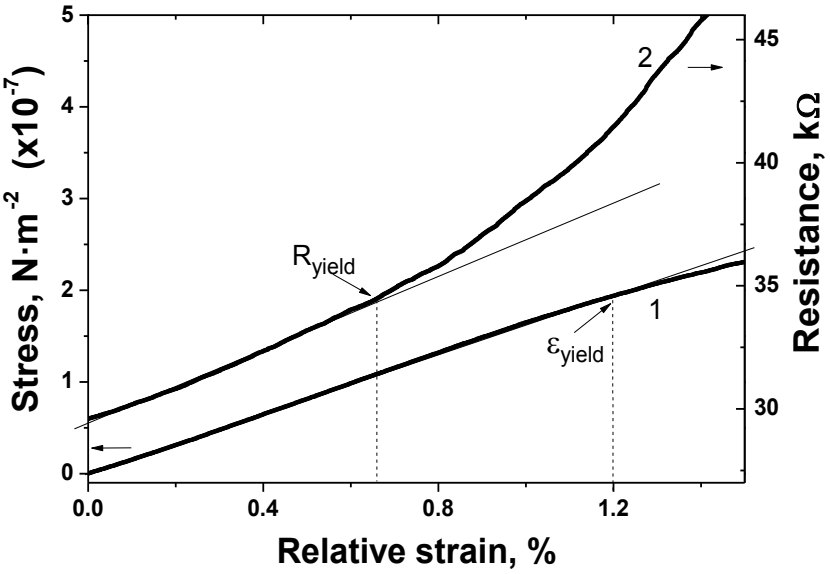

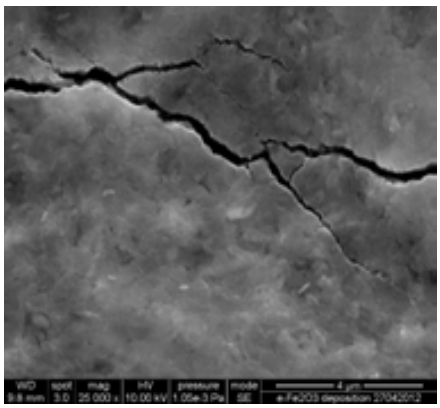

Figure 2-13. Stress-strain (curve 1) and resistance-strain (curve 2) dependences for BL films with α-(BEDT-TTF)$_2$I$_3$ (upper) and β$_H$-(BEDT-TTF)$_2$I$_3$ (middle) as active components measured in the low-strain region of the tensile tests. SEM image of the nanocracks observed in the conducting layer at relative strain higher than R$_{yield}$ value(bottom).

2.5. Piezoresistive bi-layer materials with temperature independent resistance

The preparation of a flexible strain-sensing material that does not exhibit a significant temperature change on its resistance could be of great interest for practical applications since these materials would allow fabricating strain/pressure sensing devices without using an internal temperature compensation simplifying significantly the design of the sensing device. As it was shown in the previous section, the temperature of the iodine/solvent annealing step during the BL preparation strongly affects the thickness and texture of the α-(BEDT-TTF)$_2$I$_3$ crystals of BL films.

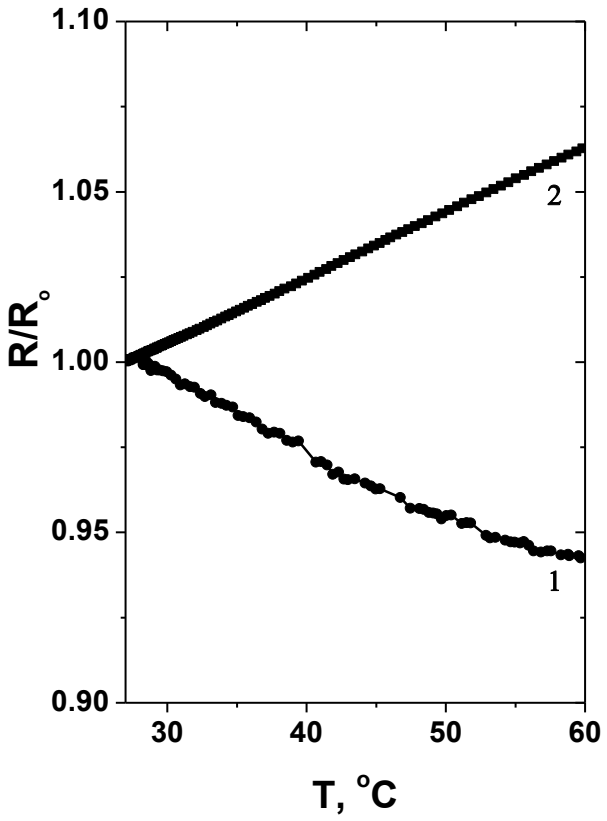

Figure 2-14. Temperature dependence of the relative resistance of BL films prepared at two different temperatures of the iodine/solvent annealing; at 7 °C (curve 1) and 33 °C (curve 2).

Together with such differences the films also exhibit a very different temperature dependence of their electrical resistance as depicted in Figure 2-14. Then, the BL film with the thinner conducting layer and the smaller crystals shows a semiconducting behavior with an increase of the resistance when lowering the temperature, while the BL films with a

thicker conducting layer exhibits a metallic-like temperature dependence of the resistance (Figure 2-14). These results are in agreement with the different intergrain contacts in both films, since it is well known that grain boundary increases the resistivity of polycrystalline samples in comparison with single crystals and may affect the resistance temperature dependence as well. [67]

The previous results also suggest that an appropriate choice of temperature for the iodine/solvent vapors annealing step could control the electric transport properties of the polycrystalline covering α-(BEDT-TTF)$_2$I$_3$ layers opening the possibility to prepare BL films that do not show any significant change of the resistance with the temperature. According with these rationales, we prepared eight BL films by annealing with iodine/CH_2Cl_2 vapor during 2 min at the following temperatures 7, 10, 15, 20, 25, 28, 30, and 33 ^oC (films **F2-1** – **F2-8**, respectively), under a controlled relative humidity of 40%. The maximum temperature used for the annealing was limited by the properties of used solvent (boiling point of CH_2Cl_2, 41 ^oC [68]) and the minimum limit (7 ^oC) due to temperature restrictions of the climate chamber used for carrying out the annealing procedure. The formation of the conductive layer of α-(BEDT-TTF)$_2$I$_3$ crystals was determined and studied by SEM and powder X-ray diffraction techniques as well as by direct current (DC) conductivity measurements. The textures of the covering α-(BEDT-TTF)$_2$I$_3$ layers were studied using the SEM technique employing always at least two replicas of each BL film.

Structure of the active layers of the BL films. The X ray diffraction data of BL films (Figure 2-15) show the presence of only (*00l*) reflections of α-(BEDT-TTF)$_2$I$_3$ crystals indicating that, regardless of the temperature of the annealing step, the conductive layers are formed exclusively by c^*-oriented crystallites of α-(BEDT-TTF)$_2$I$_3$.[69707172] Interestingly the diffractions of such textured BL films prepared at lower temperatures show additional few reflections that correspond to neutral BEDT-TTF crystals,[73] although their intensities are negligibly small in comparison with the main reflections of α-(BEDT-TTF)$_2$I$_3$ crystallites. X-ray diffraction data of the BL film samples were also used to estimate the mass of α-(BEDT-TTF)$_2$I$_3$ crystals of crystalline layer.

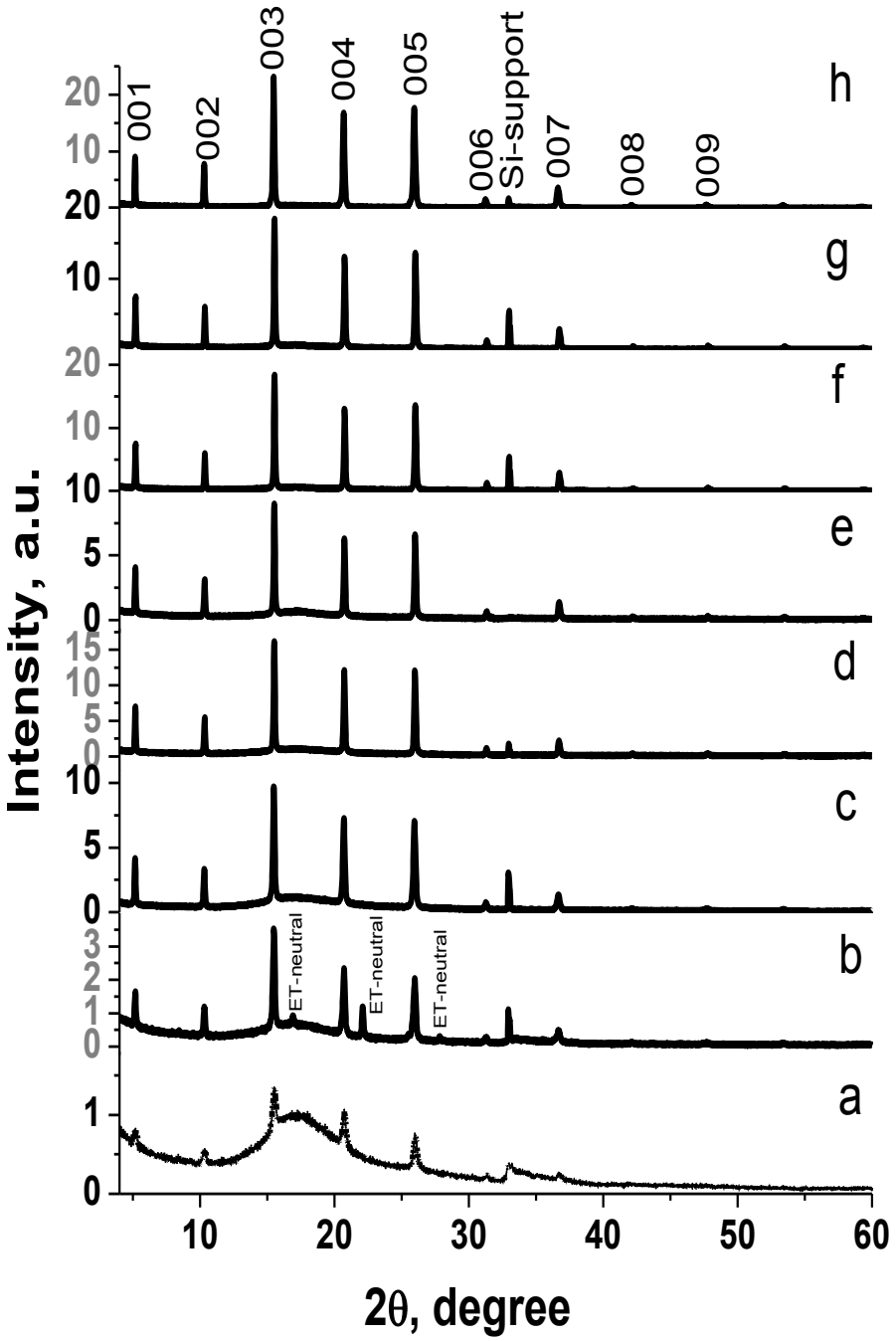

Figure 2-15. X-ray diffraction patterns of BL films prepared at different temperatures of the iodine/solvent annealing: (a) 7 °C, (b) 10 °C, (c) 15°C, (d) 20°C, (e) 25°C, (f) 28°C, (g) 30°C and (h) 33 °C. Reflections labeled as ET-neutral and Si-support are originated by neutral BEDT-TTF crystals and Si support, respectively.

To perform such estimation we used the intensity of the (*003)* reflection of α-(BEDT-TTF)$_2$I$_3$ crystals, which is the most pronounced one in the patterns. Assuming that all scanning parameters – scanning time, type of support, orientation of crystals, degree of layer ordering, and thickness of the BL film's samples, etc – are similar, the intensity of

the (*003*) reflection has to be proportional to the mass of oriented crystals. To minimize errors, the intensity of the (*003)* reflections was normalized per 1 mg of the BL film samples, hereafter referred as $I_{(003)}$. Taking the value of $I_{(003)}$ of the layer prepared at 30ºC [$I_{(003)}$(30ºC)], which is the highest one among the prepared BL films, as 100%, we calculated the relative mass yields (RY) of α-(BEDT-TTF)$_2$I$_3$ crystals at different annealing temperatures [$I_{(003)}$(T)] by eq.(3):

$$RY(T) = 100\frac{I_{003}\,(T)}{I_{003}\,(30℃)} \qquad \text{eq (2.3)}$$

Table 2-7 gives the RY values of conducting crystals resulting in the annealing at different temperatures on the BL films showing that the RY increases linearly with the temperature (Figure 2-17).

Morphology of the BL films. SEM images of the resulting α-(BEDT-TTF)$_2$I$_3$ layers of the BL films indicate that in all cases, regardless of the temperature of the iodine/solvent annealing, the crystallites are well shaped with submicron size, except for the conducting layer formed at 7 ºC where the crystallites/grains are at the nanoscale (Figure 2-16). Here it should be noted that although the BL films prepared at temperatures higher than 10 ºC have similar morphologies and sizes, they significantly differ in their transport properties.

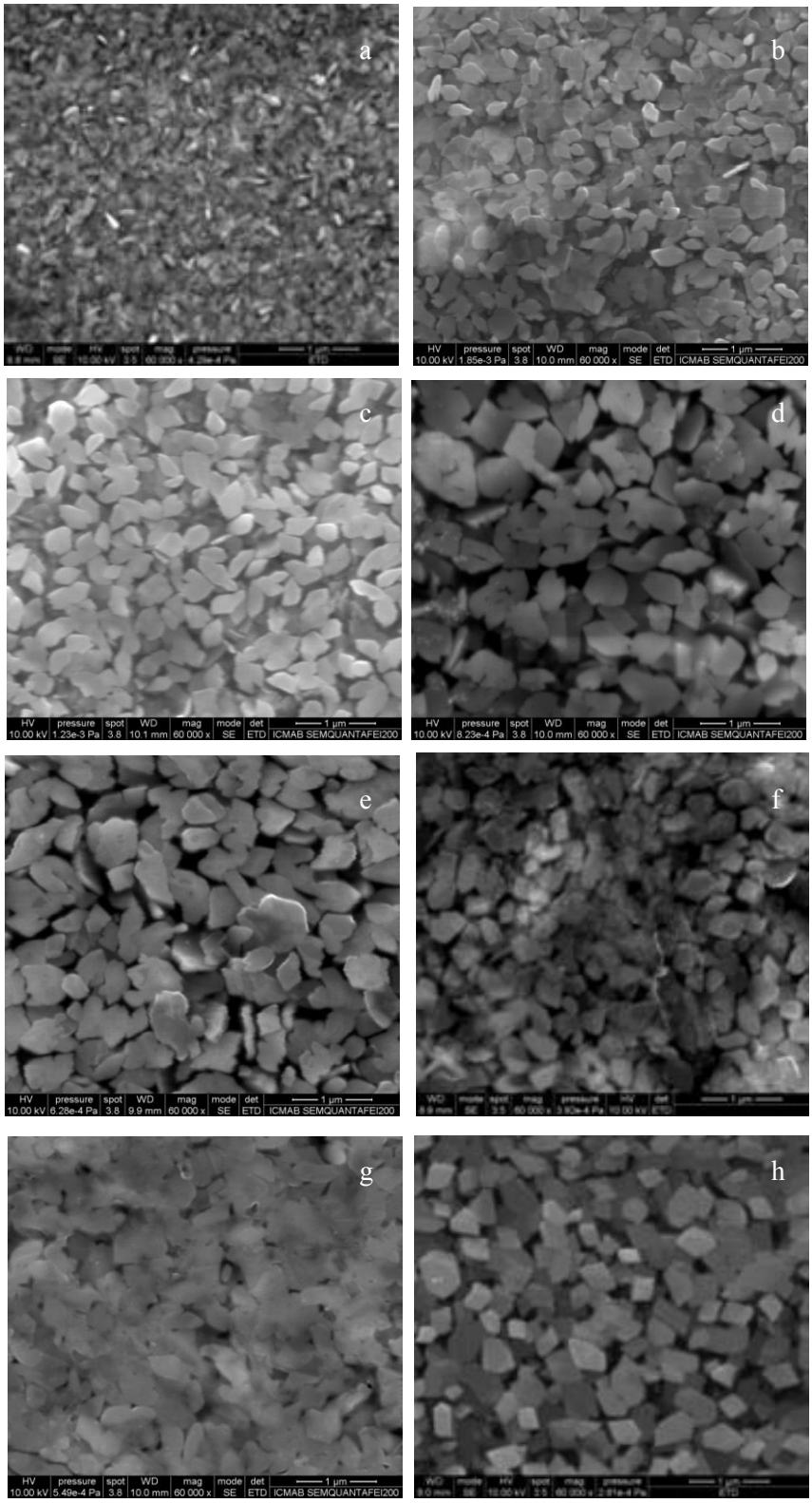

Figure 2-16. SEM images of the conductive layer of α-(BEDT-TTF)$_2$I$_3$ crystals prepared at different annealing temperatures: (a) 7 ºC, (b) 10 ºC, (c) 15ºC, (d) 20ºC, (e) 25ºC, (f) 28ºC, (g) 30ºC and (h) 33 ºC.

Electrical properties of the BL films. Table 2–7 also summarizes the electrical characteristics of the BL film prepared at different annealing temperatures, where the sheet

resistance at room temperature ($R_{\square}$) and temperature coefficient of the resistance (TCR) at room temperature, defined by eq.2.4 as the relative change of resistance when the temperature is changed by 1 degree at room temperature (T_0), are given.

$$TCR = 100\frac{[(R_T - R_0)/R_0]}{(T - T_0)} \qquad \text{eq (2.4)}$$

Table 2-7. Electrical and electromechanical properties of the BL films prepared at different iodine/solvent annealing temperatures.*

BL film sample	T, ºC	RY, %	R□, kΩ	TCR, %/deg	GF
F2-1	7	4.6	173±20	-0.20±0.02	11±1
F2-2	10	20.0	153±20	-0.07±0.01	11 ±1
F2-3	15	37.6	22±1	0.0044±0.005	9 ±1
F2-4	20	52.9	10±2	0.08±0.02	9 ±1
F2-5	25	59.2	12±2	0.20±0.05	10 ±1
F2-6	28	81.1	11±2	0.15±0.05	9 ±1
F2-7	30	100.0	9±1	0.20±0.05	9 ±1
F2-8	33	96.8	8.5±2	0.15±0.05	9 ±1

*Electrical and electromechanical properties of the conductive covering α-(BEDT-TTF)$_2$I$_3$ layers were measured in two or more replicates for each BL film.

To clarify the effect of the annealing temperature on the amount of α-(BEDT-TTF)$_2$I$_3$ crystallites generated in the BL films and the electrical properties, the estimated RY and measured $R_{\square}$ values were plotted against the annealing temperatures (Figure 2-17). In the studied temperature range the annealing significantly affects both the amount of crystals that form the conductive layer and the layer sheet resistance. Indeed, the RY values linearly increases with the raise of the annealing temperature while the sheet resistance exponentially drops down one order of magnitude, from 170 to 10 kΩ when the annealing temperature changes from 7 to 20 ºC. A further temperature increase practically does not affects the sheet resistance of BL films. Thus crystalline layers prepared at T ≥ 20 ºC have remarkable different RY values (50%≤RY≤100%) while their $R_{\square}$ values are very similar.

From this result one may conclude that for RY values larger than 50% the amount of crystallites is enough to overcome the percolation limit forming a conductive covering layer which $R_{\square}$ achieves the lowest possible value. The sheet resistance values are in good agreement with the observed morphology of crystallites since for an increase of crystallite sizes from nano to submicron dimensions is expected a decrease of the grain boundary that will in turn lead to a better conductivity.

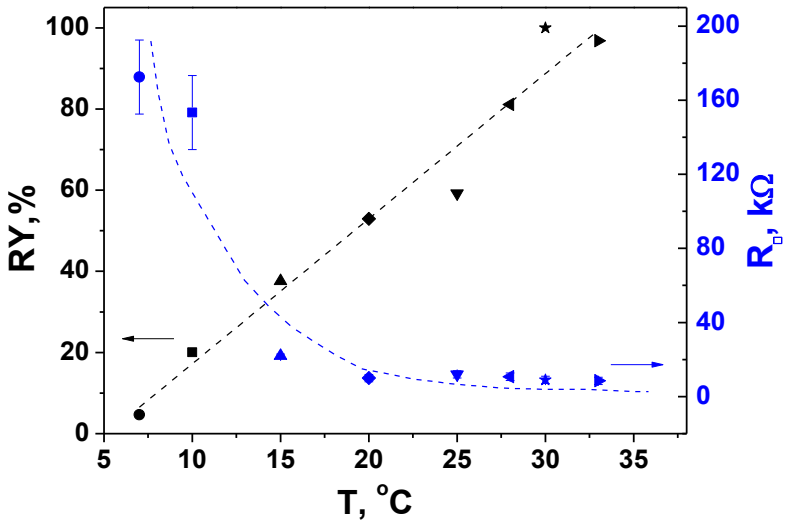

Figure 2-17. Crystallite yields (RY) and room temperature values of sheet resistance (R□) for BL films prepared at different temperature of the iodine /solvent annealing: 7 ºC (●), 10 ºC (■), 15 ºC (▲), 20 ºC (♦), 25 ºC (▼), 28 ºC (◄), 30 ºC (★) and 33 ºC (►).

As shown in the Table 2–7, temperature coefficients of resistance are also strongly dependent on the annealing temperatures of the BL film. Thus, the crystalline layers grown at 7 and 10 ºC show a semiconductor-like behavior while the layers grown at temperatures higher than 20 ºC revealed a metallic resistance temperature dependence. Interestingly, the resistance of layers formed at 15 ºC is almost temperature independent. Moreover, Table 2–7 and Figure 2-18 (left, curve 5) clearly show that the layers formed at T≥ 25 ºC have the same TCR values which corroborates that there is a minimum mass of crystallites (RY≅60%) that allows the formation of the conductive layer with efficient grain boundaries providing enough efficacious pathways to give a metallic behavior to the covering layer of α-(BEDT-TTF)$_2$I$_3$ crystals.

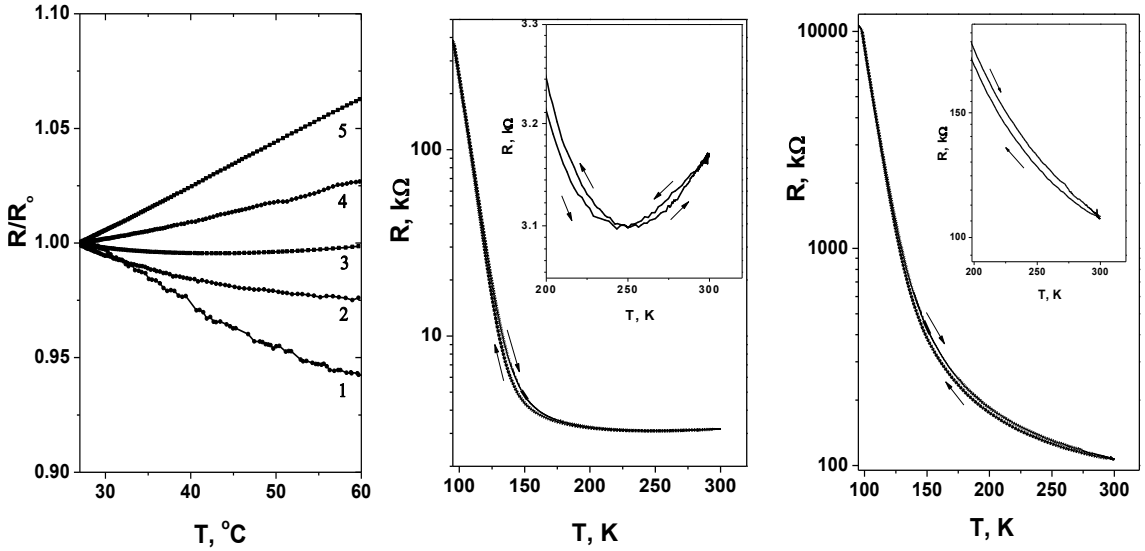

Figure 2-18. Left, resistance temperature dependence of BL films prepared at different temperature of the annealing: 7 ºC (curve 1); 10 ºC (curve 2); 15 ºC (curve 3); 20 ºC (curve 4) and 33 ºC (curve 5). Centre, R(T) dependence for metallic BL film prepared at 33 ºC. Inset shows the onset of the metal-insulator transition. Right, R(T) dependence for semiconductor BL film prepared at 7 ºC. Inset shows a zooming of the dependences in the temperature range from 200 to 300 K.

We have also studied with more details the resistance temperature dependence of BL film prepared at 33 ºC and 7 ºC, down to liquid nitrogen in order to determine if the covering α-(BEDT-TTF)$_2$I$_3$ layers mimic the metallic behavior shown by the corresponding single crystals.[45] As seen in Figure 2-18 (middle), the temperature dependence of resistance of the BL film prepared at 33 ºC, which exhibits a metal-like behaviour down to 250 K, where the resistance begins to increase with decreasing the temperature. In the 150 - 96 K range the resistance jumps up dramatically from 4.3 kΩ to 360 kΩ. This outcome shows that the metal-insulator transition in the polycrystalline α-(BEDT-TTF)$_2$I$_3$ layer is very broad and occurs at higher temperature than in single crystals which occurs at 137 K. This result can be attributed to the existence of grain boundaries in the polycrystalline layer that introduces an additional potential barrier for the carrier transport, preventing therefore the motion of carriers from one grain to another. At temperature higher than 250 K in the metallic polycrystalline α-(BEDT-TTF)$_2$I$_3$ layers the grain boundary scattering has not a significant influence on the electron transport behavior but when the temperature decreases below this temperature the grain boundary begins to demonstrate a significant influence on the transport behavior.

Electromechanical properties of the BL films. Figure 2-19 shows the electromechanical response to cyclic monoaxial deformations of the BL film **F2-3**, prepared at 15 °C, which shows a weak resistance temperature dependence. Thus, this graph depicts changes of the relative resistance ($\Delta R/R_0$) of a BL film of 4 mm in length when it is elongated under a multicyclic monoaxial deformation with a strain rate of 0.3 μm/s within elastic region of the sample, i.e. < 0.5%. The maximum elongation suffered by the BL film was 20 μm and the initial resistance without any deformation was 40 kΩ. The sensitivity of the BL film to strain is characterized by the gauge factor (GF, as the ratio between the relative resistance changes and the relative strain values, which for the BL film **F2-3** is 9. Similar electromechanical properties were shown by the rest of BL films as shown in the insets of Figure 2-20. Consequently and in contrast to electrical transport properties, the temperature of the annealing step in the preparation of the BL films does not affect their electromechanical responses. Thus, as shown in Figure 2-20, the electrical response to multi-cyclic monoaxial elongation, carried out in the elastic range of deformation with relative strains ε < 0.5%, for all prepared BL films is very reproducible following linearly the changes of relative strain.

The gauge factor is given by eq. 2.5.

$$GF = \frac{(R - R_0)/R_0}{(l - l_0)/l_0} = \frac{\Delta R/R_0}{\varepsilon} \qquad \text{eq (2.5)}$$

where l_0 and l are initial and the final dimensions of the BL film along the monoaxial elongation, respectively, and R_0 and R are the resistance of the BL film without and with elongation, respectively, and ε is the relative strain.

The gauge factors for all BL films are given in Table 2–7 and were found to be very similar, of about 9.5±2.0, showing that their electromechanical properties are governed by the nature of the conducting crystallites network rather than by their size or the contacts among them. Thus, as previously demonstrated,[13] the elastic nanometric deformation of the soft structure of crystallites forming the layer and the associated molecular movements are responsible of the macroscopic electromechanical properties of the BL films.

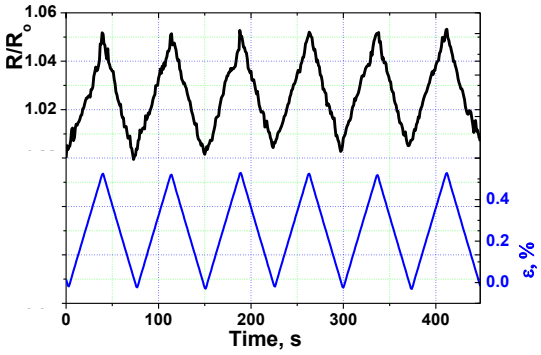

Figure 2-19. Resistance response of BL film F3 to cyclic monoaxial elongation.

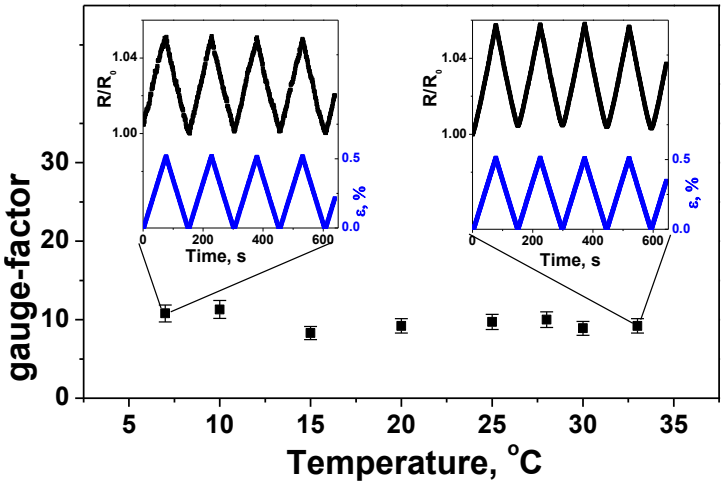

Figure 2-20. Gauge factors of the BL films prepared at different annealing temperature. Insets show resistance responses of BL films prepared at 7 and 33 °C to multi cyclic monoaxial elongation.

This study demonstrates that the temperature of the BL film formation is the key processing parameter allowing controlling both the thickness and texture of the conductive layers which are responsible for the electronic transport properties of the BL films. We have also shown that while the electromechanical properties of the BL films are invariant, their TCR can be tuned by an appropriate choice of the temperature of the annealing step to give not only metallic films but also BL films with a temperature independent behavior of their resistance. This result is of great interest for practical sensing applications because it enables to construct either pressure or strain sensors without a temperature reference which will significantly simplify the corresponding sensing device.

2.6. Scaled-up preparation of piezoresistive bi-layer films

As it was already discussed in previous sections the BL films show very high piezoresistive properties enabling their use as active sensing components in flexible strain/pressure sensing devices.[74, 75] Such applications require the obtaining of BL films with a high degree of homogeneity and with large dimensions – at least in the centimetre-scale – in a reproducible manner. The iodine/solvent method already described permits to prepare the BL films with α-(BEDT-TTF)$_2$I$_3$ crystallites showing the above mentioned characteristics. However this is not the case for the BL film with β_H-phase crystallites since all attempts made up to now with iodine/solvent annealing method lead to formation of crystalline layer of either the α-(BEDT-TTF)$_2$I$_3$.

There is only one method for obtain the BL films covered with layers of β_H-(BEDT-TTF)$_2$I$_3$ crystallites of high quality: the thermal annealing BL films with crystallites α-(BEDT-TTF)$_2$I$_3$ at temperatures between 137 and 155 ^{o}C. When such BL films are thermally annealed, the α-(BEDT-TTF)$_2$I$_3$ crystallites are converted into the metallic β_H-(BEDT-TTF)$_2$I$_3$ crystallites as occurs for single crystals. [39, 57] However in contrast with single crystals, during the $\alpha \rightarrow \beta_H$ transition of BL films a partial loss of iodine occurs due to the highly developed surface of the covering crystalline layer. In order to overcome this problem, the annealing can be carried out inside a glass chamber in which several fine crystals of iodine in equilibrium with vapor of iodine were enclosed. This procedure results very effective to obtain small samples of the BL films with β_H-(BEDT-TTF)$_2$I$_3$ crystallites but not for preparing films with large sizes of conducting surface since the resulted BL films resulted highly corrugated.

To solve this problem a novel processing procedure, based on the thermal annealing, able to avoid the iodine losing and the film corrugation was developed. This procedure was based on performing the temperature annealing of a BL film sample sandwiched between two plates as depicted in Figure 2-21. The device to perform such a process was designed and constructed so as to made an in-situ control of the $\alpha \rightarrow \beta_H$ phase transition by direct electrical resistance monitoring. Then, four gold strips deposited on the bottom glass plate permit 4-point measurements of the electrical resistance of the BL film during its temperature annealing. A platinum temperature sensor (Pt_{100}) was embedded in the aluminum frame to measure the temperature variation *in-situ*.

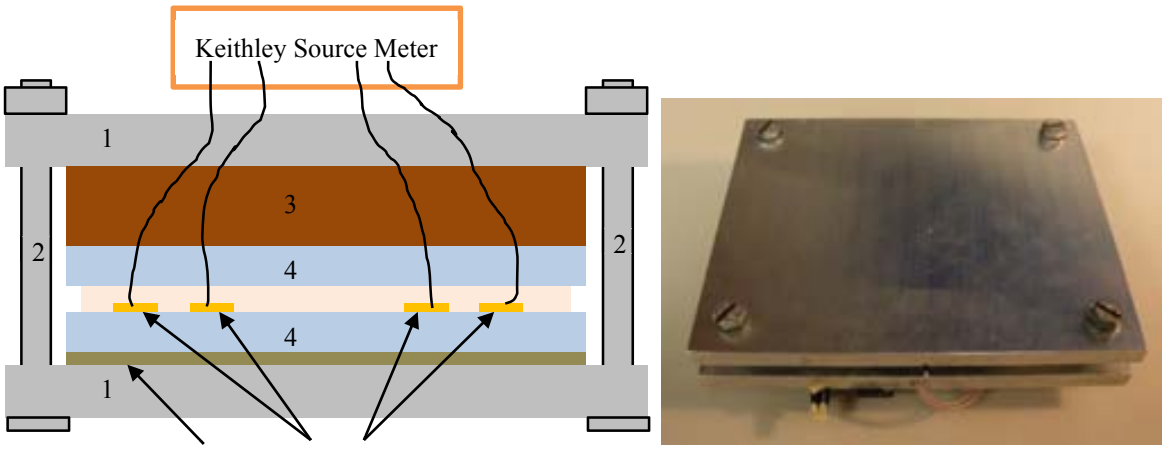

Figure 2-21. (Left) Schematic view of the designed sandwich-like architectural structure for the preparation of BL films at large scale: 1 – Al plates, 2 – screws, 3 – rubber (as a buffer layer), 4 – a flat glass support, 5 – BL film with the conducting layer faced down, 6 – gold contacts evaporated over the glass plate, 7 – a paperboard layer as an additional buffer layer. (Right) Real image of the home-made sandwich-like device.

Disk-shaped samples the BL films with α-phase crystals of 10 cm in the diameter were mounted in the home-made sandwich-like device, as shown in Figure 2-21. The device was placed within a temperature controlled chamber (Memmert D06836; Figure 2-23) and electrical connections were taken out in order to in-situ measurement of the changes in the electrical resistance of the BL film sample under temperature cycles. Electrical responses of the BL film and of the Pt-based thermometer were simultaneously monitored using a Keithley Source Meter. The BL film was subjected to temperature cycles of 27 ºC → 140 ºC → 27 ºC yielding a BL film without any corrugations and with the same structural and morphological characteristics of the BL films with smaller sizes, as observed by PXRD and SEM.

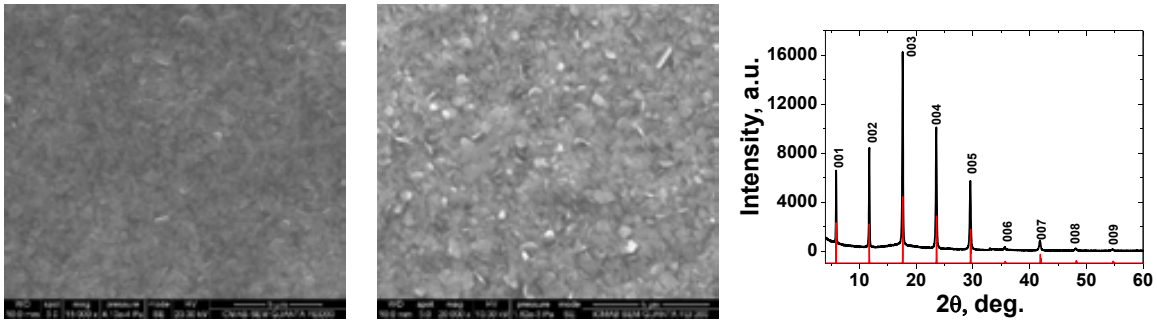

Figure 2-22. SEM images of β-(BEDT-TTF)$_2$I$_3$ crystallites of centimeter scale BL film (a) and small one (b) Typical X ray diffraction patterns of BL film that exhibit only the lines corresponding to 0 0l reflections of β_H-(BEDT-TTF)$_2$I$_3$ crystallites (c) red curve – PXRD data simulated using the crystallographic data and Material Studio program.

Figure 2-23. Image of the home-made sandwich-like device mounted within a Memmert chamber for controlled temperature annealing process.

The experimental data presented in Figure 2-24 show the electrical resistance changes occurring during the β_H-phase preparation process. Thus, up to 70 °C the electrical resistance of the initial BL film exhibits a weak temperature dependence, typical for the covering layer of α-(BEDT-TTF)$_2$I$_3$ crystallites.[76] Above 70 °C the resistance temperature dependence begins to deviate from linearity and this deviation dramatically increases when the temperature raises from 120 to 130 °C: where the resistance jumps up from 1.6 kΩ to 2.6 kΩ. When the temperature is further increased from 130 °C to 140 °C, the film resistance slightly decreases by a 0.2 %. Under cooling from 140 °C to room temperature the film resistance follows a metallic behaviour with a TCR of about 0.3%/degree; a value that corresponds to that of the β_H-(BEDT-TTF)$_2$I$_3$ layers.[77] Therefore, one may conclude that the developed process is suited for the preparation of centimetre-scale BL films with thin layers of β_H-(BEDT-TTF)$_2$I$_3$ crystallites.

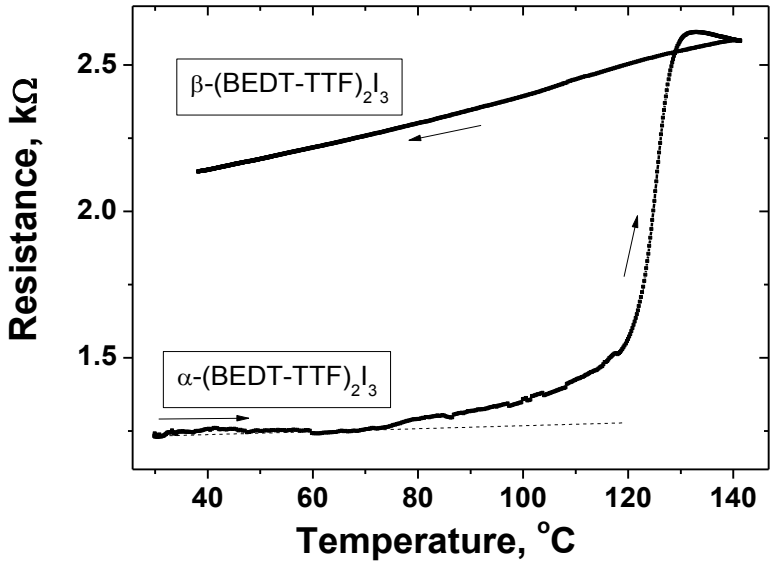

Figure 2-24. Temperature dependence of the electrical resistance of the BL film during a thermal cycle 27 ºC-140 ºC -27 ºC (arrows show the direction of the heating-cooling process) made with a temperature rate of 1,7 degree/min.

To check the reproducibility of the BL films made with the developed temperature annealing procedure several disk-shaped samples of BL films with β_H-(BEDT-TTF)$_2$I$_3$ layers and 10 centimetres in diameter were prepared using the sandwich-like device and their electronic transport properties were studied in a wide temperature range (300-1.4 K). Additionally, the temperature dependence of their resistance below 10K was also studied under different magnetic fields using a Physical Properties Measurements System (PPMS).[i]

It should be noted, that the values of the room temperature sheet resistance of these BL films vary from 1.8 to 2.0 kΩ and the overall decrease of the resistance from 300 to 5 K (R_{300}/R_5) was found about 10-12 for all prepared BL films. As shown in Figure 2-25 below 5 K, all samples showed a steeper decrease of the resistance; although the resistance does not drop to zero as it occurs with the single crystals of the β_H-(BEDT-TTF)$_2$I$_3$ at 7.5 K due to a superconductivity transition**.** In order to confirm the superconducting origin of the steeper decrease of the resistance, the temperature dependences of the resistance of the BL films under different magnetic fields was investigated (Figure 2-25, inset). It is well seen that magnetic field shifts the start of the steeper decrease of resistance to lower temperatures and at magnetic fields higher than 2 T

[i] These experiments were carried out in collaboration with Professor J.S. Brooks and Dr. E. Steven at National High Magnetic Fields Laboratory (NHMFL), Tallahassee, USA.

it is destroyed the superconducting state. The hint of superconducting transition for BL films is in agreement with the fact that poor quality single crystals of β_H-(BEDT-TTF)$_2$I$_3$ often demonstrate an incomplete superconducting transition, located around 7 K.[48] Therefore, the lower temperature of superconductivity for the BL films than that for single crystals may be explained by presence of grain boundaries in the polycrystalline conducting layers. [76]

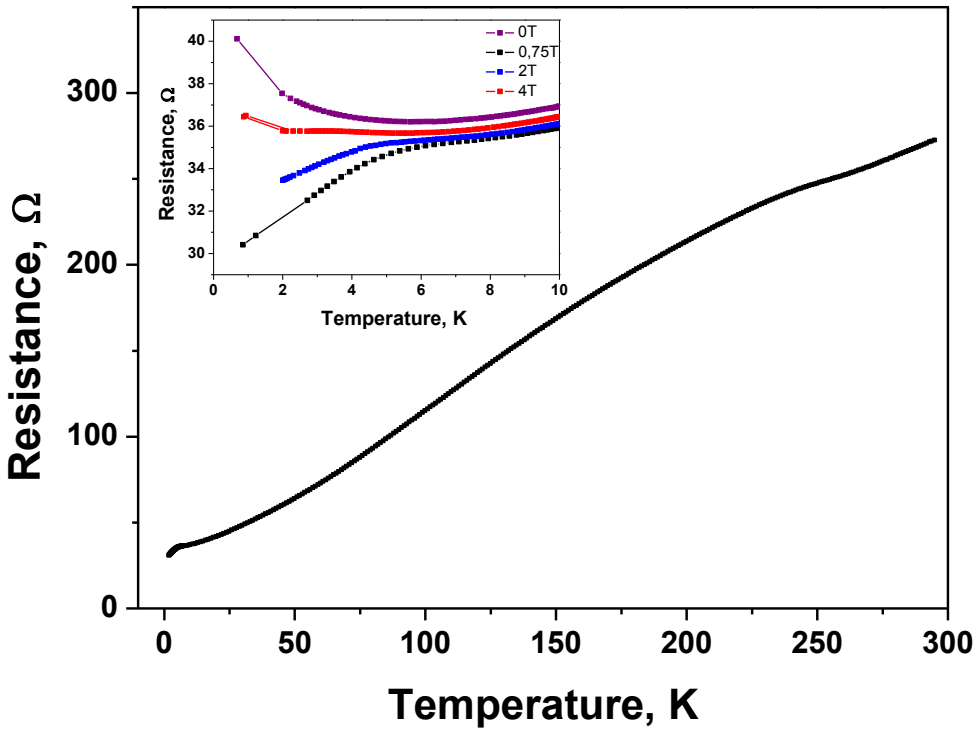

Figure 2-25. Temperature dependence of the resistance of the BL film covered with a layer of β_H-(BEDT-TTF)$_2$I$_3$ crystallites. Inset; low temperature dependence of the resistance under different magnetic fields.

As a conclusion, we can say that the home-made sandwich-like device allows preparing in reproducible manner the large sized BL films with the conducting layers of β_H-(BEDT-TTF)$_2$I$_3$ crystallites which exhibits similar electrical properties as the BL films with smaller sizes.

2.7. Piezoresistive bi-layer materials with improved sensitivity to deformation

This section is addressed to the development of BL films with enhanced sensitivity to deformation/pressure with respect those previously developed.[74, 75] To achieve this goal we

decreased the thickness of the polymer component of the BL film maintaining the same thickness of the piezoresistive crystalline layer with the expectation that under the same input the crystalline layer of the thinner BL films will suffer a larger deformation in comparison with a thicker film with similar thickness of the crystalline layer.

Preparation and characterization of BL films with different thicknesses of polymer matrix. Polycarbonate-based films of different thickness covered with the layers of β_H-(BEDT-TTF)$_2$I$_3$ crystallites were prepared following the previously reported procedure.[69, 76] At the first step, two films **F2-9** of and **F2-10** were prepared. For the preparation of the film **F2-9** a mixture of 98 wt. % of PC and 2 wt. % of BEDT-TTF was used leading to a film with a 20 μm thick, while for film **F2-10** a mixture of 92 wt. % of PC and 8 wt. % of BEDT-TTF was used providing a film with a 5 μm thickness. Different thicknesses were obtained using the same volume of a solution for drop casting of the films, with different concentrations of the polycarbonate in the CH_2Cl_2 solution, 28 mg/ml and 7 mg/ml for films **F2-9** and **F2-10**, respectively. In the second step, the surfaces of films **F2-9** and **F2-10** were exposed to vapours of saturated solutions of iodine in CH_2Cl_2 leading to the "self-metallization" of the surface of films with conductive polycrystalline layers of α-(BEDT-TTF)$_2$I$_3$. Finally the resulting BL films were thermally annealed using the above-described sandwich-like device giving the BL films **F2-11** and **F2-12** covered with crystallites of the β_H-(BEDT-TTF)$_2$I$_3$ organic metal. Both BL films were characterized by SEM and X-ray analyses (Figure 2-26 and Figure 2-27). As Figure 2-26 shows the textures of both films are not significantly different since the conductive layers are formed by a network of submicron crystallites.

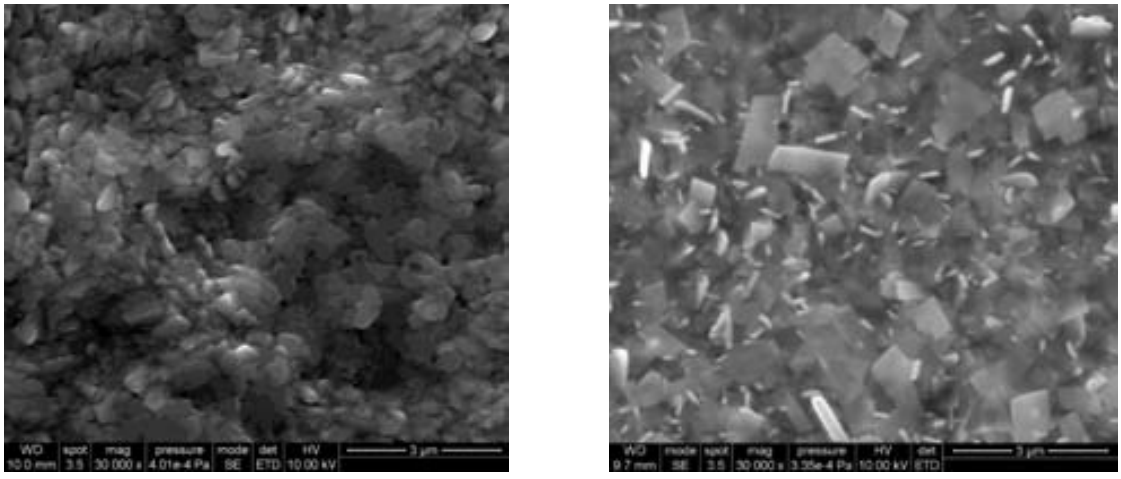

Figure 2-26. SEM images of the piezoresistive layer of BL film F2-11(right) and F2-12 (left).

The X-ray powder patterns of BL-films **F2-11** and **F2-12** (Figure 2-27) show only the presence of reflections corresponding to crystallites of β_H-(BEDT-TTF)$_2$I$_3$ with their *c**-axis oriented perpendicular to the film surfaces. As the intensities of the reflections in the X-ray diffraction patterns of both BL films are similar (Figure 2-27) and the samples were similar in size, both BL films have conducting layers with similar thickness. As it was shown before, in Section 2.3., we may estimate the upper thickness limit based on the PXRD data, that in this case the upper thickness limit is to close to 330 nm for both obtained BL films.

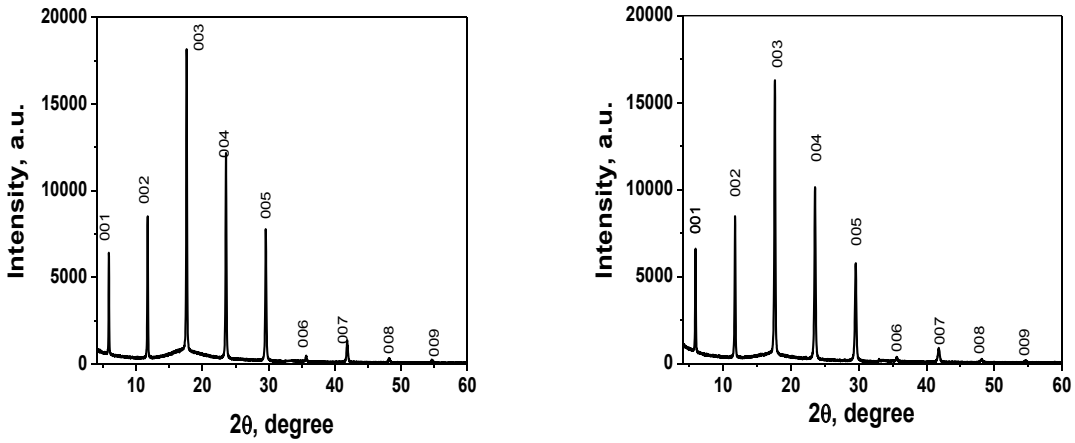

Figure 2-27. X ray diffraction patterns of BL film F2-11 (left) and BL film F2-12 (right); that exhibit only the lines corresponding to *00l* reflections of β_H-(BEDT-TTF)$_2$I$_3$ crystallites.

From the above data one may conclude that the resulting BL films **F2-11** and **F2-12** are very different in the thickness of their polymeric layers but they have similar thickness and textures of their conductive layers, as schematized in Figure 2-28.

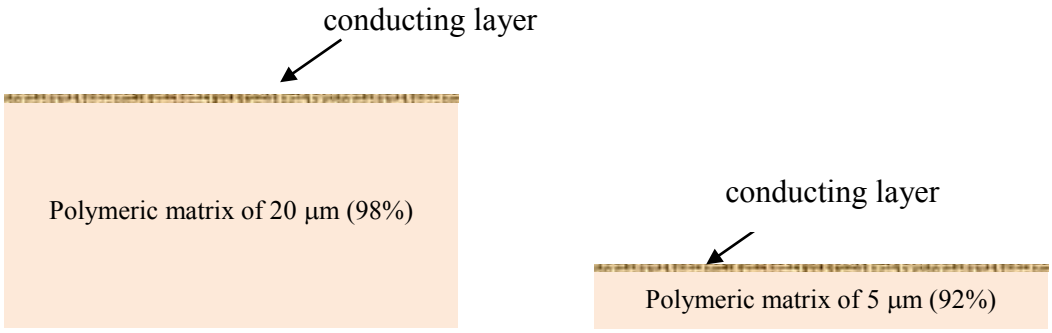

Figure 2-28. Scheme of the piezoresistive of BL films F2-11 (right) and F2-12 (left). The thickness of both polymeric matrices and conducting layers are drawn at the same scale.

Electrical properties of the BL films. The electrical properties of BL films **F2-11** and **F2-12** were examined by four probe direct current (dc) resistance measurements. The temperature dependences of the resistance of both BL films demonstrate a metallic temperature behaviour (Figure 2-29) with temperature coefficients of resistance of 0.25 %/deg. for both BL films.

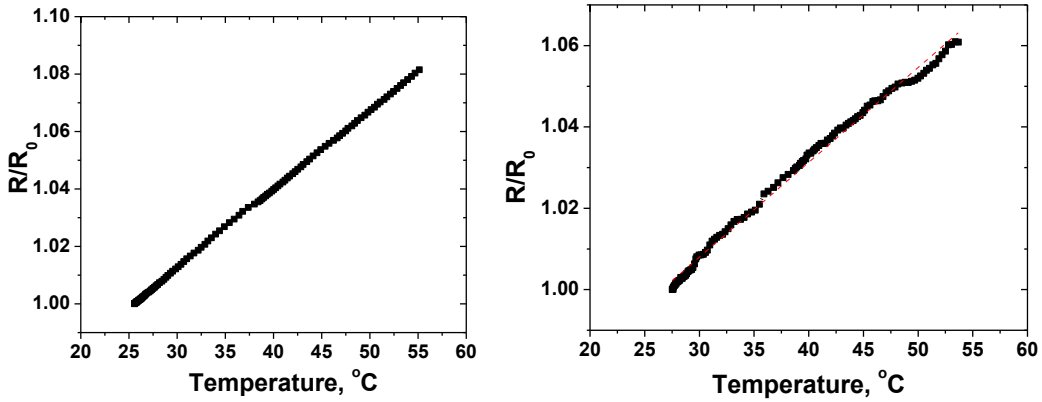

Figure 2-29. Normalized temperature resistance dependence for BL film F2-11 (left) and F2-12 (right).

Mechanical properties of the BL films under deformation parallel to the film surface. The responses of BL films **F2-11** and **F2-12** to unidirectional stress parallel to their surfaces was studied to provide an overview of their mechanical properties. As a reference, a 20 μm thick polycarbonate film was also prepared and tested. Mechanical properties of the films were studied using the same approach that was described in Section 2.3. and the experimental results are shown in Figure 2-30. The Young's modulus, yield strain and ultimate tensile strength (UTS), are summarized on Table 2-8. From such data it can be confirmed that the two BL films show the classical behaviour of rigid plastic materials with values of the elastic limit for strain well over 0.02%; which is the typical elastic limit of conventional metals.

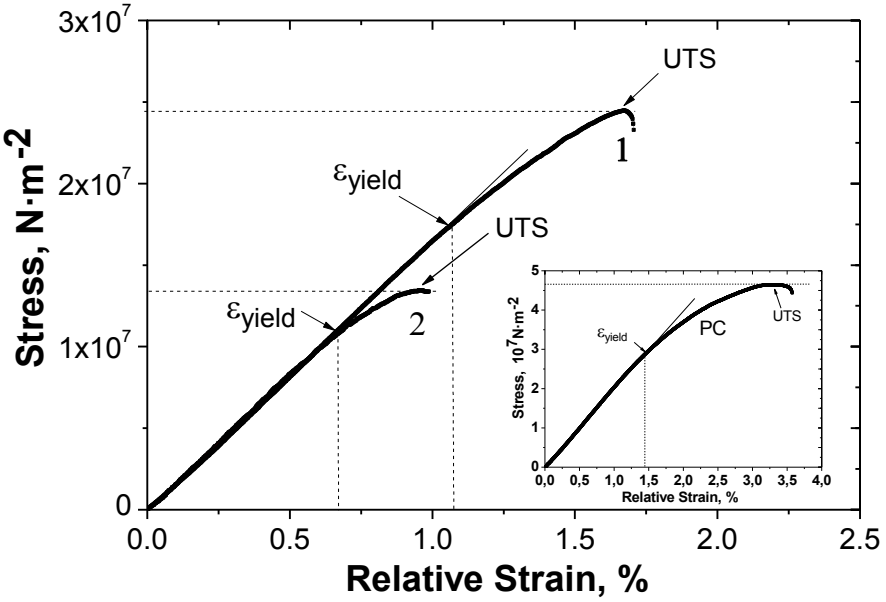

Figure 2-30. Full stress-strain curves for the BL film F2-11 (curve 1) and for BL film F2-12(curve 2); inset: stress-strain curve for the PC film 25 μm thick.

Table 2-8. Mechanical characteristics for BL films as well as for the reference PC film.

samples	Film thickness, μm	E, GPa	ε_{yield}, %	UTS, 10^7 N·m^{-2}	R_{yield} %
PC-based film	25	2.05±0.2	1.4	4.65	-
BL film **F2-11**	25	1.46±0.2	1.1	2.46	0.65
BL film **F2-12**	5	1.46±0.2	0.65	1.37	0.65

The tensile tests showed that the presence of the layer of β_H-(BEDT-TTF)$_2$I$_3$ crystallites decreases the value of Young's modulus of a polycarbonate film from 2.05 to 1.46 GPa regardless the total thickness of the films. Thus, BL films **F2-11** and **F2-12,** exhibit identical Young's moduli but differ significantly in other important mechanical characteristics, such as the ε_{yield} and UTS. The values of the latter parameters for the thinner BL film **F2-12** are approximately 40% less than those found for thicker BL film **F2-11** (Table 2-8). This result, which cannot be rationalized up to now, shows that the ratio between the thickness of a polycarbonate matrix and of the crystalline layer plays a role in

in the mechanical properties of the piezoresistive BL films along the direction parallel to their surface.

Electromechanical properties of the BL films under a deformation parallel to the film surface. The effect of uniaxial strain on the resistance of the two obtained BL films was studied by subjecting small pieces of the films with an area of ca. 4.0 mm x 2.5 mm to multicyclic monoaxial deformations. The tests were carried out with a constant strain rate of 3 μm/s in the elastic deformation range applying the strain parallel to the surface of the film and to the conducting crystallographic *ab*-planes of the oriented β_H-(BEDT-TTF)$_2$I$_3$ crystallites. The maximum applyed deformation corresponds to a relative strain (ε) value of 0.005 (i.e. 0.5%). The responses of both BL films to multycyclic monoaxial deformation are shown in Figure 2-31 where it is observed that the resistances follow linearly and reversibly the applied elongation and the gauge factors for the BL films **F2-11** and **F2-12** were as 18 and 20, respectively.

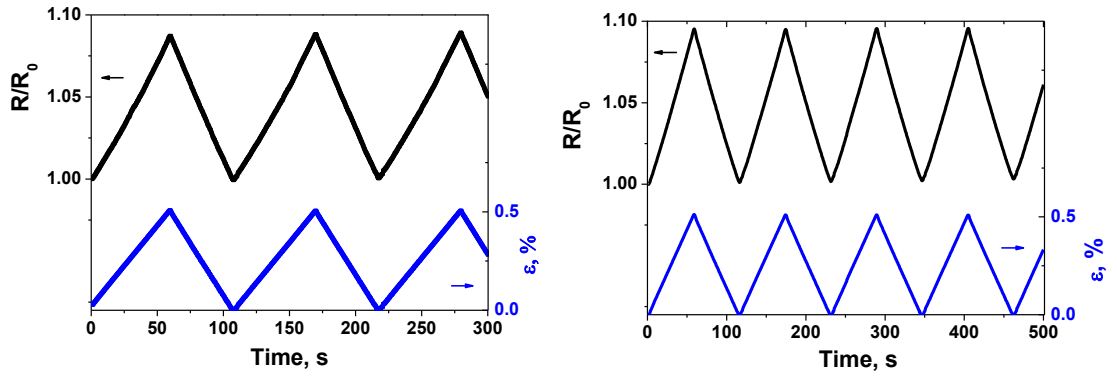

Figure 2-31. Resistance changes of BL films F2-11(left) and F2-12 (right. Resistance (black curve) and elongation data (blue curve).

As summarized in Table 2-9 BL films **F2-11** and **F2-12** with conductive layer of β_H-(BEDT-TTF)$_2$I$_3$ crystallites exhibit very similar electromechanical properties showing the same sensitivity to uniaxial deformation parallel to the film surface. To complete the electromechanical characterisation of the piezoresistive BL films **F2-11** and **F2-12** tensile testing in the elastic region coupled with direct resistance measurements were also prepared.

Table 2-9. Electromechanical properties of BL films.

BL film-based membrane	thickness, μm	R□, kΩ	TCR, %/deg.	GF
F2-11	25	2.27	0.26	18.2
F2-12	5	3.51	0.25	20.4

Figure 2-32 shows that the changes of the resistance *versus* the relative strain of both BL films deviate from a linear proportionality at the same value of relative strain indicating that both films have R_{yield} values of 0.65%. It has been shown before that the deviation of the resistance from the nonlinearity is associated with the formation of cracks perpendicular to the elongation direction that interrupt the electrical transport. Interestingly, the R_{yield} of 0.65% for BL film **F2-11** is well below the value of ε_{yield} =1.2% (Figure 2-32, inset graph) while for the BL film **F2-12** the values of R_{yield} and ε_{yield} for thin BL-film **F2-12** occur at the same relative strain of 0.65% (Figure 2-32). Based on such observations one may conclude that the values of R_{yield} observed for both BL films are determined by the nature of the conducting polycrystalline layer of β_H-(BEDT-TTF)$_2$I$_3$ while the values of ε_{yield} depend on the ratio between the thickness of a polycarbonate matrix and that of the metallic β_H -(BEDT-TTF)$_2$I$_3$ covering layer.

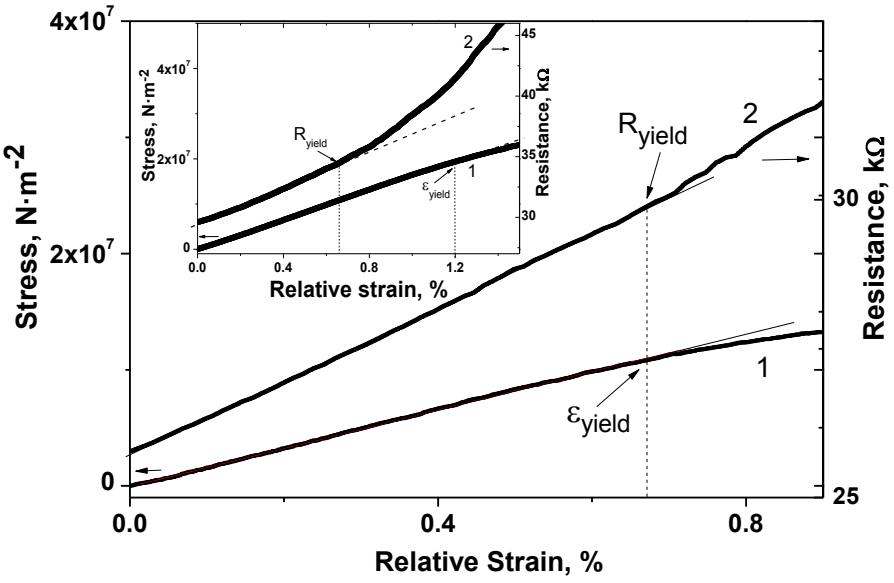

Figure 2-32. Stress-strain (curve 1) and resistance-strain (curve 2) dependences for BL films F2-12 measured at low relative strain in tensile tests. Inset graph is the stress-strain (curve 1) and resistance-strain (curve 2) dependences of BL films F2-11 measured in the same low-strain region.

Electromechanical properties of the BL films under a deformation perpendicular to the film surface. To measure the electromechanical properties of the BL films under a deformation perpendicular to the film surface we used two BL film-based membranes with a round-shape configuration of ca. 3 mm in diameter. Two membranes with such characteristics were prepared and tested: membrane **M1** from BL film **F2-11** with a thickness of 25 μm and membrane **M2** from a thinner (5 μm) BL film **F2-12.** In order to check the role of the electrical contacts in the electromechanical properties of the membranes two different types of electrical contacts were used. A linear configuration where two Pt wires of 20 μm in diameter and 2 mm distance between them were attached to the piezoresistive membranes **M1** and **M2** whereas in a dot-like configuration two point contacts separated by a distance of 2 mm were attached to membrane **M3** made from the BL film **F2-12** (Figure 2-33).

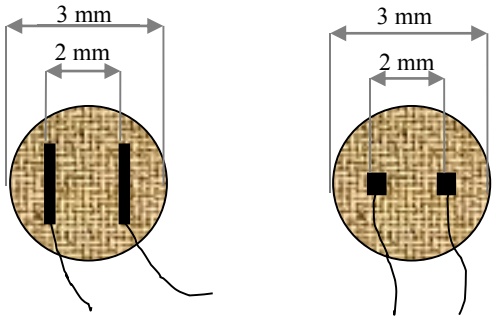

Figure 2-33. Schematic top view of the layout of electrical contacts attached to pressure membrane sensors. The linear (left) and dot-like (right) configurations.

The pressure testing experiments were performed by using a tailor-made U-tube monometer with a water column (Figure 2-34). To minimize the temperature effect, all tests were made inside a home-made thermo-insulating camera fabricated with rigid polyurethane foam.

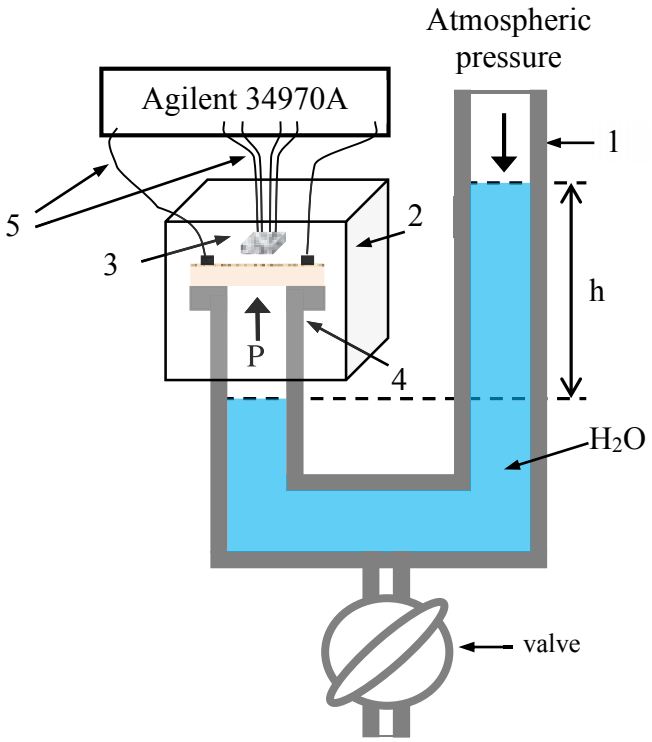

Figure 2-34. Schematic view of the setup developed for the pressure tests: 1 - water column U- tube manometer; 2 – thermo-insulating camera; 3 - Pt thermometer; 4 - glass holder with a BL film-based sensing membrane; 5 – electrical connections.

The pressure tests were conducted with a simultaneous temperature monitoring. For this purpose a Pt-thermometer was located very close to the tested membrane. The BL film-based sensing membranes were glued over a ring-like top of a glass tube of one of the orifice of the U-tube monometer as shown in Figure 2-34. In these experiments the pressure (P) of the gas (air) trapped inside of the void space of the left tube, closed by the membrane, that is generated by the column of water of a height h of the right tube of the U-tube, is greater than the atmospheric pressure produces the deformation perpendicular to the surface membrane. The bottom part of the manometer was equipped with a valve that allows decreasing the water column height that in turn results in a gas pressure decrease in the left closed end of the U-tube. The pressure applied to the membranes was measured in this setup as mm of H_2O and was changed in the range of 0 to 320 mm of H_2O.

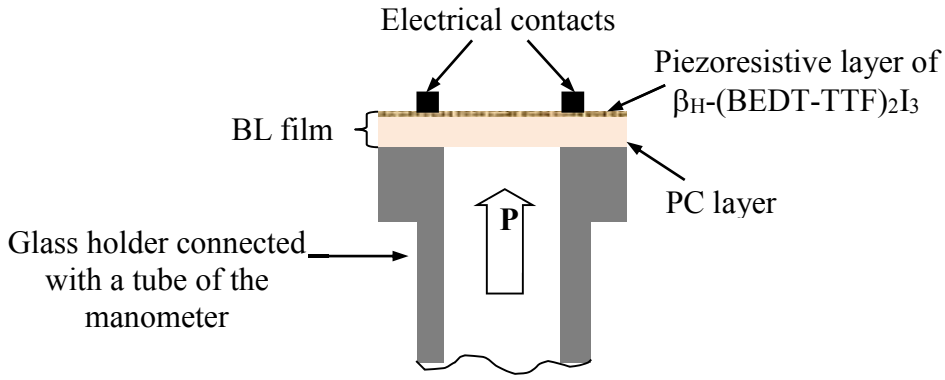

Figure 2-35. Schematic view of a sensing membrane located over the top of the left arm of the U-tube manometer.

The electrical responses of the membranes to the pressure changes generated in this U-tube manometer were measured with Agilent 34970A data acquisition system using the direct current method.

The typical response to applied pressure of membrane **M1** equipped with a linear contact configuration, at room temperature is shown in Figure 2-36 from which it can be estimated that its sensitivity to pressure changes is 1.2 Ω/mbar. [74, 75] As the room temperature resistance of the **M1** is 2273 Ω, the pressure changes may be measured with 0.1 mbar accuracy, due to the ration signal/noise for current prototype, and the resolution

of the setup. It is could be pointed out that there is a significant difference in the resistance before and after a pressure load-unload cycle, which can be assigned to temperature variations of the surrounding during experiment.

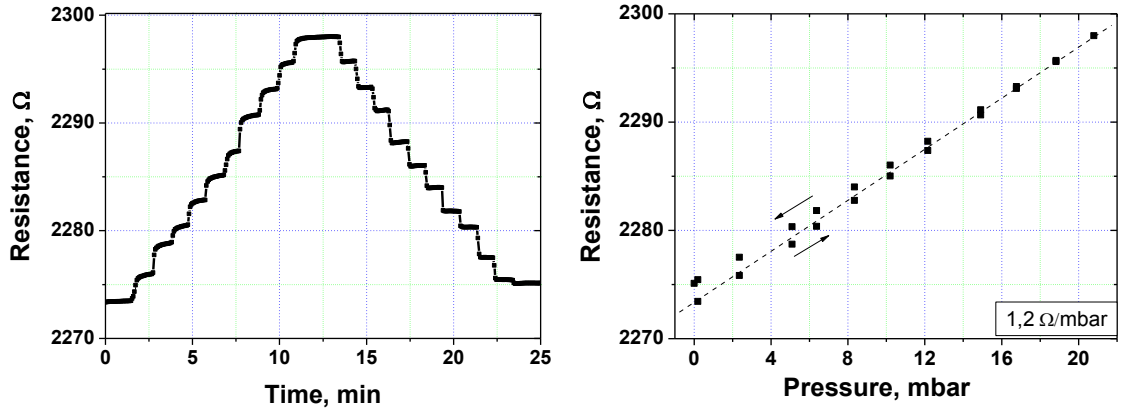

Figure 2-36. Left: Electrical response of membrane M1 based on BL film F2-11 with a thickness of 20 µm and with a linear contact configuration. Variation of pressure was made in 10 steps, each one with a duration of 2 min, going up and down with change of ca. 2 mbar. Right: Pressure dependence of the resistance based on data collected for one load-unload cycle.

The electrical response of the thinner membrane **M2,** equipped with a linear contact configuration, to pressure changes was also linear and reproducible, as shown in Figure 2-37 from which a membrane sensitivity of 6.3 Ω/mbar was estimated. This result is over 5 times larger than that of the thicker membrane **M1** confirming our previous expectation that the thickness of the polymeric layer of the membrane plays a crucial role on its sensitivity to a deformation perpendicular to the membrane surface. To check the stability of the measurements along time at a given applied pressure of thin membrane **M2** a pressure load of 32 mbar was applied during 65 min. As shown in Figure 2-37 the resistance of the membrane does not change significantly over 65 min and, therefore, the BL film with 5 µm thickness may be used for long term pressure monitoring.

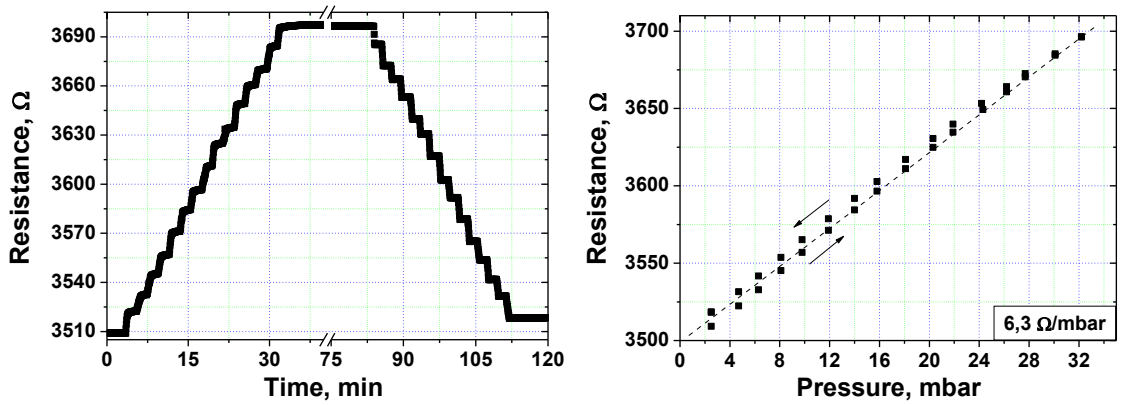

Figure 2-37. Left: Electrical response of membrane M2 based on the BL film F2-12 with a thickness 5 µm and with a linear contact configuration. Variation of pressure was made in 15 steps, each one with a duration of 2 min, going up and down with change of ca. 2 mbar. Right: Pressure dependence of the resistance based on data collected for one load-unload cycle.

The electrical response of the thinner membrane **M3**, equipped with a dot-like contact configuration, to pressure changes was also linear and reproducible, as shown in the Figure 2-38, with a sensitivity of 10 Ω/mbar. This value is larger than that shown by membrane **M2** and it is one order of magnitude larger that the sensitivity of membrane **M1**. Therefore, the response of the BL film-based membranes to the pressure depends not only on the thickness of a membrane but also on the contact configuration.

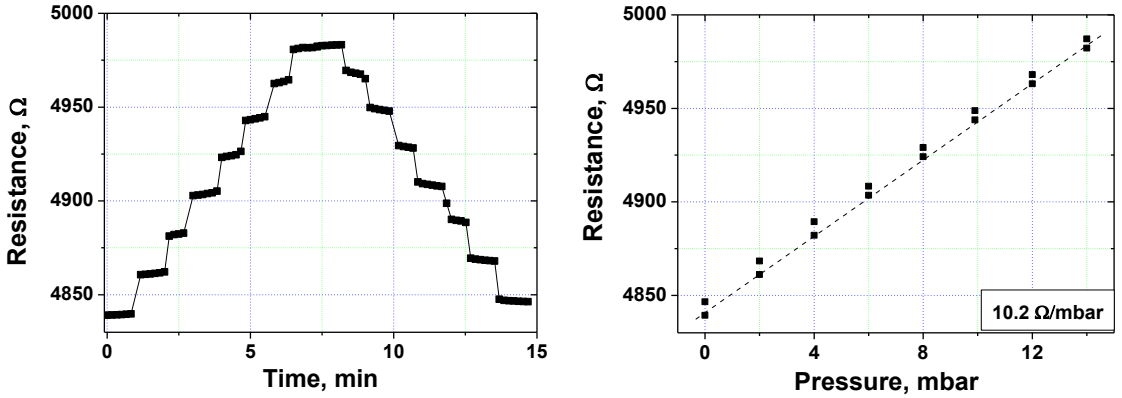

Figure 2-38. Left: Electrical response of membrane M3 based on the BL film F2-12 with a thickness 5 µm and with a dot-like contact configuration. Variation of pressure was made in 7 steps, each one with a duration of 1 min, going up and down with change of ca. 2 mbar. Right: Pressure dependence of the resistance based on data collected for one load-unload cycle.

Figure 2-39 shows a comparison of the responses of the three studied membranes to

pressure changes. The sensitivity of BL film-based membranes to pressure changes, calculated as $S_P=\Delta R/\Delta P$ are summarized in Table 2-10 being reasonable that a fourfold decrease in the thickness of the polymeric component membrane in combination with a electrical contact configuration resulted in a tenfold increase in the membrane pressure sensitivity. However, these parameters do not affect significantly the sensitivity to deformation parallel to the film surface, as evident by the similar GF values of the films.

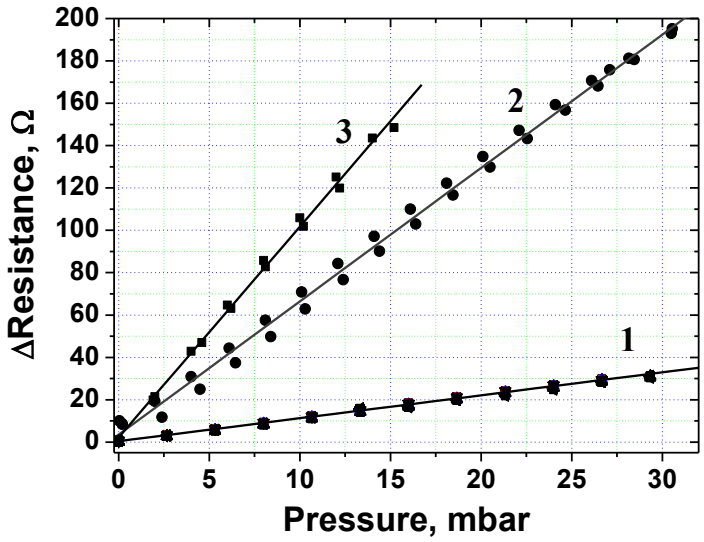

Figure 2-39. Resistance vs. pressure test results of BL film-based membranes: Curve 1 – membrane M1; Curve 2 – membrane M2; Curve 3 – membrane M3.

Table 2-10. Sensitivity of membranes M1-M3 to deformation parallel (GF) and perpendicular (S_P) to the film surface.

BL film-based membrane	thickness, μm	Contact configuration	GF	S_p, Ω/mbar
M1	25	linear	18.2	1.2
M2	5	linear	20.4	6.3
M3	5	dot-like	20.4	10.2

As mentioned before, the electrical response of membranes to pressure changes showed a small drift with time that was ascribed to temperature changes during the measurements. In order to study more in detail this point we repeated the same kind of measurements under a thermostabilized setup. For performing such experiments, a home-made thermostat was designed and fabricated. This portable thermostat was constructed of a rigid polyurethane

foam-based camera whose interior walls were faced with thin Cu plates. The thermostat was equipped with two commercial kapton flexible heaters (KHLV -102/10) that were arranged on two opposite walls and were connected with a DC power supply E3617A. Temperature inside the thermostat was controlled by a Pt-thermometer, which can be maintained constant with an accuracy of ±0.02 ºC. The pressure tests were carried at the following three constant temperatures: 26±0.02 33±0.02 and 40±0.02ºC (Figure 2-40Figure 2-42). In all experiments, the membrane was kept during 30 min under the maximum applied pressure at each temperature to check the stability of the membranes under load.

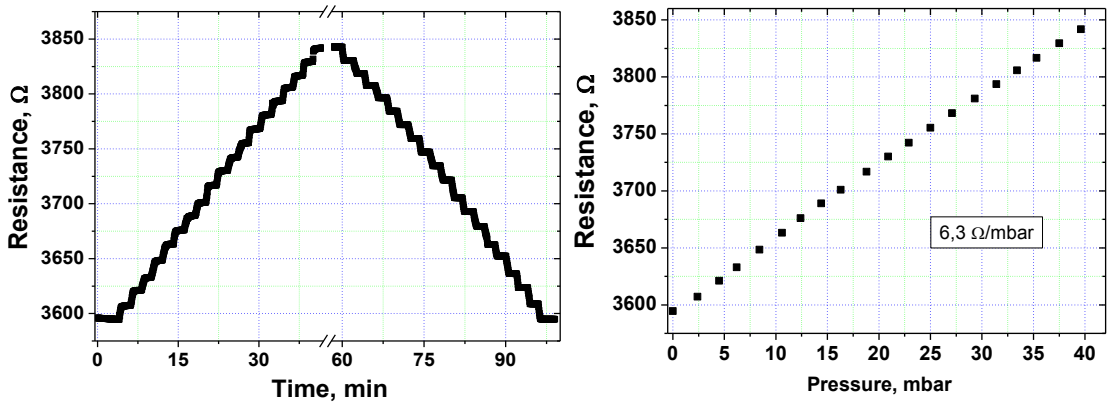

Figure 2-40. Left: Electrical response of membrane M2 at 26±0.02. Variation of pressure was made in 19 steps, each one with a duration of 2 min, going up and down of ca. 2 mbar. Right: Pressure dependence of the resistance based on the data collected for one load-unload cycle.

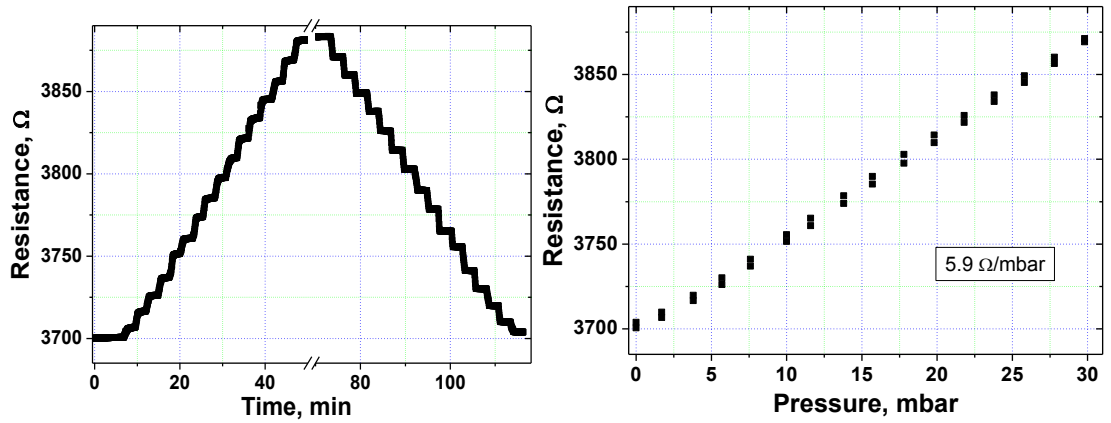

Figure 2-41. Left: Electrical response of membrane M2 at 33±0.02. Variation of pressure was made in 16 steps, each one with a duration of 2.3 min, going up and down of ca. 2 mbar. Right: Pressure dependence of the resistance based on the data collected for one load-unload cycle.

From these experiments we can conclude that the electrical response is reversible at all studied temperatures and the sensitivity slightly changes with the decrease of temperature from 6.3 Ω/mbar at 26 ºC down to 5.8 Ω/mbar at 40 ºC.

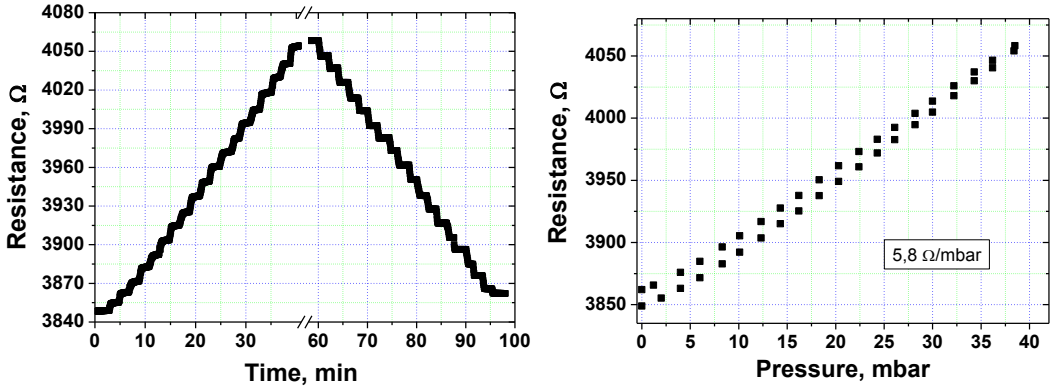

Figure 2-42. Left: Electrical response of membrane M2 corresponding to a variation of pressure in range 0 - 40 mbar (each step up and down being ca. 1.8 mbar) at 40 ºC; Right: Pressure dependence of the resistance based on data collected for load-unload cycle.

We have also studied the long-term stability of membrane **M2**, when it was kept at 26±0.5 **ºC** and ambient conditions during several days (Table 2-11). This study was made measuring the resistance of membrane **M2** along time observing that the resistance oscillates only a 0.5% during 16 days a result that indicates a good long term stability.

Table 2-11. Long-term stability of the resistance value of membrane at 26±0.5ºC.

Time, h	0	24	168	216	312	384
R, Ω	3527	3528	3516	3522	3535	3521

From the above described results we may conclude that the thickness and architecture of the electrical contacts on membranes made with BL films have a strong influence on their pressure sensitivity which can be significantly increased by the use of thinner polymeric layers and dot-like contacts. Also they show that the sensitivity to pressure of membranes depend slightly on the temperature, decreasing when the temperature increases. In addition, the film-based membranes have a good long-term stability under ambient conditions. Based on such characterisation the BL film-based membranes have a potential interest in their use for pressure monitoring in biomedical applications.

Notwithstanding temperature dependence of electrical resistance may be a source of errors in the measurement of pressure. Indeed, the temperature coefficient of resistance of the membranes indicates that the change in the resistance induced by change of 1 degree of temperature is of the same order of magnitude that the electrical response of the membrane to a pressure change of 1 mbar, limiting therefore their use in sensing applications. The temperature dependence of resistance is a very common problem for most strain/pressure sensors with an electrical detection principle. As it was mentioned in the introduction to this Chapter one possible solution is the compensation of the resistance temperature dependence using a Wheatstone bridge with a temperature reference element. For such a purpose one may use a pressure sensing membrane and the temperature reference element that should be identical in their resistance at room temperature and in their TCR but the temperature reference element must not be subjected to any pressure load. In order to compensate possible small temperature gradients the temperature reference element should be placed as close as possible to the pressure sensitive membrane. This design was experimentally tested using the BL film **F2-11** for fabricating both the pressure sensitive membrane and the temperature reference element (Figure 2-43 right). Four annealed Pt wires 20 μm in diameter were attached in a linear contact configuration using a graphite paste placing two of them attached to the conductive piezoresistive layer of the BL film-based sensing membrane and two others to the BL film-based acting as a temperature reference element. The Pt-wires were further connected to copper wires (diameter of 50 μm) and the electrical connections were configured in order to produce the minimum perturbation in the BL film-based sensing membrane. The electrical responses of the sensing membrane and the temperature reference element to pressure changes were measured simultaneously with the Agilent 34970A data acquisition system.

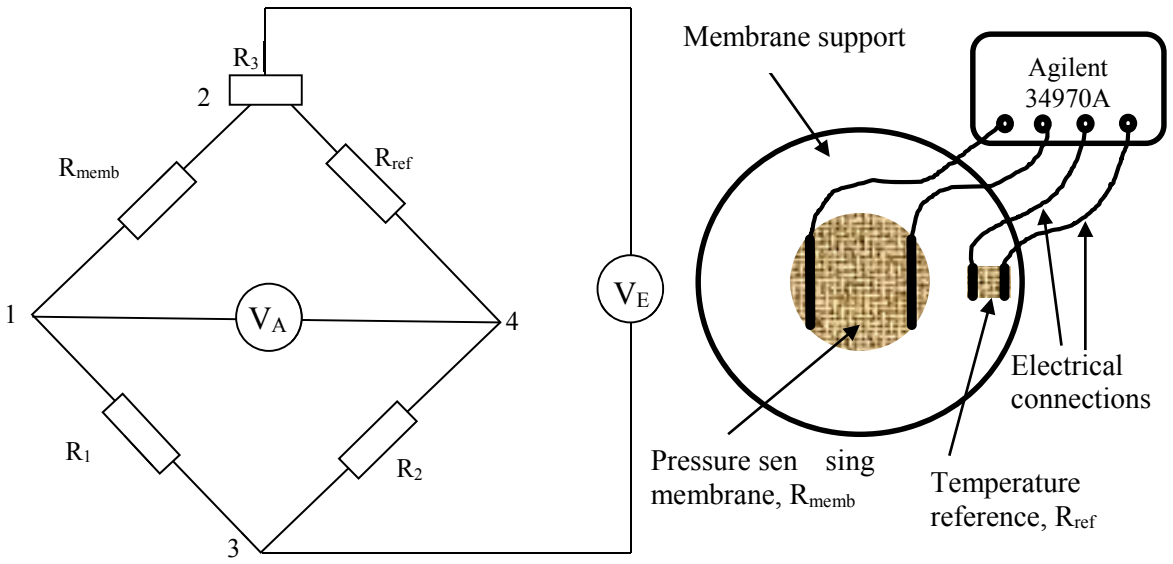

Figure 2-43. Left: Electrical s cheme o f the Wheatstone bridge dev eloped for t emperature compensation: $R_{memb.}$ – the resistance of the sensing membrane; $R_{ref.}$ – the resistance of the BL film used as a temperature reference element and $R_1 = R_2 = 10$ kΩ; R_3 – variable resistance to compensate the Wheatstone´s bridge; Right: the schematic view of the fabricated device.

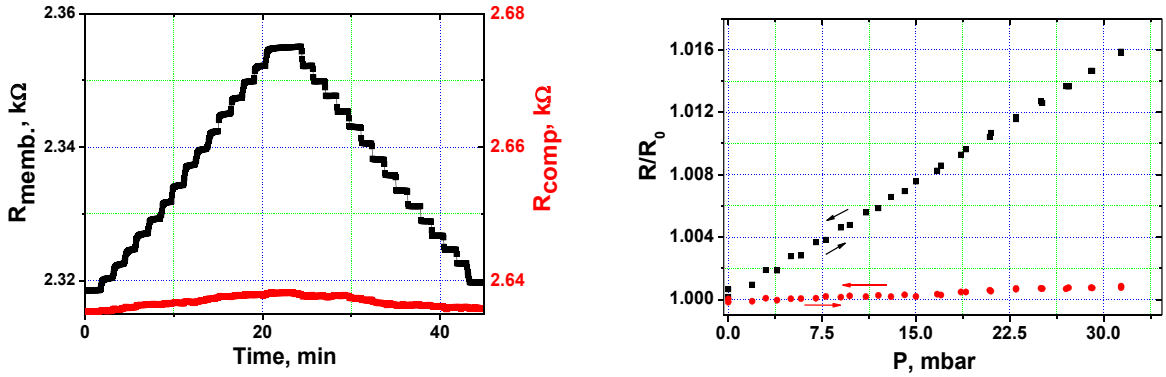

Figure 2-44. Left: Electrical resistance response of the sensing membrane M1 (black curve) and of the temperature reference element (red curve) to pressure variations in range of 0-32 mbar; made in 15 steps, each one during 1.5 min, going up and down of ca. 2.5 mbar. Right: Pressure dependence of the resistance based on the data collected for one load-unload cycle.

The pressure change cycle of this device were performed using the above described home-made U-tube manometer (Figure 2-34) at a temperature between 26 and 28 ºC. The data presented in Figure 2-44 demonstrate that the BL film-based temperature reference element does not change with the pressure load while the BL film-based pressure sensing membrane **M1** responds to the pressure changes fulfilling the requirements for their use in the Wheatstone bridge configuration.

Here the short description of the Wheatstone bridge is given for better understanding of the measurements. The Wheatstone bridges are commonly used with strain gage setups to allow easier measurement of the small changes in resistance. In addition, the Wheatstone bridges are inherently insensitive to supply-voltage fluctuations. The Wheatstone bridge circuit, which can be described as a null - measurement system shown in the left part of the Figure 2-43. A null- measurement system differs from direct measurements in that the quantity being measured is compared with a known reference quantity. This strategy avoids unwanted interaction effects and usually results in greater precision than a direct measurement which depend on the accuracy of a meter movement.

The four arm of the Wheatstone bridge are formed by the resistors R_1, R_2, R_{memb} and R_{ref}. The corner points are numbered for designating the connections. If nodes 2 and 3 – the so-called excitation diagonal – are connected to a known voltage V_E (bridge input excitation or excitation voltage) then a voltage V_A (bridge output voltage) appears between nodes 1 and 4, the so-called measurement diagonal. The main function of the Wheatstone bridge circuit is designed for precise measurement of an unknown resistance, R_{memb}, and utilizes a temperature reference element, R_{ref}, plus two known fixed resistances R_1 and R_2. It should be noted that the Wheatstone bridge may be manually balanced with $V_A = 0$ using the variable resistance R_3 before the measurements are carried out.

The circuit can be mathematically described by

$$\Delta V = \frac{U_A}{U_E} = \frac{R_2}{R_{ref} + R_2} - \frac{R_1}{R_{memb} + R_1} \qquad \text{eq (2.4)}$$

When the bridge is balanced

$$\Delta V = \frac{U_A}{U_E} = 0 \qquad \text{eq (2.5)}$$

and

$$R_{memb} = \frac{R_1 \cdot R_{ref}}{R_2} \qquad \text{eq (2.6)}$$

It should be noted that Wheatstone bridge was manually balanced using the variable resistance R_3 before the pressure was applied. Pressure tests (Figure 2-45), were carried out at a temperature of 40 ^{o}C, where a good temperature compensation is required, showing a

good reversibility but a small difference in the response of Wheatstone bridge: a pressure dependence for up sweeps increased with a slope of 41 μV/mbar while the pressure dependence for down-sweeps decreased with the slope of 39 μV/mbar. The reason of this difference may be related with a small difference in the temperature dependence of the gauge factors of the BL film-based membrane and BL film-based temperature reference element. However, the data presented in Figure 2-45 (right), show that the device has a good temperature compensation opening their use in real applications.

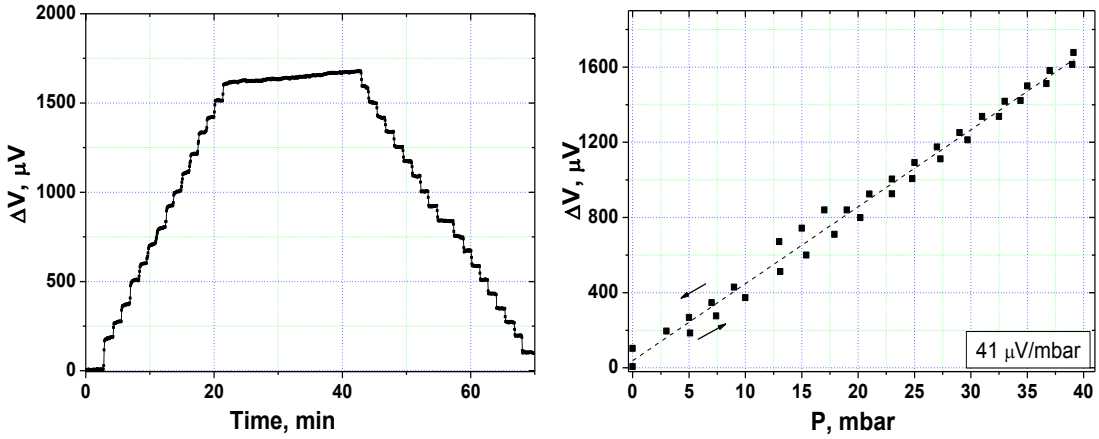

Figure 2-45. Left: Electrical resistance response of the sensing membrane M1 (black curve) and of the temperature reference element (red curve) to pressure variations in range of 0-32 mbar); made in 19 steps, each one during 1 min, going up and down of ca. 2.5 mbar. Right: Pressure dependence of the resistance based on the data collected for one load-unload cycle.

2.8. Simple prototypes for pressure monitoring based on strain sensitive BL films

Due to the high sensitivity of BL films to strain and to their relevant mechanical characteristics, we develop two prototypes working for real applications. First, we report a sensor capable to monitor the intraocular pressure of a human being in the range of mbar. Second, we describe another prototype to measure changes of pressure in the range of hundreds of bars which can be used to sense large pressure changes.

2.8.1. Hybrid contact lens prototype for monitoring the intraocular pressure

This section is devoted to describe a device for monitoring intraocular pressure (IOP) variations in a non-invasive way. The non-invasive monitoring of the IOP variations over

24 h is a strong demand in medicine[78, 79] since it would be a useful medical practice for the following up and treatment of patients with glaucoma. Among numerous attempts to continuously monitor the IOP in a non-invasive way only Leonardi et al. have developed a marketable device. [80] The key element of that device is a soft contact lens with an embedded microfabricated strain gauge (a platinum-titanium foil) allowing the measurement of changes in corneal curvature, which are correlated with the variations of IOP, together with a microchip and an antenna to transmit the electrical changes produced by the IOP variations.

Recently, in our group of research an IOP sensing device [75, 81] based on a rigid contact lens (RCL) equipped with a flexible strain membrane sensor based on the BL film with a layer of β_H-(BEDT-TTF)$_2$I$_3$ crystallites was developed. This sensing RCL device can detect deformations in the corneal curvature caused by pressure changes as small as 1-2 mbar revealing a proper sensitivity to perform continuous monitoring of IOP. However this device had two serious drawbacks. First, the rigid nature of the used RCL avoids to wear it for long time and, second, the device showed a drift in the baseline due to changes of the temperature. In this Thesis we decided to solve both problems constructing an advanced prototype that uses a hybrid contact lens (HCL) instead of RCL and containing an internal compensation element of the resistance temperature dependence of the BL films. The use of a HCL will guarantee the wearing of the device for longer periods of time because it adapts better to the patient corneal curvature due to its flexibility while the temperature compensation element will help to compensate the baseline along the time providing more reliable measurements. To fabricate such an advanced prototype the top of the rigid part of a commercial hybrid contact lens was polished in a way that generates a thin flat supporting area on the top of the rigid part of HCL, where the sensing BL film is glued, as it shown in Figure 2-46. To complete the prototype of lens-based sensor four annealed Pt wires of 20 μm in diameter were attached to the BL film graphite paste with a linear contact configuration, which were connected following a Wheatstone bridge scheme.

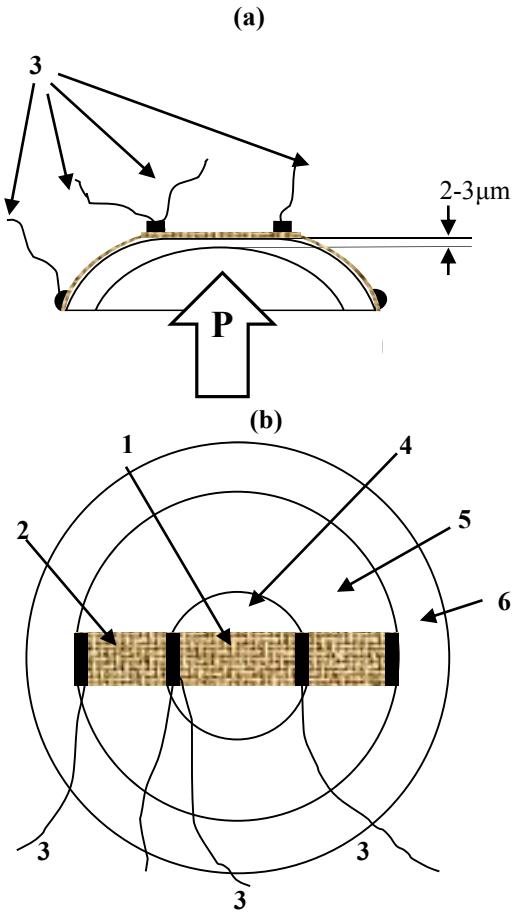

Figure 2-46. Schematic view of the different parts of an hybrid contact lens equipped with the BL film-based pressure gauge a) side view of the rigid part of the HCL; b) top view of a complete HCL. 1- strip of BL film-based sensing membrane (R_{memb}); 2- part of the BL film-based acting as a temperature resistance reference (R_{ref}); 3- electrical connections forming part of the Wheatstone bridge; 4 -flat surface part in the rigid part of the HCL; 5- rigid part of the HCL; 6- soft part of the HCL.

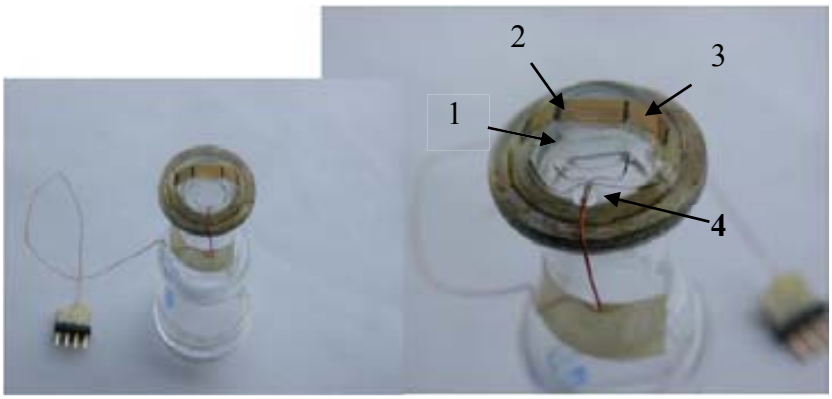

Figure 2-47. Two images with different magnifications of the sensing prototype based on a commercial hybrid contact lens installed on a glass holder for pressure tests: 1-rigid part of the hybrid lens; 2-setup of the BL film; 3- part of the BL film used as a temperature reference element; 4-electrical connections.

All pressure tests with the prototype were made using the setup shown in Figure 2-47 which connects on a ring-like glass holder and a O-ring that fix the sensing HCL to the holder. The glass holder was connected by the tube of a low-pressure controller (CPC2000 "Mensor") used for generating a controlled pressure. To minimize the influence of the ambient temperature changes on the resistance of the pressure sensitive element of the sensor, all pressure tests were made inside a thermo-insulating camera fabricated from rigid polyurethane foam. Tests were also conducted with a simultaneously temperature monitoring, for which a Pt-thermometer (Pt_{100}) located close to the sensing HCL was used. A temperature compensation scheme similar to that described in Section 2.7 was used. This approach permitted us to minimize the presence of inhomogeneities and the defects on the different parts of the BL film that can appear during a preparation process. The distance between the electrical contacts for both the pressure sensitive element and the temperature reference element were very similar in order to achieve a better temperature compensation effect enabling to detect very small changes of pressure with a high accuracy.

Pressure and temperature tests. The electrical responses of both active elements of the sensing HCL - the pressure sensing element and temperature reference element - to pressure changes were fully studied using the Agilent 34970A data acquisition system. The pressure changes were applied in steps, each step was 10 mbar going up (and down) during period of 1 min allowing a maximum of the applied pressure of 50 mbar. As it is shown in Figure 2-48 there is practically no changes in the resistance of the temperature reference element while the pressure sensing element shows its typical electrical response to pressure variations with a sensitivity of ca. 1.2 Ω/mbar, which is identical to that described in Section 2.7 for the membrane **M1** that has the same characteristic with the BL film used for the sensing HCL.

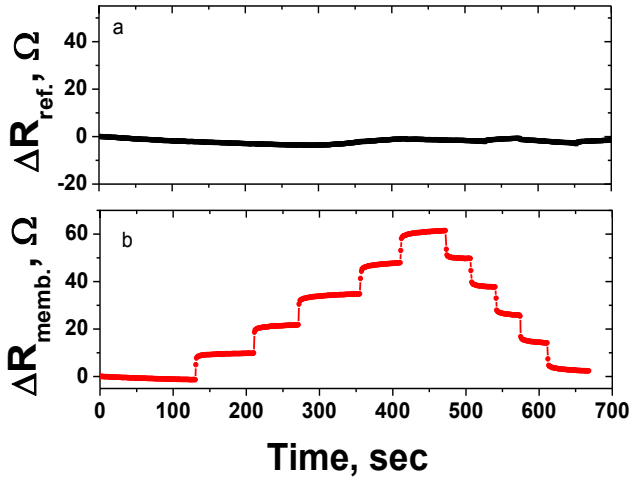

Figure 2-48. Pressure dependence of the resistance for the temperature reference element (a) and for the pressure sensing element (b) measured for in the pressure range of 0-50 mbar.

Additionally, we also measured the temperature dependences of the resistance of the pressure sensing and temperature reference elements under different pressures (0, 20, 40 and 50 mbar). The temperature dependences of the normalized resistance of both elements at 0 and 20 mbar are depicted in Figure 2-49 showing that at the different pressures the temperature dependences both elements of the sensing HCL are quite similar. Identical results were found for the measurements made at 40 and 50 mbar. This result allows us to discard any influence of the temperature on the electrical resistance of the pressure sensing element.

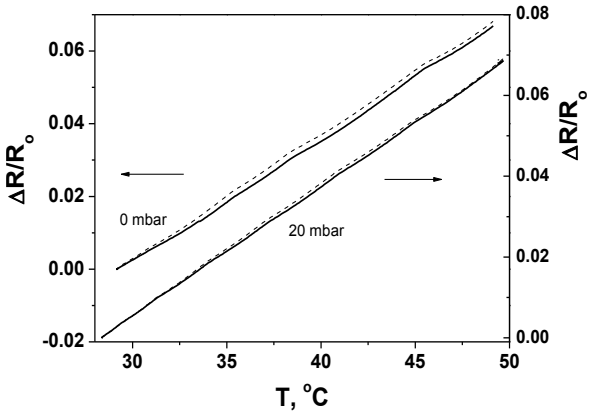

Figure 2-49. Temperature dependences of the normalized resistance of the two active elements – the pressure sensing element (solid lines) and the temperature reference element (dashed lines) of the sensing HCL at ambient pressure (0 bar) and of 20 mbar.

In order to evaluate the efficiency of the temperature compensation in the sensing HCL we have evaluated the temperature dependence of the pressure sensing element with and without a temperature compensation element at constant pressure. To do so we used the ΔR_{sens}, obtained by eq. 2.7, which enables to take into account the slight difference in the initial resistance between both active elements of the HCL and to correct the changes produced in the sensing HCL. Equation 2.7 is as follow:

$$\Delta R_{sens} = \frac{R_{memb} \cdot R_{ref_0}}{R_{ref}} - R_{memb_0} \qquad \text{(eq. 2.7)},$$

where R_{sens} and R_{sens0} are the resistances of the sensing HCL at a given temperature and at room temperature, respectively; $\Delta R_{sens} = R_{sens} - R_{sens0}$; R_{memb} and R_{memb0} are the resistances of the pressure sensing element at a given temperature and at room temperature, respectively; R_{ref} and R_{ref0} are the resistances of the temperature reference element at a given temperature and at room temperature, respectively. The comparison of the values of ΔR_{sens} and $\Delta R_{memb} = R_{memb} - R_{memb0}$ in the temperature range of 23-50 ºC (see Figure 2-50) permits us to estimate the goodness of the temperature compensation in the sensing HCL as well as to use ΔR_{sens} as an temperature independent parameter at the external temperature.

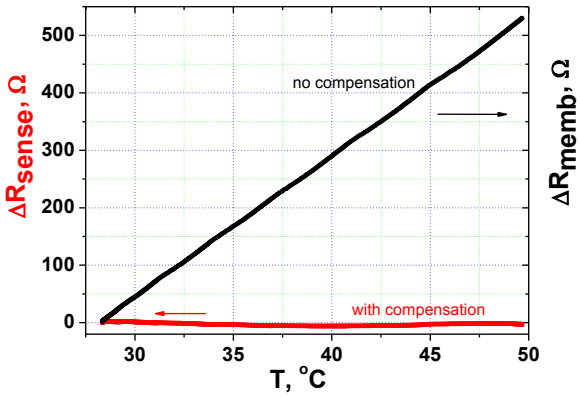

Figure 2-50. Temperature dependences of the resistances of the sensing HCL: ΔR_{sens} and the pressure sensing element ΔR_{memb} measured under a constant pressure of 20 mbar.

Finally, we performed the pressure tests with the HCL prototype using the Wheatstone bridge configuration. For such tests the applied pressure was changed from 0 to 50 mbar, which changes in each step of 10 mbar (Figure 2-51). The sensitivity of the Wheatstone

bridge was found to be about 37.1 μV/mbar. This value is quite similar with obtained for the pressure sensitive membrane **M1** described in Section 2.7.. It means that the response of BL film based membrane to pressure is same reproducible from prototype to prototype.

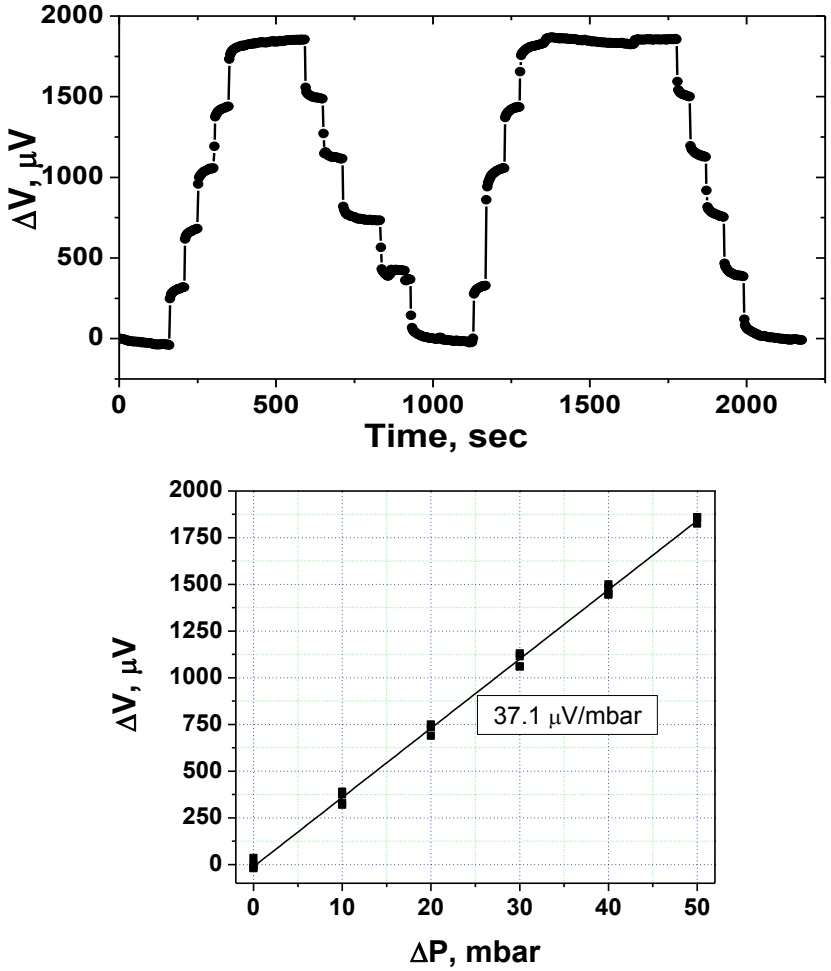

Figure 2-51. (Top): The Wheatstone bridge response (in time) under pressure applied up to 50 mbar in two cycles with 10 mbar steps and standing at high pressure about 10 min at T=29-30°C. The excitation current was 20 μA. (Bottom): Pressure dependence of the Wheatstone bridge voltage from data collected for the load-unload cycles.

Since the ultimate goal was to use the HCL sensor to control IOP variation in humans, it is necessary to know the biocompatibility of the BL film. For this purpose, a preliminary biocompatibility study was conducted with six guinea pigs[ii]. The histological study showed less inflammatory reaction in the BL film site than to the silicone bands in all samples of tissues. [81] Summarizing the experimental data presented in this Section, it may be

[ii] Biocompatible tests were made in the group of Prof Carlos Pastor, Institute for Applied Ophthalmobiology (IOBA), Universidad de Valladolid, Spain.

concluded that the pressure tests shows that the developed prototype of sensing HCL can be used for monitoring IOP changes under of the human body and the ambient temperature variations. It should be also noted that the developed prototype significantly simplifies the fabrication of an IOP sensor based on a contact lens providing a high sensitivity.

2.8.2. A prototype of a compact multi-layer pressure sensor for measuring high pressures

Precise measuring of large changes of pressure is another important demand of the industry since it can open several different types of applications. For this reason we decided to develop proper prototypes for such applications using BL films.

As already described in this Chapter the sensing devices made with the piezoresistive BL films, containing the β_H-(BEDT-TTF)$_2$I$_3$ salt, are able to detect tiny variations of the pressure when used as membrane since they are capable to transduce such variation into changes of the resistance of the such composite films. The variation of the resistance when the BL films are elongated results in a stretching of the conducting crystallographic *ab* plane of the *c**-oriented crystallites of the metallic salt which generate a slight increase of the intermolecular distances between the BEDT-TTF molecules (see Figure 2-52). This increase leads to a decrease of the intra- and inter-molecular stacks transfer integral of this molecular metal and, as a consequence, to an enormous increase of the resistance of the crystals and the BL films. A very large change of pressure may produce an undesirable rupture of the continuous layer of crystallites of the molecular metal if the applied strain exceeds the R_{yield} value. In accordance with this fact the piezoresistive BL films cannot be used as sensing element for detecting large changes of the pressure when they are used in a membrane configuration. Nevertheless, their use in other configuration may overcome such limitation. In this Section we report two prototypes which use different configurations for construct compact flexible multi-layer pressure sensor with BL films as active components. Both prototypes are based on the integration of a flexible pressure sensing element and a set of gold electrodes into a compact multi-layer pressure sensor enabling to use the ultimate highly strain sensing BL films for monitoring pressure changes in the order of hundreds of bars with an appropriate accuracy.

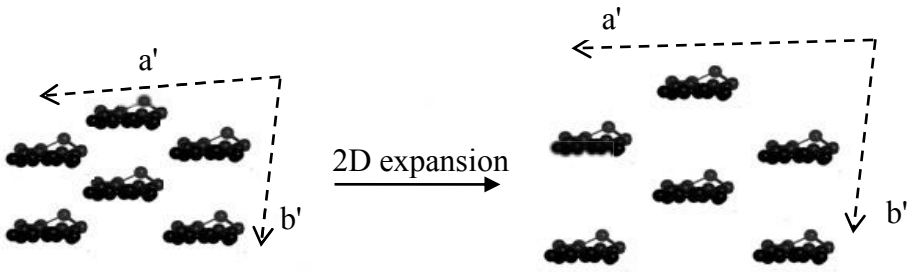

Figure 2-52. Schematic representation of the extension of the crystallographic *ab* plane of the sensing crystallites of β_H-(BEDT-TTF)$_2$I$_3$ under a deformation along the *ab* plane of crystallites. For clarity the anion layers are hidden.

One of the developed pressure sensor prototypes, the **PS1** one, operates under quasi-hydrostatic conditions while the other, the **PS2** sensor, operates by shearing deformation conditions.

Fabrication of the prototypes. The pressure sensor **PS1** was made with a piece of the BL film **F2-11** with an area of ca. 12x5 mm^2 and 25 μm thickness sandwiched between two large polycarbonate supporting films of different thicknesses and sizes, as schematically shown in Figure 2-53. On one of the supporting polycarbonate film of 200 μm thick and an area of 30x50 mm^2 four gold strips of 1 μm thick were evaporated to act as electrodes. The other polycarbonate supporting film has a thickness of 400 μm and an area of 30x30 mm^2. Then the BL film was mounted over the larger supporting polycarbonate film with the conducting layer of the BL film contacting with the gold electrodes and the smaller supporting film was deposited over it. To complete the pressure sensor four Cu wires were attached with a silver paste to the gold electrodes and fixed with a glue to the larger polycarbonate supporting film in order to avoid any stress from the contacts. The principle of this pressure sensor permits to operate under quasi hydrostatic conditions when is compressed since the high surface friction between all polycarbonate layers and with the surface of the piston of the press can act as a pressure-transmitting medium to the crystallites of the β_H-(BEDT-TTF)$_2$I$_3$. Consequently, when a compression is applied to **PS1** the crystallites will be compressed in all directions and the intra-molecular distances will decrease (see Figure 2-54) with a reduction of the resistance of the sensor.

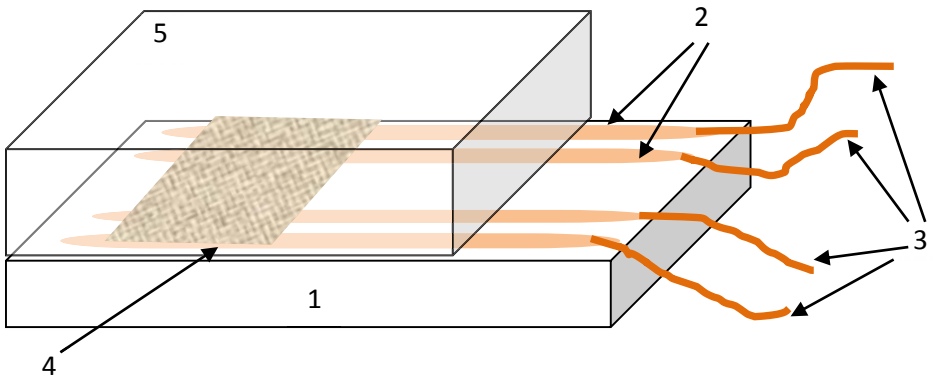

Figure 2-53. Schematic representation of the pressure sensor PS1 consisting in a BL film based sadwiched between two polycarbonate supporting films: (1) polycarbonate supporting film with four gold strips (2) were deposited; (3) four Cu wires attached to the gold strips using graphite paste; (4) BL film and the polycarbonate supporting film of 400 µm thickness and the 30 × 30 mm^2 area (5).

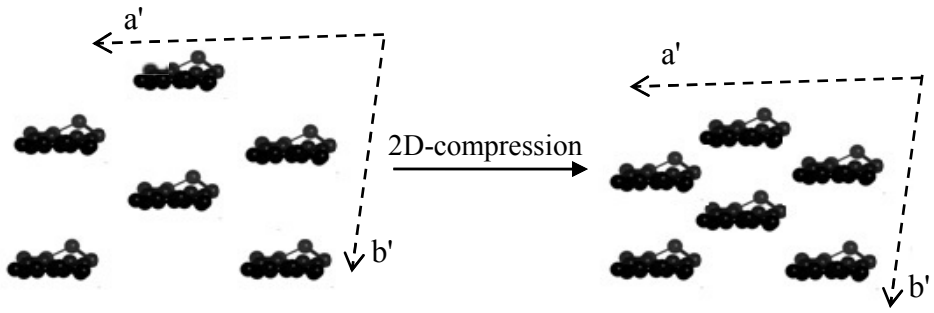

Figure 2-54. Schematic representation of the crystallographic *ab* plane of the sensing crystallites of the piezoresistive metal β_H-(BEDT-TTF)$_2$I$_3$ under a quasi-hydrostatic compression.

The pressure sensor **PS2** was made with the sensor **PS1** adding two further layers on each side consisting of a double sided scotch tape and a Kapton films of 130 µm thick with an area of 30x30 mm^2. The purpose of the added two layers is to reduce considerably the surface friction of the polycarbonate supporting layers with the piston of the hydraulic press forcing the sensor to operate under shearing deformation conditions. Thus, when the sensor is compressed three polycarbonate layers will expand laterally and the crystallites of the BL film will surfer a 2D-expantion (see Figure 2-52) increasing the resistance of the sensor.

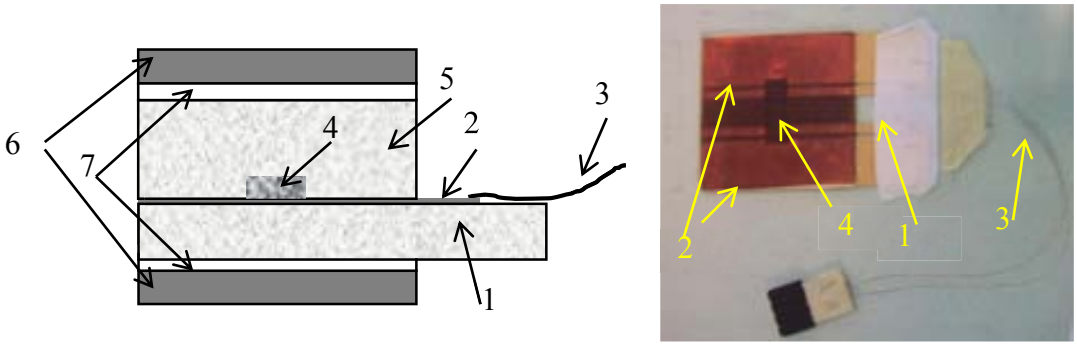

Figure 2-55. Left: Schematic view of the multi-layer pressure sensor PS2 constructed from the seven different layers: (1) polycarbonate supporting film of 200 µm thick and an area of 30x30 mm^2 on which four gold strips of 1 µm thick (2) were deposited; (3) four Cu wires attached to the gold strips using silver paste; (4) piezo-resistive BL film; (5) polycarbonate supporting film of 400 µm thick with a plane area 30x30 mm; (6) two Kapton films of 130 µm thick and with areas of 30x30 mm glued to the polycarbonate films with a double-sided film scotch tape (7). Right: photo of the prototype.

Pressure tests. To study the effect of pressure on the electrical resistance of the **PS1** and **PS2** multi-layer sensors, they were placed over the piston of the hydraulic press ("Unipress", Poland), as shown in Figure 2-56. Sensors were subjected to different step-wise pressure load-unload cycles by the hydraulic press that pushes/raises the piston and the pressure sensor against the stationary disk and the electrical response of the sensors were measured with the Multimeter Agilent 34970A in a four contacts configuration.

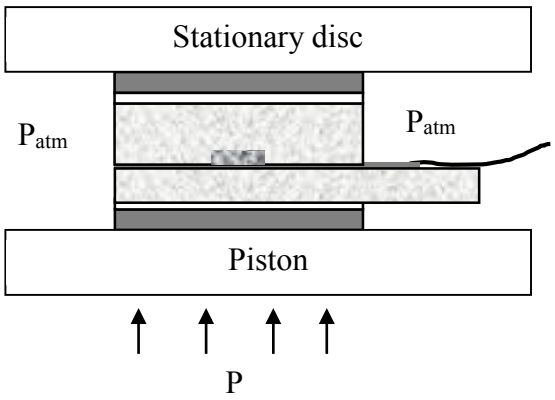

Figure 2-56. Schematic representation of the hydraulic press used for testing the sensor PS2 with step-wise load-unload cycles.

Figure 2-57 shows that the resistance of sensor **PS1** decreases when the pressure increases from 0 up to 545 bars and it is reversibly increased when the pressure decrease down to 0 bar..

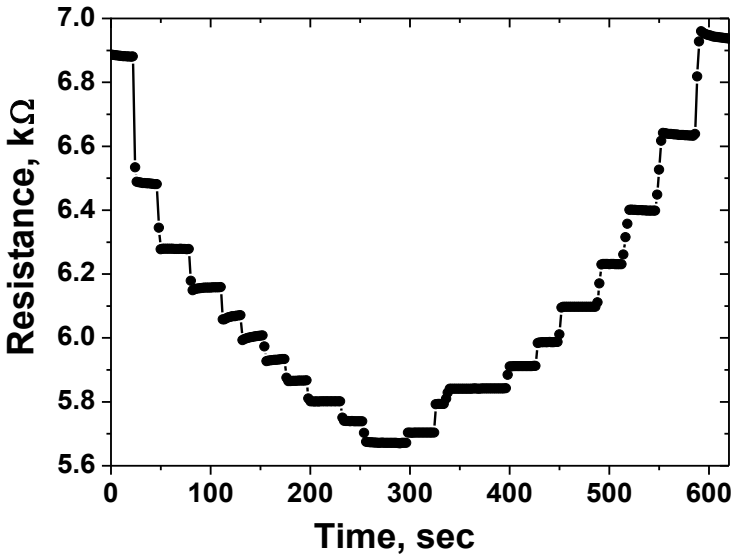

Figure 2-57. Electrical response of the sensor PS1 to the step-wise variations of the pressure in 10 steps of 55 bar each during 30 sec in the range of 0-545 bar.

Therefore, as it was initially designed, the crystallites of β_H-(BEDT-TTF)$_2$I$_3$ are isostatically compressed with a load under the quasi hydrostatic conditions applied to the sensor and as a consequence the distance between the BEDT-TTF molecules decreases increasing the intra- and inter- BEDT-TTF molecular stack transfer integrals leading to a decrease of the BL film resistance.

For a better visualization of the above presented electro-mechanical behaviour of the sensor **PS1**, the electrical resistance data, collected for pressure loading in the range 0-545 bars, are plotted in Figure 2-58 as the relative resistance changes versus the applied pressure. As it is clear from this Figure, the electrical response of sensor **PS1** to pressure deviates significantly from linearity. So, the pressure-dependent compression of the lattice parameters of the crystallites monotonically slows down when the pressure is increased from 0 up to 545 bars.

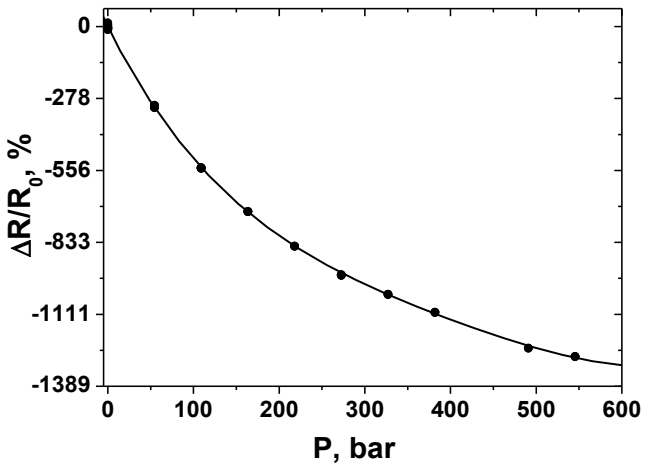

Figure 2-58. Normalized resistance changes *vs* the applied pressure of sensor PS1 in the pressure range 0-545 bar.

This nonlinear behavior represent a disadvantage for using the pressure sensor **PS1** in practical applications since it imposes the need of performing calibrations before its use.

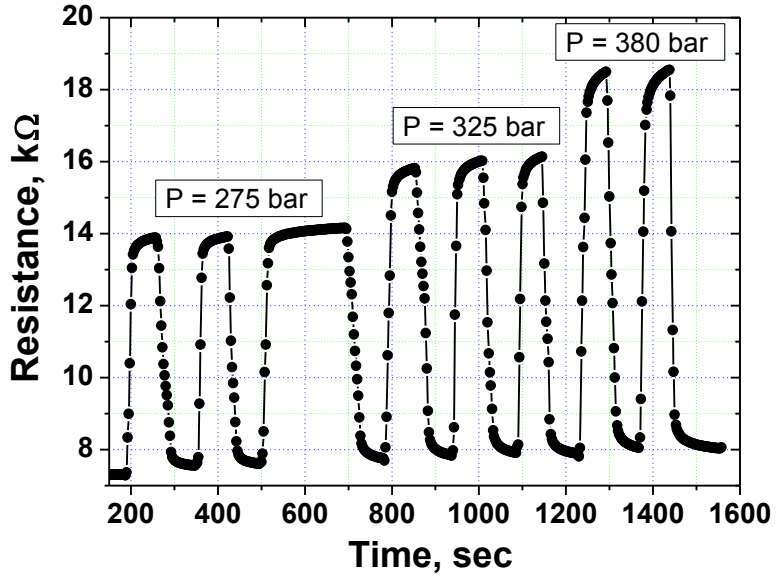

Figure 2-59. Illustration of repeatability of the respond of the sensor PS2 at different pressure cycles: 0–275-0 bar, 0-325-0 bar and 0–380-0 bar.

As shown in Figure 2-59, the electrical response of the multi-layer sensor **PS2** to pressure follows our initial design principle since an increase of the pressure produces an increase of the sensor resistance being the response to pressure very strong and highly reproducible.

Thus, the presence of the layers of a double-sided Scotch tape and a Kapton reduces considerably the surface friction of the sensor with the press's piston surface and thereby the BL film and polycarbonate supporting layers are laterally stretched under pressure resulting in an increase of the sensor resistance (Figure 2-59). As already explained this is due to the expansion of the molecules of the crystallites that decrease the transfer integrals increasing the resistance. For a better visualization of the above presented behavior of the pressure sensor **PS2**, the electrical resistance data, collected for one of the multi cyclic pressure loadings in the range 0-275 bar, are plotted as the relative resistance changes *versus* the applied pressure in Figure 2-60. This plot shows that in contrast to sensor **PS1** the electrical response of sensor **PS2** to pressure essentially does not deviate from the linearity.

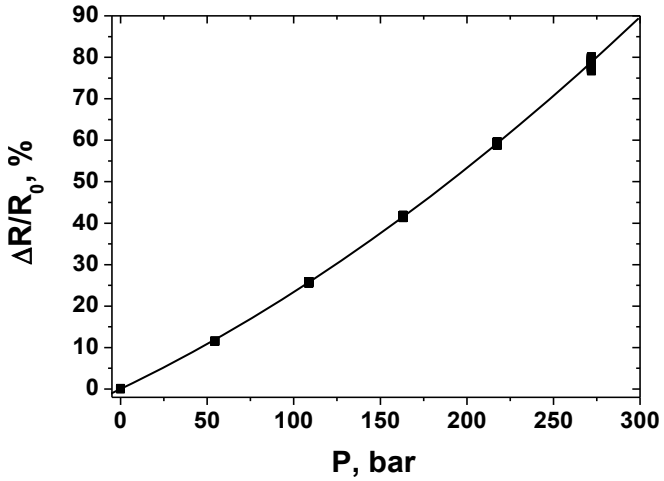

Figure 2-60 Normalized resistance changes *vs* the applied pressure of sensor PS2 is the pressure range 0-275 bar.

The sensitivity of this sensor, calculated as the ratio between the relative resistance change and the pressure change was found to be around 0.3%/bar or 23 Ω/bar, taking into account the initial resistance value of 7.6 kΩ. Therefore, the developed multi-layer prototype allows the use of thin BL films for fabricating compact flat pressure sensors that enable to measure pressure in the wide pressure range of 0-400 bar with an acceptable sensitivity and a well-defined electrical signal. As a main conclusion, we may say that sensor **PS2** is very attractive as a new generation of durable, low-cost, all-organic pressure sensors that can monitor quite large pressure changes with a good level of measurement accuracy.

2.9. Conclusions

The measured Young's moduli of α- and β_H-(BEDT-TTF)$_2$I$_3$ single crystals in different orientations are close to the reported Young's modulus of commercial polymers permitting thereby a good adhesion between layers into the composite BL films and opens the door towards practical application of the BL films.

Mechanical and electromechanical properties of BL films based on α- and β_H-(BEDT-TTF)$_2$I$_3$ molecular conductors show that both composite materials are highly sensitive strain sensors that are stable along time and robust if relative strain does not exceed of 0.6%. These characteristics bring the opportunity to develop many deformation/pressure sensors with such materials.

A fine tuning of the transport properties of the BL films, covered with crystallites of the α-(BEDT-TTF)$_2$I$_3$ semimetal, by varing the preparation conditions permits to obtain a piezoresistive BL film with a high strain sensitivity and with a temperature independent behaviour of its resistance which simplify the development of sensing devices.

Conditions to prepare highly strain sensitive BL films covered with the β_H-(BEDT-TTF)$_2$I$_3$, with large areas were developed opening the possibility to prepare in a reproducible manner centimetre-scale BL films with β_H-(BEDT-TTF)$_2$I$_3$ crystallites as an active component which can be used to made pressure sensors capable to measure changes of pressure.

Several simple prototypes based on highly strain sensitive BL films enabling to perform pressure monitoring with high accuracy in the range of mbar and hundreds bar were developed. Remarkable is the hybrid contact lens sensing device developed with one of such prototypes that fulfil the main requirements to measure the intraocular pressure of human beings.

Bibliography

1. F. Axisa, P. M. Schmitt, C. Gehin, G. Delhomme, E. McAdams and A. Dittmar, Flexible technologies and smart clothing for citizen medicine, home healthcare, and disease prevention, Ieee Transactions on Information Technology in Biomedicine, 2005, 9, 325-336.

2. T. Someya, T. Sekitani, S. Iba, Y. Kato, H. Kawaguchi and T. Sakurai, A large-area, flexible pressure sensor matrix with organic field-effect transistors for artificial skin applications, Proceedings of the National Academy of Sciences of the United States of America, 2004, 101, 9966-9970.

3. F. Carpi and D. De Rossi, Electroactive polymer-based devices for e-textiles in biomedicine (vol 9, pg 295, 2005), Ieee Transactions on Information Technology in Biomedicine, 2005, 9, 574-574.

4. R. K. Banerjee, S. V. Peelukhana and I. Goswami, Influence of newly designed monorail pressure sensor catheter on coronary diagnostic parameters: An in vitro study, Journal of Biomechanics, 2014, 47, 617-624.

5. K. Pitsillides, M. Lin, L. Griffiths, D. Uyeminami, K. Johnson and K. Pinkerton, Endovascular dual-sensor composite sensor catheter for the measurement of flow and pressure in rats using telemetry, Faseb Journal, 2013, 27.

6. M. Shikida, T. Shikano, T. Matsuyama, Y. Yamazaki, M. Matsushima and T. Kawabe, Micromachined catheter flow sensor and its applications in breathing measurements in animal experiments, Microsystem Technologies-Micro-and Nanosystems-Information Storage and Processing Systems, 2014, 20, 505-513.

7. H. C. Lim, B. Schulkin, M. J. Pulickal, S. Liu, R. Petrova, G. Thomas, S. Wagner, K. Sidhu and J. F. Federici, Flexible membrane pressure sensor, Sensors and Actuators a-Physical, 2005, 119, 332-335.

8. M. I. Azmer, Q. Zafar, Z. Ahmad, K. Sulaiman and K. S. Karimov, VOPcPhO based organic pressure sensor and displacement transducer, Synthetic Metals, 2014, 191, 120-125.

9. S.-Y. Cho, K.-W. Lee, J.-W. Kim and D.-H. Kim, Rugate-structured free-standing porous silicon-based fiber-optic sensor for the simultaneous detection of pressure and organic gases, Sensors and Actuators B-Chemical, 2013, 183, 428-433.

10. T. Aoki, Pressure sensor, has organic transistor provided on glass substrate, and channel region and gate insulating film provided in pressure-sensitive parts that work as pressure-sensitive device by generating characteristic change, Seiko Epson Corp.

11. Y.-C. Perng, J. Cho, S. Y. Sun, D. Membreno, N. Cirigliano, B. Dunn and J. P. Chang, Synthesis of ion conducting $Li_xAl_ySi_zO$ thin films by atomic layer deposition, Journal of Materials Chemistry A, 2014, 2, 9566-9573.

12. X. p. Sun, Q. Zhang, Y. Liu, N. Huang, P. Sun, T. Peng, T. Peng and X.-Z. Zhao, Photovoltaic performance improvement of dye-sensitized solar cells through

introducing In-doped TiO_2 film at conducting glass and mesoporous TiO2 interface as an efficient compact layer, Electrochimica Acta, 2014, 129, 276-282.

13. E. Laukhina, R. Pfattner, L. R. Ferreras, S. Galli, M. Mas-Torrent, N. Masciocchi, V. Laukhin, C. Rovira and J. Veciana, Ultrasensitive Piezoresistive All-Organic Flexible Thin Films, Advanced Materials, 2010, 22, 977-+.

14. E. Laukhina, R. Pfattner, M. Mas-Torrent, C. Rovira, J. Veciana and V. Laukhin, Film-based sensors with piezoresistive molecular conductors as active components: Strain damage and thermal regeneration, Sensors and Transducers, 2011, 10, 1-12.

15. J. E. Schirber, D. L. Overmyer, K. D. Carlson, J. M. Williams, A. M. Kini, H. H. Wang, H. A. Charlier, B. J. Love, D. M. Watkins and G. A. Yaconi, Pressure-temperature phase diagram, inverse isotope effect, and superconductivity in excess of 13 K in kappa-$(BEDT\text{-}TTF)_2Cu$, Phys Rev B Condens Matter, 1991, 44, 4666-4669.

16. J. M. Williams, T. J. Emge, H. H. Wang, M. A. Beno, P. T. Copps, L. N. Hall, K. D. Carlson and G. W. Crabtree, Synthetic metals based on bis(ethylenedithio)tetrathiafulvalene (BEDT-TTF) - synthesis, structure and ambient-pressure superconductivity in $(BEDT\text{-}TTF)_2I_3$, Inorganic Chemistry, 1984, 23, 2558-2560.

17. D. Jerome, Organic conductors: From charge density wave TTF-TCNQ to superconducting $(TMTSF)_2PF_6$, Chemical Reviews, 2004, 104, 5565-5591.

18. R. P. Shibaeva and E. B. Yagubskii, Molecular conductors and superconductors based on trihalides of BEDT-TTF and some of its analogues, Chemical Reviews, 2004, 104, 5347-5378.

19. G. Saito and Y. Yoshida, Development of conductive organic molecular assemblies: Organic metals, superconductors, and exotic functional materials, Bulletin of the Chemical Society of Japan, 2007, 80, 1-137.

20. R. Kondo, M. Higa, S. Kagoshima, H. Hoshino, T. Mori and H. Mori, Electrical and structural properties of theta-type BEDT-TTF organic conductors under uniaxial strain, Journal of the Physical Society of Japan, 2006, 75.

21. F. Creuzet, G. Creuzet, D. Jerome, D. Schweitzer and H. J. Keller, Homogeneous superconducting state at 8.1 K undere ambient pressure in the organic conductor beta-$(BEDT\text{-}TTF)_2I_3$, Journal De Physique Lettres, 1985, 46, 1079-1085.

22. M. V. Kartsovnik, P. A. Kononovich, V. N. Laukhin, A. G. Khomenko and I. F. Shchegolev, Investigation of the phase T-P diagram for alpha-$(BEDT\text{-}TTF)_2I_3$, Zhurnal Eksperimentalnoi I Teoreticheskoi Fiziki, 1985, 88, 1447-1451.

23. V. N. Laukhin, E. E. Kostyuchenko, Y. V. Sushko, I. F. Shchegolev and E. B. Yagubskii, Effect of the pressure on the superconductivity of beta-$(BEDT\text{-}TTF)_2I_3$, Jetp Letters, 1985, 41, 81-84.

24. H. Schwenk, F. Gross, C. P. Heidmann, K. Andres, D. Schweitzer and H. Keller, alpha-$(BEDT\text{-}TTF)_2I_3$ AND beta-$(BEDT\text{-}TTF)_2I_3$ - 2 modifications with

contrasting ground-state properties - insulator and volume superconductor, Molecular Crystals and Liquid Crystals, 1985, 119, 329-335.

25. D. A. Hardwick, The mechanical properties of thin-films - a review, Thin Solid Films, 1987, 154, 109-124.

26. G. Saito, H. Urayama, H. Yamochi and K. Oshima, Chemical and physical properties of a new ambient pressure organic superconductor with Tc higher than 10K, Synthetic Metals, 1988, 27, A331-A340.

27. M. Kund, H. Veith, H. Müller, K. Andres and G. Saito, Anisotropic uniaxial-stress dependence of the superconducting transition temperature in single crystals of κ-(BEDT-TTF)$_2$Cu[N(CN)$_2$]Br, Physica C: Superconductivity, 1994, 221, 119-124.

28. M. Maesato, Y. Kaga, R. Kondo and S. Kagoshima, Uniaxial strain method for soft crystals: Application to the control of the electronic properties of organic conductors, Review of Scientific Instruments, 2000, 71, 176.

29. M. Maesato, Y. Kaga, R. Kondo and S. Kagoshima, Control of electronic properties of α-(BEDT-TTF)$_2$MHg(SCN)$_4$ (M=K, NH$_4$) by the uniaxial strain method, Physical Review B, 2001, 64.

30. I. Tamura, H. Kobayashi and A. Kobayashi, X-ray diffraction study of α-(BEDT-TTF)$_2$I$_3$ single crystal under high pressure, Journal of Physics and Chemistry of Solids, 2002, 63, 1255-1257.

31. N. Tajima, A. Tajima, M. Tamura, R. Kato, Y. Nishio and K. Kajita, Pressure control of transport property of organic conductors; α-, θ-(BEDT-TTF)$_2$I$_3$and θ -(DIETS)$_2$[Au(CN)$_4$], Journal de Physique IV (Proceedings), 2004, 114, 263-267.

32. S. Iwai, K. Yamamoto, F. Hiramatsu, H. Nakaya, Y. Kawakami and K. Yakushi, Hydrostatic pressure effect on photoinduced insulator-to-metal transition in the layered organic salt α-(BEDT-TTF)$_2$I$_3$, Physical Review B, 2008, 77.

33. http://saitolab.meijo-u.ac.jp/research_abstract.html.

34. J. J. Roa, G. Oncins, F. T. Dias, V. N. Vieira, J. Schaf and M. Segarra, AFM as an alternative for Young's modulus determination in ceramic materials in elastic deformation regime, Physica C-Superconductivity and Its Applications, 2011, 471, 544-548.

35. J. J. Roa, G. Oncins, J. Diaz, X. G. Capdevila, F. Sanz and M. Segarra, Study of the friction, adhesion and mechanical properties of single crystals, ceramics and ceramic coatings by AFM, Journal of the European Ceramic Society, 2011, 31, 429-449.

36. J. J. Roa, G. Oncins, J. Diaz, F. Sanz and M. Segarra, Calculation of Young's Modulus Value by Means of AFM, Recent Patents on Nanotechnology, 2011, 5, 27-36.

37. E. Laukhina, C. Rovira and J. Ulanski, Organic metals as active components in surface conducting semi-transparent films, Synthetic Metals, 2001, 121, 1407-1408.

38. B. Rothaemel, L. Forro, J. R. Cooper, J. S. Schilling, M. Weger, P. Bele, H. Brunner, D. Schweitzer and H. J. Keller, Magnetic sisceptibility of alpha-phases and beta-phases of bis(ethylenedithiolo)tetrarhiafulvalene tri-iodide (BEDT-TTF)$_2$I$_3$ under pressure, Physical Review B, 1986, 34, 704-712.

39. G. O. Baram, L. I. Buravov, L. S. Degtyarev, M. E. Kozlov, V. N. Laukhin, E. E. Laukhina, V. G. Onishchenko, K. I. Pokhodnya, M. K. Sheinkman, R. P. Shibaeva and E. B. Yagubskii, Transformation of the alpha-phase (BEDT-TTF)$_2$I$_3$ to the superconducting beta-phase with T_C=6-7 K, Jetp Letters, 1986, 44, 376-378.

40. V. F. Kaminskii, T. G. Prokhorova, R. P. Shibaeva and E. B. Yagubskii, Crystal structure of the organic superconductor (BEDT-TTF)$_2$I$_3$, Jetp Letters, 1984, 39, 17-20.

41. V. N. Molchanov, R. P. Shibaeva, V. N. Kachinskii, E. B. Iagubskii, V. I. Simonov and B. K. Vainstein, Crystal and molecular structure of organic superconductor beta-(BEDT-TTF)$_2$I$_3$ at pressure of 9.5 kbar, Doklady Akademii Nauk Sssr, 1986, 286, 637-640.

42. K. Kornelsen, J. E. Eldridge, H. H. Wang and J. M. Williams, Infrared optical properties of the 10 K organic superconductor (BEDT-TTF)$_2$I$_3$, Phys Rev B Condens Matter, 1991, 44, 5235-5245.

43. L. P. Le, G. M. Luke, B. J. Sternlieb, W. D. Wu, Y. J. Uemura, J. H. Brewer, T. M. Riseman, C. E. Stronach, G. Saito, H. Yamochi, H. H. Wang, A. M. Kini, K. D. Carlson and J. M. Williams, Muon-spin-relaxation measurements of magnetic penetration depth in organic superconductors (BEDT-TTF)$_2$X: X=Cu(NCS)$_2$ and Cu, Phys Rev Lett, 1992, 68, 1923-1926.

44. P. C. W. Leung, T. J. Emge, M. A. Beno, H. H. Wang, J. M. Williams, V. Petricek and P. Coppens, Novel structural modulation in the ambient-pressure sulfur-based organic superconductor beta-(BEDT-TTF)$_2$I$_3$: origin and effects on its electrical conductivity, Journal of the American Chemical Society, 1985, 107, 6184-6191.

45. K. Bender, I. Hennig, D. Schweitzer, K. Dietz, H. Endres and H. J. Keller, Syntesis, structure and physical properties of a two-dimensional organic metal, di bis(ethylendithiolo)tetrathiofulvalene triiodide (BEDT-TTF)$_2$I$_3$, Molecular Crystals and Liquid Crystals, 1984, 108, 359-371.

46. E. B. Yagubskii, I. F. Shchegolev, V. N. Laukhin, R. P. Shibaeva, E. E. Kostyuchenko, A. G. Khomenko, Y. V. Sushko and A. V. Zvarykina, Superconducting transition in the dielectric alpha-phase of iodine-doped (BEDT-TTF)$_2$I$_3$ compound, Jetp Letters, 1984, 40, 1201-1204.

47. E. B. Yagubskii, I. F. Shchegolev, V. N. Laukhin, P. A. Kononovich, M. V. Karatsovnik, A. V. Zvarykina and L. I. Buravov, Normal pressure superconductivity in an organic metal (BEDT-TTF)$_2$I$_3$ bis(ethylendithiolo)tetrathiofulvalene triiodide, Jetp Letters, 1984, 39, 12-16.

48. I. F. Schegolev, E. B. Yagubskii and V. N. Laukhin, Superconductivity at normal pressure of some organic metals of (BEDT-TTF)-I system, Molecular Crystals and Liquid Crystals, 1985, 126, 365-377.

49. R. P. Shibaeva, V. F. Kaminskii and E. B. Yagubskii, Crystal structures of organic metals and superconductors of (BEDT-TTF)-I system, Molecular Crystals and Liquid Crystals, 1985, 119, 361-373.

50. M. H. Korayem and M. Taheri, Modeling of various contact theories for the manipulation of different biological micro/nanoparticles based on AFM, Journal of Nanoparticle Research, 2013, 16.

51. L.-Y. Lin and D.-E. Kim, Measurement of the elastic modulus of polymeric films using an AFM with a steel micro-spherical probe tip, Polymer Testing, 2012, 31, 926-930.

52. A. Solmaz, T. Aytun, J. K. Deuschle and C. W. Ow-Yang, Nanoscale Elastic Modulus Variation in Loaded Polymeric Micelle Reactors, Langmuir, 2012, 28, 10592-10596.

53. P. Alemany, J.-P. Pouget and E. Canadell, Essential role of anions in the charge ordering transition of α-$(BEDT\text{-}TTF)_2I_3$, Physical Review B, 2012, 85.

54. H. H. Wang, J. R. Ferraro, K. D. Carlson, L. K. Montgomery, U. Geiser, J. M. Williams, J. R. Whitworth, J. A. Schlueter, S. Hill, M. H. Whangbo, M. Evain and J. J. Novoa, Electron spin resonance infrared spectroscopic, and molecular paking studies of the thermaly induced conversion of semiconducting alphaT-$(BEDT\text{-}TTF)_2I_3$, Inorganic Chemistry, 1989, 28, 2267-2271.

55. J. M. Torres, N. Bakken, C. M. Stafford, J. Li and B. D. Vogt, Thickness dependence of the elastic modulus of tris(8-hydroxyquinolinato)aluminium, Soft Matter, 2010, 6, 5783-5788.

56. E. Laukhina, V. Tkacheva, A. Chekhlov, E. Yagubskii, R. Wojciechowski, J. Ulanski, J. Vidal-Gancedo, J. Veciana, V. Laukhin and C. Rovira, Polymorphism of a new bis(ethylenedithio)tetrathiafulvalene (BEDT-TTF) based molecular conductor; Novel transformations in metallic BEDT-TTF layers, Chemistry of Materials, 2004, 16, 2471-2479.

57. E. Laukhina, J. Ulanski, A. Khomenko, S. Pesotskii, V. Tkachev, L. Atovmyan, E. Yagubskii, C. Rovira, J. Veciana, J. Vidal-Gancedo and V. Laukhin, Systematic study of the $(ET)_2I_3$ reticulate doped polycarbonate film: Structure, ESR, transport properties and superconductivity, Journal De Physique I, 1997, 7, 1665-1675.

58. M. F. Ashby, in Materials Selection in Mechanical Design (Fourth Edition), ed. M. F. Ashby, Butterworth-Heinemann, Oxford, 2011, pp. 31-56.

59. J. William D. Callister, David G. Rethwisch, Materials Science and Engineering: An Introduction, Wiley Canada, 2009.

60. A. R. Vaz, M. C. Salvadori and M. Cattani, in Ismanam 2003: Metastable, Mechanically Alloyed and Nanocrystalline Materials, eds. C. S. Kiminami, C. Bolfarini and W. J. BottaF, Trans Tech Publications Ltd, Stafa-Zurich, 2004, pp. 758-762.

61. R. Wojciechowski, J. Ulanski, M. Kryszewski, A. Tracz, J. K. Jeszka, H. Muller, S. Lefrant and E. Faulques, Transformation of $(BEDT\text{-}TTF)_2I_3$ networks in polymer

films into superconducting beta(t) phase as studied by resonant Raman spectroscopy, Synthetic Metals, 1998, 94, 27-30.

62. A. Tracz, J. K. Jeszka, A. Sroczyńska, J. Ulański and T. Pakula, Properties and microstructure of crystalline BEDT-TTF polyiodide network in polycarbonate matrix, Advanced Materials for Optics and Electronics, 1996, 6, 335-342.

63. I. Saarikoski, M. Suvanto and T. A. Pakkanen, Modification of polycarbonate surface properties by nano-, micro-, and hierarchical micro–nanostructuring, Applied Surface Science, 2009, 255, 9000-9005.

64. M. A. Angadi and V. Thanigaimani, Size effect in thickness dependence of Young modulus of MNTE and MNSE films, Journal of Materials Science Letters, 1994, 13, 703-704.

65. J. M. Torres, N. Bakken, C. M. Stafford, J. A. Li and B. D. Vogt, Thickness dependence of the elastic modulus of tris(8-hydroxyquinolinato)aluminium, Soft Matter, 2010, 6, 5783-5788.

66. A. Schwab, O. Meissner and C. Holste, Atomic force microscopy of slip lines on the surface of a fatigued nickel single crystal, Philosophical Magazine Letters, 1998, 77, 23-31.

67. A. Tschöpe, E. Sommer and R. Birringer, Grain size-dependent electrical conductivity of polycrystalline cerium oxide: I. Experiments, Solid State Ionics, 2001, 139, 255-265.

68. M. Rossberg, W. Lendle, G. Pfleiderer, A. Tögel, E.-L. Dreher, E. Langer, H. Rassaerts, P. Kleinschmidt, H. Strack, R. Cook, U. Beck, K.-A. Lipper, T. R. Torkelson, E. Löser, K. K. Beutel and T. Mann, in Ullmann's Encyclopedia of Industrial Chemistry, Wiley-VCH Verlag GmbH & Co. KGaA, 2000.

69. E. Laukhina, R. Pfattner, L. R. Ferreras, S. Galli, M. Mas-Torrent, N. Masciocchi, V. Laukhin, C. Rovira and J. Veciana, Ultrasensitive piezoresistive all-organic flexible thin films, Adv Mater, 2010, 22, 977-981.

70. J. Ulanski, A. Tracz, G. Debrue and R. Deltour, Connectivity of conducting crystalline networks in reticulate doped polymers, Journal of Physics D-Applied Physics, 1987, 20, 1512-1518.

71. A. Tracz, J. K. Jeszka, A. Sroczynska, J. Ulanski, J. Plocharski, H. Yamochi, S. Horiuchi and G. Saito, New transparent, colorless, metallically conductive polymer films and their electrochemical transformations, Synthetic Metals, 1997, 86, 2173-2174.

72. P. Polanowski, J. Ulanski, R. Wojciechowski, A. Tracz, J. K. Jeszka, S. Matejcek, E. Dormann, B. Pongs and H. W. Helberg, Thin layers of ET_2I_3 obtained by in situ crystallization - the role of polymer matrix, Synthetic Metals, 1999, 102, 1789-1790.

73. A. Tracz, J. K. Jeszka, J. Ulanski, T. Pakula and J. P. Rabe, Structure and optical properties of polycarbonate films with microcrystallites of BEDT-TTF polyiodides, Synthetic Metals, 1998, 94, 17-22.

74. V. Laukhin, I. Sánchez, A. Moya, E. Laukhina, R. Martin, F. Ussa, C. Rovira, A. Guimera, R. Villa, J. Aguiló, J.-C. Pastor and J. Veciana, Non-invasive intraocular pressure monitoring with a contact lens engineered with a nanostructured polymeric sensing film, Sensors and Actuators A: Physical, 2011, 170, 36-43.

75. I. Sanchez, V. Laukhin, A. Moya, R. Martin, F. Ussa, E. Laukhina, A. Guimera, R. Villa, C. Rovira, J. Aguilo, J. Veciana and J. C. Pastor, Prototype of a nanostructured sensing contact lens for noninvasive intraocular pressure monitoring, Invest Ophthalmol Vis Sci, 2011, 52, 8310-8315.

76. E. E. Laukhina, V. A. Merzhanov, S. I. Pesotskii, A. G. Khomenko, E. B. Yagubskii, J. Ulanski, M. Kryszewski and J. K. Jeszka, Superconductivity in reticulate doped polycarbonate films, containing $(BEDT\text{-}TTF)_2I_3$, Synthetic Metals, 1995, 70, 797-800.

77. E. E. Laukhina, V. A. Merzhanov, S. I. Pesotskii, A. G. Khomenko, E. B. Yagubskii, J. Ulanski, M. Kryszewski and J. K. Jeszka, Superconductivity in reticulate doped polycarbonate films, containing $(BEDT\text{-}TTF)_2I_3$, Synthetic Metals, 1995, 70, 797-800.

78. B. Svedbergh, Y. Backlund, B. Hok and L. Rosengren, The IOP-IOL - A probe into the eye, Acta Ophthalmologica, 1992, 70, 266-268.

79. M. L. Wolbarsht, J. Wortman, B. Schwartz and D. Cook, A Scleral buckle pressure gauge for continuous monitoring of intraocular pressure, International Ophthalmology, 1980, 3, 11-17.

80. M. Leonardi, P. Leuenberger, D. Bertrand, A. Bertsch and P. Renaud, First steps toward noninvasive intraocular pressure monitoring with a sensing contact lens, Invest Ophthalmol Vis Sci, 2004, 45, 3113-3117.

81. V. Laukhin, I. Sanchez, A. Moya, E. Laukhina, R. Martin, F. Ussa, C. Rovira, A. Guimera, R. Villa, J. Aguilo, J.-C. Pastor and J. Veciana, Non-invasive intraocular pressure monitoring with a contact lens engineered with a nanostructured polymeric sensing film, Sensors and Actuators a-Physical, 2011, 170, 36-43.

Chapter 3

Developing piezoresistive bi-layer composites based on TTF conducting salts derivatives

3.1. Introduction

As reported in Chapter 2, BL films based on conducting BEDT-TTF ion-radical salts exhibit excellent piezoresistive properties that bring many opportunities for practical applications. However, the high price[1] of the commercially available BEDT-TTF makes it inappropriate for some kinds of uses. For this reason it was interesting to look for an alternative to this compound that can be obtained at the gram-scale and with a low costs. At first glance, tetrathiafulvalene (TTF) looks the most promising candidate because it can be obtained at the gram-scale very easily and it forms a large variety of conducting salts by oxidation with iodine. In this Chapter the preparation, characterization and study of the piezoresistive properties of BL films covered with crystals of charge transfer salts derived from TTF, are described.

3.2. Results and Discussion

The ability of iodine to form stable species like I^-, $I_3^-$and I_5^- lead to the formation of multiple phases of charge transfer salts with a $(TTF)I_x$ composition during the oxidation of TTF with I_2 in solution.[2-7] These salts significantly differ in their conducting properties since the stoichiometric phases, $(TTF)I_x$, with x=2 and 3, are non-conducting while the non-stoichiometric ones, $(TTF)I_x$, with x=0.71 and 2.3, behave as one-dimensional conducting systems.[4] Remarkably are the salts with stoichiometries $(TTF)_7I_5$ and $(TTF)_{11}I_8$, here named as $(TTF)I_{0.7+\delta}$, because they show a high conductivity and are easily to prepare. However, attempts to prepare selectively the conducting phase with a TTF_7I_5 composition, by reacting stoichiometric amounts of TTF with iodine in solution always resulted in complex mixtures of both phases.[4] Therefore, the covering of a polymeric film with a homogeneous crystallite layer of a conducting salt with the non-stoichiometric composition $(TTF)_7I_5$ was a challenge. This drawback made that we decided first to determine the best conditions to prepare crystals of a pure phase of such an ion-radical salt and to have all characteristic data before attempting to cover polymeric films with its polycrystalline layer. For a detailed description of this study see Annex 1.

Preparation and characterization of BL films with $(TTF)I_{0.7+\delta}$ crystals. The oxidation of TTF by non-equimolar amounts of iodine makes this process attractive for preparing conductive TTF-based layers on the surface of polymeric films. With this objectives in mind, we assumed that small amounts of iodine at the swollen surface of a polymeric film

may yield crystals of conductive (TTF)$I_{0.7+\delta}$ salts as covering layers. In line with the BL film preparation method previously reported for BEDT-TTF [8] we first prepared 25–30 μm thick polymeric films containing 2 (or 8) wt. % of TTF well-dispersed in three different polymeric matrices: polycarbonate, PC, (film **F3-1** with 2% and BL film **F3-2** with 8% of TTF); cellulose triacetate, CTA, (BL film **F3-3** with 2% of TTF); and cellulose acetate propionate, CAP, (BL film **F3-4** with 2% of TTF). To cover these films with polycrystalline layers of (TTF)$I_{0.7+\delta}$ salts we exposed during 6-8 min the surface of such films to vapors of a saturated solution of iodine in dichloromethane. The formation of conductive covering layers in the resulting BL films were tested by direct current resistance measurements.

The composition of the conductive layers was determined by EDX analysis. This technique provides the S:I ratio of the conducting layers formed on the surfaces of all BL films, which varies from 4:0.80 to 4:0.89, being very close to the calculated value of ca. 4:0.7 for (TTF)$I_{0.7+\delta}$ salts. The conducting layers were also characterized with Raman spectroscopy were a complete absence of the characteristic bands of I_3^- corresponding to ν_{I-I}, $\nu_{[I-I\cdots I]^-}$, $\nu_{[I-I\cdots TTF]^-}$ and $\nu_{[I-I-I]^-}$ vibration modes, were observed.[9-11] This result confirmed that neither I_3^- anions nor any other iodine-based adducts are formed during the oxidation with iodine under such conditions. Therefore, iodine exists entirely as I^- anions in agreement with the structural data for the phases of (TTF)$I_{0.7+\delta}$ type (vide infra).

The SEM images of the conductive covering layers of (TTF)$I_{0.7+\delta}$ crystals revealed different textures for BL films **F3-1** – **F3-4** (Figure 3-1 and Figure 3-2). Thus, the surface of BL film **F3-1** showed the presence of a network of needle-like crystals with a low density and with sizes of 2 μm in length and with lateral dimensions ranging from 80 to 200 nanometres (Figure 3-1). The BL film **F3-2** containing 8% of the TTF donor shows crystals with similar shape and size but with a higher density, as expected from the larger content of TTF molecules. This difference in the crystal density of both BL films is in agreement with the measured values of sheet resistance of 30-40 kΩ/□ and 4-5 kΩ/□ for BL films **F3-1** and **F3-2**, respectively. The SEM image of films **F3-3** and **F3-4** (Figure 3-2) revealed the presence of worm-like and plate-like crystallites, respectively, of (TTF)$I_{0.7+\delta}$ crystallites showing similar sizes as in the BL film **F3-1** and exhibiting also a good conductivity. The different textures found for all BL films testified that the nature of a polymeric matrix controls in some way the morphology of the polycrystalline conductive covering layer formed at the surface of the polymer. This result that can be

rationalized taking into account the different physical properties of the polymers. Thus, since the viscosity of the swollen surface layer is dependent on the nature of a polymer, the mass transfer characteristics, which are responsible for the self-assembling of molecules to generate the polycrystalline layer of (TTF)$I_{0.7+\delta}$, should be different for the three studied materials.

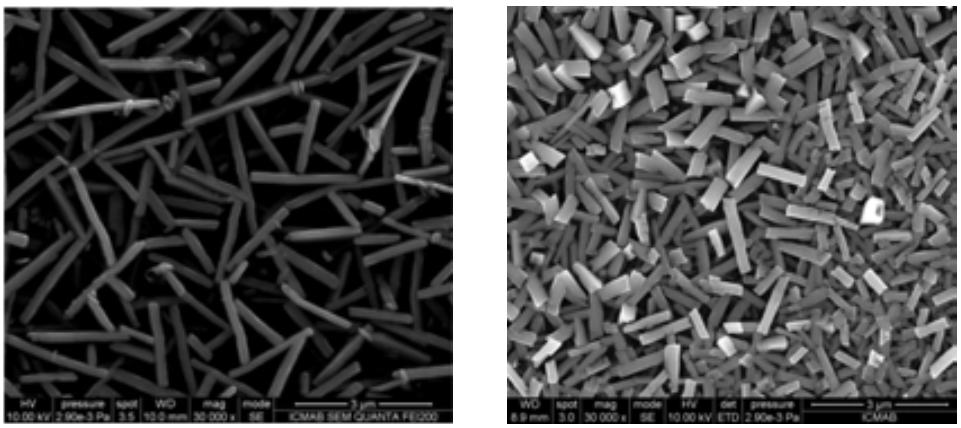

Figure 3-1. SEM images of the conducting layers of (TTF)$I_{0.7+\delta}$ crystallites formed on the surface of BL films F3-1 (left) and film F3-2 (right) using polycarbonate as a polymer matrix.

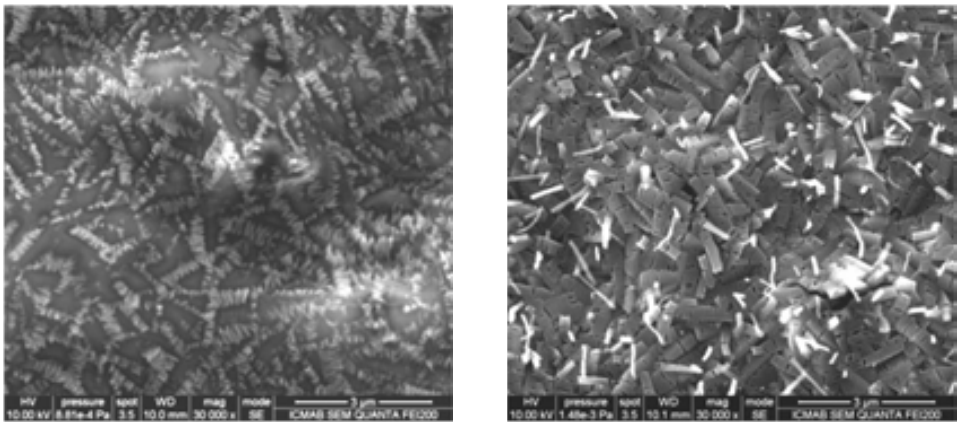

Figure 3-2. SEM images of the conducting layers of (TTF)$I_{0.7+\delta}$ crystallites formed on the surface of BL films F3-3 (top) and F3-4 (bottom) using cellulose triacetate and cellulose acetate propionate, respectively, as polymeric matrices.

The X-ray powder diffraction patterns of BL films samples similar in size (2.3 cm^3) **F3-1** – **F3-3** showed the characteristic wide bands due to the polymeric substrate along with narrow Bragg peaks from the crystalline phases present in the conductive layers (Figure 3-3).

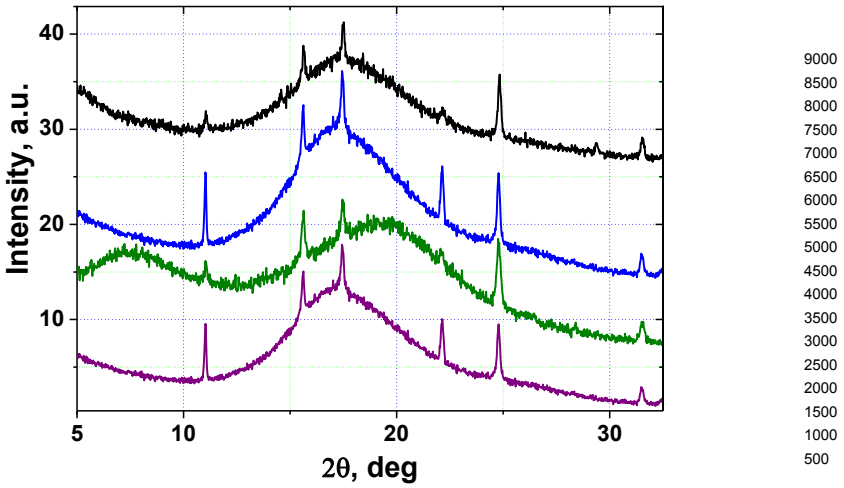

Figure 3-3. X-ray diffraction patterns of BL film F3-1 (black line), BL film F3-2 (blue line), BL film F3-3 (green line), BL film F3-4 (purple line).

Interestingly, two families of Bragg peaks were observed and one of such families was presented in the four BL films whereas the BL film **F3-4** exhibits additionally the second family of the peaks. The narrow Bragg peaks, observed in all BL films, can be indexed in a tetragonal unit cell with dimensions $a = b = 11.37$ Å and $c = 3.79$ Å; which are close to the values 11.34 and 3.77 Å reported by Scott et al.[4] for the $(TTF)_7I_5$ salt. To find an adequate model for the structure of the conductive layer, an additional 8 hours powder diffraction measurement was performed for the BL film **F3-1** in the region of $2\theta = 10 – 60^o$. Two crystal structures, corresponding to single crystals of $TTF_{11}I_8$ and TTF_7I_5 salts, were used as model structures for the Rietveld refinement with the program MRIA. [12] The final Rietveld plot for the case of $(TTF)_{11}I_8$ resulted in slightly better R-factors as compared with $(TTF)_7I_5$. In the refinements, the atomic coordinates were fixed, while the unit cell dimensions, peak shapes and background parameters were varied. To take into account preferred orientation effects, the March-Dollase texture formalism[13] was used. In the Rietveld refinements, several directions of preferred orientations were tested and then remarkably better *R*-factors were obtained for the two model structures, $TTF_{11}I_8$ and TTF_7I_5, when [010] was chosen as the direction of preferred crystalline orientations. In the case of the $TTF_{11}I_8$ model structure, the texture parameter *r* was refined to 0.39(2) and the maximum texture correction multiplier (~16) for calculated $F^2(hkl)$ was applied to *0k0* reflections. It means, that most of the coherently scattering regions of the conductive layer are oriented with the direction [010] perpendicular to the surface of the substrate, i.e. the *ac* plane of the unit cell of $TTF_{11}I_8$ structure is parallel to the substrate surface, while axis *b* is perpendicular (Figure 3-5, left). In the case of the TTF_7I_5 model structure,

when [010] was chosen as the direction of preferred crystalline orientation, the texture parameter *r* was refined to 0.44(2), revealing thus the same orientation of the conductive layer on the substrate surface (Figure 3-5, right).

Therefore, all TTF stacks in the conducting $(TTF)I_{0.7+\delta}$ crystalline layers of the BL films are approximately parallel to the substrate surface. There are two types of TTF stacks, named as *A* and *B*, in the structures of TTF_7I_5 and $TTF_{11}I_8$ phases. In the *A* type, the double bonds C=C of TTFs are nearly parallel to the [100] direction in the TTF_7I_5 phase while for $TTF_{11}I_8$ are parallel to the [10-1] one

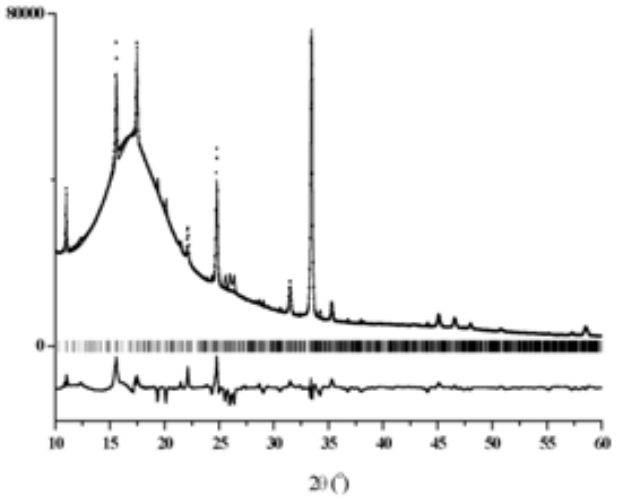

Figure 3-4. The final Rietveld plot for the X-ray diffraction pattern of BL film F3-1 using the crystal structure of $TTF_{11}I_8$ as a model structure. The experimental diffraction profile is indicated by black dots. The calculated diffraction profile is shown as the upper solid lines, the difference profile is shown as the bottom solid line and the vertical bars correspond to the calculated positions of the Bragg peaks.

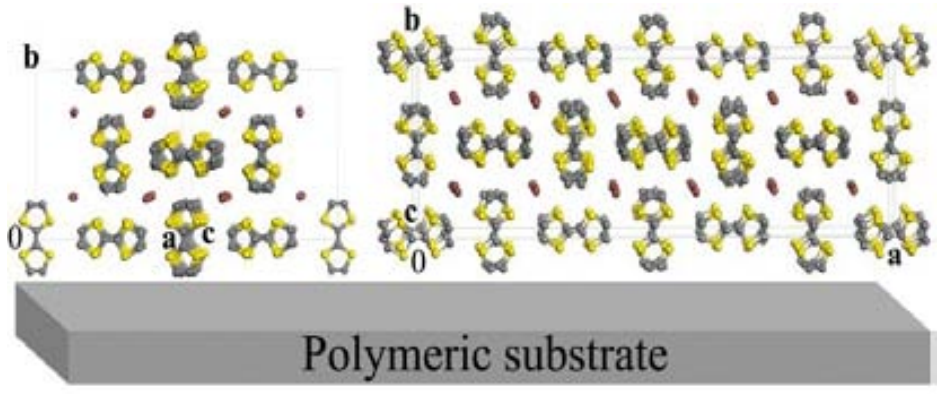

Figure 3-5. Idealized representation of $(TTF)I_{0.7+\delta}$-based layer deposited on a polymeric substrate for the crystal structures of $TTF_{11}I_8$ (left) and TTF_7I_5 (right).

By contrast, in the type *B* stacks, such double bonds of TTFs are nearly parallel to the *b*

axis in both structures. Accordingly with this observation, the conductivity along the *A* and *B* stacks should be of one-dimensional nature because both of them are parallel to the *c* axis in the TTF_7I_5 structure and to [101] in the $TTF_{11}I_8$ one. Therefore, in an ideal case of existing only one-domain of $(TTF)I_{0.7+\delta}$ microcrystals we could observe strictly one-dimensional conductivity along the crystallographic directions [001] and [101] for TTF_7I_5 and $TTF_{11}I_8$, respectively.

3.3. Electromechanical properties of BL films with $(TTF)I_{0.7+\delta}$ crystals

Two-contact resistance measurements on the BL films **F3-1**, **F3-3** and **F3-4** show sheet resistances of 25-30, 6-8, and 16-20 kΩ/□, respectively, suggesting that the number of continuous conducting paths extend uniformly through the crystalline layers on the surfaces of the films. The resistances of such films increase when the temperature is decreased in the range of 25 to 70 °C exhibiting temperature resistance coefficients for all films of 1.1 %/deg (Figure 3-6).

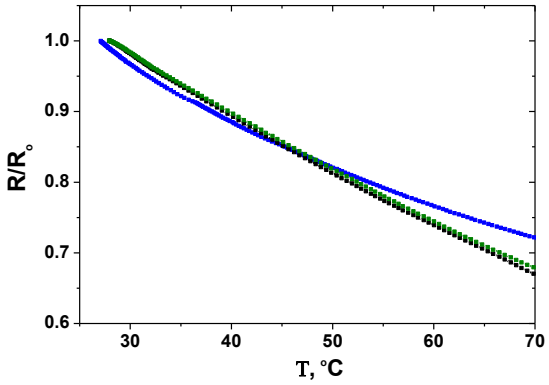

Figure 3-6. Temperature dependence of normalized electrical resistance of BL films F3-1 (black line), F3-2 (blue line) and F3-3 (green line).

The Young's moduli (E), given by the slope of the stress-strain curves in the elastic region, was found to be 1.90 and 1.85 GPa for BL films **F3-1** and **F3-3**, respectively. Taking into account that for a pristine (non-covered) polycarbonate film such a parameter is E=2.05 GPa (with σ_{yield}=1.4%),[11] and for a cellulose triacetate film it is E=2.06 GPa, [14] the covering of polycarbonate and cellulose triacetate films with a layer of $(TTF)I_{0.7+\delta}$ crystals does not adversely affect their mechanical characteristics. Figure 3-7 also shows that the resistance changes with the strain deviate from a linear regime at relative strains of 0.7 and 0.6% for BL films **F3-1** and **F3-3**, respectively. By analogy with the elastic

limit point, this threshold can be termed as the resistance proportional limit of the BL film (R_{yield}).[15] The nonlinearity observed for the resistance dependence on the strain above the R_{yield} limit can be associated with the appearance of nano-cracks formed perpendicularly to the elongation direction.[15] Therefore, the R_{yield} values of BL films correspond to the elastic limit point of their polycrystalline conductive layers. The fact that the R_{yield} values for BL films **F3-1** (0.70%) and film **F3-3** (0.62%) are close to the values of σ_{yield} evidence a good robustness of both flexible films. The experimental data presented in Figure 3-7, additionally permitted us to plot the R *versus* stress dependence for BL films **F3-1** and **F3-3**, as depicted in Figure 3-8. In the current case the stress σ=F/A where F is a force applied for an area A has the same units that the applied pressure along the sample. For monoaxial loads applied along to the BL film (i.e. parallel to the conducting surface), the electrical response depends linearly on stress/pressure in the range from 0 to 10 MPa (or that is the same 100 bar). Thus, the sensitivity of the films to stress was determined from the slope of the R(stress) dependence as 0.4 %/MPa and 0.35 %/MPa (or 0.04 %/bar and 0.035%/bar) for the BL films **F3-1** and **F3-3**, respectively.

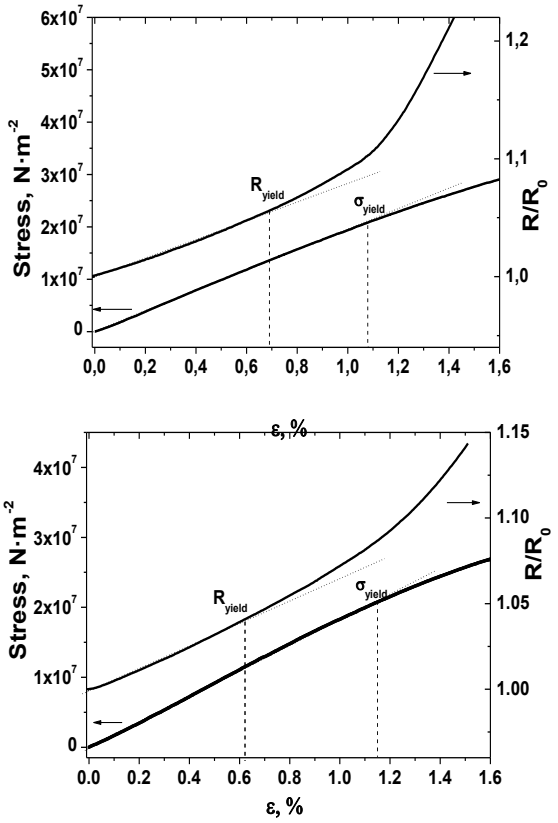

Figure 3-7. Stress–strain and resistance-strain curves for the BL films F3-1 (top) and F3-3 (bottom); where the strain is given by ε=(L-L₀)·100/L₀ being L₀ and L the lengths of the film-based gauge without and under elongation, respectively.

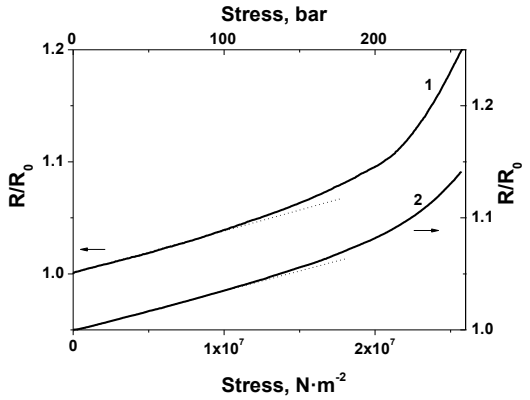

Figure 3-8. Normalized electrical resistance response of BL films F3-1 (curve 1) and F3-2 (curve 2) to monoaxial loads.

Finally, as shown in Figure 3-9, the electrical responses of films to multi-cyclic monoaxial elongations, carried out in the elastic domain of deformations, are very reproducible depending linearly on applied strain. The gauge factors, calculated, as the ratio between the relative resistance change and the relative strain value, were found to be 7.7, 6.5 and 6.4 for BL films **F3-1**, **F3-3** and **F3-4**, respectively. These values are not very different from those reported for piezoresitive BL films based on the α-(BEDT-TTF)$_2$I$_3$ molecular semimetal.[16] As the gauge factor is controlled by the softness of the crystal structure of the organic molecular conductor, one may conclude that the 1-D structures of the organic conductor (TTF)I$_{0.7+\delta}$ and 2-D organic conductor α-(BEDT-TTF)$_2$I$_3$ do not exhibit significant differences in their softness.

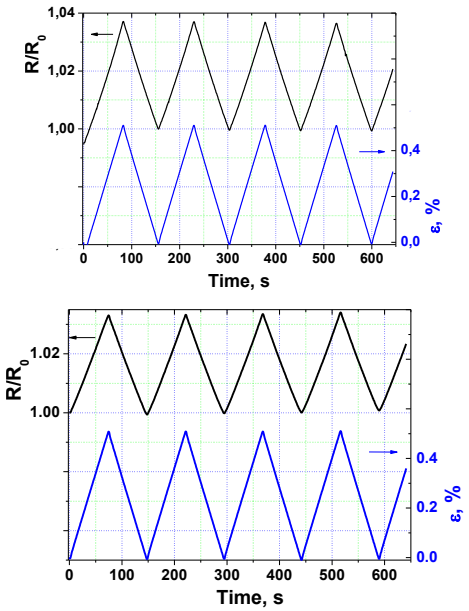

Figure 3-9. Normalized resistance response of the BL films F3-1 (top) and F3-3 (bottom) to cyclic elastic elongations with a ε_{max} = 0.5%.

3.4. Conclusions

As a conclusion we may say that the piezoresistive BL films based of TTF conducting salts exhibit somewhat lower values of gauge-factor than that was obtained with the piezoresistive BL films based on BEDT-TTF. However BL films made with TTF have the additional advantage of its lower cost and that they may be prepared in a one-step processing procedure.

Bibliography

1. http://www.sigmaaldrich.com.

2. R. J. Warmack, T. A. Callcott and C. R. Watson, dc conductivity of tetrathiofulvalene bromide (TTF-Br_n) and TTF in syngle crystals, Physical Review B, 1975, 12, 3336-3338.

3. R. B. Somoano, A. Gupta, V. Hadek, T. Datta, M. Jones, R. Deck and A. M. Hermann, Electrical and magnetic properties of (TTF)$I_{0.71}$, Journal of Chemical Physics, 1975, 63, 4970-4976.

4. B. A. Scott, S. J. Laplaca, J. B. Torrance, B. D. Silverman and B. Welber, Crystal chemistry of organic metals - composition, structure, and stability in tetrathiofulvalenium-halide systems, Journal of the American Chemical Society, 1977, 99, 6631-6639.

5. R. C. Teitelbaum, T. J. Marks and C. K. Johnson, Crystal structure and properties tetrathiofulvalenium triiodide, Journal of the American Chemical Society, 1980, 102, 2986-2989.

6. I. Smirani, R. Lipiec, A. Brau, J. P. Farges and A. Graja, Electrical properties of new organic composites obtained by mechanochemical synthesis, Journal of Materials Science, 2001, 36, 1227-1230.

7. L. Gomez and R. Rodriguez-Amaro, Nucleation and growth of thin films of the organic conductor TTF-iodide over glassy carbon. Electrochemical and spectroelectrochemical study, Langmuir, 2009, 25, 4799-4803.

8. J. K. Jeszka, A. Tracz, J. Ulanski and M. Kryszewski, Surface conductive polymer films by reticulate doping with organic metals, Journal of Physics D-Applied Physics, 1985, 18, L167-L170.

9. P. Deplano, J. R. Ferraro, M. L. Mercuri and E. F. Trogu, Structural and Raman spectroscopic studies as complementary tools in elucidating the nature of the bonding in polyiodides and in donor-I_2 adducts, Coordination Chemistry Reviews, 1999, 188, 71-95.

10. R. Wojciechowski, J. Ulanski, M. Kryszewski, E. Laukhina and V. Tkacheva, Mixtures of trihalide anions in isostructural BEDT-TTF salts as seen by Raman spectroscopy, Molecular Crystals and Liquid Crystals, 2001, 355, 351-358.

11. V. Mukherjee and N. P. Singh, Theoretical vibrational spectra and thermodynamics of organic semiconductive tetrathiafulvalene and its cation radical, Spectrochimica Acta Part a-Molecular and Biomolecular Spectroscopy, 2014, 117, 315-322.

12. V. B. Zlokazov and V. V. Chernyshev, MRIA - A program for a full profile analysis of powder multiphase neutron diffraction time of flight (direct and fourier) specra, Journal of Applied Crystallography, 1992, 25, 447-451.

13. W. A. Dollase, Correction of the intensities for preferred orientation in powder diffrectometry - application of the March model, Journal of Applied Crystallography, 1986, 19, 267-272.

14. F. A. Akhmedov, B. I. Aikhodzhaev, G. S. Talipov and V. M. Surovkin, Effect of crystallization on the mechanical properties of cellulose triacetate and acetosorbates, Polymer Mechanics, 1968, 4, 626-629.

15. E. Laukhina, R. Pfattner, M. Mas-Torrent, C. Rovira, J. Veciana and V. Laukhin, Film-based Sensors with Piezoresistive Molecular Conductors as Active Components: Strain Damage and Thermal Regeneration, Sensors & Transducers Journal, 2011, pp. 1-12.

16. E. Laukhina, R. Pfattner, L. R. Ferreras, S. Galli, M. Mas-Torrent, N. Masciocchi, V. Laukhin, C. Rovira and J. Veciana, Ultrasensitive piezoresistive all-organic flexible thin films, Advanced Materials, 2010, 22, 977-981.

Chapter 4

Developingt of piezoresistive bi-layer materials based on the conductive single-component molecular conductor $[Au(\alpha\text{-tpdt})_2]^o$

4.1. Introduction

Most of the known molecular conductors are charge-transfer salts where conductivity is ensured by the partial oxidation (or reduction) of a molecular electron donor (or acceptor) species. [1-5] Nevertheless very recently a few number of molecular conductors based on neutral molecules have also been reported. [6-9] Among the latter compounds the conductor $[Au(\alpha\text{-tpdt})_2]^0$ (tpdt=2,3-thiophenedithiolate) (Figure 4-1) could be very attractive for using as a conductive component in the BL films for two reasons. First, powder-like samples of this compound displays a very high value of electrical conductivity together with a paramagnetic properties being therefore a good candidate for preparing a conducting material with a low crystallinity.[8] And second, for such a type of solids no problems associated with polymorphism and grain boundaries are expected, and, consequently, they could form a film-like material on the top of the BL films with a huge spatial homogeneity of electrical transport properties. [10]

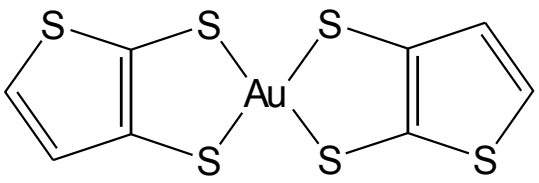

Figure 4-1. The structural formula of $[Au(\alpha\text{-tpdt})_2]^0$.

Due to above mentioned conditions we addressed to develop flexible BL films with $[Au(\alpha\text{-tpdt})_2]^o$ as an active component which were obtained with the developed procedure for the preparation of BL films[11-13] but using the following reaction for the vapour/oxidation annealing step.

$$[(C_4H_9)_4N]^+[Au(\alpha\text{-tpdt})_2]^- + 1/2I_2 \rightarrow [Au(\alpha\text{-tpdt})_2]^0 + [(C_4H_9)_4N]^+I^- \qquad (\mathbf{4\text{-}1})$$

The obtained BL films contained a conducting layer with the single component molecular conductor $[Au(\alpha\text{-tpdt})_2]^0$. They showed a metallic temperature dependence of its electrical resistance at temperatures higher than 280 K and a semiconductor-like behavior below this temperature. Moreover, such BL films also exhibit interesting piezoresistive properties enabling to use them as strain sensors.

4.2. Preparation, characterization and properties of BL films with [Au(α-tpdt)2]0-based active layer

Preparation of BL films. First we prepared a 25-30 μm thick polycarbonate film with a 3 wt. % of the a tetraalkylammonium salt of $[Au(\alpha\text{-tpdt})_2]^-$, as the precursor for $[Au(\alpha\text{-tpdt})_2]^0$. Then, we exposed the film to vapours of a saturated solution of iodine in dichloromethane promoting the swelling of the polymer and facilitating the migration of the precursor from the bulk of the film to the surface where the $[Au(\alpha\text{-tpdt})_2]^-$ ions are oxidized to neutral $[Au(\alpha\text{-tpdt})_2]^0$ molecules by the iodine. This redox process induces a rapid nucleation of the highly insoluble $[Au(\alpha\text{-tpdt})_2]^0$ species and a conductive layer of the single component conductor is formed on the top of the BL film (Table 4-1). Dichloromethane of two different commercial grades for the swelling of the polycarbonate matrix and two different tetraalkylammonia salts of $[Au(\alpha\text{-tpdt})_2]^-$ showing different solubility were investigated. For this purpose we prepared the thin films containing a 2.6 wt. % of $[(C_2H_5)_4N]^+[Au(\alpha\text{-tpdt})_2]^-$ and with a 3.8% of the considerably less soluble $[(C_4H_9)_4N]^+[Au(\alpha\text{-tpdt})_2]^-$ precursor. It should be noted that both films should be able to release the same amount of $[Au(\alpha\text{-tpdt})_2]^0$ together with the corresponding $[R_4N]I$ salt. To minimize the effect of other processing parameters, the annealing of the thin films was made under a controlled temperature of 23 ºC and a relative humidity of 40 %. Finally, the formation of the conductive covering layers was tested by direct current conductivity measurements enabling to compare the values of room temperature resistances. As it can be noted from Table 4-1, that summarize the obtained results, the electrical properties of the resulting BL films depend on the duration of vapour exposure and also on the quality of dichloromethane used for the film swelling and the nature of the precursor salt. Thus, to obtain a metallic layer of $[Au(\alpha\text{-tpdt})_2]^0$ the film surface must be treated for a short period of time, with dichloromethane packed under nitrogen. On another hand, very low conducting BL films were formed when the film surface was treated by vapours of an iodine solution based on dichloromethane that had previously stored during 14 hours under controlled atmospheric conditions similar to that we used for the preparation of films (23 ºC and relative humidity of a 40 %). It is well known that upon prolonged contact with atmospheric water, dichloromethane hydrolyses to produce hydrogen chloride and formaldehyde that may be responsible for the observed differences. [14] It can be noted from the Table 4-1 that depending on the quality of solvent

and the nature of the precursor salt we can obtain highly conductive BL films, such as BL films **F4-4** and **F4-6**.

Table 4-1. Preparation conditions and electrical transport properties of the sensing BL films.

BL film	R in $R_4N[Au(\alpha\text{-tpdt})_2]$	Treatment		$R_{300\ K}$ (kΩ)	R(T) behaviour 100 K ≤ T ≤ 300 K
		Type of CH_2Cl_2	duration (min)		
F4-1	C_4H_9	SDS*	6	25	
F4-2	C_4H_9	SDS*	10	3	semiconducting
F4-3	C_4H_9	SDS*	15	3	semiconducting
F4-4	C_4H_9	SDS*	20	2	semiconducting
F4-5	C_4H_9	Aldrich*	3	10	metallic at T>250 K
F4-6	C_4H_9	Aldrich*	5	10	semiconducting
F4-7	C_4H_9	Aldrich*	8	8-10	metallic at T>280 K
F4-8	C_4H_9	Aldrich**	5	>5000	metallic at T>280 K
F4-9	C_4H_9	Aldrich**	8	>2000	–
F4-10	C_2H_5	SDS*	15	>2000	–
F4-11	C_2H_5	SDS*	20	450	–
F4-12	C_2H_5	Aldrich*	8	>1000	

*SDS-dichloromethane of a 99.95 % quality standard and Aldrich - dichloromethane of an anhydrous standard (99.8%) stored under N_2; **Saturated solution of iodine in CH_2Cl_2 kept for 14 hours under controlled ambient conditions at 23 ºC and at relative humidity level of 40 %

Therefore, it can be concluded that the chemical deposition of $[Au(\alpha\text{-tpdt})_2]^0$ on the top of the BL films as a highly conductive layer is very sensitive to the procedure conditions and to the above mentioned impurities and dichloromethane quality. Also the nature and solubility of the precursor salt is important since only the highly soluble salt $[(C_4H_9)_4N]^+[Au(\alpha\text{-tpdt})_2]^-$ yield a BL film with a metallic behaviour. Furthermore, the formation of the highly conductive facing layer of $[Au(\alpha\text{-tpdt})_2]^0$ is a reproducible process. As a matter of example we can mention that BL films **F4-4** and **F4-6** were reproduced three times obtaining samples with the same properties.

Characterization of the BL films. The composition of the conducting layers of BL films was determined by EDX analysis and Raman spectra. As it can be noted from EDX data in The texture, morphology and structure of the conductive layers in the BL films were studied by different microscopic techniques, like AFM, SEM and by X-ray spectroscopy.

The SEM images of the topmost layer of the highly conductive BL films **F4-1** – **F4-7** revealed close packed aggregates of the $[Au(\alpha\text{-tpdt})_2]^0$ showing textures with very poorly defined structures of submicron and nano sizes. In some cases conducting network of plate- and needle-like crystals can be distinguished.

Table 4-2, the ratio between sulphur and gold in $[Au(\alpha\text{-tpdt})_2]$ varies from S:Au = 6.0:1.0 to 6.4:1.0; which are very close to the theoretical S:Au ratio of 6.0:1.0 calculated for the neutral compound $[Au(\alpha\text{-tpdt})_2]$: $C_8H_4AuS_6$. By contrast, the stoichiometry between gold and iodine has a large variability going from Au:I = 1:0.7 to 1:1.6 being those closer to the theoretical value of 1:1 expected if all the iodine atoms exist as a I^- species. Taking into account that the low frequency Raman spectrum is a very sensitive probe for the different entities in which iodine can be presented,[15, 16] we applied the Raman technique as a tool for determining the type of iodine in the BL films. The lack of characteristic bands in the low frequency Raman spectra corresponding to the ν_{I-I}, $\nu_{[I-I\cdots I]^-}$ and $\nu_{[I-I-I]^-}$ vibration modes [15, 16] of I_3^- suggests that iodine must exist mainly as I^- in such samples. These anions, combined with the tetraalkylammonium cations are not able to form any conducting structures together with $[Au(\alpha\text{-tpdt})_2]^0$ and, therefore, they do not contribute in the composition of the highly conductive covering layers. It is likely that the $R_4N^+I^-$ salt is concentrated deeper in the treated film surface. Therefore, both EDX and Raman data indicate that the conducting covering layers are mainly build up by the single component conductor $[Au(\alpha\text{-tpdt})_2]^0$. Like the previously reported BL films that contain conducting layers of charge transfer salts, the resulting BL films with $[Au(\alpha\text{-tpdt})_2]^0$ reveal a good long-term stability since their chemical composition and electrical transport properties do not change for several months.

The texture, morphology and structure of the conductive layers in the BL films were studied by different microscopic techniques, like AFM, SEM and by X-ray spectroscopy.

The SEM images of the topmost layer of the highly conductive BL films **F4-1** – **F4-7** revealed close packed aggregates of the $[Au(\alpha\text{-tpdt})_2]^0$ showing textures with very poorly defined structures of submicron and nano sizes. In some cases conducting network of plate- and needle-like crystals can be distinguished.

Table 4-2. EDX data of BL film samples with an area of 25 μm² and the corresponding stoichiometry of the conducting layers.

sample	EDX data, at. %			[S:Au]:I stoichiometry	
	S	Au	I	from EDX data	corrected with the reference sample*
F4-1	79.60	12.23	8.17	$[S_{6.5}Au]I_{0.7}$	$[S_{6.1}Au]I_{0.7}$
F4-3	77.99	11.97	10.05	$[S_{6.5}Au]I_{0.8}$	$[S_{6.1}Au]I_{0.8}$
F4-4	80.49	11.76	7.74	$[S_{6.8}Au]I_{0.7}$	$[S_{6.4}Au]I_{0.7}$
F4-7	75.47	11.15	13.38	$[S_{6.8}Au]I_{1.2}$	$[S_{6.4}Au]I_{1.2}$
F4-11	71.29	11.09	17.62	$[S_{6.4}Au]I_{1.6}$	$[S_6Au]I_{1.6}$

*Crystals of $[(C_4H_9)_4N]^+[Au(\alpha\text{-tpdt})_2]^-$ were used as a reference sample, Cal. S 85.71%; Au 14.29 % (S_6Au). Exp. S 86.49%; Au 13.51% ($S_{6.4}Au$)

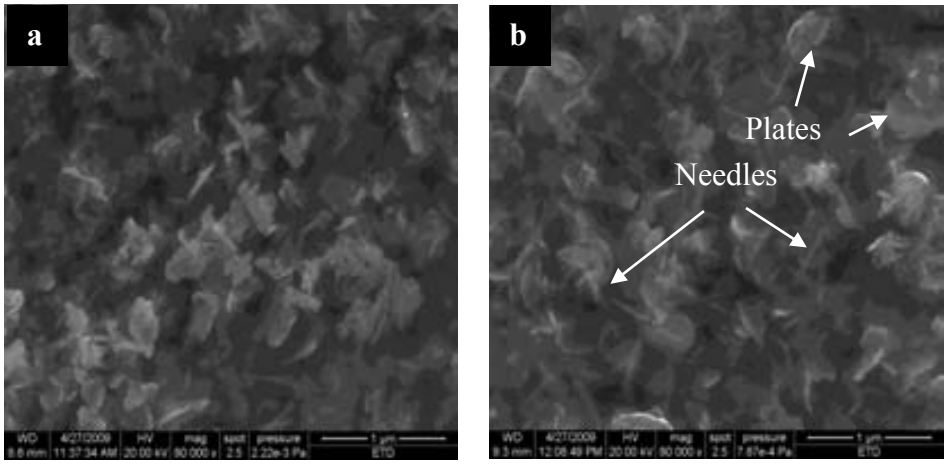

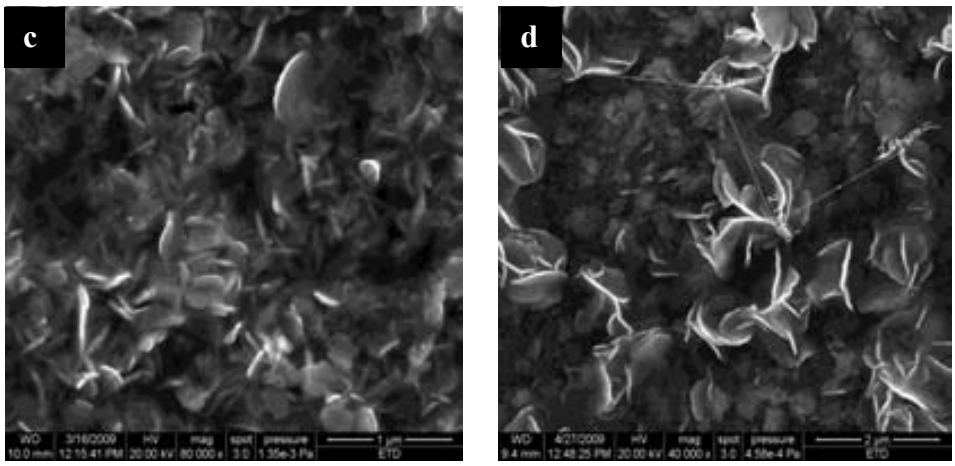

Figure 4-2. SEM images of the conducting layer of BL films F4-3 (a), F4-4 (b), F4- 6 (c) and of the highly resistive BL film F4-11 (d).

By contrast, the SEM images of the topmost layer of the highly resistive BL films, **F4-8** – **F4-12**, show well developed rosebud-like structures formed over the film surface which appears separated by 2-4 micron. As a result of such morphology, electrical resistance of BL films **F4-8** – **F4-12** are much larger.

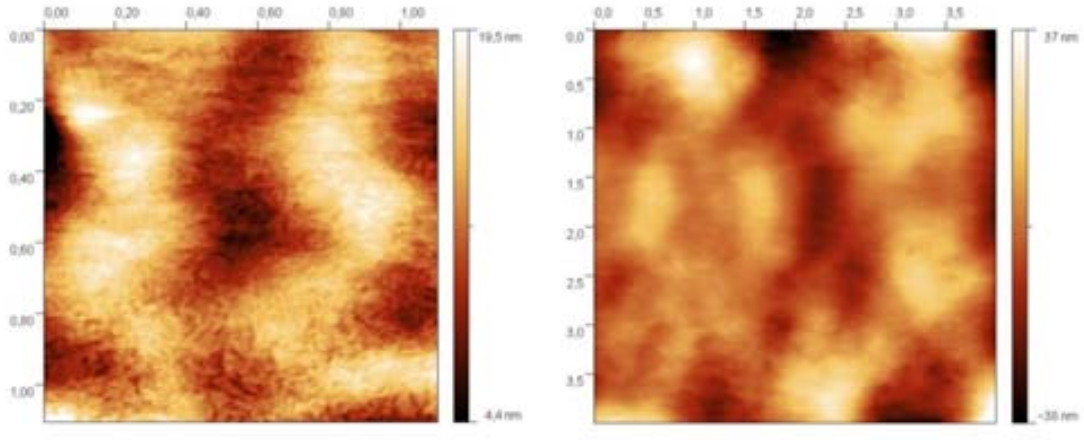

Figure 4-3. AFM images at different magnifications of the BL film F4-4.

BL films were also studied by X-ray diffraction. Figure 4-4 shows the PXRD patterns of representative metallic BL films **F4-4** and **F4-6** as well as of the highly resistive BL film **F4-11**. PXRD patterns of these BL films exhibits a wide intense diffusing halo at $15^{o}<2\theta<35^{o}$ that differs in its shape from that of the reference polycarbonate film (Figure 4-4). The lack of well-defined reflections in these patterns suggests that the topmost layers of films **F4-3** and **F4-4** have a very low degree of crystallinity being mainly amorphous.

On the contrast, for the metallic films **F4-6** and **F4-7**, in addition to the wide intensive diffusing halo from PC matrix, the PXRD patterns show a very weak reflection at $2\theta = 5.3°$, that correspond to an interplanar spacing is 16.6 Å, as well as its second, forth, and fifth order reflections at $2\theta = 10.5°$, 21.3° and 26.4°, respectively.

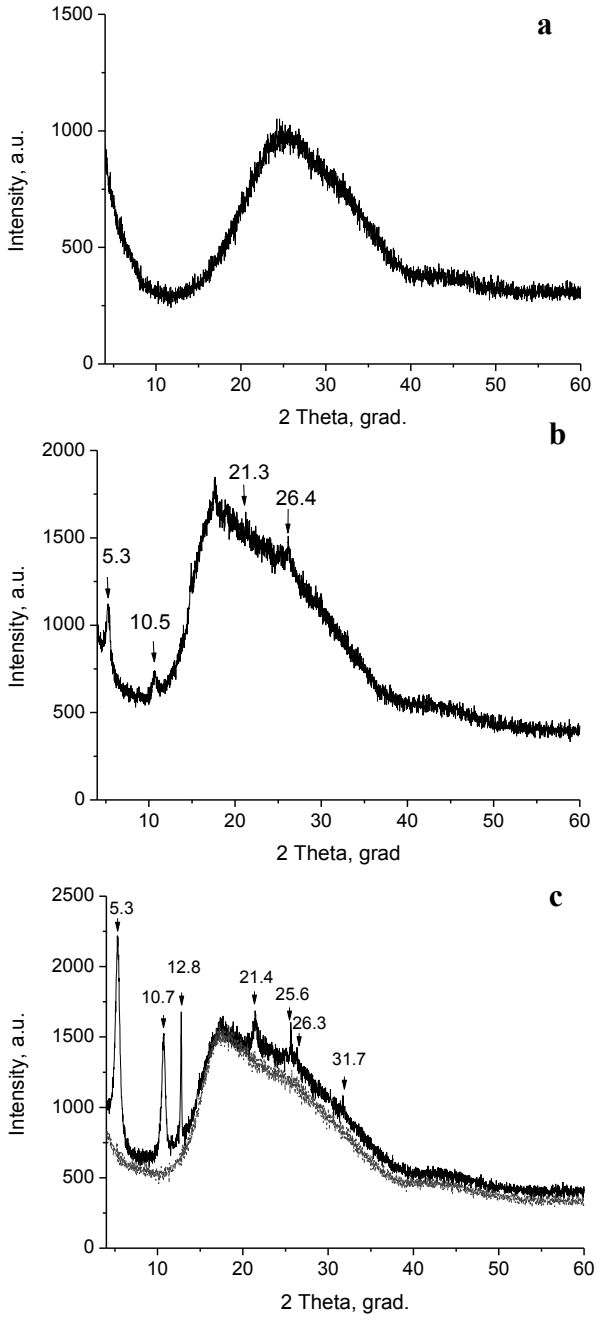

Figure 4-4. X-ray diffraction patterns of representative BL films: F4-4 (a), F4-6 (b), F4-11 (c) (black) and the reference polycarbonate film (achromatic). The investigated samples had an area of 2.3 cm^2 and a thickness of 20-25 µm.

Taking into account that the interplanar spacing of 16.6 Å can be correlated with the longest molecular axis of the $[Au(\alpha\text{-tpdt})_2]^0$ molecule,[6] the presence of only such reflections can be considered as an indication of molecular clusters in which the $[Au(\alpha\text{-tpdt})_2]^0$ molecules are highly oriented with the longest molecular axis perpendicular to the film surface and, consequently, they are able to produce conducting zones parallel to the film surface. It should be noted that, although, there exists this trend of molecular order, the metallic layers of BL films **F4-6** and **F4-7** are highly amorphous, as revealed by the very weak and diffusing reflections (Figure 4-4 b).

The PXRD pattern of the highly resistive BL film **F4-11** (Figure 4-4 c; black), which contains the rosebud-like structures, also shows the diffusing halo from the polycaronate matrix as well as a reflections at $2\theta = 5.3°$ and its high order reflections, but in this case the relative intensities of these reflections are much higher than those of films **F4-6** and **F4-7** by a factor of 2. In this case the intensity of the line at $2\theta = 5.3°$ is high enough to conclude that the covering conducting layer of the film contains well developed structures build up by oriented molecules whose longest molecular axis is perpendicular to the film surface. Nevertheless this pattern also demonstrates an extra narrow line at $2\theta=12.8^o$ (d-space of 6.9 Å) and its second order reflexion at $2\theta=25.6^o$ being characteristic of other orientation of the $[Au(\alpha\text{-tpdt})_2]^0$ molecules.

Electrical transport properties of BL films. In order to correlate the morphology of the conducting layer with the pathways for electrical conduction we studied some representative samples with current sensing Atomic Force Microscope (CS-AFM). In most cases the *I–V* response collected from the highest conducting areas of BL films **F4-4** (area a, Figure 4-5) and **F4-7** (Figure 4-6) show an ohmic character with conductance of about 20 μS (Figure 4-5, curve 1; Figure 4-6, green and black curves). Less conductive areas of BL films **F4-4** (areas **b** and **c** in Figure 4-5), and **F4-7** behave differently. Then, while in BL film **F4-4** we also observed a *I–V* responses showing ohmic behaviours (Figure 4-5, curves 2 and 3), in BL film **F4-7** the *I–V* curves have a non ohmic behaviour characterized by different experimental energy gaps (Figure 4-6, blue and red curves).

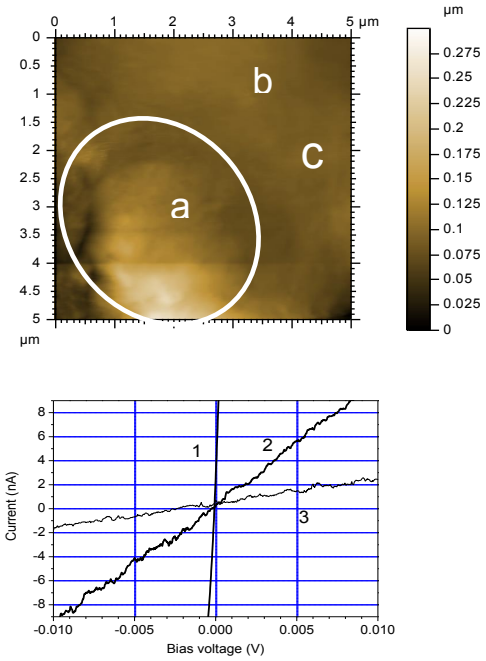

Figure 4-5. Current sensing AFM measurements of BL film F4-4. (Top) morphology and (bottom) I-V responses 1, 2, and 3 measured at the marked locations a, b, and c, respectively.

These results give an indication of the ability of the discrete aggregates of $[Au(\alpha\text{-tpdt})_2]^0$ to get metallic interconnections, as shown in Figure 4-5 (top).

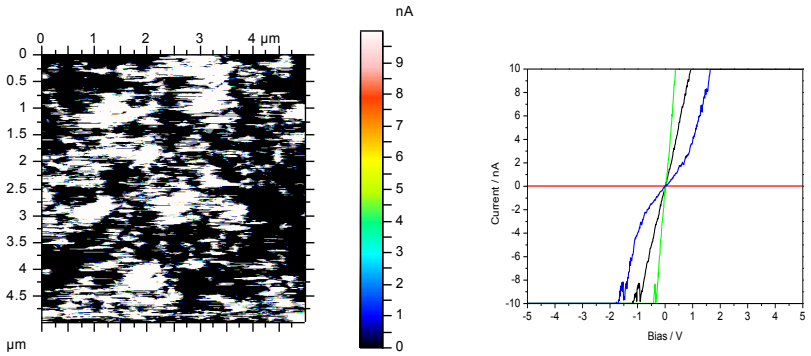

Figure 4-6. Current sensing AFM measurements of BL film F4-7. (Left) conducting map. (Right) I-V responses measured from highly conductive white areas (ohmic green and black curves) and low conductive black areas (non ohmic blue and red curves).

BL film **F4-3** mainly exibits non-ohmic *I–V* responses (Figure 4-7, curves blue and black). In contrast, the *I-V* responses, which are collected from the few highest conducting areas (white areas), show an ohmic character (Figure 4-7 green curve). It should be noted that the number of continuous metallic paths extending through the conducting layer of this BL films is below the percolation limit and not enough extended to show a metallic macroscopic properties (Figure 4-9 curve 2). Thus, the film shows a

semiconductor-like temperature dependence of the resistance with a very small value of the activation energy (4.4 meV) (Figure 4-7 blue curve). This value is lower than the activation energy reported for a polycrystalline samples compressed as a pellet by a factor of 4.5, suggesting that the aggregates of $[Au(\alpha\text{-tpdt})_2]^0$ are more strongly connected in the covering layers than in the pellets. The conducting layers of BL films **F4-1**, **F4-2**, and **F4-5** also exhibit a semiconductor-like temperature dependence in their resistances (Figure 4-8, a (curve 1) and c).

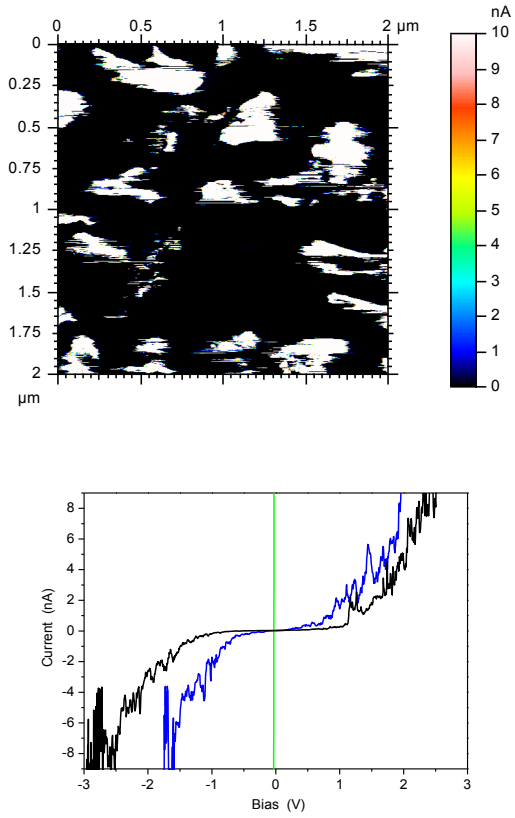

Figure 4-7. Current sensing AFM measurements of BL film F4-3: Current map obtained at 100 mV (top) and *I-V* responses monitored from the high conducting (green) and low conducting (blue and black) areas (bottom).

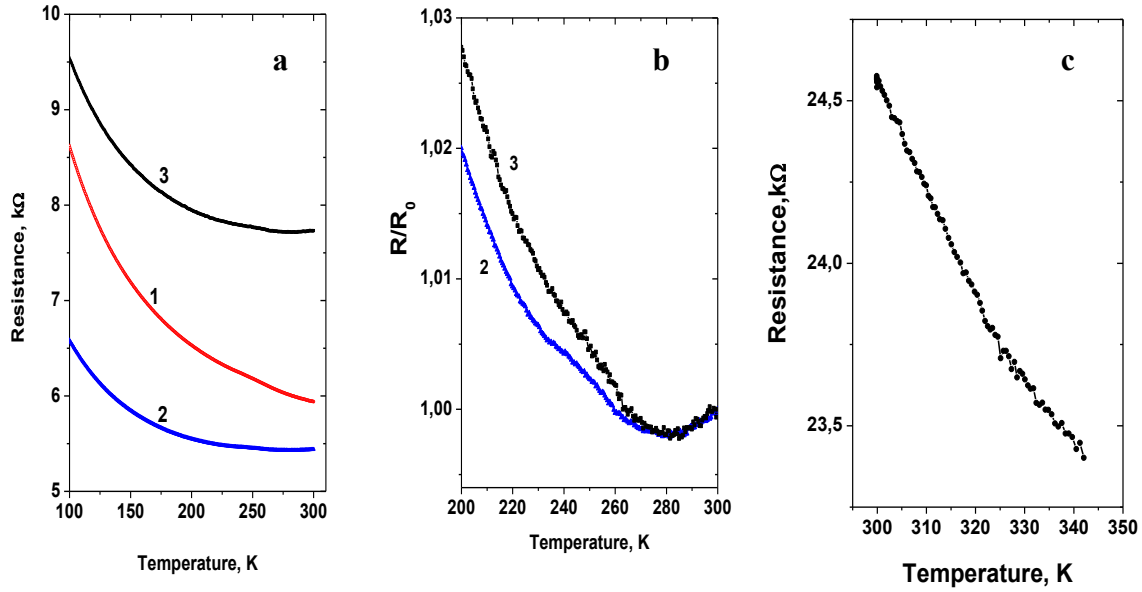

Figure 4-8. Temperature dependences of the resistance for the BL films F4-5 (curve 1), F4-6 (curve 2) and F4- 7 (curve 3). The high temperature zooming of R(T) show metallic behaviors of the electrical resistance for the covering layers of: BL films F4-6 3and F4-7 (b) as well as BL film F4-1 (c).

The temperature dependence of the resistance was measured by the four probe dc technique revealing that the number of continuous paths extending through the conducting layers of BL films **F4-4, F4-6** and **F4-7** is enough high to show macroscopic metal-like properties at T>280 K (Figure 4-9, curve 1; Figure 4-8 b). This is an additional prove that the single component conductor $[Au(\alpha\text{-tpdt})_2]^0$ is a metallic system, as previously claimed.[8] Surprisingly, $[Au(\alpha\text{-tpdt})_2]^0$ is able to form a metallic interconnection network uniquely in the thin layer prepared by the above method demonstrating that the semiconductor-like temperature dependence of electrical resistance is due to the inter-particle resistance effects.[8]

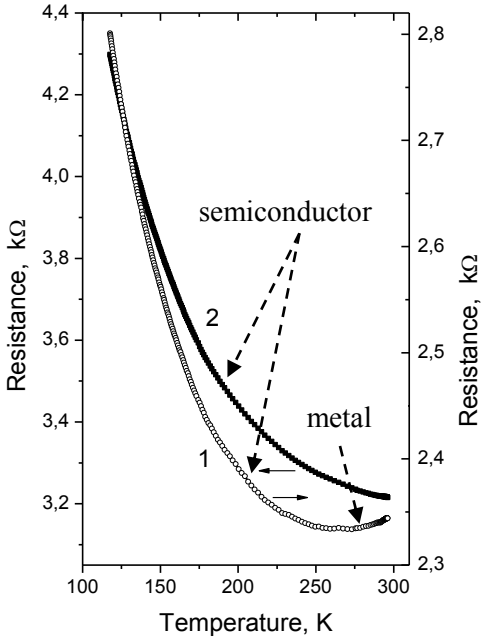

Figure 4-9. Temperature dependence of the electrical resistance of BL films F4-4 (curve 1) and F4- 3 (curve 2).

Mechanical and electromechanical properties of BL films. We studied the responses of the films covered with $[Au(\alpha\text{-tpdt})_2]^0$ to monoaxial stress to provide an overview of their mechanical and electromechanical properties. For this purpose their tensile testing in the elastic range was coupled with direct resistance measurements. For reference, a 25 μm thick polycarbonate film was also prepared and tested. The tensile test (Figure 4-10) performed on a BL films with a 25 μm thickness showed that the metallization of a polycarbonate film with $[Au(\alpha\text{-tpdt})_2]^0$ tends to decrease slightly the value of Young's moduli of a polycarbonate film from 2.05 to 1.70 GPa. The metallization also reduced moderately the value of the polycarbonate elastic limit (ε_{yield}) from 1.4 to 1.2 %. In spite of the above minor differences, the mechanical characteristics of the developed films are close to those of the reference polycarbonate film. Therefore, the self-metallization of polycarbonate with $[Au(\alpha\text{-tpdt})_2]^0$ did not adversely affect its mechanical properties.

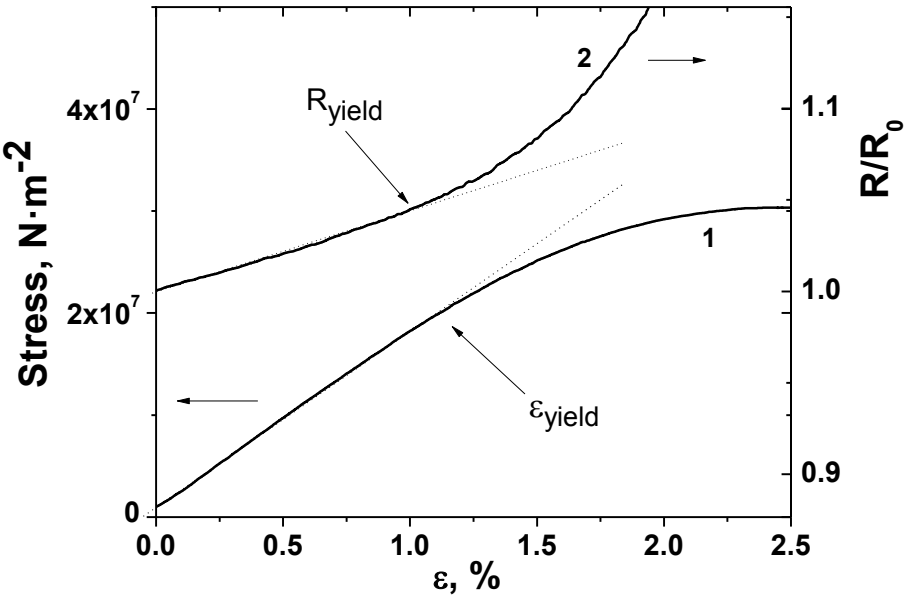

Figure 4-10. Stress-strain (curve 1) and resistance-strain (curve 2) curves for the polycarbonate film metallized with $[Au(\alpha\text{-tpdt})_2]^0$ (BL film F4-6); E=stress/ε =1.70 GPa (ε is relative strain), ε_{yield}=1.2%.

Figure 4-10 also shows that resistance changes versus strain deviate from a linear regime at a relative strain of 1.0 %; that is the R_{yield} is of 1.0 %. From Figure 4-11 the sensitivity of the BL film to the stress was calculated to be 300 Ω/MPa (or 30 Ω/bar). This means 0.23 %/MPa (0.023%/bar) for this type of material and contacts configuration limits of linear dependence is 14 MPa (140 bar), this value is 40 % larger than that was obtained for BL films with $TTF_{11}I_8$ crystallites. Interestingly, these BL films surpass the recently reported highly piezoresitive films [17] in elasticity since the same tensile tests showed that the value of R_{yield} for the polycarbonate metallized with organic molecular metal β-$(BEDT\text{-}TTF)_2I_3$ is only 0.65 %. Therefore, covering polymeric films with a metallic layer with a low crystallinity like $[Au(\alpha\text{-tpdt})_2]^0$ can significantly enhance the resistance limit (R_{yield}) of BL films and extend their capabilities of monitoring different deformations.

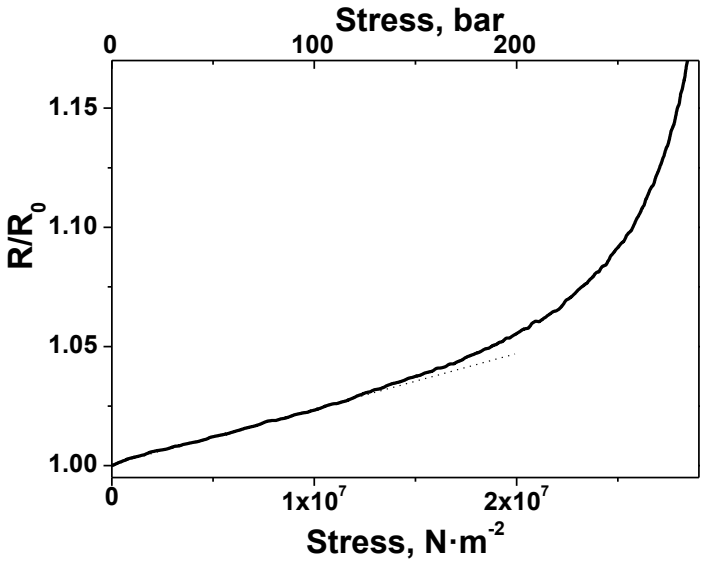

Figure 4-11. Normalized electrical resistance response of film F4-6 to monoaxial load.

As shown in Figure 4-12, the electrical response of the BL film **F4-6** to multi-cyclic monoaxial elongations, carried out in the elastic range of deformation, is very reproducible and depends linearly on the relative strain. The gauge factor, calculated as the ratio between the relative resistance change and the relative strain value, was found to be 4.4 which is somewhat lower than that reported for other piezoresitive BL films previously reported in this Thesis. [17] However, it matchs to the Pt-foil gauge factor of that shows the most pronounced strain resistive effect among inorganic metals. [18]

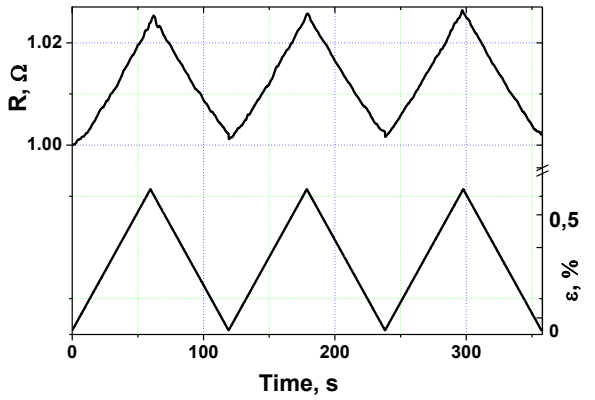

Figure 4-12. Resistance response of the metallic covering layer of $[Au(\alpha\text{-tpdt})_2]^0$ of BL film F4-6 to cyclic elastic elongations.

4.3. Conclusions

We have developed a simple procedure to obtain BL films based on polycarbonate and covered with either a metallic or a semiconductor-like layer of the single component molecular conductor $[Au(\alpha\text{-tpdt})_2]^0$. The conductive layers of such BL films are in a low crystallinity state that, as far as we know, is unprecedented for conducting molecular materials whose electrical transport properties are controlled by their supramolecular structures. Moreover, the low grain boundary resistance of the amorphous conductor enable to show metallic-like electrical properties. This kind of conducting material may find a number of applications usally reserved for flexible highly conductive materials, especially, there requiring high values of the resistance proportional limit.

Bibliography

1. J. M. Williams, Organic Superconductors (including Fullerenes): Synthesis, Structure, Properties, and Theory, Prentice Hall, 1992.

2. G. Saito, in Organic Molecular Solids: Properties and Appplications, CRC Press, 1997.

3. D. Jerome, Organic conductors: From charge density wave TTF-TCNQ to superconducting $(TMTSF)_2PF_6$, Chemical Reviews, 2004, 104, 5565-5591.

4. R. P. Shibaeva and E. B. Yagubskii, Molecular conductors and superconductors based on trihalides of BEDT-TTF and some of its analogues, Chem Rev, 2004, 104, 5347-5378.

5. C. Rovira, Bis(ethylenethio)tetrathiafulvalene (BET-TTF) and related dissymmetrical electron donors: From the molecule to functional molecular materials and devices (OFETs), Chemical Reviews, 2004, 104, 5289-5317.

6. H. Tanaka, Y. Okano, H. Kobayashi, W. Suzuki and A. Kobayashi, A three-dimensional synthetic metallic crystal composed of single-component molecules, Science, 2001, 291, 285-287.

7. A. Kobayashi, H. Tanaka and H. Kobayashi, Molecular design and development of single-component molecular metals, Journal of Materials Chemistry, 2001, 11, 2078-2088.

8. D. Belo, H. Alves, E. B. Lopes, M. T. Duarte, V. Gama, R. T. Henriques, M. Almeida, A. Perez-Benitez, C. Rovira and J. Veciana, Gold complexes with dithiothiophene ligands: A metal based on a neutral molecule, Chemistry-a European Journal, 2001, 7, 511-519.

9. N. Tenn, N. Bellec, O. Jeannin, L. Piekara-Sady, P. Auban-Senzier, J. Iniguez, E. Canadell and D. Lorcy, A Single-Component Molecular Metal Based on a Thiazole Dithiolate Gold Complex, Journal of the American Chemical Society, 2009, 131, 16961-16967.

10. T. P. I. Saragi, T. Spehr, A. Siebert, T. Fuhrmann-Lieker and J. Salbeck, Spiro compounds for organic optoelectronics, Chemical Reviews, 2007, 107, 1011-1065.

11. J. K. Jeszka and A. Tracz, A new method of growing crystalline networks in polymer matrices by simultaneous CT complex formation and in situ crystallization, Polymers for Advanced Technologies, 1992, 3, 139-142.

12. M. Mas-Torrent, E. Laukhina, C. Rovira, J. Veciana, V. Tkacheva, L. Zorina and S. Khasanov, New transparent metal-like bilayer composite films with highly conducting layers of theta-(BET-TTF)$_2$Br center dot 3H_2O nanocrystals, Advanced Functional Materials, 2001, 11, 299-303.

13. E. Laukhina, C. Rovira and J. Ulanski, Organic metals as active components in surface conducting semi-transparent films, Synthetic Metals, 2001, 121, 1407-1408.

14. K. M. Kadish and J. E. Anderson, Recommended methods for the purification of solvents and tests for impurities - Purification of solvents for electroanalysis - beinitrile dichloromethane 1,1-dichloroethane and 1,2-dichloroethane, Pure and Applied Chemistry, 1987, 59, 703-714.

15. P. Deplano, J. R. Ferraro, M. L. Mercuri and E. F. Trogu, Structural and Raman spectroscopic studies as complementary tools in elucidating the nature of the bonding in polyiodides and in donor-I_2 adducts, Coordination Chemistry Reviews, 1999, 188, 71-95.

16. R. Wojciechowski, J. Ulanski, M. Kryszewski, E. Laukhina and V. Tkacheva, Mixtures of trihalide anions in isostructural BEDT-TTF salts as seen by Raman spectroscopy, Molecular Crystals and Liquid Crystals, 2001, 355, 351-358.

17. E. Laukhina, R. Pfattner, L. R. Ferreras, S. Galli, M. Mas-Torrent, N. Masciocchi, V. Laukhin, C. Rovira and J. Veciana, Ultrasensitive piezoresistive all-organic flexible thin films, Adv Mater, 2010, 22, 977-981.

18. N. Nakamura and H. Masumoto, Strain-gauge factor and electrical properties of Fe-Cr-Co-W and Fe-Cr-Co-Mo alloys, Journal of the Japan Institute of Metals, 1987, 51, 1201-1208.

Chapter 5

Developing pyroresistive bi-layer materials based on the α´-(BEDT-TTF)$_2$I$_x$Br$_{(3-x)}$ molecular conductor for precise temperature monitoring

5.1. Introduction

Temperature measurements are important for numerous applications which span from industrial, [1] commercial goods, and medical uses being also a key component in many geophysical issues related with weather, soil, [2] and water. [3, 4] As a result, nowadays, many techniques and devices for measuring temperature exist. [5, 6] One possibility to register the surface temperature of an object or a media is a direct-contact measurement with a thermistor or a thermocouple. [7-9] This strategy gives highly accurate measurements compared to non-contact approaches but they require long detection times being therefore not useful for applications where fast temperature measurements are required. Precision thermometry can provide clinically relevant information about cardiovascular health, cognitive state, malignancy and many other important aspects of human physiology. [10, 11] Traditional methods for skin thermography, [12, 13] for instance, use either high-tech infrared digital camera systems for special imaging or simple paste-on temperature sensors for local direct-contact measurements. The aforementioned and other related techniques do have value in certain context but do not permit low-cost and large-area precision mappings of zones requiring flexibility. This characteristic can be afforded by organic/polymeric materials bringing many opportunities for human health care. [14, 15] In this context, organic materials, which have already shown a huge potential in a wide range of electronic applications, exhibit promising expectations when integrated in sensing systems.

In this Chapter, the development of BL films, composed of a polymeric matrix with a covering layer of the conducting ion-radical salt α´-(BEDT-TTF)$_2$I$_x$Br$_{(3-x)}$ is reported. This nanocomposite material is able to sense, either in a direct-contact and a non-contact way, changes of temperature in a fast and reversible manner with a sensitivity that is one order of magnitude larger than most of commonly used metal (or alloys) based temperature sensors and some non-contact devices. In addition, this material exhibit the properties of polymers like elastic, lightweight and has a simplicity of processing. Finally, proof-of-concept devices based on this novel nanocomposite material integrated in a fabrics for wearable devices will be reported. Moreover, a thermoelectric device and a simple infrared sensor prototype are described. All such prototypes demonstrate that flexible, low-weight and soft BL films are very attractive as a new generation of durable and low-cost temperature sensors, for which highly promising applications in areas such as biomedicine, human health care, smart textiles, and robotics are expected.

5.2. Preparation and characterization of temperature sensing materials

Preparation. Temperature sensitive BL films containing a polycrystalline conducting layer of sub/microcrystals of the α′-(BEDT-TTF)$_2$I$_x$Br$_{(3-x)}$ salt were prepared employing the same methodology as previously reported. [16-18] Indeed, the BL films were prepared in a single-stage procedure from a casted thin film (10-25 μm in thickness) of a solid solution of 2-8 % of neutral BEDT-TTF completely dispersed in polycarbonate. The film surfaces of such casted films were annealed with a 0.5 M solution of IBr in CH_2Cl_2 at 30 °C with a relative humidity of 40 % leading to the BL film formation.

As it was known from previous studies, crystals of α′-phase of (BEDT-TTF)$_2$I$_x$Br$_{(3-x)}$ may be converted into the β-phase by a thermal annealing at 160 °C.[19 20] However, in contrast to the (BEDT-TTF)$_2$I$_3$ salts, discussed in the Chapter 2, the α′→β conversion of (BEDT-TTF)$_2$I$_x$Br$_{(3-x)}$ is very drastic and seems to have a martensitic character; i.e. a phase change that occurs without a long-range diffusion of the atoms (molecules) but through a cooperative way. It should be noted that in the structure of both phases of this ion-radical salt the cation and anion layers are closer to each other than in the α and β$_H$ phases of the (BEDT-TTF)$_2$I$_3$ salt having a higher conformability. In order to perform the phase transition from the α′-phase to the β-one of (BEDT-TTF)$_2$I$_x$Br$_{(3-x)}$ the same device shown in Chapter 2.6 was used. It allowed a precise control of the phase transition which results in BL films covered with the β-(BEDT-TTF)$_2$I$_x$Br$_{(3-x)}$ organic metal or with mixture of both α′ and β-phases. Resistance data obtained for a BL film with a 20 μm in thickness using the above mentioned setup are plotted in Figure 5-1. The α′ → β structural phase transition starts approximately at 150 °C and accelerates at 160 -165 °C in agreement with the data reported for single crystals. [19] At the beginning of the phase transition the BL film exhibits a semiconductor-like temperature dependence of its electrical resistance, whereas after the phase conversion heating (up to 165 °C) the resistance drops one order of magnitude showing the metallic behavior characteristic for single crystals of the β-(BEDT-TTF)$_2$I$_x$Br$_{(3-x)}$ phase.

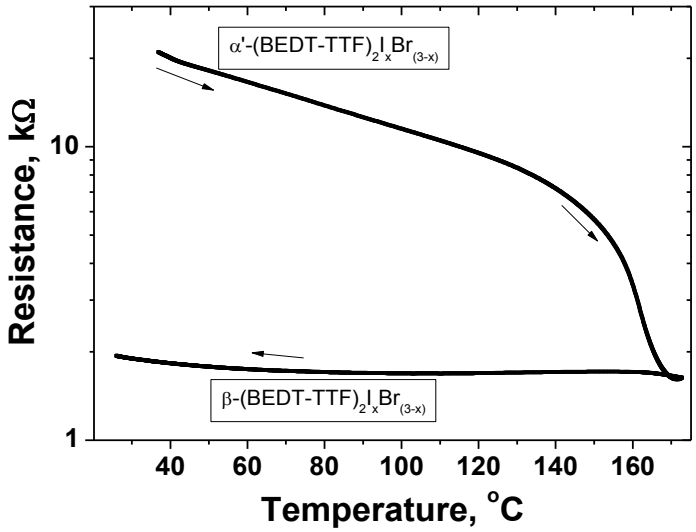

Figure 5-1. Temperature dependence of the electrical resistance of the BL film during a thermal annealing. Arrows show the direction of the heating-cooling process.

Structural and morphological characterization. The resulting BL films after the phase transition were fully characterized by scanning electron microscopy (SEM) and powder X-ray diffraction (PXRD) techniques and their composition was analyzed by EDX.

The powder X-ray diffraction data (Figure 5-2) exhibit only the presence of very sharp (*00l*) reflections of either of the α′- or the β-phase of $(BEDT\text{-}TTF)_2I_xBr_{(3-x)}$ crystals revealing that the microcrystals have a high degree of a structural orientation with respect the film surface. It could be noted that in contrast to BL films with $(BEDT\text{-}TTF)_2I_3$ crystals, where both phases are prepared separately, for BL films with $(BEDT\text{-}TTF)_2I_xBr_{(3-x)}$ it is possible to obtain by the thermal annealing mixtures of α′- or β-phases on the surface of polymeric matrix, as shown in Figure 5-2. As already mentioned the X-ray analysis indicates the presence of only (*00l*) reflections for all studied films, demonstrating that the crystals of the α′-and β-phases are randomly oriented with the *c* axis perpendicular to the film surface and, consequently, with the molecular conducting layers parallel to it. Such crystal texture, together with the high-quality contacts between the crystals and the large film-coverage density, are responsible for the excellent conducting and pyroresistive properties of the BL films (vide infra).

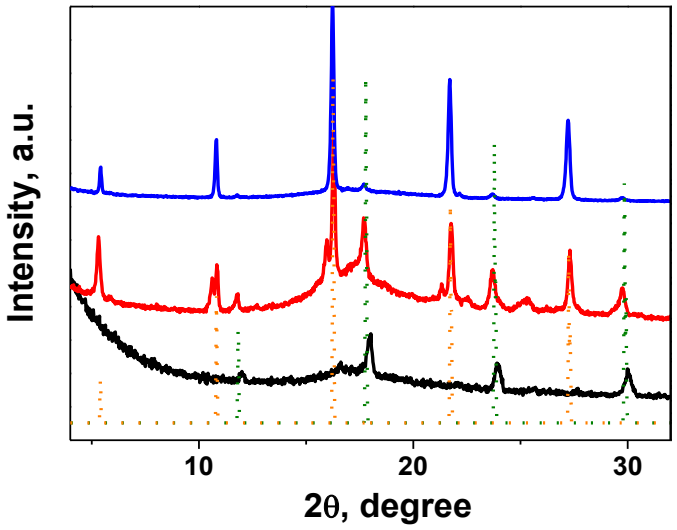

Figure 5-2. X-ray diffraction patterns of the films covered with different ratios of the α′- and β-phases of (BEDT-TTF)$I_xBr_{(3-x)}$ salt. Blue line - α′-phase, red line - α′-phase/β-phase (64:36), black line – β-phase. Orange and green lines are calculated from data for of α′- and β-phases, respectively, using the data of single crystals from the Cambridge Crystallographic Data Centre.

EDX analysis shows that the I:Br ratio in the BL films slightly changes for each sample being in the range of 1:1.5 to 1:2.1, so the *x* value in the formula $(BEDT\text{-}TTF)_2I_xBr_{(3-x)}$ is from 1.0 to 1.2, in a good agreement with data from the literature. [21]

Typical SEM images of α′-and β-$(BEDT\text{-}TTF)_2I_xBr_{(3-x)}$ are shown in Figure 5-3 indicating, for both phases, the presence of well-shaped submicron crystals with sizes of 300 and 1000 nm that are densely connected among them.

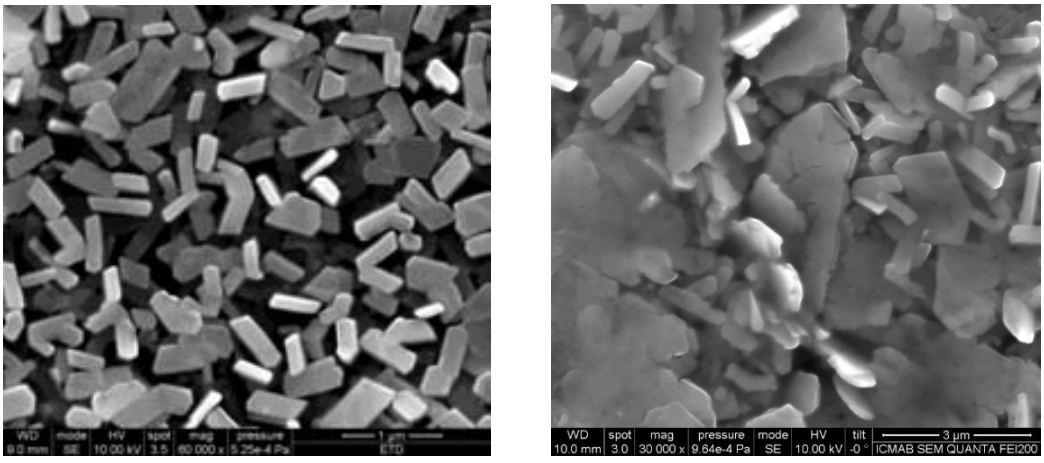

Figure 5-3. Typical SEM images of BL film with α′- (left) and β-$(BEDT\text{-}TTF)_2I_xBr_{3-x}$ (right) crystallites.

Electromechanical properties. Figure 5-4 shows the reversible electromechanical response in the elastic range of deformation to cyclic monoaxial deformations of three BL films containing different ratios of the α′- and β-phases. The BL films with crystallites of α′-phase has similar electromechanical properties that the film with mixture of both phases with a gauge factor of 8±1; while that containing only the β-phase has a gauge factor that is practically twice as larger GF 15±1. So, both GF values follow the same trend observed for BL films with α- and β_H-phases of the $(BEDT\text{-}TTF)_2I_3$ salt and can be rationalized in terms of the higher compactness of the β-phase. Also the lower GF value for BL films with crystallites of β-$(BEDT\text{-}TTF)_2I_xBr_{(3-x)}$ phase in comparison with that of BL film with the β-phase of $(BEDT\text{-}TTF)_2I_3$ can be explained by the smaller radius of Br respect to the I radius and its consequent compactness. Notwithstanding the similar electromechanical properties of the BL films with only α′-phase and that with a mixture of phases cannot be explained with simple arguments.

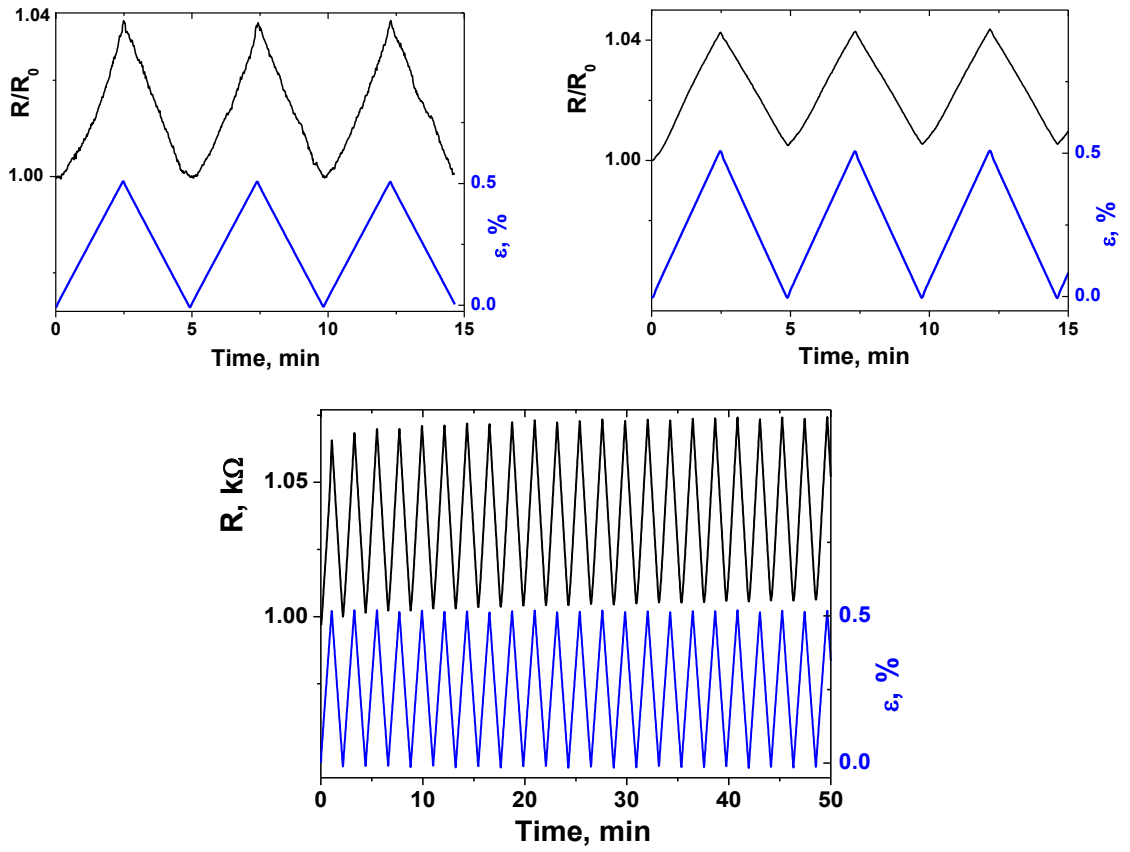

Figure 5-4. Resistance response of BL films with different ratios of α′- and β-phases of the $(BEDT\text{-}TTF)I_xBr_{(3-x)}$ to cyclic monoaxial elongations. Top left - α′-phase; top right – mixture of α′- and β-phases (64:36); bottom – β-phase.

Electrical properties. BL films with β-(BEDT-TTF)$I_xBr_{(3-x)}$ crystallites shows room temperature sheet resistance in the range of 1-2 kΩ. They exhibit a metallic behavior in the temperature range of 120 – 300 K (Figure 5-5), with a TCR value varying from 0.1 to 0.2 %/deg depending on the sample. This variation can be related with the different composition of the counteranions i.e., the I:Br ratio. Finally, around 180 K the films show a step increase in the resistance due to the well-known charge order-disorder transition.

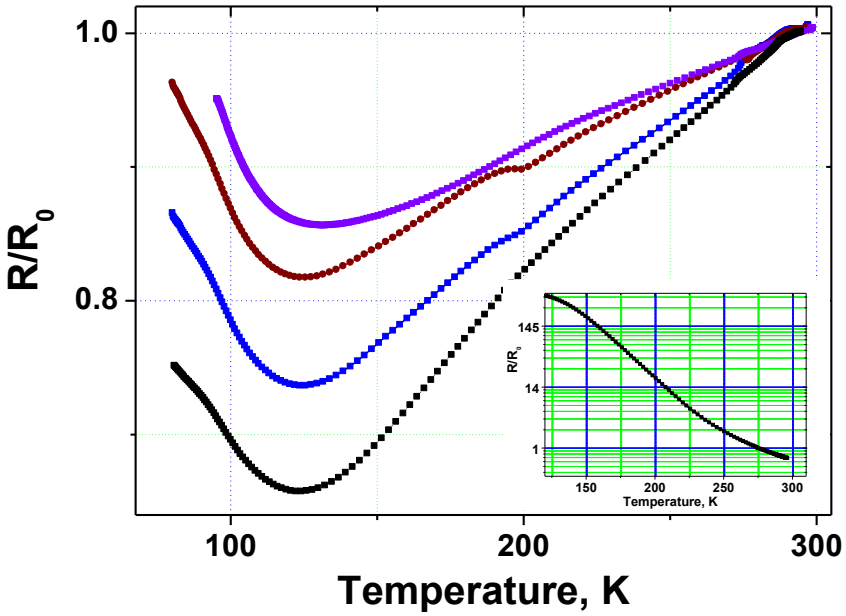

Figure 5-5. Temperature dependence of the relative resistance of several BL film samples covered with β-phase of the (BEDT-TTF)$_2I_xBr_{(3-x)}$ salt. Colors correspond to different film samples. Inset Typical temperature dependence of the resistance of a BL film with α´-(BEDT-TTF)$_2I_xBr_{(3-x)}$ crystallites.

BL films with α´-(BEDT-TTF)$_2I_xBr_{(3-x)}$ exhibit room temperature sheet resistance values in the range of 15 - 50 kΩ and a semiconductor-like behavior in the range of 120 – 300 K (Figure 5-5 inset) with a TCR value of 1.3 %/deg at room temperature.

Since our mayor interest was to develop BL films for biomedical applications such as to control of the body temperature, we studied more in detail the electrical properties of both BL films in temperature range between 25 and 50 °C. Figure 5-6 summarizes this study showing that BL films with α´- and β-phases show a linear dependence of the resistance with temperature with TCR value of 1.3 %/deg and 0.2 %/deg, respectively. For comparison also the resistance-temperature curve for a commercial available platinum Pt_{111} temperature sensor is shown.

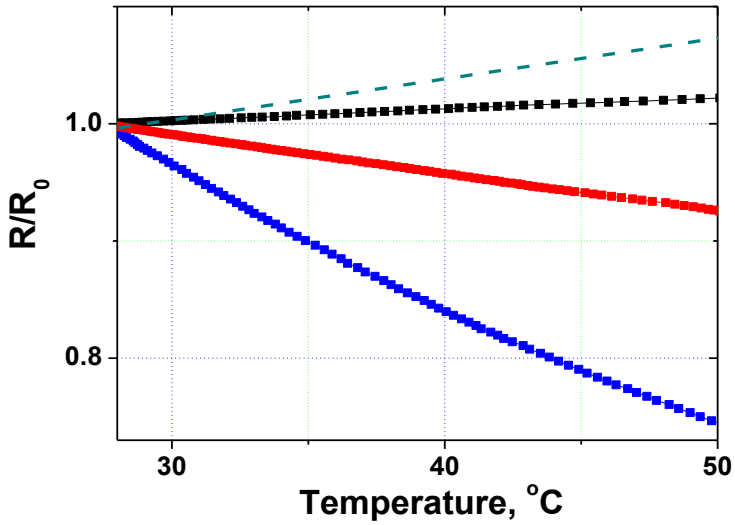

Figure 5-6 Normalized temperature dependence of the resistances of BL-films with different ratios of the α′- and β-phases. Blue line - α′-phase; red line – mixture of α′and β phases (64:36); black line - β-phase; dash line - a resistance-temperature curve a commercial platinum Pt_{111} temperature sensor.

A worth noticing point in the sensitivity of BL films with crystallites of α′-phase is that it in 4 times larger than that of platinum thermometer (TCR_{Pt111} = 0.3 %/deg) at room temperature. Such a high sensitivity makes BL films with the α′-phase very promising for biomedical applications.

Thermoelectric properties of BL films. Thermoelectric properties are based on the Seebeck and Peltier effects which describe the reversible conversion of thermal energy into electrical energy and viceversa. When the two extremes of a material are subjected to a temperature difference a drop in the electrical potential between them is produced (Seebeck effect) and, conversely, when an electrical current flows through a material, there appears a flow of heat energy (Peltier effect) (Figure 5-7). Thus, heat transfer and current flow are coupled phenomena because the charge carriers are also heat carriers. The origin of such phenomena is as follows: if a heat source is applied to one face of a conducting material a voltage drop will appear across this face and the colder one. As one face is heated, the kinetic energy of the mobile charge carriers on the hotter side increase and they gradually start to diffuse across the material to the colder face. Charge carriers continue moving across the thermal gradient until a sufficient amount of charge has

accumulated on the colder face creating a difference in the electrical potential across the material that limits a further movement.

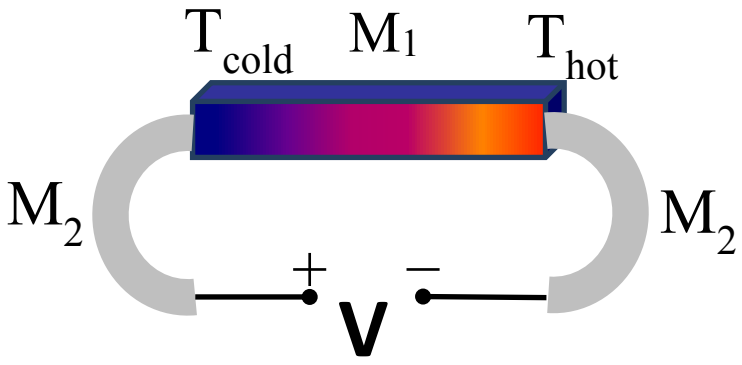

Figure 5-7. Schematic representation of the thermoelectric effect in a conducting material.

In the literature there were not too many studies on the thermoelectrical properties of organic molecular conductors. [22-24] The most remarkable results were those obtained for single crystals of β-(BEDT-TTF)$_2$I$_3$ [25] or for TTF-TCNQ [26] which show Seebeck coefficients (S= - $\Delta V/\Delta T$), also named thermopower, of 20-30 μV/K. Since BL films where composed of organic conductors and have several advantages with respect single crystals we decided to study their thermoelectric properties.[iii] The Seebeck coefficients of the BL films were calculated from the linear slope of the stationary value of ΔV *vs.* ΔT plot (a temperature gradient in 1 degree was applied). Figure 5-8 shows that the Seebeck coefficients of tested BL films are practically independent on the temperature in the range 200-300 K and the highest coefficient is shown by the BL film of α´-(BEDT-TTF)$_2$I$_x$Br$_{(3-x)}$ with a positive value of +50 μV/K indicating that the majority of carriers are holes.

[iii] This study was performed in collaboration with Professor Francisco Rivadulla at Centro de Investigación en Química Biológica y Materiales Moleculares (CIQUS, Universidad de Santiago de Compostela), Spain.

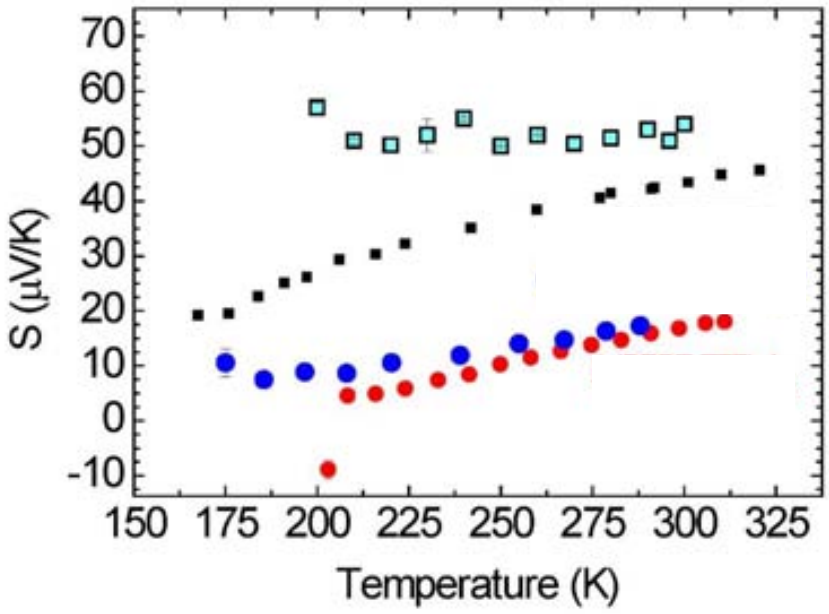

Figure 5-8. Temperature dependence of Seebeck coefficients for different BL films containing crystals of α´-(BEDT-TTF)$_2$I$_x$Br$_{(3-x)}$ (□); α-(BEDT-TTF)$_2$I$_3$ (■); β-(BEDT-TTF)$_2$I$_3$ (●);and (BEDT-TTF)$_x$Br$_y$(H$_2$O)$_n$ (●).

Here it should be noted that the main characteristic parameter for a thermoelectric material is the non-dimensional thermoelectric figure of merit (*ZT*), which measures the thermoelectrical performance of the material and is calculated by $ZT = S^2\sigma/\kappa$, where S is the Seebeck coefficient, σ is electrical conductivity and κ is the thermal conductivity. Thus, the higher is ZT the better the thermoelectric property of a material is. A higher ZT can be achieved by a higher Seebeck coefficient and an electrical conductivity and by a lower thermal conductivity. The best thermoelectric material reported up to date is Bi_2Te_3 with a ZT = 1. [27] We expected for the composite BL films good thermoelectric properties because they combine a high Seebeck coefficient together with a high electrical conductivity. Unfortunately, we were not able to measure the thermal conductivity of the films, due to their thickness. However it is possible to estimate from the literature data the thermal conductivity as an additive function of the properties of the materials forming the composite. In this way we obtained for the α´-(BEDT-TTF)$_2$I$_x$Br$_{(3-x)}$ an estimate value for κ of $5\cdot10^{-3}$ W/cm·K that with $S \approx 50$ μV/K and $\sigma \approx 0.5$ $(\Omega cm)^{-1}$ gives a ZT value of $7.5\cdot10^{-5}$ which is comparable with other organic materials, such as pentacene ($ZT=7.5\cdot10^{-5}$). [28]

So, we may conclude that the BL films with crystals of the α´-phase have a thermoelectric figure of merit similar to the organic materials reported up to date but they have additional properties, like flexibility and lightweight, that make BL films worth to be developed for particular applications.

5.3. Proof-of-concept devices based on pyroresistive BL films

5.3.1. A thermomodule based on pyroresistive BL films

As already mentioned, the thermoelectric properties and flexibility and lightweight characteristics of the BL films with crystals of α´-(BEDT-TTF)$_2$I$_x$Br$_{(3-x)}$ make interesting to use them as active components for thermomodules capable to generate a current by the Seebeck effect. For its construction a module with four BL films were connected thermally in parallel and electrically in series permitting in this way to increase four-fold the yield of the thermoelectric module (Figure 5-9). A Cu(Fe) thermocouple was used for monitor the temperature difference at the two Cu strips at each side of the films. The Cu strips were used for heating-cooling homogeneously all four BL films.

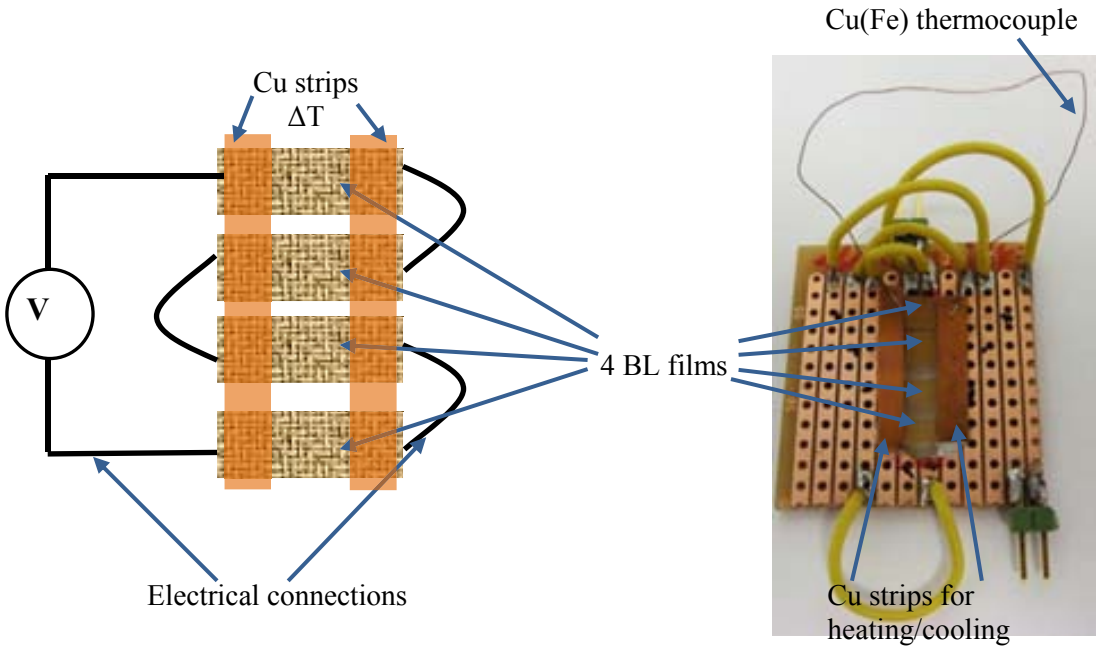

Figure 5-9. Left: scheme of the thermomodule; right: image of the developed thermoelectric module based on four BL films.

The data obtained for the setup show a fast response of the output voltage of the battery under application of the temperature gradients. So, a temperature gradient of 27 K provokes an output voltage of 5.2 mV/K for one BL film. The hysteresis observed in the

measurement, shown in the right part of Figure 5-10 (48 to 55 μV/K for heating and cooling, respectively) is due to the different rate of heating and cooling (due to a heat capacitance of the used support) obtained from the left part of the figure. The above results open the possibility to create the thermoelectric devices based on pyroresistive BL films with the α´-$(BEDT\text{-}TTF)_2I_xBr_{(3-x)}$ crystals with high performances. So, if higher power levels are required, ΔT could be increased as well as the number of the BL films used in a thermomodule. So using, for example, 100 BL films and exposing them to a temperature gradient of ΔT = 100 K, the theoretical output voltage could be as high as 0.5 V. Consequently, a thermomodule based on a numerous BL films, could offer a realistic alternative to current thermoelectrics for using in lightweight, flexible and portable electronics.

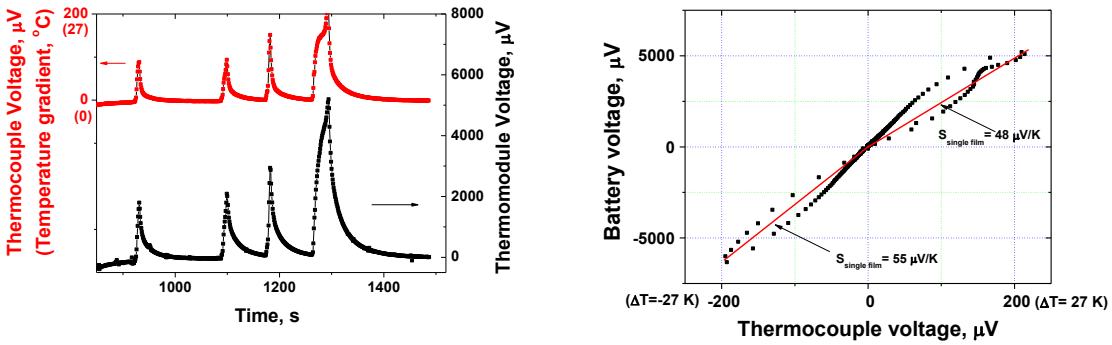

Figure 5-10. Left: the output voltage of the thermoelectric module consisting of 4 BL films under a thermal gradient stimuli in time; Right: the battery output voltage for cooling and heating at the opposite sides of the BL films.

5.3.2. Conductive wearable fabrics based on pyroresistive BL films

Particularly interesting is the integration of conductive sensing materials in human wearable interfaces, such as fabrics, since wearable electronics offer advantages in personalized healthcare, security and comfort.[29] Recently, our group has reported the integration of a polycarbonate film metalized with the highly strain sensitive β-$(BEDT\text{-}TTF)_2I_3$ metal in a polyester textile demonstrating that the strain sensing properties of the BL films can be transferred to a fabric. [30] The possibility of embedding a BL film with a temperature sensing properties in textiles was highly attractive since it could permit to create wearable temperature sensors with a wide range of applications.

Here we present such a development that provides a wearable temperature sensing fabric capable to measure the temperature of a human body with an accuracy higher than most of the commercial wearable sensors.

Two different prototypes prepared by an impregnation and by a molding procedures (vide infra) were developed using BL films with the α´-$(BEDT\text{-}TTF)_2I_xBr_{(3-x)}$ crystals to which two gold electrodes where thermally evaporated resulting in an active sensing area of 40x12 mm. The electrical properties of this BL film sample was determined by sandwiching it between two glass slides within an Al frame that includes a commercial Pt_{111} temperature sensor. The electrical resistance in the temperature range from -25 to 140 °C was measured with a Keithley 2400 SourceMeter exhibiting a typical semiconductor behavior with a very small hysteresis between heating and cooling cycles (Figure 5-11). A worth noticing point of this BL film was that the temperature dependence of the conductance (1/R) is linear in the temperature range of -25 to 140 °C with sensitivity of ca. 1.3%/degree. Moreover, taking into account the sheet resistance at room temperature of the film (25 and 100 kΩ/cm^2 for the films containing 2% and 8% of BEDT-TTF, respectively) and its thermal sensitivity of 1.3%/degree one should expect changes of the resistance of 300 - 1000 Ω per degree at room temperature. Therefore, the samples of the BL film would be capable of measuring very small temperature changes of around 1 - 3 millidegrees with significant changes of the resistance of about 1 Ω.

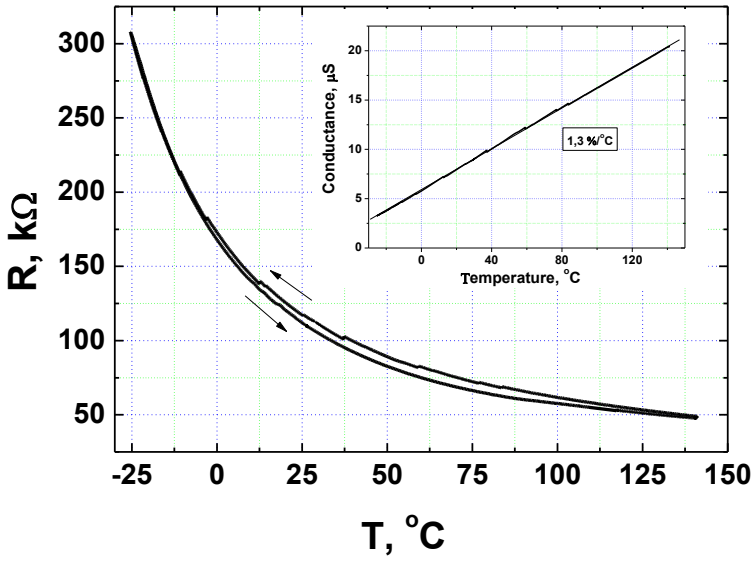

Figure 5-11. Temperature dependence of the electrical resistance of the BL films with α´-$(BEDT\text{-}TTF)_2I_xBr_{(3-x)}$ crystals used for developing the conductive fabrics. Inset, temperature dependence of the conductance (1/R) of the same BL film.

Prototype prepared by impregnation. To develop this prototype a polyester textile was first impregnated with a viscous solution of polycarbonate in CH_2Cl_2. The CH_2Cl_2 makes

the textile to be swollen and the polycarbonate fills the space between the textile fibers. This process makes the treated region of the textile much more robust avoiding practically any deformation in comparison with the rest of textile. Then, the previously prepared BL film with a size of 20×5mm^2 was attached to the swollen surface of the impregnated textile with the impregnating face in contact with the textile. Due to such textile impregnation the BL-based sensor is attached to part of textile that is not experiencing any strain when the textile is deformed measuring only changes of the temperature. Finally, electrical contacts were attached with graphite paste to the conductive temperature sensing layer.

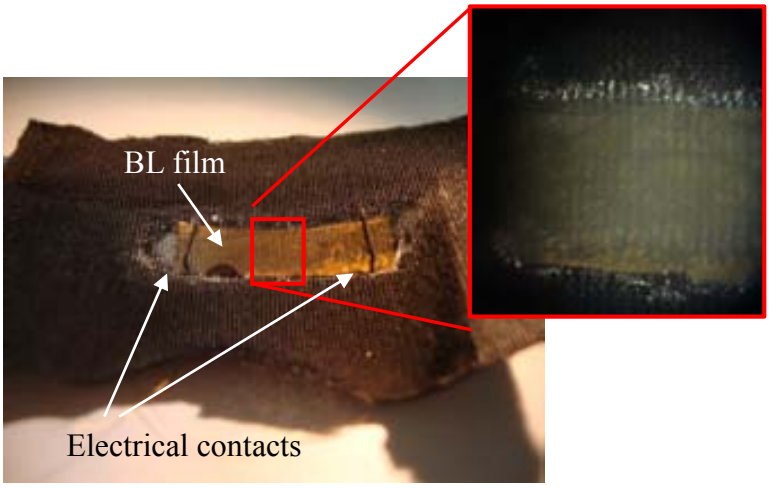

Figure 5-12. Image of a conductive fabric prepared by an impregnation.

Prototype prepared by molding. The second prototype was made by melting the zone of the textile which will be used for the BL film location. The melted part of polyester textile loses its texture and becomes continuous and much more rigid than the rest of the textile. In order to do that the part of the textile, in which the sensor will be located, was placed between microscopic glass slides and heated up through these glasses by a solder to temperature about 250 °C, visually controlling the textile plastification process. Then the BL film was placed over the plasticized part of the textile using any glue which does not destroy the polycarbonate film (Figure 5-13).

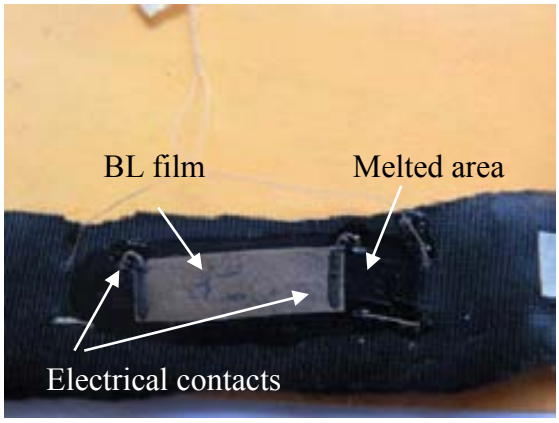

Figure 5-13. Image of a conductive fabric prepared by melting.

This procedure permits to plasticize the heated part of textile becoming smother than when prepared using the impregnation technique permitting to embed the pyroresistive BL film into the fabric without any damage. As it seen in the Figure 5-14 the conducting film embedded by the impregnation technique has some cracks on the conducting surface, which seems to be due to the textile texture, whereas the film placed on the smooth rigid melted part does not show any imperfectness.

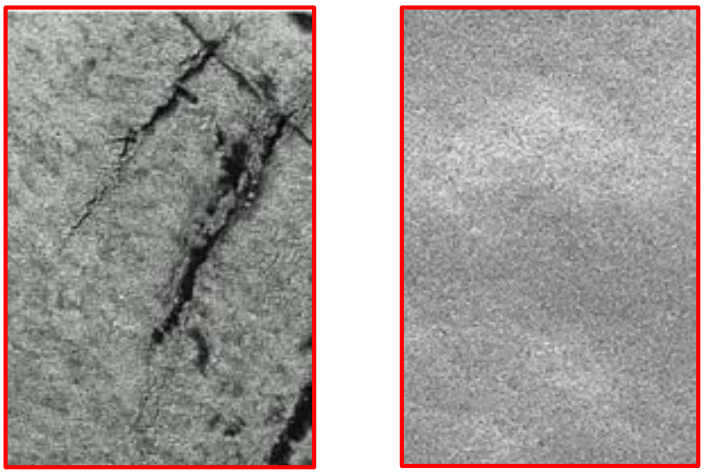

Figure 5-14. SEM images of the BL film after placing onto a textile. Left: by impregnation; right: by melting procedure.

Sensing properties of conducting fabrics. Due to the homogeneity of the conducting fabric prepared by melting procedure without the presence of cracks on the conducting surface, only this prototype was characterized as a temperature sensor. The tested fabric was also heated up to 60 °C and cooled down to room temperature several times

(Figure 5-15) showing a high degree of reversibility. Furthermore, the sensitivity to the temperature of the conductive fabric was maintained at the same level that with the BL film; *i.e.* with a -1.2 %/deg. at room temperature region. Thus, the electrical response is reversible and repeatable as well as stable in time.

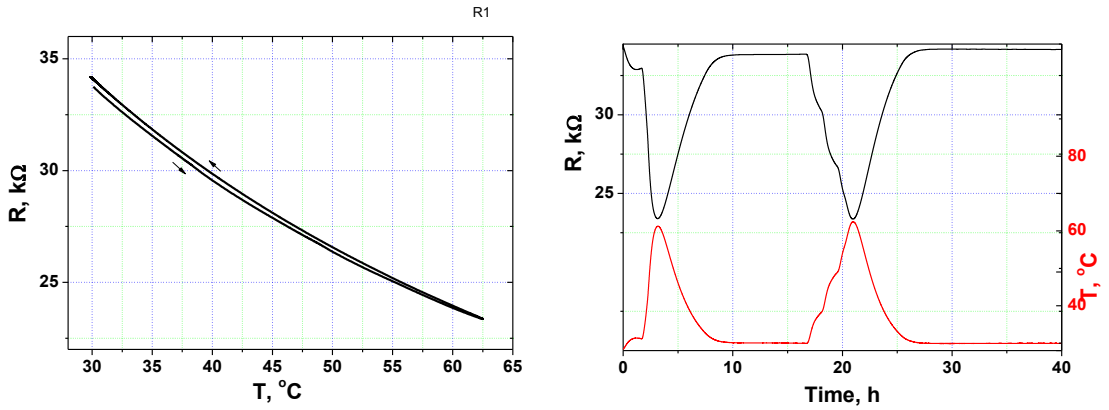

Figure 5-15. Temperature dependence (left) and time stability (right) of the electrical resistance of the conductive fabric prepared by melting.

This result shows that the pyroresistive BL film can be successfully used as temperature sensing components in smart wearable fabrics enabling to measure very small temperature changes.

5.3.3. Bolometer based on pyroresistive BL film

There has been a tremendous evolution in the development of bolometers since their discovery by Langley at 1878. [31] Since then sophisticated designs, including quite recently dual-gated structures employing graphene as active material, have arisen. [32, 33] Bolometers are suitable to detect ultra-small temperature variations of a body that emits heat energy in the form of electromagnetic radiation being therefore possible to make with them contact-less temperature sensors.

The design principle of a bolometer includes two fundamental parts. First of all it should contain a pyroresistive material capable to absorb the radiation in the desired wavelength to be detected and second this material should be supported in a device with the minimum possible mass and with a lower heat-dissipation showing in addition a low transparency in the desired wavelength. In this context, pyroresistive BL films based on crystals of α´-(BEDT-TTF)$_2$I$_x$Br$_{(3-x)}$ seemed a priori good candidates to fabricate a

bolometer if they are made with the minimum amount of the polymer acting as a support. To develop such bolometers it is interesting to analyze the UV-Vis-IR transmission spectra of thin films made with pure polycarbonate, polycarbonate with the molecularly dispersed neutral BEDT-TTF molecules, as well as of a pyroresistive BL films with a total thickness of 5 µm made with 8 wt% of BEDT-TTF donor. All these thin layers were mounted on the top of a KBr pellet used for UV-Vis and IR spectroscopy allowing to analyze the contribution of the different components of the BL films. Also it is interesting to compare the adsorption of the films with the normalized radiation spectrum of an ideal black body source at 37 °C, calculated applying the Planck's law (Figure 5-16). As described by the Planck's law and the Wien's displacement law the wavelength at the maximum of the IR radiation emitted by an ideal black body at 37 ^{o}C, the temperature of a human body, occurs at a $\lambda = 9.3$ µm while the maximum at 3000 ^{o}C is at 0.8 µm.

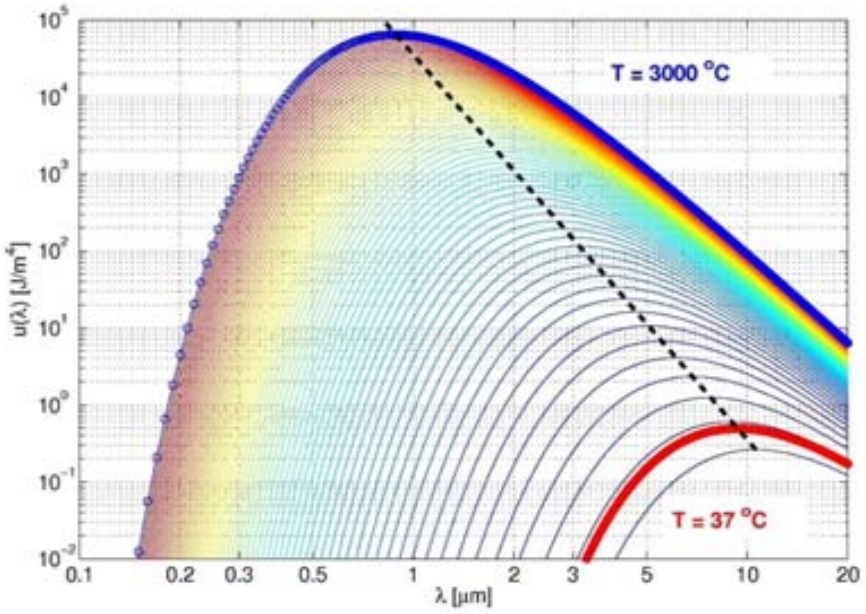

Figure 5-16. Energy density u(λ) of an ideal black body given by the Planck's law. The energy per unit volume of an ideal black body was calculated from T = 0^{o}C to T = 3000 ^{o}C (*i.e.* tungsten filament used in light bulbs) with the black dashed line showing the Wien's displacement law. The bold red curve shows the wavelength distribution of a black body radiator at a temperature of 37 ^{o}C; *i.e.* the temperature of the human body.

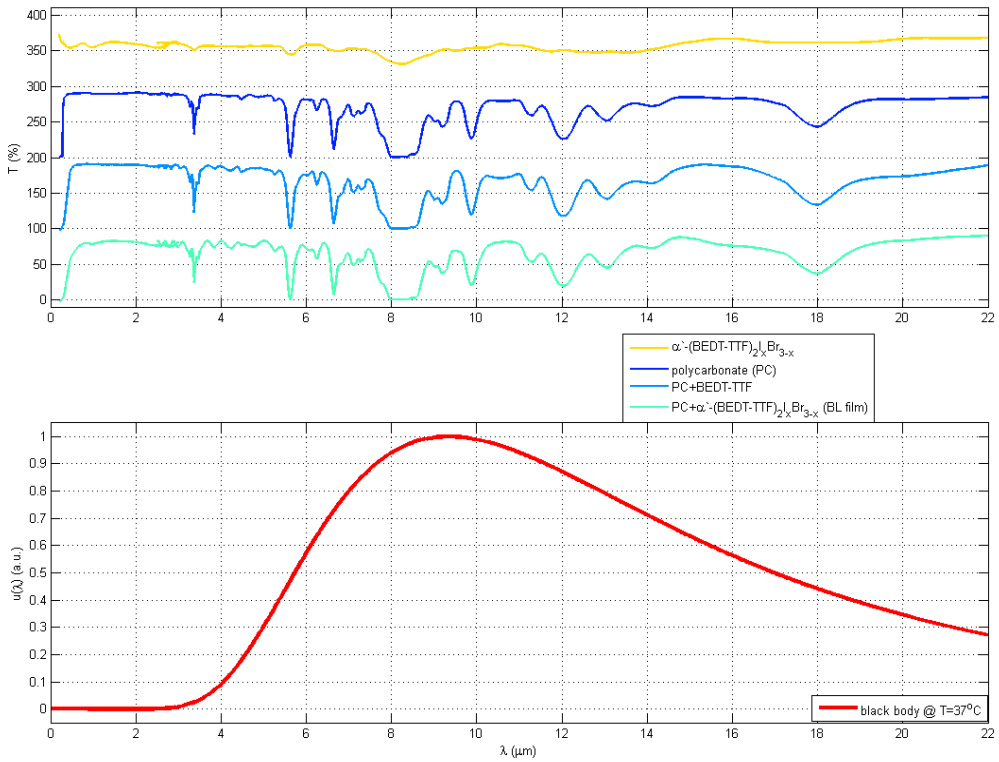

Figure 5-17. Top: UV-Vis and IR spectra of neutral BEDT-TTF dispersed in a polycarbonate matrix (PC + BEDT-TTF), a α´-(BEDT-TTF)$_2$I$_x$Br$_{3-x}$ BL-film (PC+α´-(BEDT-TTF)$_2$I$_x$Br$_{3-x}$), a thin polycarbonate film (PC) and α´-(BEDT-TTF)$_2$I$_x$Br$_{3-x}$ polycrystalline layer on KBr pellet (α´-(BEDT-TTF)$_2$I$_x$Br$_{3-x}$). All spectra were taken at T = 26 ºC. Bottom: normalized emission spectrum of an ideal black body at T = 37ºC calculated according to Planck's law.

Interesting is the fact that the pyroresistive BL film shows multiple absorption peaks in the range between 5 and 16 μm, where the radiation of an ideal black body at 37 °C has a 60% of its maximum value. The strongest absorption peaks of BL film were observed between 7.6 and 8.8 μm. So, the BL films appeared appropriate to detect in contact-less way temperature changes around 37 °C. The setup used for evaluating the performance of the pyroresistive BL film as a bolometer is shown in Figure 5-18 that includes a Fresnel lens (FL) to focus the radiation on the sensor element made with the BL film, a Styrofoam box for a thermal stabilization and a hotplate with a controlled temperature that can be located at different distances was used to simulate a black body radiator. This setup avoids that a heating of the BL film by convection occurs and at the same time to concentrate on the BL film the heating by radiation.

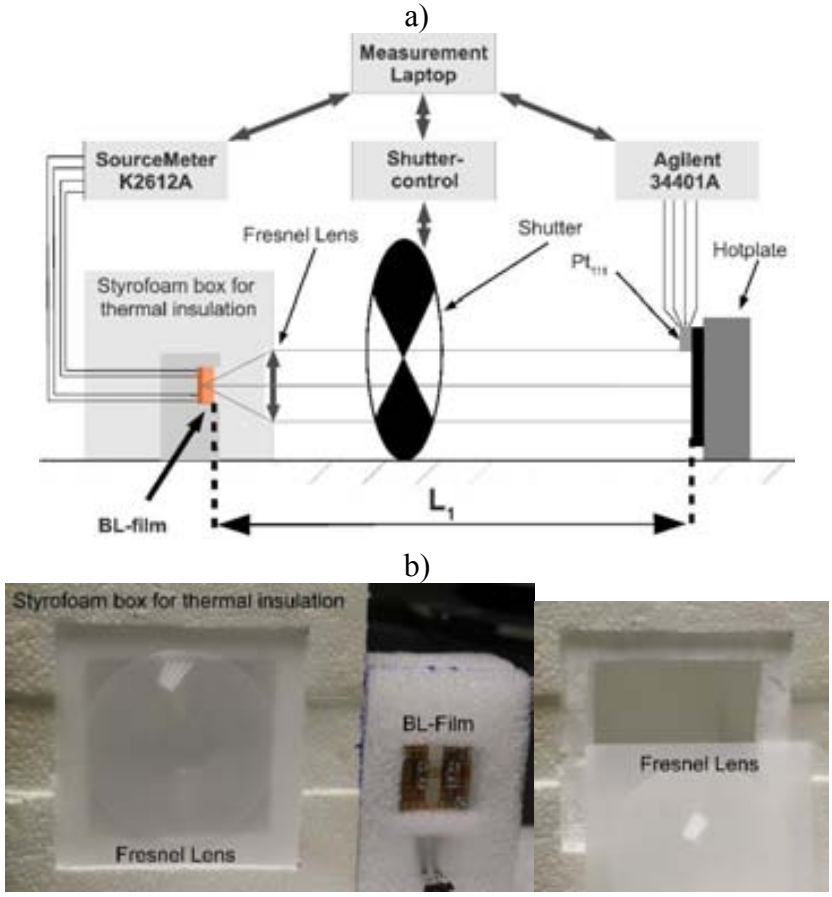

Figure 5-18. a) Experimental setup employed to measure the variation of the electrical resistance upon exposure to IR-radiation emitted by a hotplate at different temperatures. A shutter was used to chop the IR-radiation focused by Fresnel lens arriving to the sensor element which was mounted within a Styrofoam box for thermal insulation. All electrical measurements were performed in a four wire configuration. L1 represents the distance between the hotplate and the BL-film . b) Styrofoam box with incorporated Fresnel lens with a focal length of 5.5 cm.

The changes of the electrical resistance ΔR of the film inside this device was extracted as follows. The mean value of the electrical resistance, measured on 20 points, before closing the beam with the shutter was subtracted from the mean value of 20 points, before opening the beam. ΔT was measured as the temperature difference between the surface of the hotplate and the temperature inside the Styrofoam box at each measured point given by two thermometers (Pt_{111} and Pt_{1000}, respectively). This approach was used to extract data from more than 2000 cycles of opening and closing the IR-beam hitting the sensor element at L_1 = 30, 40, 50, 100 and 110 cm. The first significant result of such measurements was that a change of the distance L_1 does not have any significant influence on the resistance changes.

BL-films of three different thicknesses were studied with this setup observing that an increase of the film thickness leads to a higher absorption of the radiation providing larger temperature and resistance changes (Figure 5-19). On the other side, by increasing the film thickness, the response speed (determined by the first derivative of the time dependence of the resistance changes) is decreased. Remarkable the fact that for temperature differences of up to $\Delta T = 40\ ^{o}C$ the response of the bolometer can be fitted to a linear function with a fairly good approximation. On the contrary, when the temperature difference was increased up to $\Delta T = 120\ ^{o}C$ a non-linear behavior was observed.

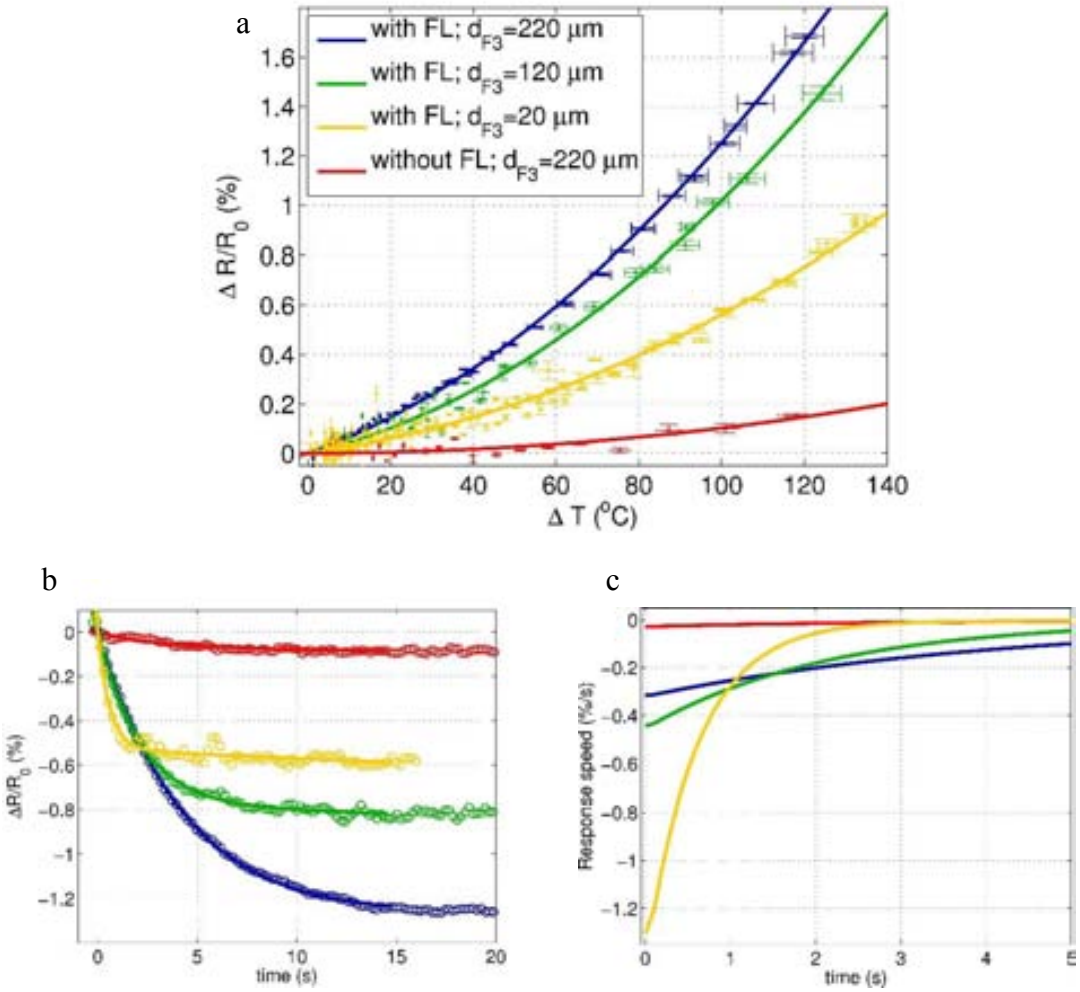

Figure 5-19. a) Resistance-temperature response of BL film sensors with different thicknesses heated by a IR-radiation employing a hotplate at a distance of L_1 = 110 cm with and without the Fresnel lens, b) change of resistance of the sensor during the time with the hotplate at temperature about 120ºC and c) response speed, as obtained by the first derivative, decreasing with sample thickness.

To unravel the underlying mechanism of the resistance change under a radiation exposition, the response of the pyroresistive BL film was studied with samples mounted inside a cryostat on a circular holder made of a plastic with a low mass/heat-capacitance minimizing the heat transfer between sensor element and the substrate. Electrical contacts were done with 25 µm thick gold wires and small graphite-paste contacts. Employing a laser diode with a tunable intensity that illuminates with a λ of 635 nm on the full sensing area. The electrical response of BL film was studied both under vacuum and at ambient air (Figure 5-20).[iv] The maximum relative resistance change extracted after a stabilization of the signal (*i.e.* t = 20 s) scales linearly with the laser power (P_{Laser} = 0.13, 0.48, 0.77 and 1.04 mW), as shown in Figure 5-20 and 5–21. This means that the material responsivity (R_M), given by the relative change of resistance divided by the incident radiation power, is constant (Figure 5-21) being R_M an intrinsic material parameter of the active material that measures the sensitivity of the material to the thermal radiation.

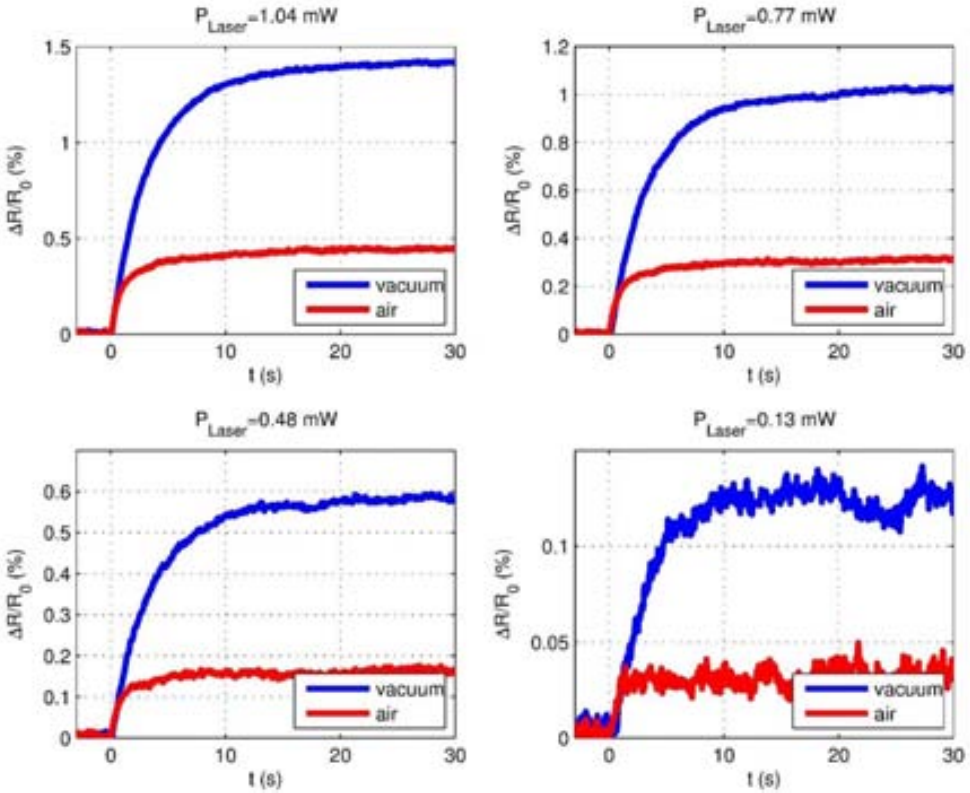

Figure 5-20. Relative resistance changes measured in air and vacuum at different laser powers with a λ of 635 nm.

[iv] This study was performed in collaboration with Professor Gerasimos Konstantatos and Dr. Francisco Pelayo García de Arquer at solution-processed nanophotonic devices laboratory, the Institute of Photonic Science, ICFO, Castelldefels, Spain.

The fact that the BL film shows a higher R_M value under vacuum compared to ambient air verifies the hypothesis that the radiation is the driving force of this temperature sensor. Interesting is the observation that the heating of the sensing element and the dissipation of heat when the sensor is not exposed to the laser beam do perfectly overlap in measurements both in air and vacuum, exhibiting a high reversibility.

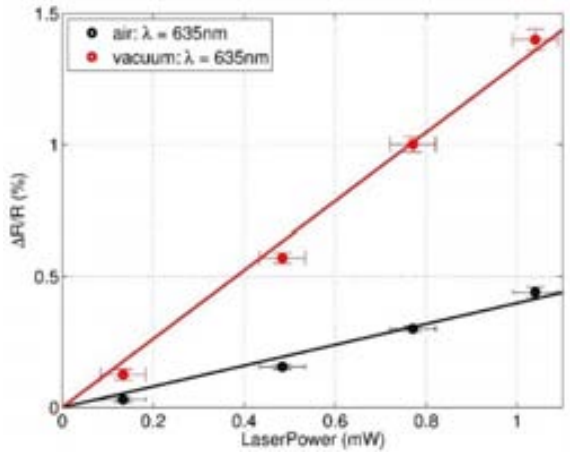

Figure 5-21. Electrical response of BL-film upon an exposure to a laser beam (λ = 632 nm) as a function of the laser power in air and in vacuum.

With the aim to look deeper into the mechanism of the pyroresistive BL film, the R_M was studied at different wavelengths. In a typical photonic IR sensor, the R_M is expected to depend on the wavelength of the incident light because the material has different absorption at each wavelength. On another hand, in the case of a thermal IR sensor (*i.e.* a bolometer) the R_M is expected to be wavelength independent. Therefore, R_M was measured at different wavelengths ranging from 532 of up to 6960 nm and with laser power between 0.1 and 22 mW using a laser beam diameter equal to the active sensing area (Figure 5-22). [v]

[v] This study was performed in collaboration with Prof. Majid Ebrahim-Zadeh, and Drs. Suddapalli Chaitanya Kumaramd and Badarla Venkata Ramaiah at optical parametric oscillators laboratory, the institute of photonic science, ICFO, Castelldefels, Spain.

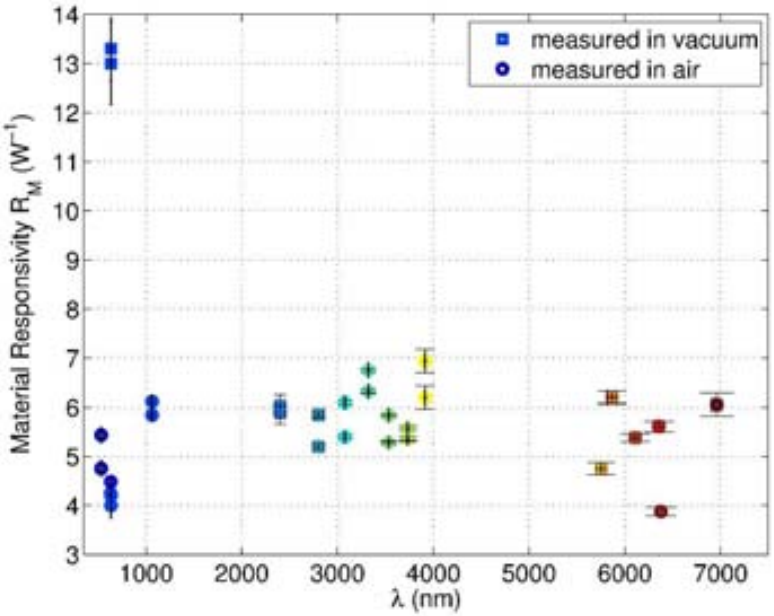

Figure 5-22. Material responsivities (R_M) of the pyroresistive BL film measured in vacuum (square) and in air (circles) using laser sources of different wavelengths with power between 0.1 mW and 22 mW. Error bars correspond to the maximum absolute errors.

If one analyzes the relative changes of resistances upon varying the laser power a clear linear dependence is observed (Figure 5-23). So, such results demonstrate that the pyroresistive BL films behave thermal IR sensors being possible to use as bolometers.

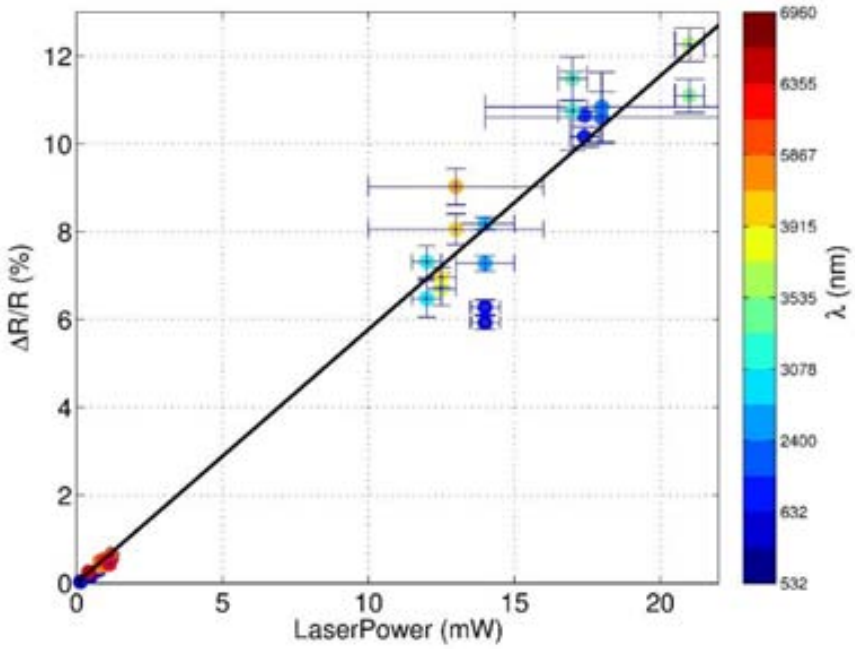

Figure 5-23. Relative resistance changes at different laser power and wavelengths exhibiting a linear dependence with the showing that the material responsivity (R_M) is constant over the full measured range of wavelengths. Error bar correspond to the maximum absolute errors of the resistance and the errors in measuring the laser power.

5.4. Conclusions

Pyroresistive BL films allow the fabrication of low-cost temperature sensors with a temperature resistance coefficient one order of magnitude higher than conventional metal (or alloy) based sensors. Such pyroresistive BL films may also be successfully embedded into textiles permitting to use them as wearable fabrics for temperature monitoring. Additionally, these BL films show a great potential as passive thermal IR sensors capable to be used as bolometer. Therefore, these BL films offer a great potential for high-tech temperature sensors in a wide range of applications.

Bibliography

1. M. McSherry, E. Lewis and C. Fitzpatrick, Development of temperature sensitive glassware for monitoring temperatures in harsh industrial environments, Sensors and Actuators a-Physical, 2005, 123-24, 408-417.

2. J. Jia and F. Yi, Atmospheric temperature measurements at altitudes of 5-30 km with a double-grating-based pure rotational Raman lidar, Applied Optics, 2014, 53, 5330-5343.

3. G.-M. Jiang and R. Liu, Retrieval of Sea and Land Surface Temperature From SVISSR/FY-2C/D/E Measurements, IEEE Transactions on Geoscience and Remote Sensing, 2014, 52, 6132-6140.

4. F. Gan, J. Huang, W. Zhao, Z. Xu and B. Liu, Design of intelligent multi-sensor fire detector, 2006.

5. T. Fu, J. Liu, J. Tang, M. Duan, H. Zhao and C. Shi, Temperature measurements of high-temperature semi-transparent infrared material using multi-wavelength pyrometry, Infrared Physics & Technology, 2014, 66, 49-55.

6. M. S. K. Mutyala, J. Zhao, J. Li, H. Pan, C. Yuan and X. Li, In-situ temperature measurement in lithium ion battery by transferable flexible thin film thermocouples, Journal of Power Sources, 2014, 260, 43-49.

7. X. Fu and X. Luo, Can thermocouple measure surface temperature of light emitting diode module accurately?, International Journal of Heat and Mass Transfer, 2013, 65, 199-202.

8. M. Genix, P. Vairac and B. Cretin, Local temperature surface measurement with intrinsic thermocouple, International Journal of Thermal Sciences, 2009, 48, 1679-1682.

9. M. A. Marr, J. S. Wallace, S. Chandra, L. Pershin and J. Mostaghimi, A fast response thermocouple for internal combustion engine surface temperature measurements, Experimental Thermal and Fluid Science, 2010, 34, 183-189.

10. S. Bauer, Flexible electroonics sophisticated skin, Nature Materials, 2013, 12, 871-872.

11. R. C. Webb, A. P. Bonifas, A. Behnaz, Y. Zhang, K. J. Yu, H. Cheng, M. Shi, Z. Bian, Z. Liu, Y.-S. Kim, W.-H. Yeo, J. S. Park, J. Song, Y. Li, Y. Huang, A. M. Gorbach and J. A. Rogers, Ultrathin conformal devices for precise and continuous thermal characterization of human skin, Nature Materials, 2013, 12, 938-944.

12. F. G. A. M. van Haren, L. Kadic and J. J. Driessen, Skin temperature measured by infrared thermography after ultrasound-guided blockade of the sciatic nerve, Acta Anaesthesiologica Scandinavica, 2013, 57, 1111-1117.

13. N. Zaproudina, O. Airaksinen and M. Narhi, Are the infrared thermography findings skin temperature-dependent? a study on neck pain patients, Skin Research and Technology, 2013, 19, E537-E544.

14. M. E. Roberts, A. N. Sokolov and Z. Bao, Material and device considerations for organic thin-film transistor sensors, Journal of Materials Chemistry, 2009, 19, 3351-3363.

15. T. Someya, T. Sekitani, S. Iba, Y. Kato, H. Kawaguchi and T. Sakurai, A large-area, flexible pressure sensor matrix with organic field-effect transistors for artificial skin applications, Proceedings of the National Academy of Sciences of the United States of America, 2004, 101, 9966-9970.

16. E. Laukhina, V. Tkacheva, I. Chuev, E. Yagubskii, J. Vidal-Gancedo, M. Mas-Torrent, C. Rovira, J. Veciana, S. Khasanov, R. Wojciechowski and J. Ulanski, New flexible low-density metallic materials containing the (BEDT-TTF)$_2$(I_xBr_{1-x})$_3$ molecular metals as active components, Journal of Physical Chemistry B, 2001, 105, 11089-11097.

17. E. Laukhina, V. Tkacheva, S. Khasanov, L. Zorina, J. Gomez-Segyra, A. P. del Pino, J. Veciana, V. Laukhin and C. Rovira, Linked crystallites in the conducting topmost layer of polymer bilayer films controlled by temperature: From micro- to nanocrystallites, Chemphyschem, 2006, 7, 920-923.

18. E. Laukhina, V. Tkacheva, R. Shibaeva, S. Khasanov, C. Rovira, J. Veciana, J. Vidal-Gancedo, A. Tracz, J. K. Jeszka, A. Sroczynska, R. Wojciechowski, J. Ulanski and V. Laukhin, New conducting molecular metal polycarbonate bilayered composites: (ET)$_2$IBr$_2$/PC-, (BET)$_2$IBr$_2$/PC- and (BET)$_2$I$_3$/PC-films, Synthetic Metals, 1999, 102, 1785-1786.

19. N. V. Avramenko, A. V. Zvarykina, V. N. Laukhin, E. E. Laukhina, R. B. Lyubovskii and R. P. Shibaeva, Pis'ma v ZhETF, 1988, 48, 429.

20. H. H. Wang, K. D. Carlson, L. K. Montgomery, J. A. Schlueter, C. S. Cariss, W. K. Kwok, U. Geiser, G. W. Crabtree and J. M. Williams, Solid State Commun., 1988, 66, 1113.

21. E. Laukhina, V. Tkacheva, A. Chekhlov, E. Yagubskii, R. Wojciechowski, J. Ulanski, J. Vidal-Gancedo, J. Veciana, V. Laukhin and C. Rovira, Polymorphism of a new bis(ethylenedithio)tetrathiafulvalene BEDT-TTF based molecular conductor; Novel transformations in metallic BEDT-TTF layers, Chemistry of Materials, 2004, 16, 2471-2479.

22. W. Kang, D. Jerome, L. Valade and P. Cassoux, Thermopower measurments of the organic conductor TTF(Ni(DMIT)$_2$)$_2$ at ambient pressure, Synthetic Metals, 1991, 42, 2343-2345.

23. V. A. Merzhanov, D. A. Hits, E. B. Yagubskii, M. L. Doublet and E. Canadell, Electronic properties of isostructural organic conductors (ET)$_3$(HSO$_4$)$_2$ AND Ni(DDDT)$_2$ (ET)$_3$(HSO$_4$)$_2$ – thermopower and tight-binding calculations, Synthetic Metals, 1995, 71, 1867-1868.

24. H. Yoshino, H. Nakada, S. J. Krivickas, H. Mori, G. C. Anyfantis, G. C. Papavassiliou and K. Murata, in Physica Status Solidi C: Current Topics in Solid State Physics, Vol 9, No 5, ed. R. Swietlik, 2012, pp. 1193-1195.

25. K. Mortensen, J. M. Williams and H. H. Wang, Anisotropic Thermopower of the organic metal beta-(BEDT-TTF)$_2$I$_3$, Solid State Communications, 1985, 56, 105-110.

26. H. Yoshino, G. C. Papavassiliou and K. Murata, Low-dimensional organic conductors as thermoelectric materials, Journal of Thermal Analysis and Calorimetry, 2008, 92, 457-460.

27. H. J. Goldsmid, Recent trends in thermoelectric materials research I - Semiconductors and semimetals - Introduction, Recent Trends in Thermoelectric Materials Research I, 2001, 69, 1-24.

28. N. Kim, B. Domercq, S. Yoo, A. Christensen, B. Kippelen and S. Graham, Thermal transport properties of thin films of small molecule organic semiconductors, Applied Physics Letters, 2005, 87.

29. F. Axisa, P. M. Schmitt, C. Gehin, G. Delhomme, E. McAdams and A. Dittmar, Flexible technologies and smart clothing for citizen medicine, home healthcare, and disease prevention, Ieee Transactions on Information Technology in Biomedicine, 2005, 9, 325-336.

30. L. R. Ferreras, R. Pfattner, M. Mas-Torrent, E. Laukhina, L. Lopez, V. Laukhin, C. Rovira and J. Veciana, Highly piezoresistive textiles based on a soft conducting charge transfer salt, Journal of Materials Chemistry, 2011, 21, 637-640.

31. S. P. Langley, On the measurement of radiant energy, Science (New York, N.Y.), 1880, 1, 288-289.

32. P. L. Richards, Bolometers for infrared and millimeter waves, Journal of Applied Physics, 1994, 76, 1-24.

33. D.-H. Kim, N. Lu, R. Ma, Y.-S. Kim, R.-H. Kim, S. Wang, J. Wu, S. M. Won, H. Tao, A. Islam, K. J. Yu, T.-i. Kim, R. Chowdhury, M. Ying, L. Xu, M. Li, H.-J. Chung, H. Keum, M. McCormick, P. Liu, Y.-W. Zhang, F. G. Omenetto, Y. Huang, T. Coleman and J. A. Rogers, Epidermal Electronics, Science, 2011, 333, 838-843.

Chapter 6

Developing hygroresistive bi-layer materials based on molecular conductors for precise relative humidity monitoring

6.1. Introduction

Humidity and temperature are among the most frequently measured physical quantities in science and technology. Measurements of water vapor content of a gaseous atmosphere appears much more complex than temperature measurements which can be done nowadays with a satisfactory accuracy and sensitivity (see Chapter 5). Therefore monitoring and controlling environmental humidity is receiving ever wider attention, mainly for comfort purposes and for industrial processes.[1] Sometimes it is necessary to monitor the absolute humidity, or the dew point, but more often it is important to measure the relative humidity (RH) of an atmosphere. It has become evident in the recent years that the influence of humidity is of paramount importance in diverse areas, such as for moisture sensitive products, in medical and biological applications, in security and detection systems, in food processing, textile technology, storaging areas, computer rooms, hospitals, museums, libraries, high voltage engineering, etc. [2-4] Consequently, there is a great demand for reliable, cheap, sensitive, and small-sized humidity sensing materials as well as whole sensor systems thereof. The choice of a suitable sensor is difficult and must be based on materials that show good sensitivity, rapid and reproducible responses, long-term stability, low temperature dependence, high stability to contaminations and low cost. Diverse operating conditions and, therefore, different kinds of humidity sensors have been developed in order to meet the different requirements. [5] At the present time, the most common materials of commercially humidity sensors are organic polymer films and porous ceramics. Another type of humidity sensors are the electrolyte ones [6] which were used for over 40 years. However, such sensors show a slow response time and are unable to operate in very humid environments or in the presence of ammonia or organic solvents. Another important aspect of sensors is the transduction principle they use that may be based on capacitance, resistance or impedance changes. Nevertheless, resistance[7, 8] and impedance[9, 10] are the most frequently transducer principles used nowadays.

Sensors based on conducting polymer films cannot operate at high temperature and high humidity and usually they show hysteresis, slow response times, long-term drifts and degradation upon their exposure to some solvents or to electrical shocks. The problems for ceramic humidity sensors are mainly related to the need for their periodic regeneration by a heat cleaning process to recover their humidity-sensitive properties. Prolonged exposure to humid environments leads to the gradual formation of stable

chemisorbed OH^- ions on their surfaces causing a progressive drift in the resistance of the ceramic sensors. Moreover, humidity sensors are usually exposed to atmospheres that may contain several impurities, such as dust, dirt, oil, smoke, alcohol, solvents, etc. and the adhesion or adsorption of these compounds on the ceramic surfaces causes irreversible changes in their response to relative humidity. The surface-related phenomena of humidity sensing by ceramic sensors make these materials less resistant than polymers to surface contamination because of their porous structure.

Recently, Yamochi and coworkers reported a BL film containing the $(BEDO\text{-}TTF)_2Br(H_2O)_3$ salt whose electrical resistance changes with the humidity but only in the range of 0-60 % RH.[11] This result stimulated us to search for other BL films able to detect RH over a wides humidity range. In this Chapter we present the development of BL films with conductive polycrystalline layers capable to sense RH changes in the whole range of relative humidity.

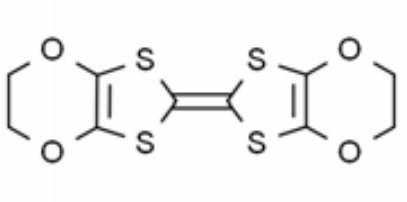

Figure 6-1. Formula of BEDO-TTF.

For such a development, we choose as conducting layer of a BL film a charge-transfer salt containing in its crystalline structure H_2O molecules together with a halogenated ion, like the $(BEDT\text{-}TTF)_xBr_y(H_2O)_n$ salts, with the expectation that the water of the atmosphere might be exchanged reversible with the conducting salt altering the structure and thereby its resistance of the BL film.

Here it should be noted that there have been reported two different conducting crystalline compounds with a $(BEDT\text{-}TTF)_xBr_y(H_2O)_n$ formula: $(BEDT\text{-}TTF)_2Br(H_2O)_3$ [12, 13] and $(BEDT\text{-}TTF)_3Br_2(H_2O)_2$, [14, 15] the latest existing in two polymorphic phases. The crystal lattices of the known salts are given below in Table 6-1.

6.2. Preparation and characterization of humidity sensitive BL films

Preparation and characterization. Humidity sensitive BL films containing a polycrystalline layer of the $(BEDT\text{-}TTF)_xBr_y(H_2O)_n$ salt were prepared using the

previously reported method of the BL film preparation process. Indeed, BL films were prepared from casted films of 10-25 μm thickness containing a solid solution of 2-8% of neutral BEDT-TTF, dispersed in polycarbonate, which were annealed with a $0.5 \cdot 10^{-3}$ M solution of Br_2 in CH_2Cl_2 at 30 °C with a relative humidity of 40 % leading to the formation of the BL films. The resulting BL films were fully characterized by scanning electron microscopy and X-ray powder diffraction and analyzed by energy-dispersive X-ray spectroscopy.

The ratio between S and Br in the BL films was determined by EDX analysis. The S:Br ratio of the conductive layers formed on the surfaces for all BL films shows a high variability ranging from 1:0.081 to 1:0.161. Such values contrast with the theoretically expected ones for the two known salts that are 1:0.063 and 1:0.082 for $(BEDT\text{-}TTF)_2Br(H_2O)_3$ and $(BEDT\text{-}TTF)_3Br_2(H_2O)_2$, respectively. The large variability of S:Br ratio from film to film might be related with the presence of small amounts of Br_2 aggregates on the conducting surface of BL films. Anyhow from the observed S:Br ratios is not possible to determine which is the exact composition of the crystalline phase of the obtained BL films.

The SEM images of the conductive covering layers of BL films revealed slightly different textures for the obtained films showing crystals with two different shapes – plate-like and needle-like – and with sizes varying from 500 nm to 2 μm (Figure 6-2). This result points out the presence of more than one crystalline phase forming the conducting layer of BL films.

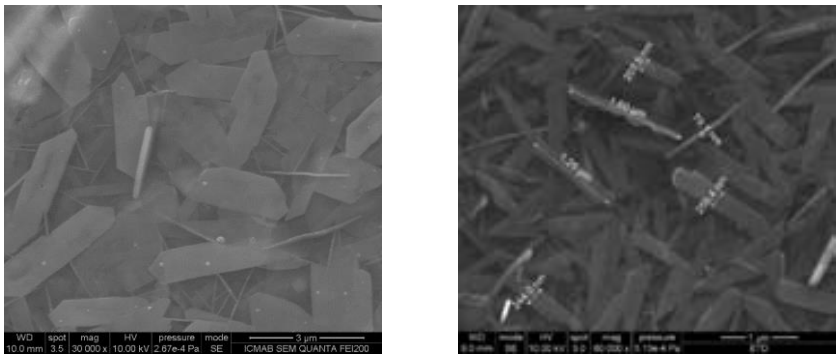

Figure 6-2. Typical SEM images of humidity sensitive BL films.

The powder X-ray diffraction data of all BL films showed two sets of the reflections, marked as 1-5 and I-V in Figure 6-3, corresponding to the (*00l*) reflections of two different crystalline phases oriented on the surface of the polymer matrix with their *ab* crystallographic plane parallel to the film surface (see Figure 6-3 bottom). Indeed the experimentally obtained diffractions can be approximately reproduced by the sum of the oriented crystalline phase $(BEDT\text{-}TTF)_2Br(H_2O)_3$ and $(BEDT\text{-}TTF)_3Br_2(H_2O)_2$ in different proportion with a predominance of the latter one.

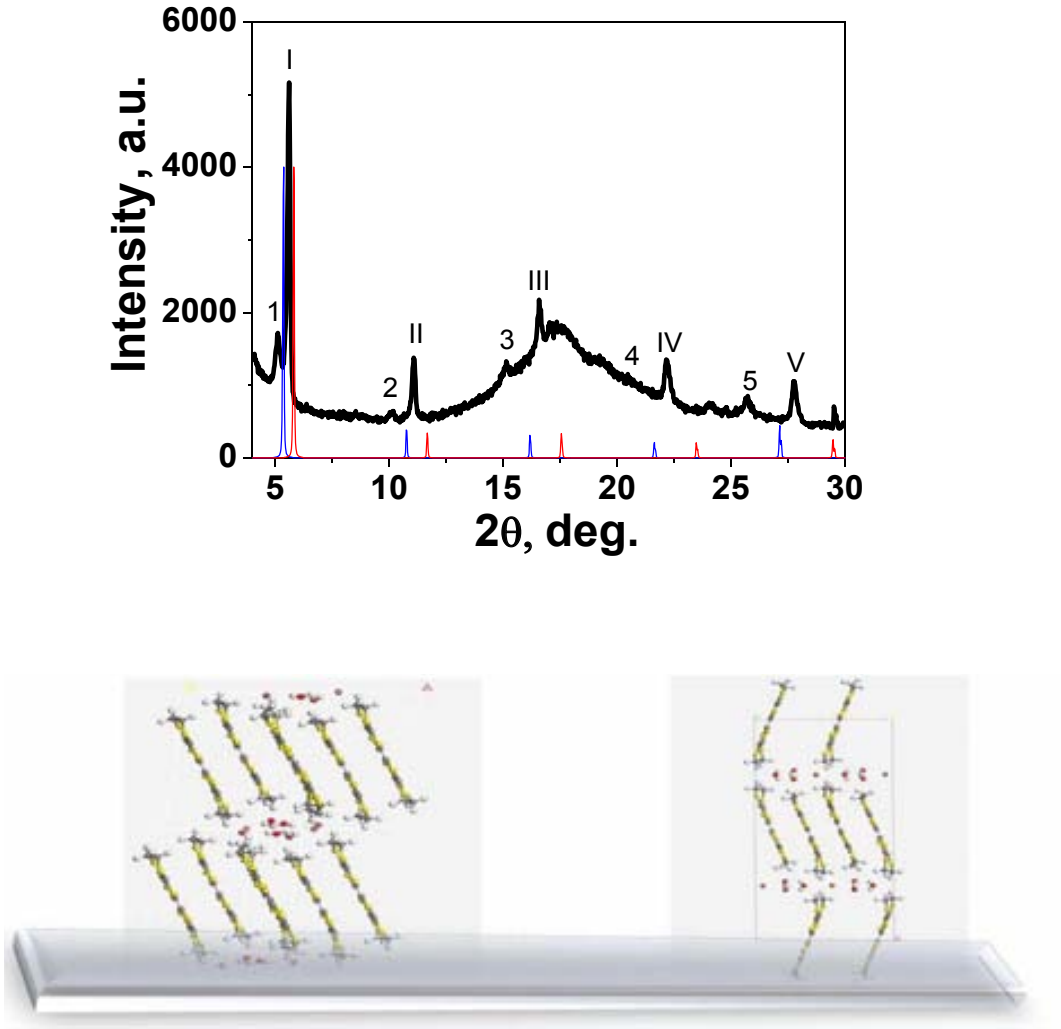

Figure 6-3. Top: X-ray diffraction pattern of a representative BL film (black line). Simulated diffractions using data from the Cambridge Crystallographic Data Center of $(BEDT\text{-}TTF)_3Br_2(H_2O)_2$ (red) and $(BEDT\text{-}TTF)_2Br(H_2O)_3$ (blue) single crystals with. Bottom: Orientation of the two crystalline phases on the polymeric substrate. Left: $(BEDT\text{-}TTF)_3Br_2(H_2O)_2$ and right $(BEDT\text{-}TTF)_2Br(H_2O)_3$, C, S, H and Br atoms are grey, yellow, white and red, respectively.

From the presented data we may suggest that the conducting layer of the BL films are formed by a mixture of two phases with a prevalence of $(BEDT\text{-}TTF)_3Br_2(H_2O)_2$ one both showing certain degree of texture.

X-ray grazing incidence diffraction (GID) technique was also used to characterize the BL films. A 2D-GID image of a representative BL film obtained at the XRD1-ELETTRA synchrotron facility is shown in Figure 6-4. This technique reveals the presence of reflections characterized by ring and arc shapes suggesting the simultaneous presence of crystalline grains randomly oriented together with others of a particular texture.

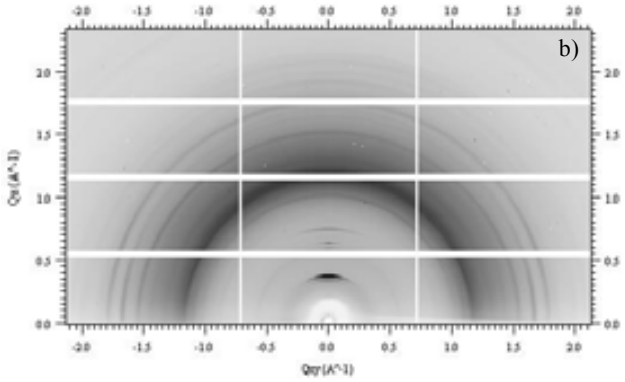

Figure 6-4. The 2D GID image of BL film sample performed at XRD1 at the ELETTRA synchrotron facility.

Table 6-1. Crystallographic data for the known conductive $(BEDT\text{-}TTF)_xBr_y(H_2O)_n$ salts.

Empirical formula	*$(BEDT\text{-}TTF)_3Br_2(H_2O)_2$* *14, 15*	*$(BEDT\text{-}TTF)_2Br(H_2O)_3$* *12, 13*
F_w, g·mol^{-1}	1587	903.26
Crystal system	triclinic	orthorhombic
Space group	*P-1*	*Pcca*
Z	2	4
a, Å	11.225(2)	32.779(4)
b, Å	13.964(3)	6.734(1)
c, Å	16.141(3)	14.993(6)
α, deg	94.48(3)	90
β, deg.	109.01(3)	90
γ, deg	97.08(3)	90
V, Å^3	1345.49	3309(1)
D_{calc} (g cm^{-3})	1.9	1.813

Mechanical and electromechanical properties. We studied the response of the BL films with the $(BEDT\text{-}TTF)_xBr_y(H_2O)_n$ salts to uniaxial stress to provide an overview of their

mechanical and electromechanical properties. For this purpose a tensile test was coupled with two electrical contacts for direct resistance measurements. All tested films showed the classical behavior of rigid plastic materials with values of the elastic limit (ε), the ultimate tensile strength (UTS) and the Young's modulus (E) of 1.0 %, 3.5 GPa and 2.2 GPa, respectively.

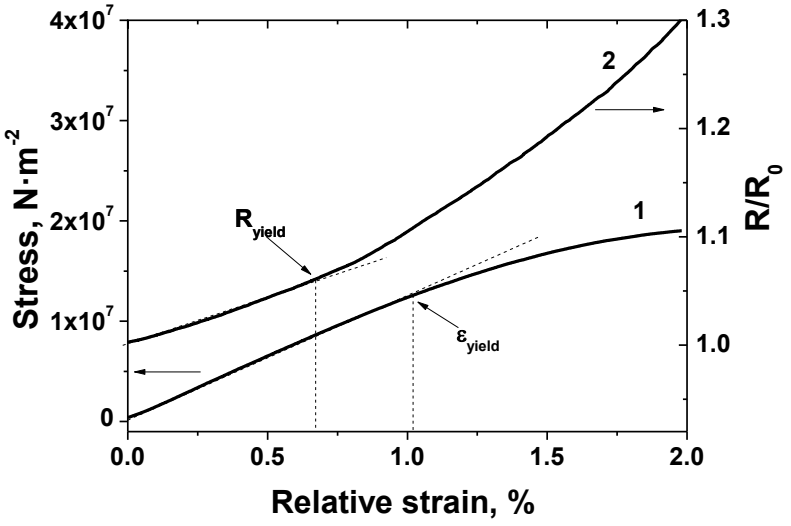

Figure 6-5. Stress-strain (curve1) and resistance-strain (curve 2) dependences of a representative BL film measured in the low-strain region of the tensile test.

A polycarbonate film with thickness similar to the BL films was also tested for comparison showing the following mechanical properties: E=2.05 GPa and ε = 1.4 % highlighting that the covering of a PC film with a layer of crystals did not affect significantly mechanical properties of the latter. Figure 6-5 also shows that the resistance changes with a strain deviate from a linear trend at a value of 0.65 % which is well below the elastic limit of 1.0 %, as also occurs for the BL films with α- and β-(BEDT-TTF)$_2$I$_3$ salts described in Chapter 2.

Electromechanical properties of the BL films were also studied. As shown in Figure 6-6, the electrical responses of the BL films to multi-cyclic monoaxial elongations, carried out in the elastic domain of deformation, were highly reproducibly and depended linearly on the applied strain showing a gauge factor of 6.5±0.5. Although this value is somewhat lower than those found for other piezoresistive BL films, it is still higher than those exhibited by most of conventional metals.

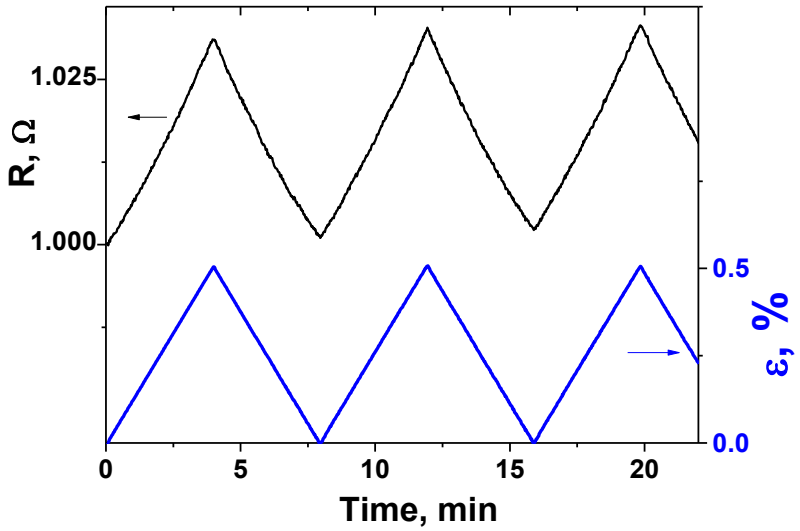

Figure 6-6. Electromechanical response of a representative BL film with the $(BEDT\text{-}TTF)_xBr_y(H_2O)_n$ salt to cyclic monoaxial elongations.

Electrical properties. BL films with $(BEDT\text{-}TTF)_xBr_y(H_2O)_n$ crystallites show a very high sheet resistance of ca. 200 Ω at room temperature being this value the lowest one for all BL films presented in this Thesis. The temperature dependence of the resistance exhibits a metallic behavior in the temperature range of 250-350 K (Figure 6-7) with a TCR value of ca. 0.2 %/deg. At lower temperatures it shows a semiconductor behavior increasing the resistance by factor 1.6 when temperature decrease from 250 to 80 K. Such results are in agreement with the previously reported behaviours of single crystals of $BEDT\text{-}TTF)_2Br(H_2O)_3$ and $(BEDT\text{-}TTF)_3Br_2(H_2O)_2$ which both are metallic down to 150 K and 80 K, respectively. [12, 15] It is remarkable the small TCR value of 0.2 % over room temperature region for practical applications since the small changes in a device containing this BL film could be easily compensated using the Wheatstone bridge configuration.

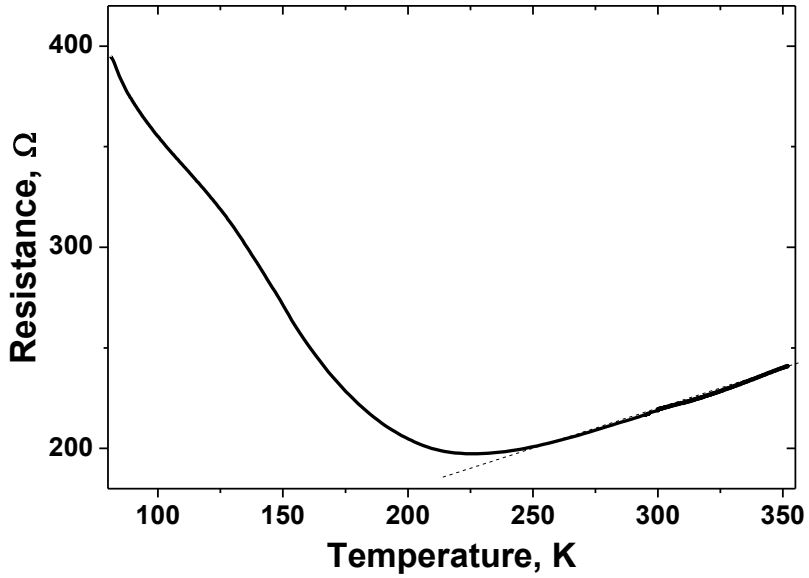

Figure 6-7. Temperature dependence of the electrical resistance of a representative BL film covered with $(BEDT\text{-}TTF)_xBr_y(H_2O)_n$ salt.

Hygroresistive properties of BL films. The sensing capability to humidity of BL films with $(BEDT\text{-}TTF)_xBr_y(H_2O)_n$ were studied in a climate chamber equipped with a Peltier element (Memmert HPP 108). The relative humidity in the climate chamber was measured by a capacitive humidity sensor with an accuracy of 0.5 % and the temperature with a Pt100 sensor in 4-wire circuit with an accuracy of 0.1 °C%. Samples with sizes of 8x8mm were cut from the BL films and fixed with a very small amount of silicon grease on a copper substrate in order to eliminate temperature fluctuations during the measurements of resistance (Figure 6-8). Four graphite contacts were painted on each BL film and connected with 20 µm thick platinum wires to the measurement equipment capable to measure two samples simultaneously.

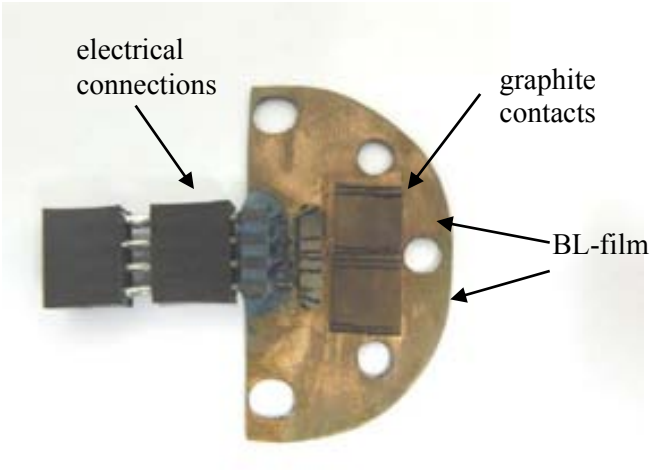

Figure 6-8. Image of the copper support with two samples of BL films for simultaneous measurement of relative humidity changes on the electrical resistance.

Tests for sensing the humidity with BL films were carried out at different temperatures in order to check the temperature influence on the humidity sensitivity of BL films. Measurements were made always with two replicates of each BL film. The electrical response to relative humidity changes increases when rising the temperature (Figure 6-9) as occurs with other polymeric humidity sensors working with a resistance detection principle. [4] The experiments also show that the electrical response of the BL films to RH changes is quite fast and it is completely reversible being dependent on the value of the RH (Figure 6-9). Indeed, the response of a BL film is stable along time (for a couple of hours) at a fixed RH, as it is shown in Figure 6-9 right. The latter result demonstrates that there is any saturation effect on the film response with time at a given RH value. Therefore it suggests that the ambient water molecules cannot be incorporated into the crystalline structure of the sensing layer of BL films since there always is an enormous excess of H_2O molecules in the ambient enough to saturate the crystalline lattice. Thus, another mechanism must be operative.

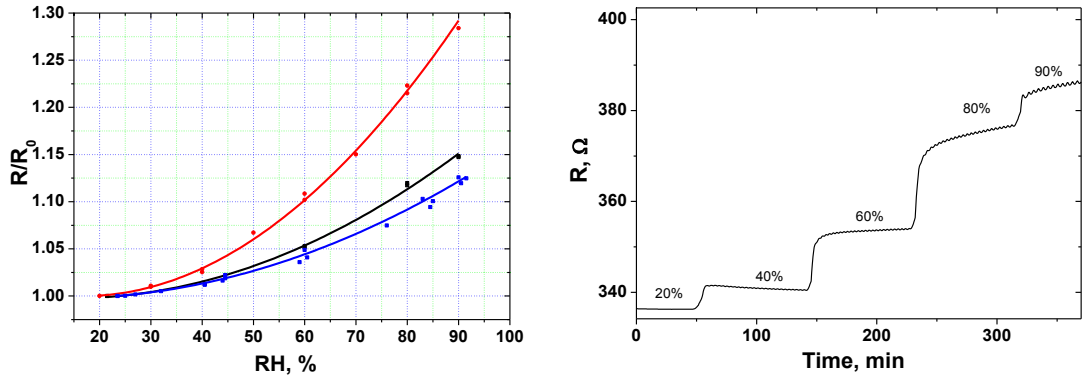

Figure 6-9. Left: Relative humidity dependence of normalized electrical resistance of a representative BL film at different temperatures: 15 °C (blue line), 25 °C (black line) and 40 °C (red line). Right: electrical resistance changes at fixed values of relative humidity of the climate chamber performed at 40 °C.

In order to understand the possible mechanism of the humidity sensing a PXRD study of the BL films at different RH values was performed. The PXRD measurements were carried out on BL samples mounted in a home-made humidity chamber by means of a double-side tape and then installed on the goniometer of the diffractometer. The chamber was also provided with two kapton windows allowing the incident X-ray beam to reach the sample surface and the reflected/diffracted beam the detector.[v] The chamber was also equipped with a commercial hygrometer probe and connected to a gas tube, through which a flow of a nitrogen was seeped, in order to reach a constant RH value. Using the nitrogen flux it was not possible to reach a RH value higher than 82 %. So, for higher RH values we used a saturated solution of $BaCl_2$ in water that permits to achieve a 95 % of RH inside of the chamber keeping it constant for more than 20 hours

This setup allowed to monitor the evolution of PXRD peaks during the RH variation. We first recorded the changes in a wide 2θ range (3-40 deg) in order to choose the most suitable reflections for this study and then, a smaller angular range (2θ from 4 to 6 deg) was used to investigate the changes produced by the humidity. Finally, we choose the most intense reflections of the two crystalline phases presented in the conducting layer of BL film for preparing this study (Figure 6-10).

[v] This part of work was performed in collaboration with Dr. Silvia Milita, Dr. Fabiola Liscio and Laura Ferlauto (CNR-IMM Sezione di Bologna), Bologna, Italy

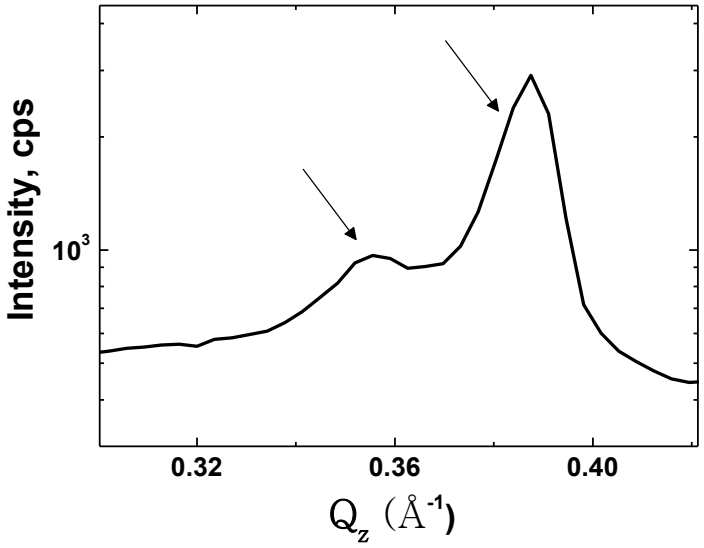

Figure 6-10. X-ray diffraction of BL film in a narrow 2Θ range. Q_z was calculated using the Bragg's law; i.e., $Q_z = (4\pi/\lambda) \sin\theta$, where λ is the used X-ray radiation wavelength.

The X-ray measurements showed that an increase of the RH in the range 10 - 80 % (Figure 6-11) affects the position of the first (left) peak, which progressively increases its intensity and shifts towards smaller Q_z values, while the position and intensity of the second peak remains unchanged.

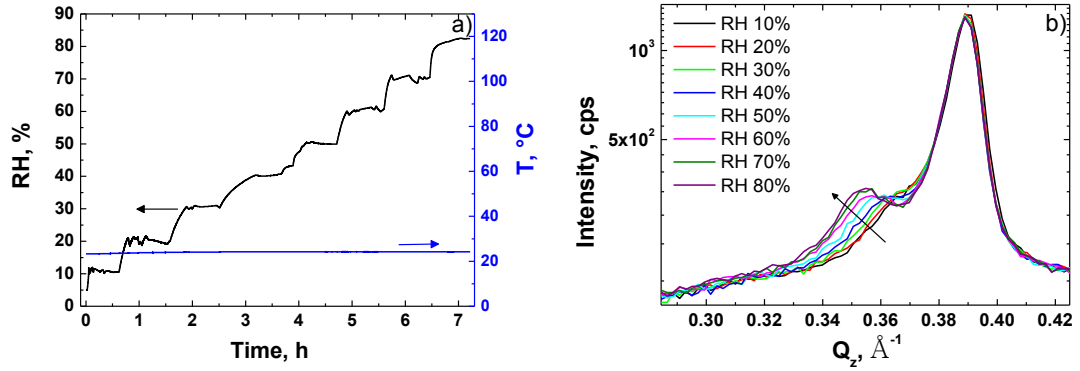

Figure 6-11. Evolution of the selected reflections during the increasing of RH% from 10% to 80% at constant temperature of 25 °C following the RH ramp used during the experiment (left).

Similar changes occur when the humidity increases from 43 % up to 95 % as it shown in Figure 6-12.

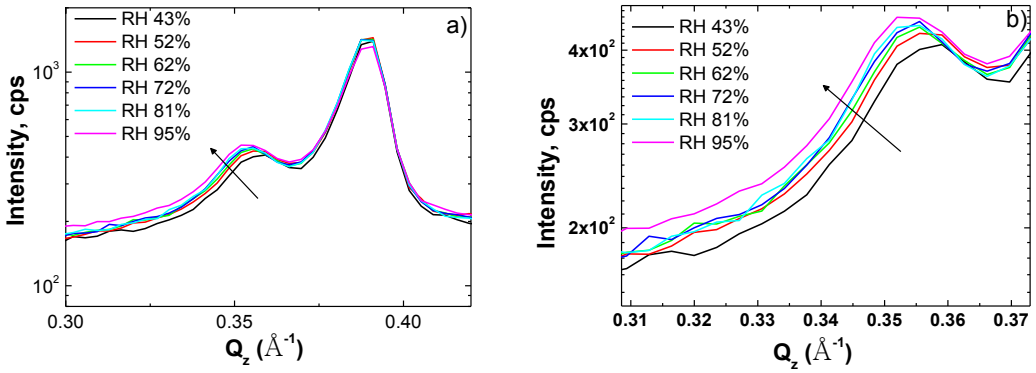

Figure 6-12. a) Set of PXRD of BL film with $(BEDT\text{-}TTF)_xBr_y(H_2O)_n$ crystallites recorded during the increasing of the relative humidity inside the chamber and b) zoom of the first (left) peak.

The first peak returns to the initial position when the humidity decreases down to 10 % (Figure 6-13). Such changes confirm that the shift of the first peak is completely reversible and it is produced by the humidity changes resulting in some tiny change on its crystal structure. It also demonstrates that apparently only one of the two crystalline phases, the $(BEDT\text{-}TTF)_2Br(H_2O)_3$, of the BL film is sensitive to the relative humidity variation.

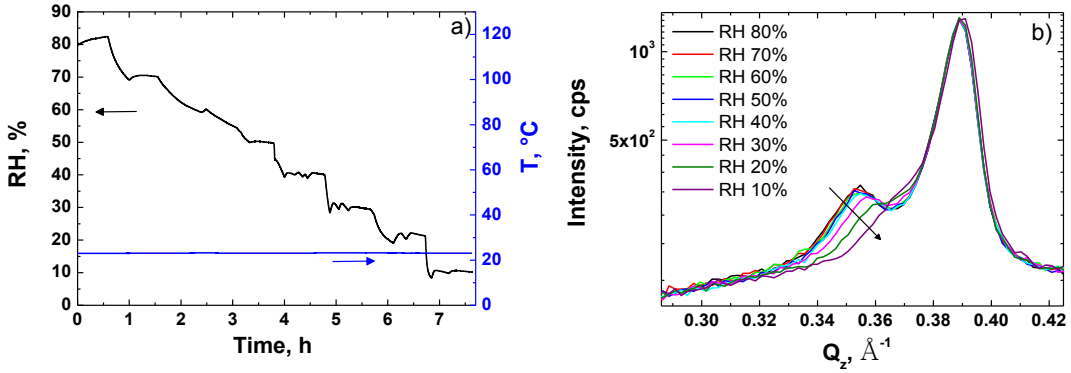

Figure 6-13. Evolution of the selected reflections during the decreasing of RH% from 80% to 10% at constant temperature of 25 °C following the RH ramp used during the experiment (left).

Moreover, the shift in the position of the first peak centered at $Q_z \approx 0.355$ Å^{-1}, indicates an expansion of the d-spacing of the $(BEDT\text{-}TTF)_2Br(H_2O)_3$ crystallites in the direction perpendicular to the BL film surface with an increase of relative humidity being this shift linear as shown in Figure 6-14.

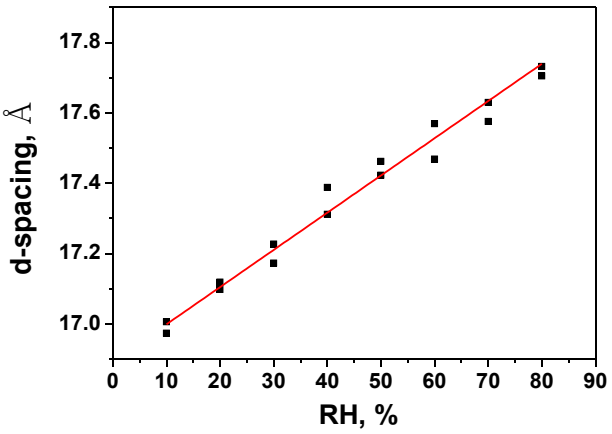

Figure 6-14. The d-spacing of the RH sensitive crystalline phase vs relative resistance.

On the other hand, the slight increase of the intensity of such peak suggests a slight increase of the crystalline ordering. A possible explanation of both observations could be associated with the physisorption of the water on the surface of such crystallites providing layers of adsorbed water of different thickness depending on the RH value. Such layers of water could have influence by their dipolar interactions with the Br^- anions on the crystal structure expanding the d-spacing of the crystals (Figure 6-15). We do not believe that the ambient water penetrate inside the crystalline lattice since in this case a saturation of the signal would be observed with time at a constant humidity.

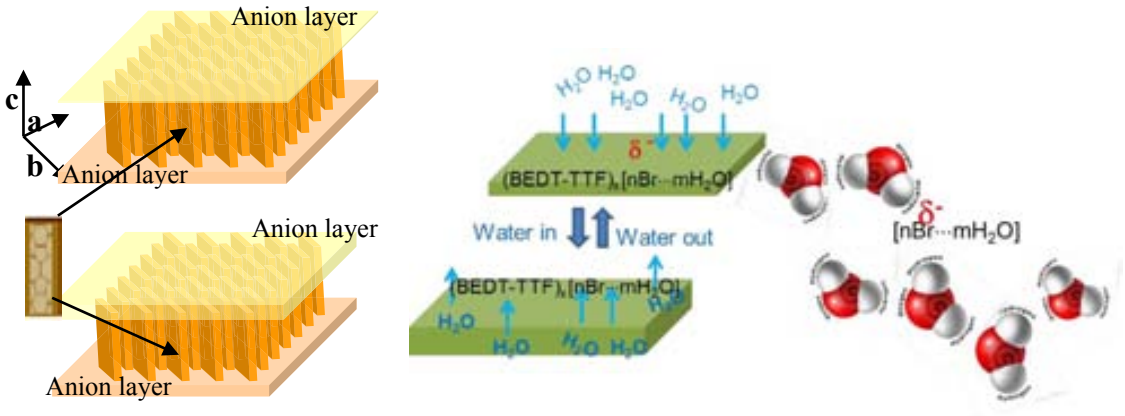

Figure 6-15. Schematic representation of possible interaction between the conducting layer of the BL film and dipoles of atmospheric water.

In order to understand if the sensing capability is an exclusive property of the BL film with $(BEDT\text{-}TTF)_xBr_y(H_2O)_n$ salt, the humidity tests were also carried out with other conductive BL films based on salts derived from BEDT-TTF (Figure 6-16). Such

experiments showed that only the BL films containing salts with Br^- anions exhibit some capability to sense the changes of RH while those with I^- anion do not show any sensitivity. It is interesting to compare the sensing of the BL films based on (BEDT-TTF)$_x$Br$_y$(H$_2$O)$_n$ with that of previously reported one, based on the (BEDO-TTF)$_2$Br(H$_2$O)$_3$ salt. The developed BL film is three times more sensitive to RH in comparison with the reported in Ref. [11] as shown in Figure 6-16. All these results demonstrate that the RH sensitivity of BL films strongly depends on the nature of molecular conductors that forms a conducting layer of BL film and that the presence of bromine anions play an important role.

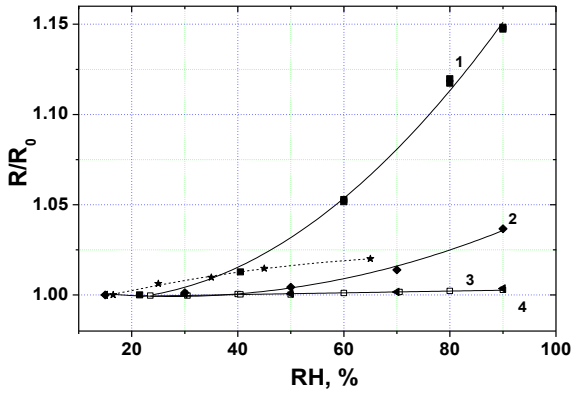

Figure 6-16. Humidity dependence of the normalized electrical resistances at 25 °C for the BL films with: 1) (BEDT-TTF)$_x$Br$_y$(H$_2$O)$_n$; 2) α´-(BEDT-TTF)$_2$I$_y$Br$_{(3-x)}$; 3) α-(BEDT-TTF)$_2$I$_3$ and 4) β-(BEDT-TTF)$_2$I$_3$. Dashed line – BL film with (BEDO-TTF)$_2$Br(H$_2$O)$_3$ from Ref. [11].

According to the published data for the BL film with (BEDO-TTF)$_2$Br(H$_2$O)$_3$, the changes in the electrical resistance are related with the adsorption of water molecules on the conducting surface of the BL film. Such BL films exhibit a different sensitivity to humidity in the region of RH from 2 to 10 %, where the electrical resistance increases by 80 %, than in the region from 20 to 60 % where such change is only of 2 %. Authors related such a large difference to the fact that hydrated BEDO-TTF complex with bromine forms distinctly different crystal structures at relative humidity below 5.4% and above 8.6%. In order to check if something similar occurs in our BL films we performed experiments in drier conditions for the BL films with (BEDT-TTF)$_x$Br$_y$(H$_2$O)$_n$ crystallites.[vi] The results are shown in Figure 6-17, revealing that changes in the resistance are much smaller in a dry atmosphere than it was reported for

[vi] This part of work was performed in collaboration with Prof. Ryszard C Jachwicz and Dr. Jerzy Weremczuk from Warsaw University of Technology, Poland.

$(BEDO\text{-}TTF)_2Br(H_2O)_3$ crystals. Such measurements also reveal that below a RH of 5 % the resistance increases when RH decreases while at RH higher than 5 % the resistance decreases. The behavior in the drier region can be related to the lose of some molecules of water from the crystalline lattice of $(BEDT\text{-}TTF)_xBr_y(H_2O)_n$ that may lead to a new phase with an increase in its electrical resistance.

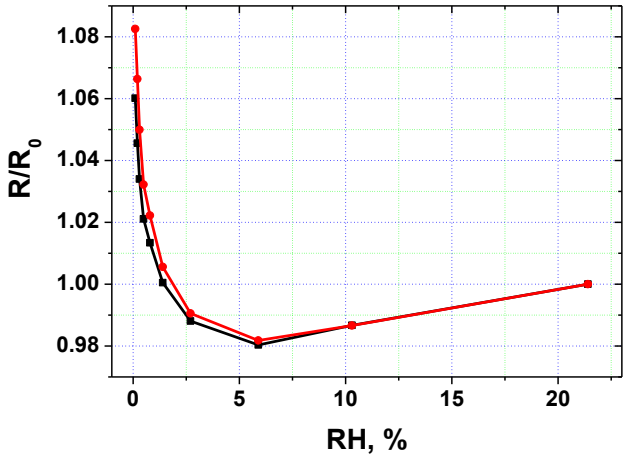

Figure 6-17. Humidity dependence of normalized electrical resistance at 25 °C for two representative BL films with $(BEDT\text{-}TTF)_xBr_y(H_2O)_n$ crystallites.

6.3. Hygroresistive BL films based on $TTF_{11}I_8$ salt

The BL film with $TTF_{11}I_8$ crystallites reported in Chapter 3 also exhibit hygroresistive properties. For this reason we studied in detail such BL films (**F3-1**, **F3-2** and **F3-3**) using the same X-ray setup.

It was found that the dependence of resistance with the relative humidity was not the same for all the BL films that were made with different polymeric matrices. Thus, the resistance dependence of **F3-1** with a PC matrix changes linearly in the humidity range from 20 to 90 % increasing by 5% when relative humidity achieves 90% (Figure 6-18). A similar behavior was also found for BL film **F3-2** with PC matrix contained larger amount of the conducting salt. By contrast, the BL film **F3-3** with a CPA matrix shows an exponential dependence on humidity. It was found that the film resistance increases by 7.5% and 12.5%, when RH changes from 20 to 60% and to 90%, respectively (Figure 6-19). In these BL films the changes of electrical resistance were reversible and after decreasing the relative humidity the resistance practically recover its initial value.

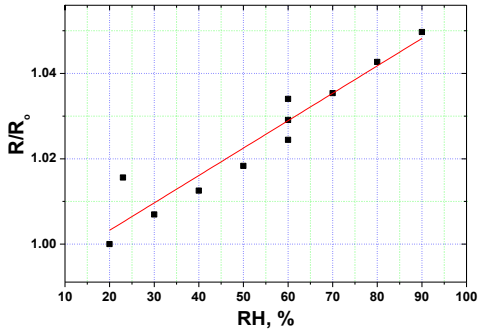

Figure 6-18. Dependence of the normalized resistance on the relative humidity of BL film F3-1 with polycarbonate matrix.

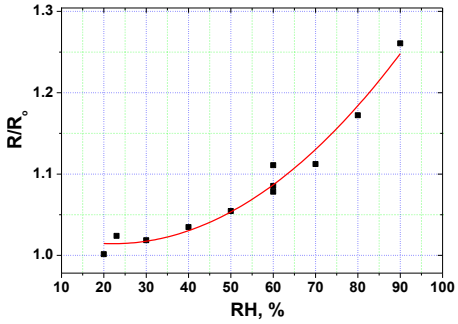

Figure 6-19. Dependence of the normalized resistance on the relative humidity of BL film F3-3 with cellulose acetate propionate matrix.

In order to understand the mechanism involved in the resistance changes produced by the humidity we also performed X-ray experiments under a controlled atmosphere for BL films **F3-1** and **F3-3**.

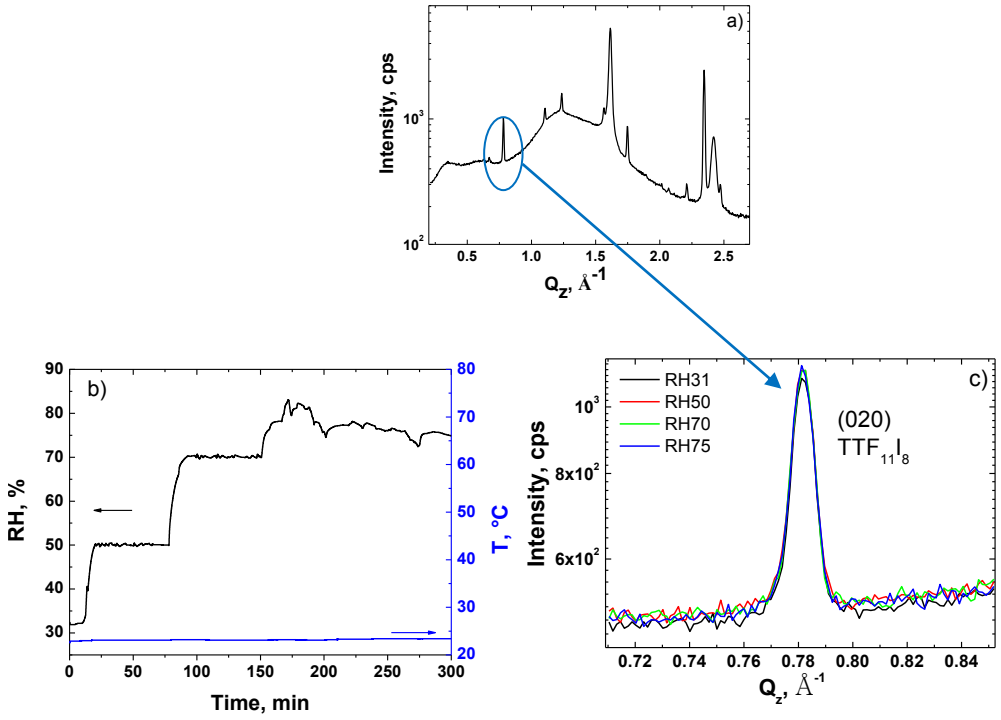

Figure 6-20. Wide range of θ/2θ scan of BL films F3-1 (a); Evolution of the selected reflection during RH% increasing at a constant temperature of 25 °C (c) following the RH ramp depicted in (b).

The obtained results are depicted in Figure 6-20 -Figure 6-22 for BL films **F3-1**, **F3-2** and **F3-3**, respectively. These measurements show that no significant changes in the position nor in the intensity of the different peaks were observed for any of the studied BL films.

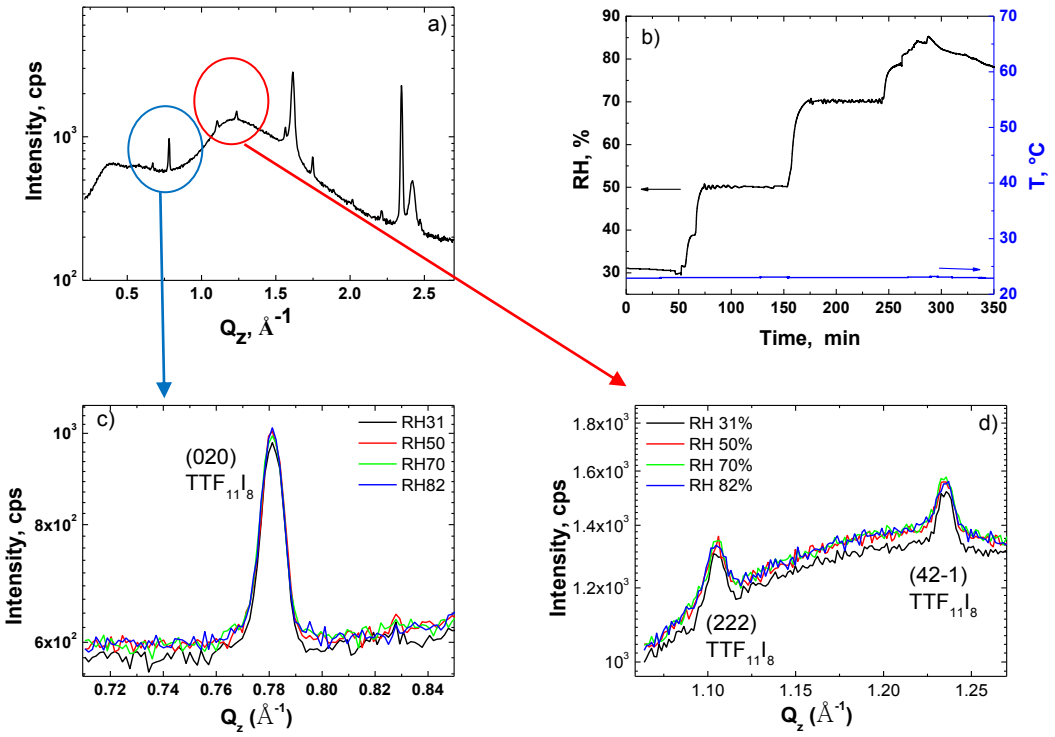

Figure 6-21. Wide range of θ/2θ scan of BL films F3-2 (a); Evolution of the selected reflections during RH% increasing at a constant temperature of 25 °C (c and d) following the RH ramp depicted in (b).

Based on these data, it can be assumed that even at the high levels of RH, water molecules are not able to penetrate inside of the crystalline structures of the conducting layers and changes are related with a physisorption of water layers on the surface of the BL films. This could explain the observed differences of the BL films made with CPA and PC matrices since the first one is more hygroscopic and, consequently, adsorbs water easier than a polycarbonate matrix.

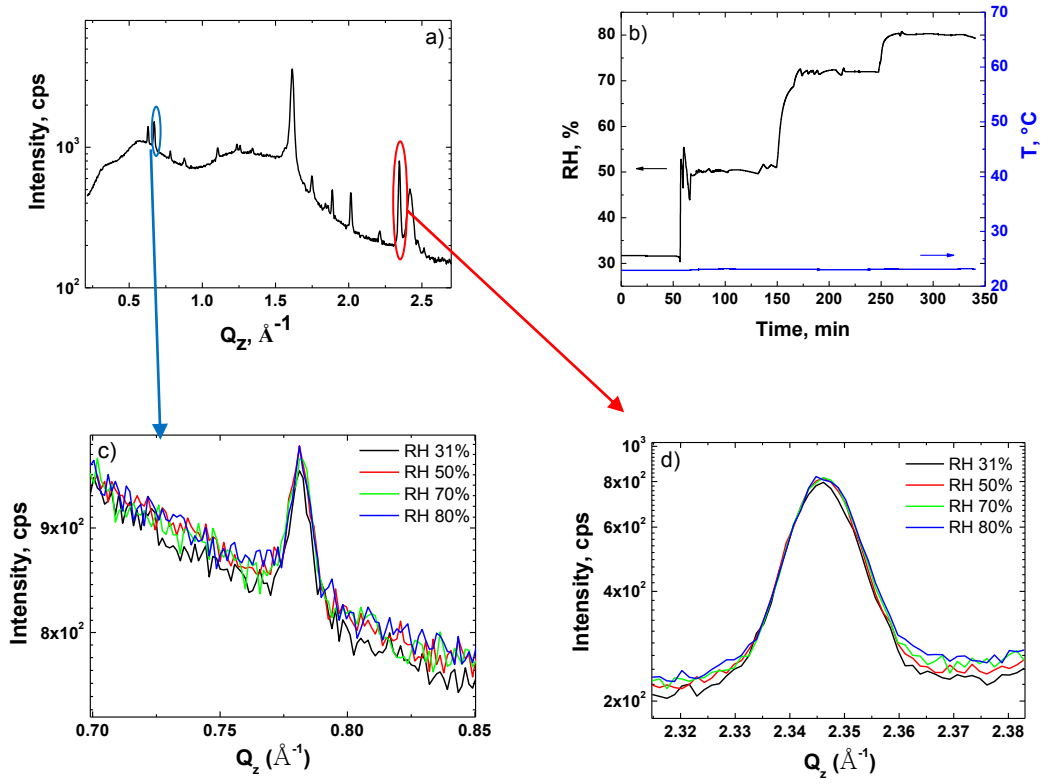

Figure 6-22. Wide range of θ/2θ scan of BL films F3-2 (a); Evolution of the selected reflections during RH% increasing at a constant temperature of 25 °C (c and d) following the RH ramp depicted in (b).

Consequently we can conclude that the electrical response of sensing BL films to humidity is related to the physical adsorption of water molecules on the surface of the BL films. At low RH values, water molecules are primarily physisorbed onto the available active sites of the film surface through hydrogen bonds, forming what is called physisorbed layer of water. In this regime, the water molecules are unable to move freely because of the restriction from hydrogen bonds. As the RH increases, a multilayer physical adsorption of water molecules occurs and the water molecules become mobile and progressively more identical to those in the bulk liquid. As the multilayer adsorption further progress, the physisorbed water can produce an electrostatic field on the counteranions that perturb the crystalline structure of the salt changing its resistance.

6.4. Conclusions

The hygroresistive BL films covered by a mixture of crystalline $(BEDT\text{-}TTF)_2Br(H_2O)_3$ and $(BEDT\text{-}TTF)_3Br_2(H_2O)_2$ salts show a reversible and reproducible electrical resistance variations according to the relative humidity being highly sensitive to small changes of RH. It was also found that other BL films containing conducting $TTF_{11}I_8$ salt are also sensitive to RH changes and in this case the sensitivity shows a strong dependence on the polymeric matrix used for BL film preparation. The sensitivity to humidity of all these BL films seems to be a result of the physisorption of water in their surfaces that perturb their crystal structures of their active sensing layers. Both types of BL films are highly promising for practical applications. However, the use of the BL films with $(BEDT\text{-}TTF)_xBr_y(H_2O)_n$ crystallites is more promising due to its lower TCR value and higher long term stability.

Bibliography

1. B. M. Kulwicki, Humidity sensors, Journal of the American Ceramic Society, 1991, 74, 697-708.
2. V. Matko and D. Donlagic, Sensor for high-air-humidity measurement, Sensors and Actuators a-Physical, 1997, 61, 331-334.
3. J. Feng, L. Peng, C. Wu, X. Sun, S. Hu, C. Lin, J. Dai, J. Yang and Y. Xie, Giant Moisture Responsiveness of VS2 Ultrathin Nanosheets for Novel Touchless Positioning Interface, Advanced Materials, 2012, 24, 1969-1974.
4. Z. Chen and C. Lu, Humidity sensors: A review of materials and mechanisms, Sensor Letters, 2005, 3, 274-295.
5. N. Yamazoe and Y. Shimizu, Humidity sensors – principles and applications, Sensors and Actuators, 1986, 10, 379-398.
6. F. W. Dunmore, An electric hygrometer and its application to radio meteorography, Journal of Research of the National Bureau of Standards, 1938, 20, 723-744.
7. H. Kitagawa, Li-Te and Ca-Te thin-film junctions as humidity sensors, Sensors and Actuators, 1989, 16, 369-378.
8. S. Mukode and H. Futata, A semiconductive humidity sensor, Sensors and Actuators, 1989, 16, 1-11.
9. Y. Sakai, Y. Sadaoka, M. Matsuguchi, Y. Kanakura and M. Tamura, A humidity sensor using polytetrafluoroethylene-graft-quaternized-polyvinylpyridine, Journal of the Electrochemical Society, 1991, 138, 2474-2478.
10. S. Tsuchitani, T. Sugawara, N. Kinjo, S. Ohara and T. Tsunoda, A humidity sensor using ioniv copolymer and its application to a humidity temperature sensor module, Sensors and Actuators, 1988, 15, 375-386.
11. T. Haneda, A. Tracz, G. Saito and H. Yamochi, Continuous and discontinuous water release/intake of $(BEDO\text{-}TTF)_2Br(H_2O)_3$ micro-crystals embedded in polymer film, Journal of Materials Chemistry, 2011, 21, 1621-1626.
12. M. Y. Luo, T. Ishida, A. Kobayashi and T. Nogami, Electrical conductivities and crystal and band-electronic structures of a new phase of BEDT-TTF-bromide salt, $(BEDT\text{-}TTF)_2Br(H_2O)_3$, Synthetic Metals, 1998, 96, 97-102.
13. Q. C. Zhang, P. J. Wu, Y. Li and D. B. Zhu, Synthesis, structure and physical properties of ET_2Br center dot $3H_2O$, Synthetic Metals, 1998, 98, 129-133.
14. H. Urayama, G. Saito, T. Sugano, M. Kinoshita, A. Kawamoto and J. Tanaka, Preparation, structure, and physical properties of an organic conductor, $(BEDT\text{-}TTF)_3Br_2(H_2O)_2$, Synthetic Metals, 1988, 27, A401-A406.
15. S. S. Khasanov, L. V. Zorina, R. P. Shibaeva, S. I. Pesotskii, M. V. Kartsovnik, L. F. Veiros and E. Canadell, Molecular conductors based on radical cation hydrated halides: new crystal phase of the $(BEDT\text{-}TTF)_3Br_2 \cdot 2H_2O$ organic metal, Synthetic Metals, 2002, 131, 41-48.

Chapter 7

Developing processes for transfer the conducting layer of bi-layer materials to sculpted substrates

7.1 Introduction

The purpose of this Chapter is to show how the functional crystalline layers of BL films can be transferred under soft conditions to target substrates of different shapes and nature. Such transfer processes may yield novel composite materials enable further applications of the conducting crystalline layers. Indeed, a large number of articles and patents have been recently published showing that different conducting layer-transfer methods are widely used for obtaining several types of electronic products. To date, in many cases the transfer conducting inorganic layers to various substrates has been achieved using a polymer coating as a temporary rigid support. [1-4] Unfortunately, in many cases these methods have the disadvantage of using numerous steps to achieve the layer transfer. On the other hand the poor adhesion of transferred conductive inorganic materials to polymers limits the range of potential applications of such layered structures. [5, 6] As a result, there exists a growing interest in making devices based on flexible sculpted materials that contain a thin layer of an organic conductor. Unfortunately, the method for preparing BL films developed in our group is not appropriate to cover large substrates with variable (sculpted) shapes and compositions. For example, it is very difficult to disperse homogeneously BEDT-TTF molecules into silk-based materials prior to the oxidation due to either solvent incompatibilities or the tendencies of BEDT-TTF molecules to crystallize on the silk prior to the oxidation process. Also it is difficult to prepare thin layer of described BEDT-TTF-based molecular conductors on sculpted substrates.

Here we report a couple of methods for transferring the active layer of piezoresistive BL films containing α- and β-phases of $(BEDT\text{-}TTF)_2I_3$ on polycarbonate to a film made of Bombyx mori silk substrate.[vii] In addition to silk substrates, these layer transfer methods can also be applied for other target substrates made of rubber, silica, glass, plastic products, and paper with various shapes and geometries. The resulting composite materials exhibit the original piezoresistive properties of the pristine BL films demonstrating that the transfer layer methods do not change too much the structure of the transferred conducting crystalline layers

[vii] These experiments were carried out in collaboration with Professor J.S. Brooks and Dr. E. Steven at National High Magnetic Fields Laboratory (NHMFL), Tallahassee, USA.

7.2 Results and discussion

To cover different substrates with $(BEDT\text{-}TTF)_2I_3$ active layers of α- and β-phases, we have developed two different procedures (Figure 7-1) that allow the transfer of conducting layers from BL films to receiving substrates.

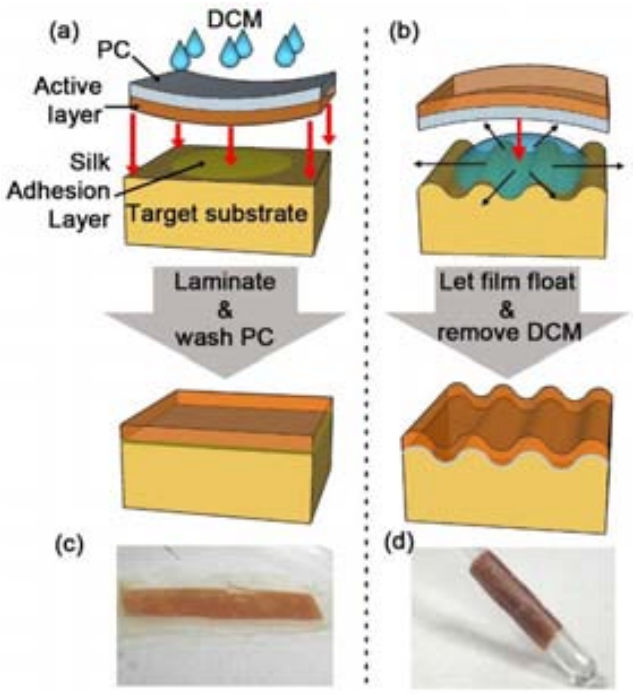

Figure 7-1. Schemes of the two developed layer transfer methods: face-down (a) and face-up (b). Photographs of the transferred layers of α-$(BEDT\text{-}TTF)_2I_3$ crystals to a silk film via the face-down method (c) and to a glass tube of ∅ 3 mm via the face-up method (d).

The first procedure, named hereafter as the "face-down layer transfer method", where the conducting layer face of the pristine BL film is oriented down towards the receiver substrate, is most suitable for covering flat substrates (Figure 7-1 c). The second procedure, named as the "face-up layer transfer method", where the conducting layer is faced up with respect the receiver substrate, is more universal since it allows the covering of sculpted substrates (Figure 7-1 d). In both cases, the transfer involves the separation of the conducting layer from the parent polycarbonate substrate by dissolving the PC layer using small amounts of CH_2Cl_2.

7.2.1. Face-down layer transfer method

The face-down approach was developed using as a receiver surface a Bombyx mori silk films since this material is considered ideal for implantable devices. [78] The silk film was prepared via drop casting of a ~ 8 % (wt/vol) solution of silk fibers in water on a

polystyrene dish. [9] The silk fibers solution was previously obtained by extraction from raw Bombyx mori cocoons (purchased from Aurora Silk) using a 0.02 M Na_2CO_3 solution, followed by dissolving the fibers in a 9.3 M LiBr solution, purification by dialysis (Slide-A-Lyzer G-2 dialysis cassette, 3500 MWCO), and low temperature centrifugation. [10] This solution was drop casted and the resulting film annealed with water for 24 hours at 50 mbar to make it insoluble in water. [11] Then, a fresh Bombyx mori silk solution is deposited on the silk film to act as an adhesive layer. The BL films were laminated onto the wet silk surface by putting the conductive crystalline layer of the BL film face down on the silk substrate. To remove the polycarbonate layer, it was washed with a CH_2Cl_2 solution at an angle to allow the solvent containing the dissolved PC to flow away. The complete removal of PC layer can be checked by either measuring the electrical resistance of the transferred layer or through an observation under an optical microscope (Figure 7-2).

Figure 7-2. Photo images showing the gradual removal of the polycarbonate substrate of the pristine BL film by washing with CH_2Cl_2. The the images were obtained using an optical microscope.

Morphology of the transferred layers. The face-down layer transfer method allowed us for the first time to study the texture of the reverse side of the conductive α-(BEDT-TTF)$_2I_3$ layer of BL films formed at the interface with the PC film. Surface analysis was performed using a SEM with an EDX technique. As presented in Figure 7-3 a, we

observed a small number of crystallite aggregates (zone *b*) together with a large smooth area (zone *a*).

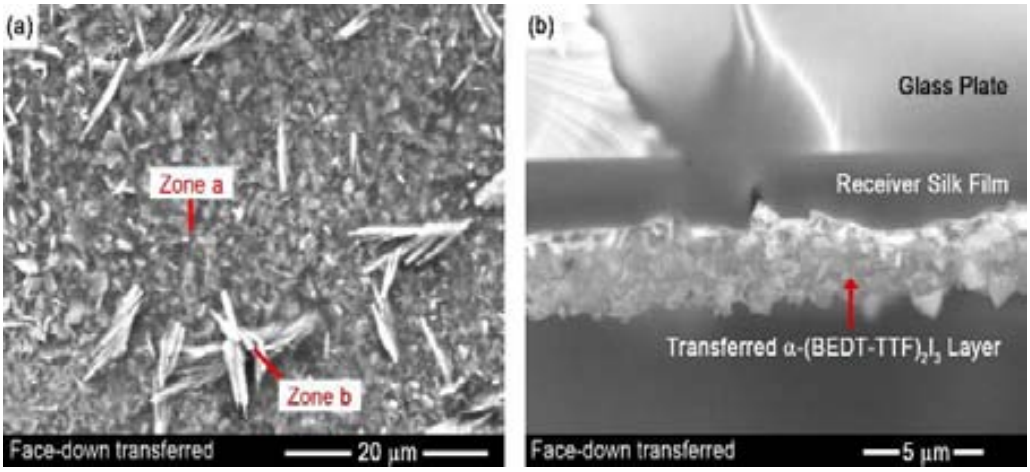

Figure 7-3. SEM images of face-down transferred layer of α-(BEDT-TTF)$_2$I$_3$ crystallites. (a) Surface and (b) cross-section profile of a silk/α-(BEDT-TTF)$_2$I$_3$ bi-layer in which the silk film was cast on a glass slide. The surface profile reveals the back side arrangement of the conductive α-(BEDT-TTF)$_2$I$_3$ crystals initially formed on the parent PC film. Zones a and b correspond to the reacted and un-reacted BEDT-TTF molecules, respectively, during the annealing process.

Using EDX analysis the I:S atomic ratio of zone *a* was found to be 18:82 that corresponds to an average composition (BEDT-TTF)$_2$I$_{3.5}$ that is in reasonable agreement with the expected stoichiometric formula of the α-(BEDT-TTF)$_2$I$_3$ phase. In contrast, the zone *b* contains a very small amount of iodine since the I:S ratio was found as 1.5:98.5. This suggests that during the BL film preparation process, [11-13] unreacted neutral BEDT-TTF molecules crystallize on the back side of the conductive layer.

Electromechanical and electrical properties of the transferred layers. The α- and β-(BEDT-TTF)$_2$I$_3$ layers before and after the layer transfer process were examined by four probe direct current resistance measurements. As shown in Figure 7-4, both the original and the transferred α- and β-(BEDT-TTF)$_2$I$_3$ layers exhibit similar temperature behaviors of their resistances. It should be noted that in comparison with the original α-(BEDT-TTF)$_2$I$_3$ crystalline layer of the pristine BL film, the transferred layer exhibits a slightly broader semimetal-to-insulator transition.

Strain measurements were also performed at a strain rate of 0.3 μm/s with the transferred α-(BEDT-TTF)$_2$I$_3$ layer on a silk film (Figure 7-4 c). Such measurements show a reversible linear response to strain with a gauge factor of 9, which is in a good agreement with the reported value for pristine BL films with α-(BEDT-TTF)$_2$I$_3$

crystallites on polycarbonate (see Chapter 2 of the Thesis). This outcome demonstrates that this layer transfer method leads to similar electromechanical properties of the novel composite material as the original one.

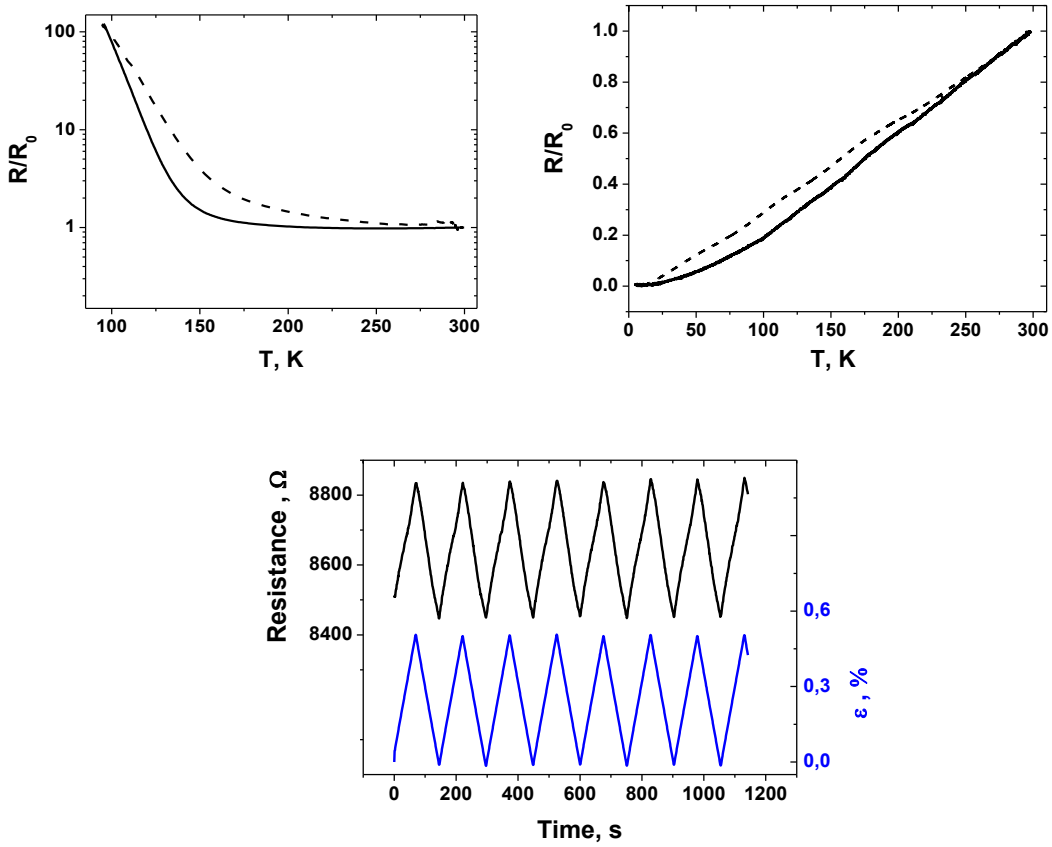

Figure 7-4 Electrical and electromechanical properties of the face-down transferred crystalline layers on a silk film. Temperature dependence of the normalized resistance of the original and transferred layers of (a) α- and (b) β-(BEDT-TTF)$_2$I$_3$ crystals (c). Resistance changes of the transferred α-(BEDT-TTF)$_2$I$_3$ layer on a silk film upon several cycles of monoaxial elongation.

7.2.2. Face-up layer transfer method

For applications requiring the covering of sculpted substrates, an alternative method was developed. In this method the topmost conductive (BEDT-TTF)$_2$I$_3$ layer of a BL film was faced up with respect the receiver substrate. Whereas the face-down layer transfer relies on the effectiveness of mechanical lamination, the face-up layer transfer is based on the thinning and swelling of the underlying PC layer resulting in an active layer that naturally adapts to the shape of the target substrate. In this case, unlike the face-down layer transfer where the PC is completely removed, the face-up layer transfer requires a thin PC-based under-layer to maintain the integrity of the transferred conducting (BEDT-TTF)$_2$I$_3$ layer

and for the adhesion to the target substrate. The general approach of the face-up layer transfer is outlined in the following steps (see Figure 7-5): (i) A pool of DCM is deposited on a target substrate; (ii) the BL film is placed on the surface of the pool with the PC support facing down and the conducting side of the BL film facing up; (iii) after the BL film floats and softens for some seconds, the DCM-based pool is removed using an absorbent; (iv) the conductive sensing $(BEDT\text{-}TTF)_2I_3$ layer then conforms to the surface geometry of the target substrate.

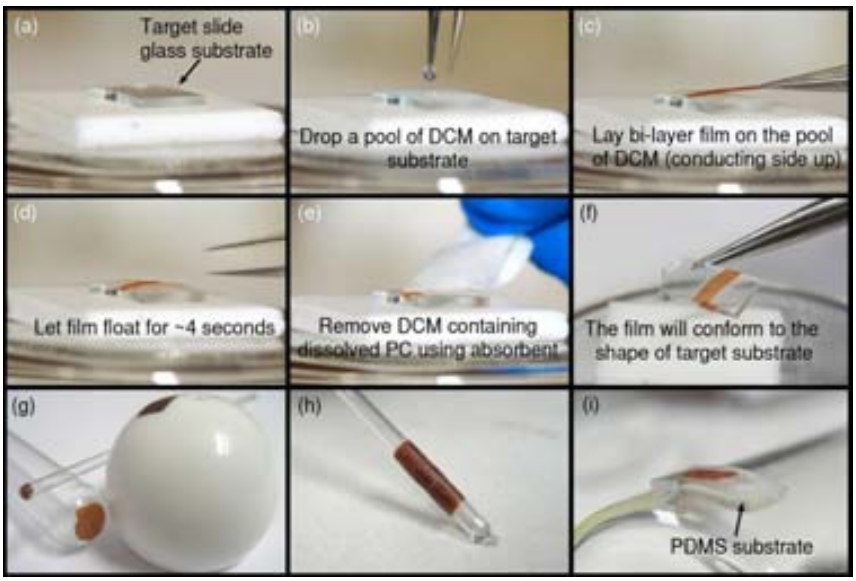

Figure 7-5. Outline of the transfer process stages of the face-up method for the α-$(BEDT\text{-}TTF)_2I_3$ conducting layer. Target substrates different in their narure and shapes were used (g-i).

The SEM images (Figure 7-6) of the crystalline transferred layers demonstrates that minimal cracking occurs after the transfer process.

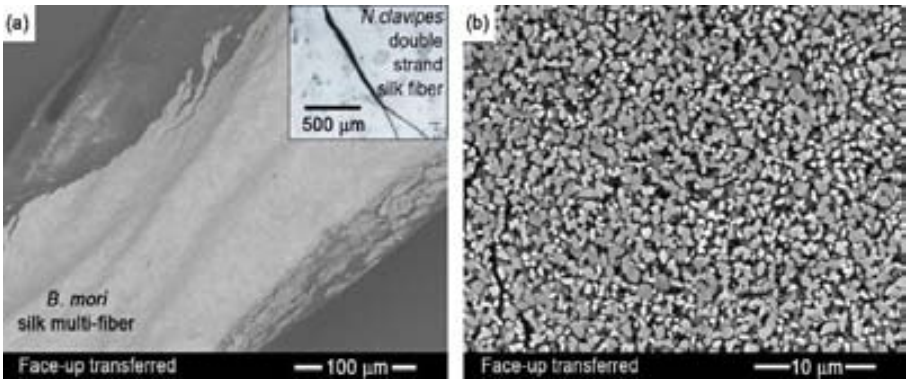

Figure 7-6. SEM images of the face-up transferred α-$(BEDT\text{-}TTF)_2I_3$ layer. (a) Low and high (b) magnification images of the face-up transferred layer on a Bombyx mori silk multi-fiber. Inset in (a) corresponds to an image of double-strand dragline silk fibers.

7.3 Conclusions

To the best of our knowledge the obtained results give the first demonstration of the capability to cover substrates of different compositions and shapes with flexible conductive sensing layers of molecular conductors since the layer transfer processes do not significantly change the electrical and electromechanical properties of the polycrystalline layers of the $(BEDT\text{-}TTF)_2I_3$ conductors that are initially formed on the pristine polycarbonate substrate of BL films. Thus both methods open the possibility to engineer conductive substrates that can be incorporated into various electronic devices.

Bibliography

1. X. Huang, S. Huang, Q. Zhang, X. Guo, D. Li, Y. Luo, Q. Shen, T. Toyoda and Q. Meng, A flexible photoelectrode for CdS/CdSe quantum dot-sensitized solar cells (QDSSCs), Chemical Communications, 2011, 47, 2664-2666.

2. Y. Wang, S. W. Tong, X. F. Xu, B. Oezyilmaz and K. P. Loh, Interface Engineering of Layer-by-Layer Stacked Graphene Anodes for High-Performance Organic Solar Cells, Advanced Materials, 2011, 23, 1514-1518.

3. W. Regan, N. Alem, B. Aleman, B. Geng, C. Girit, L. Maserati, F. Wang, M. Crommie and A. Zettl, A direct transfer of layer-area graphene, Applied Physics Letters, 2010, 96.

4. L. Wang, Z. Xue, X. Liu and B. Liu, Transfer of asymmetric free-standing TiO_2 nanowire films for high efficiency flexible dye-sensitized solar cells, Rsc Advances, 2012, 2, 7656-7659.

5. S. Pimanpang, P. I. Wang, G. C. Wang and T. M. Lu, Self-assembled monolayer growth on chemically modified polymer surfaces, Applied Surface Science, 2006, 252, 3532-3540.

6. S. Joo and D. F. Baldwin, Adhesion mechanisms of nanoparticle silver to substrate materials: identification, Nanotechnology, 2010, 21.

7. D.-H. Kim, J. Viventi, J. J. Amsden, J. Xiao, L. Vigeland, Y.-S. Kim, J. A. Blanco, B. Panilaitis, E. S. Frechette, D. Contreras, D. L. Kaplan, F. G. Omenetto, Y. Huang, K.-C. Hwang, M. R. Zakin, B. Litt and J. A. Rogers, Dissolvable films of silk fibroin for ultrathin conformal bio-integrated electronics, Nature Materials, 2010, 9, 511-517.

8. S.-W. Hwang, H. Tao, D.-H. Kim, H. Cheng, J.-K. Song, E. Rill, M. A. Brenckle, B. Panilaitis, S. M. Won, Y.-S. Kim, Y. M. Song, K. J. Yu, A. Ameen, R. Li, Y. Su, M. Yang, D. L. Kaplan, M. R. Zakin, M. J. Slepian, Y. Huang, F. G. Omenetto and J. A. Rogers, A Physically Transient Form of Silicon Electronics, Science, 2012, 337, 1640-1644.

9. G. Saito and Y. Yoshida, Development of conductive organic molecular assemblies: Organic metals, superconductors, and exotic functional materials, Bulletin of the Chemical Society of Japan, 2007, 80, 1-137.

10. D. N. Rockwood, R. C. Preda, T. Yucel, X. Wang, M. L. Lovett and D. L. Kaplan, Materials fabrication from Bombyx mori silk fibroin, Nature Protocols, 2011, 6, 1612-1631.

11. Q. Lu, X. Hu, X. Wang, J. A. Kluge, S. Lu, P. Cebe and D. L. Kaplan, Water-insoluble silk films with silk I structure, Acta Biomaterialia, 2010, 6, 1380-1387.

12. T. Alfrey, E. F. Gurnee and W. G. Lloyd, Diffusion in glassy polymers, Journal of Polymer Science Part C-Polymer Symposium, 1966, 249-&.

13. Y. J. Weitsman, Anomalous fluid sorption in polymeric composites and its relation to fluid-induced damage, Composites Part a-Applied Science and Manufacturing, 2006, 37, 617-623.

Chapter 8

Experimental part

8.1. BL film preparation

Compounds bis(ethylenedithio)tetrathiafulvalene (BEDT-TTF), tetrathiafulvalene (TTF), poly(Bisphenol A carbonate), (polycarbonate, PC, average Mw ca. 64,000), cellulose triacetate (CTA), cellulose acetate propionate (CAP) were purchased from Aldrich. Organic solvents -1,1-dichloroethane (1,1-DCE), benzonitrile (BN), 1,2-chlorobenzene (o-DCB), and dichloromethane (DCM)- of analytical grade from Aldrich were used. The Bu_4NI_3 salt was synthesized as previously published.[1]

Precursors of the single component molecular conductor $[Au(\alpha\text{-tpdt})_2]^0$, such as tetraalkyl ammonium salts $[(C_2H_5)_4N]^+[Au(\alpha\text{-tpdt})_2]^-$ and $[(C_4H_9)_4N]^+[Au(\alpha\text{-tpdt})_2]^-$, were synthesized as previously described. [2]

PC, CAP and CTA films (5 - 25 μm in thickness) with molecularly dispersed BEDT-TTF or TTF compounds of different concentrations with respect to the polymeric matrix (2-8 wt%) were prepared by drop casting a solution of BEDT-TTF (or TTF) and polymer in 1,2-dichlorobenzene with polymer concentration from 0.3 wt% to 1.5wt% for films of 5 and 25 μm in thickness, respectively on a glass surface inside an oven preheated up to T = 130 °C. The samples were kept in the oven for 20-30 minutes to let the solvent evaporate. Subsequently, the film surface was treated with halogen vapours from a solution of I_2, IBr or Br_2 in CH_2Cl_2. In a first step, a glass chamber ($V_{chamber}$ = 14 ml) containing the halogen/CH_2Cl_2 solution (V = 4 ml) and halogen/CH_2Cl_2 vapours (V = 10 ml) was enclosed in a temperature and humidity controlled environment chamber (Memmert HPP 108) and left to equilibrate at a constant temperature and relative humidity for 60 min. Then, the samples were vapor/annealed by placing the drop casted films as a lid at the top of the glass chamber. The films with α- $(BEDT\text{-}TTF)_2I_3$, $TTF_{11}I_8$, $[Au(\alpha\text{- tpdt})_2]^0$ crystallites were prepared employing a saturated solution of I_2 in CH_2Cl_2 (c = 1.76 M [3]). The BL films with α′-$(BEDT\text{-}TTF)_2I_xBr_{(3-x)}$ and $(BEDT\text{- }TTF)_xBr_y(H_2O)_n$ crystallites were prepared employing a IBr/CH_2Cl_2 (c = 0.5 M) and IBr/CH_2Cl_2 (c = $0.5\cdot10^{-3}$ M) solutions, respectively. The time of oxidation was varied as describe in each Chapter from 30 second to 10 minutes. BL films with β-$(BEDT\text{-}TTF)_2I_3$ and β-$(BEDT\text{-}TTF)_2I_xBr_{(3-x)}$ were prepared by thermal annealing of those containing α-$(BEDT\text{-}TTF)_2I_3$ and α′-$(BEDT\text{-}TTF)_2I_xBr_{(3-x)}$, respectively, protected with a glass slide or Al foil to avoid loss of iodine, at T = 150 °C for 30 minutes [4] and T = 160 °C for 15 minutes in case of $(BEDT\text{-}TTF)_2I_3$ and $(BEDT\text{-}TTF)_2I_xBr_{(3-x)}$, respectively.

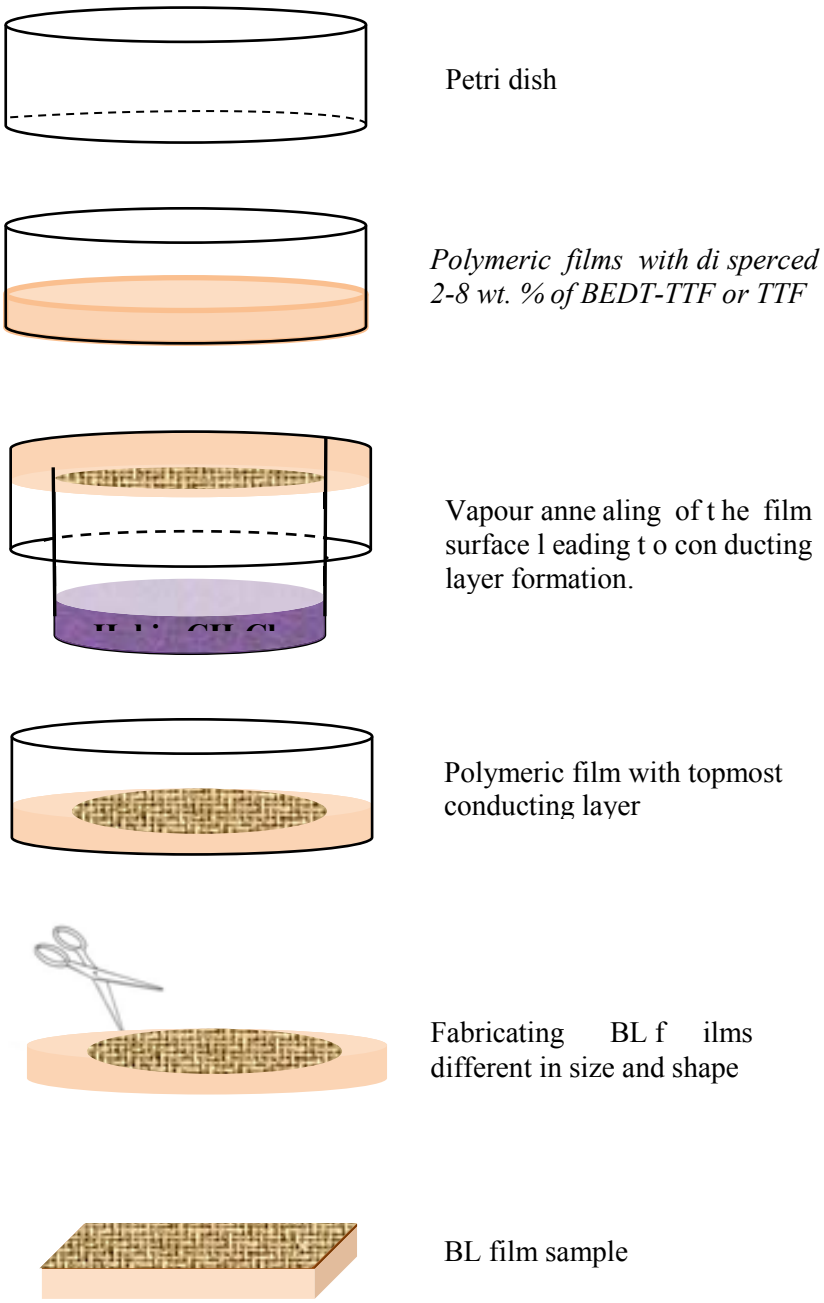

Figure 8-1. Scheme of preparation processing of BL films.

8.2. BL film characterizations

Structure of conductive crystalline layers of BL film. X-ray powder diffraction data for bilayer films w ere c ollected in reflection mode using a X-Ray powder dif ractometer RIGAKU model "Rotaflex" RU-200B in the re flection mode (λ (CuKα1) =

1.540598Å)(λ (CuKα2) = 1.544418 Å), normal conditions -: 50 kV 80 mA (max 60 kV 200mA).

The X-ray characterizations under controlled humidity atmosphere were carried out in collaboration with the "CNR-Instituto per la Microelettronica e Microsistemi (IMM)", Bologna, Italy. X-ray analysis to solve the crystal structure of new synthesized $TTF_{11}I_8$ as well as the confirmation $BEDT\text{-}TTF)_2Br(H_2O)_3$ crystallite structure for known single crystals and the orientation of α- and β-$(BEDT\text{-}TTF)_2I_3$ single crystals for Young's moduli determination were performed in collaboration with Dr. X. Fontrodona from the Serveis Tecnics de Recerca, "Universitat de Girona", Girona, Spain.

Morphology and chemical composition of topmost conductive crystalline layers. The elemental analysis of the covering layers of polymers was performed with a scanning electron microscope (SEM) ''Quanta FEI 200 FEG-ESEM'' with an EDX instrument operating at 10 kV. Single crystals, whose compositions and structures are known, [5, 6] were used as standards.

Electron paramagnetic resonance spectra. EPR spectra were obtained in an X-Band Bruker ELEXYS E500 spectrometer equipped with a TE102 microwave cavity, a Bruker variable temperature unit and a field frequency lock system Bruker ER 033 M. The signal to noise ratio of spectra was increased by accumulation of scans using the F/F lock accessory to guarantee large field reproducibility. Line positions were determined with an NMR Gaussmeter Bruker ER 035 M. The modulation amplitude was kept well below the line width, and the microwave power was well below saturation. To avoid dipolar line broadening from dissolved oxygen, solutions were always carefully degassed with pure Argon.

IR spectra. Spectra of the films were recorded in solid state using a Perkin Elmer, Spectrum One FT-IR Spectrometer.

Ultraviolet-visible Spectroscopy (UV-Vis): UV-Vis spectra were recorded with a Cary 5000 UV-Vis NIR Varian spectrophotometer

AFM topographic images. Images were acquired in AC mode using a MFP-3D AFM (Asylum Research, Santa Barbara, CA). Samples were glued on a glass slide with epoxy cement in order to ensure a mechanical stability. In the case of samples composed of individual crystallites, several minutes were lagged before adding the crystallites on top the epoxy so as to prevent that they would sink in the epoxy. Care was taken to ensure that the crystallites were placed in the correct orientation. For samples where crystallites were embedded on a polymeric matrix, no special precautions were considered. By

means of the optical system attached to the AFM, target sample regions were chosen and analyzed both topographically and mechanically. The spring constant of the used rectangular silicon AFM probes (MikroMasch CSC37, Tallin, Estonia) was individually measured by means of the thermal noise routine implemented in the software. [7] Prior to mechanical experiments, the AFM probes were rinsed with acetone (analysis grade, Merck, WhiteHouse Station, NJ), ethanol (anhydrous RSE for electronic use, Carlo Erba, Rodano, Italy) and Milli-Q water (Millipore, Billerica, MA). After that, probes were cleaned in a PSD Ultra-Violet/Ozone decontamination unit (Novascan Technologies, Ames, IA). Radius of AFM probes (*R*) were measured using the SPIP reconstruction software (Image Metrology, Hørsholm, Denmark) and a test grating with nanometrically sharp spikes (NiOProbe, Aurora Nanodevices, Nanaimo, Canada).

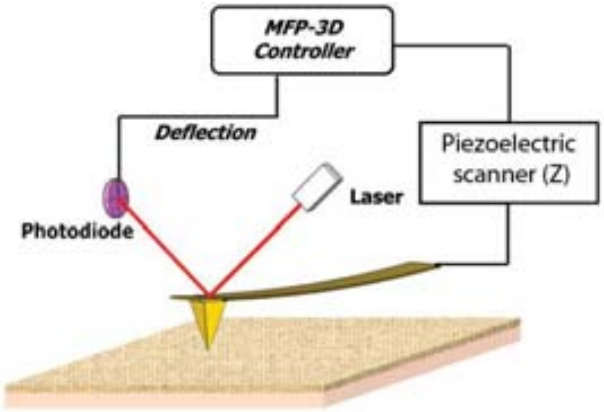

Figure 8-2. Principal scheme of the Young's modulus measurement by nanoindentation.

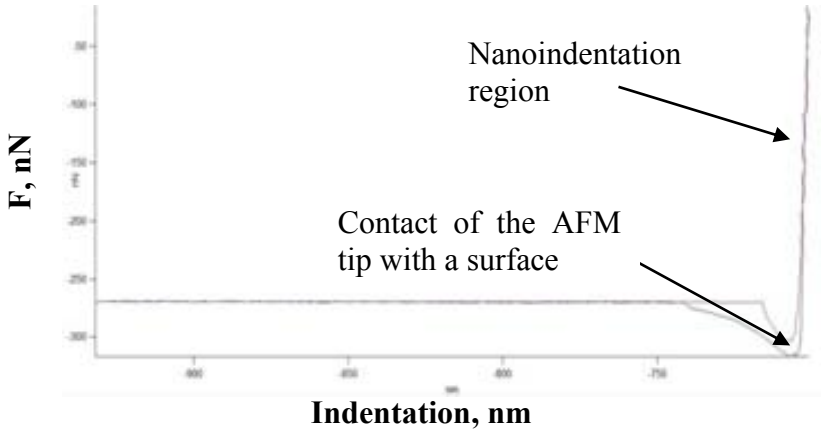

Figure 8-3. Typical Force-Indentation curve obtained for the BL film in the elastic region.

Calculation of Young modulus. Hertz model was used to find the Young's modulus value of a material. It is the simplest model available; as it considers that there is no long range interaction between the tip and the sample. The model used eq. 8.1:

$$F = (\frac{3}{4}E_{eff}\sqrt{R})h_e^{3/2} \qquad \text{eq. 8.1}$$

where F is the applied vertical force, E_{eff} is the effective Young's modulus, R corresponds to the tip radius calculated using SPIP program, and h_e is the indentation depth.

For calculation of Young's modulus, we found plot F *vs.* $h_e^{3/2}$ and then calculate the slope of the contact region we want to extract Young's modulus with eq.8.2.

$$slope = (\frac{3}{4}E_{eff}\sqrt{R}) \qquad \text{eq. 8.2}$$

From this it is possibleto extract the Young's modulus for the material. E_{eff} can be obtained with eq.8.3.

$$\frac{1}{E_{eff}} = \frac{1-\nu^2}{E} + \frac{1-\nu_i^2}{E_i} \qquad \text{eq. 8.3}$$

where ν is the Poisson ratio. Subindex i corresponds to the mechanical properties of the AFM probe (SiO_2 E_i = 76 GPa and ν_i = 0.17). The Poisson ratio was taken 0.33 for both BL films and single crystals since it is the average value for most of organic materials.

Macroscopic electrical properties. Room temperature resistances of single crystals and BL films as well as their resistance temperature dependences were measured by a standard four-probe dc-method. In the case of BL films, rectangular pieces of ca. 4x2mm^2 were cut from the film samples. Four annealed platinum wires (Goodfellow) with a diameter of 20 μm were attached to the single crystal or to conductive covering layer of BL films with a conducting graphite paste (Dotite paint, XC-12, JEOL datum LTD, Tokyo, Japan) The distance between potential contacts was kept of about 1 – 1.5 mm (Figure 8-4).

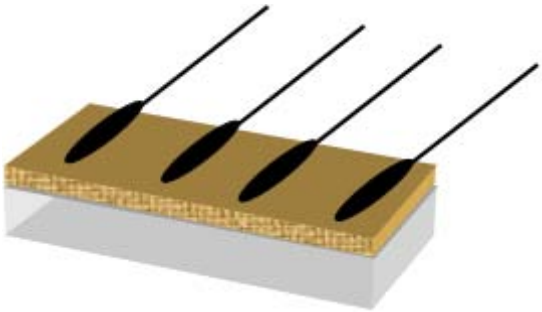

Figure 8-4. Schematic representation of the sample electrical connection for electrical properties measurements.

Uniaxial cyclic elongation tests. Measurements were conducted on an electromechanical positioning system *Parker* Actuator 401XR with a Compax3S Servo Drive System. The electromechanical positioning system was equipped with two homemade clamps to monitor the resistance response of BL films to strain, as shown in Figure 8-5. The electromechanical positioning system was connected via a serial bus (COM) to a computer. The BL film resistance was measured with a Keithley 2400 SourceMeter in a four wire configuration connected via GPIB bus to the same computer. A specific program to control both devices and to determine resistance and movement was written in Matlab R2007b with Instrument Control Toolbox 2.5. [8]

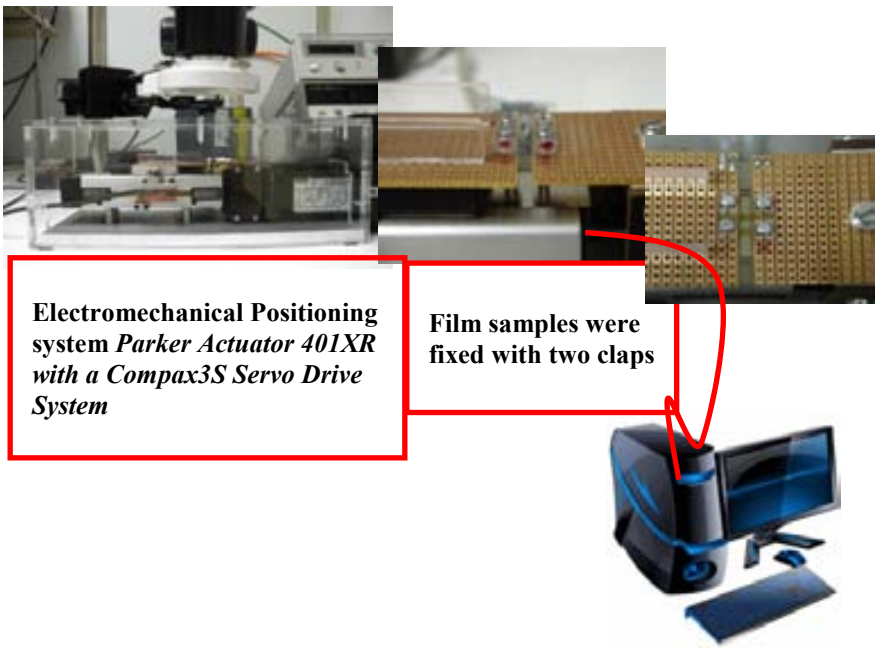

Figure 8-5. Schematic representation of the setup for electromechanical characterizations of the BL films.

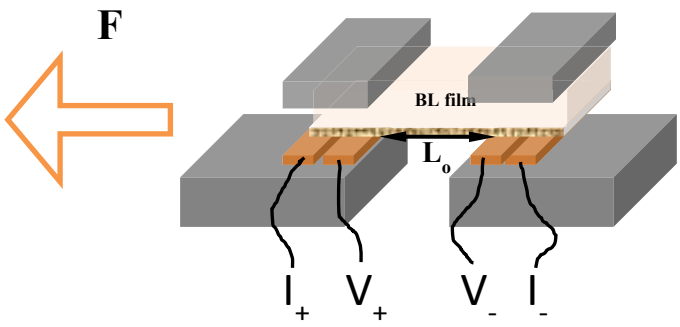

Figure 8-6. Schematic view of the BL film mounting for elecromechanical measurements.

A typical sample used for the electromechanical properties characterization was 12x2.5 mm^2 which was pressed with two clamps towards Cu-supports (conducting layer down) to which were connected wires from the measurement system. There sistance measurements were done by a standard four-probe dc-method. The work distance between potential contacts was 4 mm. In order to measure electrical response in the elastic region a cyclic deformation of 20 µm was applied that corresponds to a 0.5 % of relative strain. Speed load-unload was 0.3 µm/s, and the data were collected every 0.2 s.

Tensile tests. Mechanical and electromechanical properties of the films were studied using a 5848 MicroTester with a 1 kg load cell (Instron). Tester was additionally equipped with two electrical contacts and the resistance change under tensile testing was monitored using Agilent 34410A equipment. Film strips of dimensions of ca. 28×2 mm^2 and free from physical imperfections were held between two clamps positioned at a distance of ca. 18 mm. During measurements, the strips were pulled by the top clamp with velocity being 2.0 µm/s. Measurements were run in two replicates for each film.

The electrical resistance measurements at different relative humidity values. The humidity tests were studied in a constant climate chamber equipped with Peltier element (Memmert HPP 108). The relative humidity (RH) in the climate chamber was measured by a capacitive humidity sensor with an accuracy of 0.5 % and the temperature with a Pt100 sensor in 4-wire circuit with an accuracy of 0.1 °C%. Samples with sizes of 8x8mm were cut from the BL films and fixed with a very small amount of silicon grease on a copper substrate in order to eliminate temperature fluctuations on the measurements of resistance (Figure 8-7). Four graphite contacts were painted on the BL film and connected with 20 µm thick platinum wires to the measurement equipment capable to measure two samples simultaneously. The humidity values were kept

constant during about 30 min to stabilize the humidity in each point inside the climate chamber.

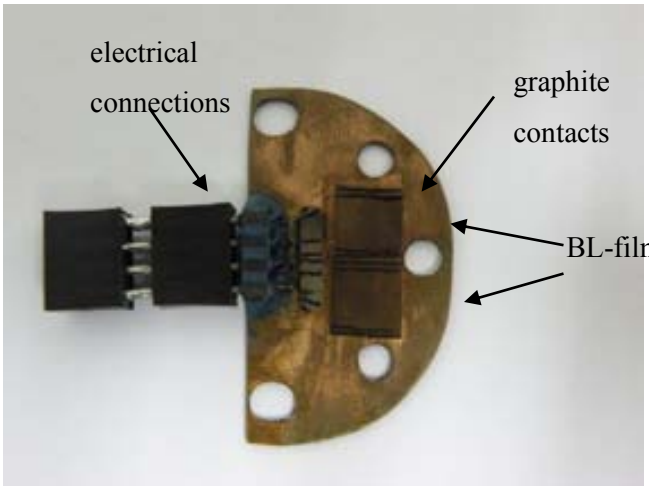

Figure 8-7. Image of the copper support with two samples of BL films for simultaneous measurement of relative humidity changes on the electrical resistance.

Bibliography

1. F. D. Chattaway and G. Hoyle, Perhalides of quaternary ammonium salts, Journal of the Chemical Society, 1923, 123, 654-662.

2. D. Belo, H. Alves, E. B. Lopes, M. T. Duarte, V. Gama, R. T. Henriques, M. Almeida, A. Perez-Benitez, C. Rovira and J. Veciana, Gold complexes with dithiothiophene ligands: A metal based on a neutral molecule, Chemistry-a European Journal, 2001, 7, 511-519.

3. K. Shinoda and Hildebra.Jh, Irregular solutions of iodine, Journal of Physical Chemistry, 1965, 69, 605-&.

4. E. E. Laukhina, V. A. Merzhanov, S. I. Pesotskii, A. G. Khomenko, E. B. Yagubskii, J. Ulanski, M. Kryszewski and J. K. Jeszka, Superconductivity in reticulate doped polycarbonate films, containing $(BEDT\text{-}TTF)_2I_3$, Synthetic Metals, 1995, 70, 797-800.

5. E. B. Yagubskii, I. F. Shchegolev, V. N. Laukhin, R. P. Shibaeva, E. E. Kostyuchenko, A. G. Khomenko, Y. V. Sushko and A. V. Zvarykina, Superconducting transition in the dielectric alpha-phase of iodine-doped $(BEDT\text{-}TTF)_2I_3$ compounds, Jetp Letters, 1984, 40, 1201-1204.

6. B. A. Scott, S. J. Laplaca, J. B. Torrance, B. D. Silverman and B. Welber, Crystal chemistry of organic metals - composition, structure, and stability in tetrathiofulvalinium halide systems, Journal of the American Chemical Society, 1977, 99, 6631-6639.

7. E. L. Florin, M. Rief, H. Lehmann, M. Ludwig, C. Dornmair, V. T. Moy and H. E. Gaub, Sensing specific molecular interactions with the atomic force microscope, Biosensors & Bioelectronics, 1995, 10, 895-901.

8. E. Laukhina, R. Pfattner, L. R. Ferreras, S. Galli, M. Mas-Torrent, N. Masciocchi, V. Laukhin, C. Rovira and J. Veciana, Ultrasensitive piezoresistive all-organic flexible thin films, Adv Mater, 2010, 22, 977-981.

Chapter 9

General conclusions

- ✓ The developed method for preparing BL films permitted obtaining of conductive composite materials in a reproducible, reliable, and scale-up manner.

- ✓ Mechanical properties such as Young's modulus of $(BEDT\text{-}TTF)_2I_3$ single crystals and BL films containing such crystals, measured at different crystallographic directions have enabled to correlate the mechanical properties of both single crystals and BL films with their crystal structure. The similar values of the elastic constants for single crystals, conducting BL films and polymers seems to be the origin of the good adhesion between the conducting layer and the polymeric matrix in BL film composites.

- ✓ Two methods for transfer the conducting layers of BL films to sculpted surfaces with different shapes and nature have been developed allowing obtaining novel composite materials without losing the attractive sensing properties of BL films.

- ✓ Piezoresistive BL films with high sensitivity to strain that exceed one order of magnitude those of commercial metals and alloys have been obtained using as active components the following salts: α-$(BEDT\text{-}TTF)_2I_3$, β_H-$(BEDT\text{-}TTF)_2I_3$, $[Au(\alpha\text{-}tpdt)_2]^0$ and the new crystalline phase of $TTF_{11}I_8$.

- ✓ Pyroresistive obtained BL films with α'-$(BEDT\text{-}TTF)_2I_xBr_{(3-x)}$ crystallites are able to detect with a high sensitivity small temperature changes in a reproducible and reversible manner when used in a direct contact configuration and in a non-contact one.

- ✓ Hygroresistive BL films based on $(BEDT\text{-}TTF)_xBr_y(H_2O)_n$ and $TTF_{11}I_8$ crystallites were obtained showing a long-term stability with reproducible, reversible and fast response to the relative humidity changes without the need to periodical regeneration of the sensor.

- ✓ Several proof-of-concept devices and prototypes using the developed piezo-, pyro- and hygroresistive BL films were engineered showing the high potential for practical applications of the BL films.

Annex 1

Synthesis of single crystals of conducting charge-transfer salts

Selective preparation of single crystals of $(TTF)I_3$

Iodine ($13.7 \cdot 10^{-5}$ mol) was added to a hot solution (80 °C) of TTF ($14.6 \cdot 10^{-5}$ mol) in 30 mL of a 1,1-DCE/BN mixture (50/50 v/v) under argon. Then, the resulting solution was cooled to 25 °C with a rate of 1 deg/hour, and plate-like black crystals were obtained. The yield of the crystals was around 70% in two batches. The crystallographic parameters of the crystals (Figure A-1) corresponded to the known stoichiometric $(TTF)I_3$ phase reported by R. C. Teitelbaum et al.. [1]

Selective preparation of single crystals of $(TTF)_{11}I_8$

Method 1: Iodine ($7.6 \cdot 10^{-5}$ mol) was added to a hot solution (80 °C) of TTF ($14.0 \cdot 10^{-5}$ mol) in 30 mL of a 1,1-DCE/BN mixture (50/50 v/v) under argon. Then, the resulting solution was cooled to 25 °C with a rate of 1 deg/hour and the new polymorph $(TTF)_{11}I_8$ was obtained as bar-like black crystals 1mm in length. The total yield of the crystals was around 70%. Method 2: $n\text{-}Bu_4NI_3$ salt ($7.1 \cdot 10^{-5}$ mol) was added to a hot solution (80°C) of TTF ($2.4 \cdot 10^{-5}$ mol) in 30 mL of a 1,1-DCE/BN mixture (50/50 v/v) under argon. Then, the resulting solution was cooled down to 25 °C with a rate of 1 deg/hour, and bar-like black crystals of $(TTF)_{11}I_8$ were obtained. The yield was around 60%.

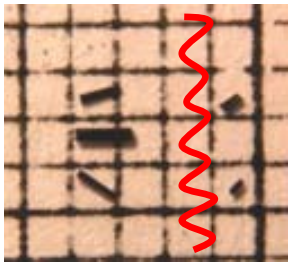

Figure A-1. Image of $TTF_{11}I_8$ (left) and $(TTF)I_3$ (right) crystals obtained using oxidation of TTF with iodine (see experimental part of this chapter); cells: 1 x1 mm^2.

Characterization of conductive crystalline materials

Single crystal structure of $(TTF)_{11}I_8$. X-ray data (Table A-1) were collected at room temperature on a *BRUKER SMART APEX CCD* diffractometer using graphite-monochromated Mo *K*α radiation (λ = 0.71073 Å). The measurements were made in the range 1.93 to 28.32° for θ. Full-sphere data collection was carried out with ω and φ scans. A total of 79687 reflections were collected of which 24664 [R(int)=0.0379] were unique. Programs used: data collection, Smart;[2] data reduction, Saint+;[3] absorption correction, SADABS.[4] Structure solution and refinement was done using SHELXTL.[5]

Table A-1. Relevant crystallographic data of iodine-containing TTF salts.

Empirical formula	$(TTF)I_3$	$(TTF)_{11}I_8$ [a]
F_w, $g \cdot mol^{-1}$	1587	3263
Crystal system	monoclinic	monoclinic
Space group	*P21/n*	*C2*
Z	12	4
a, Å	7.79	26.38
b, Å	18.81	16.06
c, Å	9.43	24.24
β, deg.	103.16	101.2
V, $Å^3$	1345.49	10072(1)
D_{calc} ($g\ cm^{-3}$)	-	2.5

[a] The same data were obtained for crystals prepared with methods 1 and 2.

The structure of the new polymorph $(TTF)_{11}I_8$ was solved by direct methods and refined by full-matrix least-squares methods on F^2. The non-hydrogen atoms were refined anisotropically. The H-atoms were placed in geometrically optimized positions and forced to ride on the atom to which they are attached. The crystal was solved and refined in *C2* space group as a racemic twin. Possible higher symmetry was suspected and trials to find a solution in space group *C2/c* were made. A possible solution was found, but efforts to refine the structure in *C2/c* were unsuccessful. Details are given on the refine special details section of the cif file. Final R indices [I>2θ(I)]: R1=0.0406, wR2=0.0878; R indices (all data): R1=0.1487 and wR2 = 0.1310. CIF file is available at CCDC deposition number 949070.

Selective synthesis of $(TTF)I_3$ and $(TTF)_{11}I_8$ salts. We discovered that there exist optimal reaction conditions, concerning the amount of iodine, solvent, and temperature, which are capable to control selectively the formation of crystals of either the $(TTF)I_3$ phase or the new non-stoichiometric $(TTF)_{11}I_8$ salt. Interestingly, the oxidation of TTF by non-equimolar amount of iodine in a 1,1-DCE/BN mixture (50/50 v/v) proceed with an excellent selectivity when a hot reagent solution was cooled from 80 to 25 ºC with a cooling rate of 1 deg/hour. Thus, the $(TTF)I_3$ salt[6] was obtained when the molar ratio of $TTF:I_2$ was 1:0.9 while the new non-stoichiometric phase was selectively formed when the molar ratio was 1:0.5 or even lower. Both salts were reproducibly prepared in good

yields being stable in air for several months. The new phase that corresponds to the $(TTF)_{11}I_8$ salt (*vide infra*), can be also prepared pure by mixing solutions of TTF and Bu_4NI_3, using the later reagent in a large excess. In this case the oxidant agent was also the I_2 formed in a small amounts due to the well-known dissociation process of I_3^- into I_2 and I^-.[7]

Characterization of the new $(TTF)_{11}I_8$ phase. The composition of the crystals prepared by a direct chemically oxidation process with I_2 or with Bu_4NI_3 was studied by EDX analysis. The S:I stoichiometry determined for several crystals varies from 4:0.70 to 4:0.75; close to the calculated value of S:I=4:0.7 for a salt $(TTF)_{11}I_8$ type. Single crystal X-ray diffraction data reveal that these crystals correspond to salt $(TTF)_{11}I_8$ is a new member of the non-stoichiometric $(TTF)I_{0.7+\delta}$ salts. The $(TTF)_{11}I_8$ crystals are monoclinic of the chiral space group *C*2. The crystal structure of the new $TTF_{11}I_8$ salt is close to that of TTF_7I_5 salt, reported by Johnson *et al.*[8] The crystal structure of TTF_7I_5 phase (Fig. 1 top) has the asymmetric unit that contains 15 independent iodide ions and 20 TTF moieties in general positions, and the halves of two TTF moieties situated on inversion centers. All TTF moieties in this phase were considered planar and centrosymmetric and were used in the structure determination and refinement as identical rigid units.[6] The crystal structure of $(TTF)_{11}I_8$ phase (Figure A-2, bottom), determined from single crystal X-ray data, shows that the structure is modulated showing lateral displacements about the axis along each TTF and iodine columns. The asymmetric unit contains 8 independent iodide ions and 10 TTF moieties in general positions, and the halves of two TTF moieties situated on two-fold rotational axes arranged into two columns of five and a half molecules each. The TTF moieties are non-planar being slightly twisted with S–C=C–S torsion angles varying from 0.06(3) up to 2.8(3)º. It is worth to mention that the crystal packing features of TTF_7I_5 and $TTF_{11}I_8$ are very close. In both phases TTF moieties are stacked into columns, which propagate in one direction; along the [10-1] one in $TTF_{11}I_8$ and along [001] in TTF_7I_5. The columns of TTF molecules are packed in such way that they form channels filled with iodine species. As all distances between the iodide atoms in the $(TTF)_{11}I_8$ structure are significantly bigger than those in I_2, $[I\text{-}I\cdots I]^-$ and I_3^- (Table A-2), the channels between TTF's columns are filled with mono atomic iodine anions (I^-). Iodide anions have contacts with several sulphur atoms from the neighboring columns of TTF moieties with I···S distances less than the sum of van der Waals radii of I and S (3.8 Å).

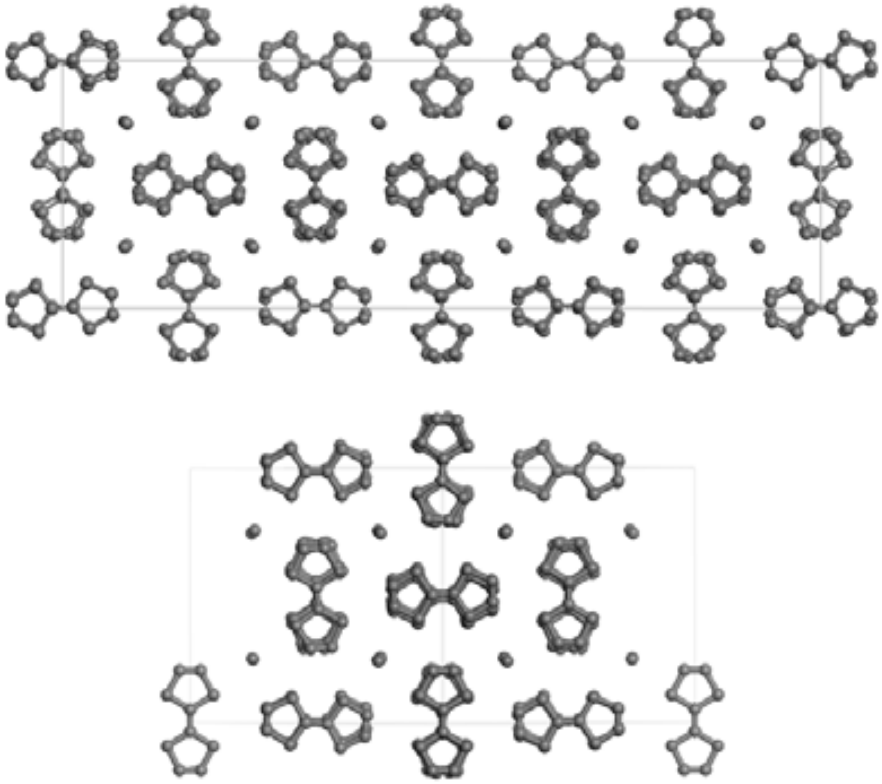

Figure A-2. Crystal packing of TTF_7I_5 phase viewed along the [001] direction (top) and of $TTF_{11}I_8$ phase viewed along the [10-1] direction (bottom). The unit cell box is shown for each structure. Hydrogen atoms have been omitted for clarity.

Table A-2. Distances between iodine species extracted from the resolved crystal structure of $TTF_{11}I_8$, as well as the values of the bond length in I-I and $(I\text{-}I\text{-}I)^-$ added for comparison.

Number of I^-	Object1	Object2	Length, Å
1	I8	I3	4.883(5)
2	I4	I3	4.900(6)
3	I7	I4	4.892(6)
4	I1	I5	4.928(5)
5	I5	I6	4.864(6)
6	I6	I2	4.875(6)
I-I			**2.68-2.72[9]**
I_3^-			**2,79-3,11[10]**

Specifically, each iodide anion in TTF_7I_5 has three of four contacts with I···S distances lying in the range 3.53 – 3.71 Å, while in $TTF_{11}I_8$ the iodide anions have from one to four short contacts in the range 3.53 – 3.73 Å. In spite of close similarity of both TTF_7I_5 and $TTF_{11}I_8$ phases their crystal structures cannot be transformed one into another, so they are

in fact two distinct phases of the non-stoichiometric $TTFI_{0.7+\delta}$ type, where δ=0.014 and 0.027 for TTF_7I_5 and $TTF_{11}I_8$, respectively. The calculated values of the charge transfer degree, based on the bond length ratio showed that the charges on TTF molecules range from +0.700 to +1.295 (Table A-3). This clearly points out that a conjugative electronic system is formed in the $(TTT)_{11}I_8$ crystals. It should be kept in mind, that the relation between charge transfer and geometry is only approximate. [11]

Table A-3. The central C^1=C^4 and C^4-S^4 bond lengths extracted from the crystal structure of $TTF_{11}I_8$. The charge transfer of each molecule of TTF in the asymmetric unit was calculated using following equation r=0.762+0.049q, where r is ratio between bond lengths and q is a charge of TTF species.

Molecule TTF	Atom1	Atom2	Length, Å	ratio, r=(L(C^1=C^4)/L(C^4-S^4))	charge, q
A	S4	C4	1.723	0,796	0,700
	C1	C4	1.372		
B	S4	C4	1.722	0,809	0,958
	C1	C4	1.393		
C	S4	C4	1.712	0,801	0,804
	C1	C4	1.372		
D	S4	C4	1.722	0,809	0,958
	C1	C4	1.393		
E	S4	C4	1.732	0,798	0,733
	C1	C4	1.382		
F	S4	C4	1.722	0,797	0,721
	C1	C4	1.373		
G	S4	C4	1.722	0,803	0,840
	C1	C4	1.383		
H	S4	C4	1.722	0,809	0,958
	C1	C4	1.393		
I	S4	C4	1.712	0,807	0,923
	C1	C4	1.382		
J	S4	C4	1.712	0,813	1,043
	C1	C4	1.392		
K	C1	C4	1.414	0,825	1,295
	S1	C4	1.713		
L	S4	C4	1.722	0,810	0,970
	C1	C4	1.394		

Transport properties of $TTF_{11}I_8$ crystals. The resistance temperature dependence of a single crystal was measured with a four probe along the longest axis of the crystal. The magnitude of conductivity at room temperature varies from 50 to 130 $\Omega^{-1}cm^{-1}$. These values are not too different from those previously reported for single crystals of $(TTF)_7I_5$

(100-400 $\Omega^{-1}cm^{-1}$).[18] As Figure A-3 shows, the resistance of $TTF_{11}I_8$ significantly increases with decreasing the temperature revealing the change of the slope of R(T) dependence around 200 K. The observed feature probably is related to a second order phase transition.

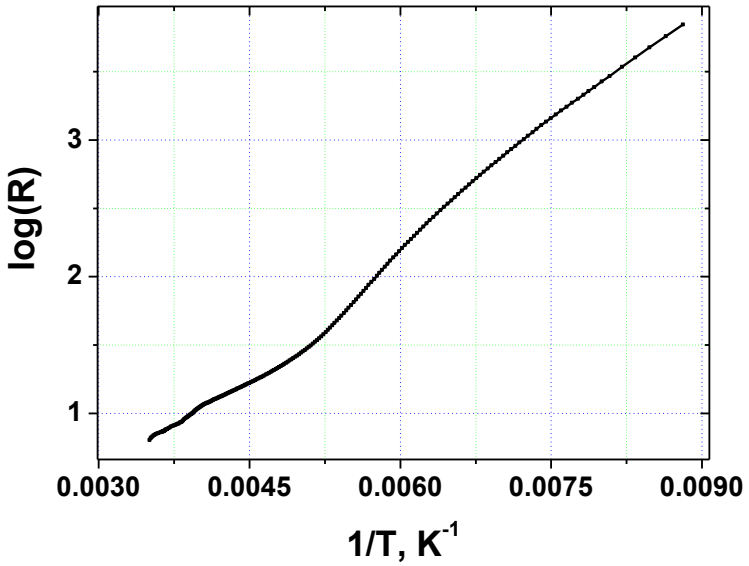

Figure A-3. Temperature dependence of electrical resistance of a single crystal of $TTF_{11}I_8$.

Preparation of single crystals of $(BEDT\text{-}TTF)_2Br(H_2O)_3$

Method 1a: Bromine ($0.5 \cdot 10^{-5}$ mol) was added to a hot solution (80 °C) of BEDT-TTF ($5.2 \cdot 10^{-5}$ mol) in 10 mL of a chlorobenzene with a 0.2 mL of water under argon. Then, the resulting solution was cooled to 25 °C with a rate of 1 deg/hour resulting in elongated plate-like black crystals about 1 mm in length. The total yield of the crystals was around 85%.

Method 1b: Bromine ($0.4 \cdot 10^{-5}$ mol) was added to a hot solution (80 °C) of BEDT-TTF ($3.8 \cdot 10^{-5}$ mol) in 10 mL of a 1,1,2-trichloroethane with a 0.2 mL of water under argon. Then, the resulting solution was cooled to 25 °C with a rate of 1 deg/hour resulting in needle-like black crystals about 1.3 mm in length. The total yield of the crystals was around 70%.

Method 2: n-Bu_4NBr salt ($0.8 \cdot 10^{-5}$ mol) was added to a hot solution (80°C) of BEDT-TTF ($1.3 \cdot 10^{-5}$ mol) in 10 mL of a benzonitrile with a 0.1 mL of water under argon in cell for electrochemical crystallization (Figure A-4). The constant current 0.3 μA was applied resulting in 1 week plate-like crystals from 1 to 2.5 mm in length; the total yield was around 50%.

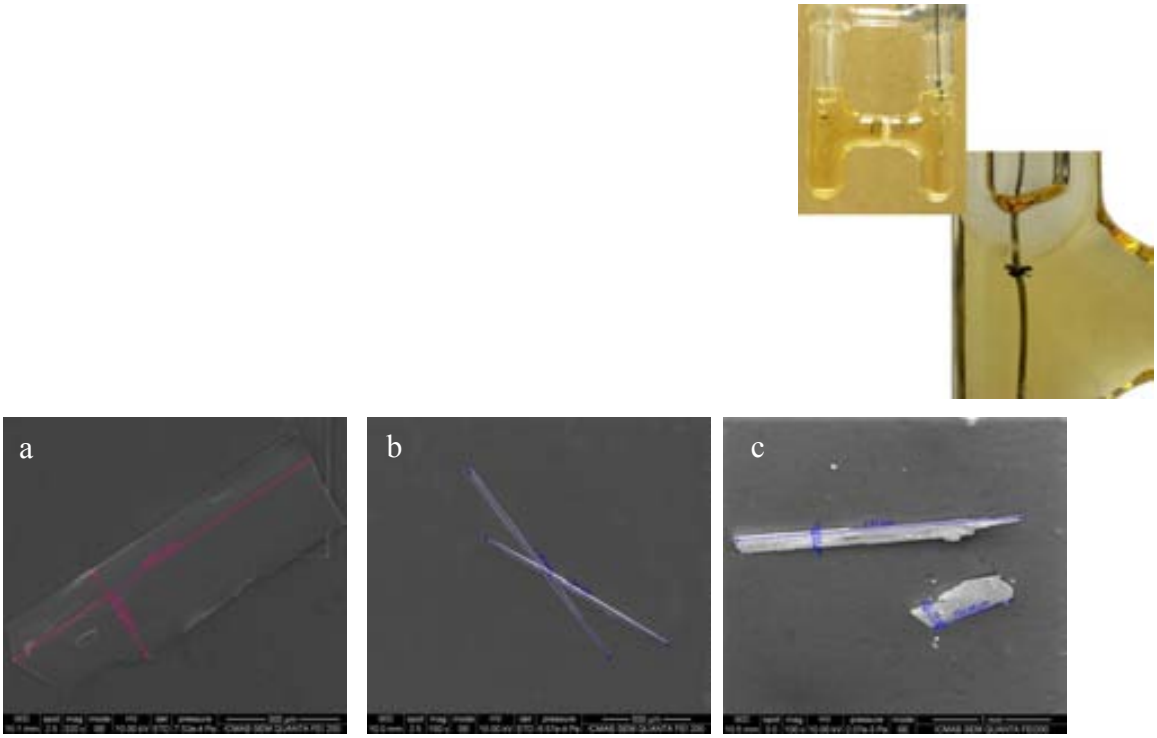

Figure A-4. SEM images of the single crystals of $(BEDT\text{-}TTF)_2Br(H_2O)_3$ prepared by different methods: method 1a (a); method 1b (b); method 2 (c). Top left corner photo image of the cell for electrochemical crystallization showing the crystal formation on the Pt-electrode.

Characterization of conductive crystalline materials

Single crystal structure of (BEDT-TTF)$_2$Br(H$_2$O)$_3$ X-ray experimental data (Table A-4) were collected at room temperature on a *BRUKER SMART APEX CCD* diffractometer using graphite-monochromated Mo *K*α radiation (λ = 0.71073 Å). The measurements were made in the range 1.93 to 28.32° for θ. . A total of 38218 reflections were collected of which 9573 [R(int)=0.0229] were unique. Programs used: data collection, Smart;[2] data reduction, Saint+;[3] absorption correction, SADABS.[4] Structure solution and refinement was done using SHELXTL.[5]

The structures of the all single crystals, prepared by different methods, were solved by direct methods. Final R indices [I>2θ(I)]: R1=0.0683, wR2=0.2032; R indices (all data): R1=1.104.

Table A-4. Relevant crystallographic data of (BEDT-TTF)$_2$Br(H$_2$O)$_3$ salt.

Empirical formula	***(BEDT-TTF)$_2$Br(H$_2$O)$_3$***	
	experimental	literature
F_w, g·mol^{-1}	903	903
Crystal system	orthorhombic	orthorhombic
Space group	*P21/n*	*Pcca*
Z	5	4
a, Å	32.802	32.779(4)
b, Å	6.739	6.734(1)
c, Å	14.998	14.993(6)
α=*β*=*γ*, deg.	90	90
V, Å^3	3315	3309(1)
D_{calc} (g cm^{-3})	1449	1813

Transport properties of (BEDT-TTF)$_2$Br(H$_2$O)$_3$ crystals. The resistance temperature dependence of a single crystal was measured with a four probe along the longest axis of the crystal. The magnitude of conductivity at room temperature varies from 20 to 60 Ω^{-1}cm^{-1}. These values are not too different from those previously reported for single crystals of *(BEDT-TTF)$_2$Br(H$_2$O)$_3$* (3-10 Ω^{-1}cm^{-1}).[18] As Figure A-5 shows, the resistance of obtained *(BEDT-TTF)$_2$Br(H$_2$O)$_3$* crystals has a metallic behavior decreasing when the

temperature decreased revealing the change of the slope of R(T) dependence around 220 K presenting the temperature coefficient of the resistance of 0.54%/deg. At temperature down 220 K the resistance starts increasing indicating the metal-insulator transition. This data is in agreement with the literature.[12]

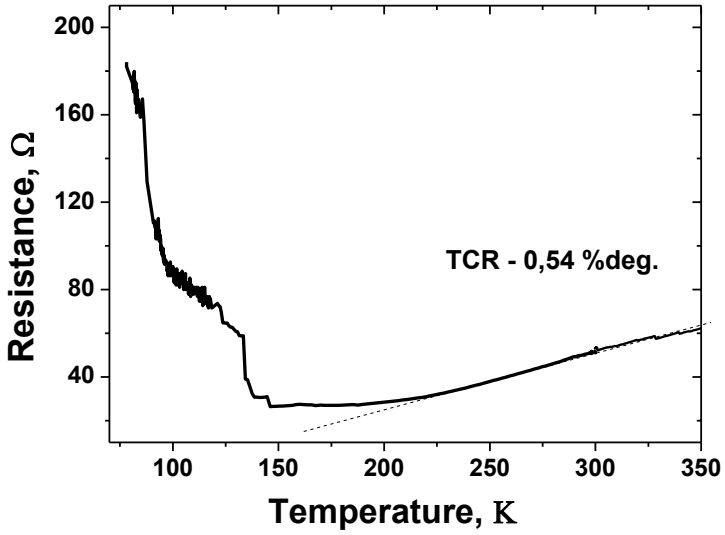

Figure A-5. Temperature dependence of electrical resistance of a single crystal of (BEDT-TTF)$_2$Br(H$_2$O)$_3$.

Bibliography

1. R. C. Teitelbaum, T. J. Marks and C. K. Johnson, Crystal structure and properties of tetrathiafulvalenium triiodide, Journal of the American Chemical Society, 1980, 102, 2986-2989.

2. Bruker, Advanced X-ray Solutions. SMART Version 5.631, 1997-2002.

3. Bruker, Advanced X-ray Solutions. SAINT +, Version 6.36A, 2001.

4. G. M. Sheldrick, Empirical Absorption Correction Program, Universität Göttingen, 1996 Bruker Advanced X-ray Solutions. SADABS Version 2.10, 2010.

5. G. M. Sheldrick, , Program for Crystal Structure Refinement, Universität Göttingen, 1997 Bruker Advanced X-ray Solutions. SHELXTL Version 6.14, 2000-2003.

6. B. A. Scott, S. J. Laplaca, J. B. Torrance, B. D. Silverman and B. Welber, Crystal chemistry of organic metals – compositio, structure, and stability in tetrathiofulvalinium halide systems, Journal of the American Chemical Society, 1977, 99, 6631-6639.

7. E. E. Laukhina, V. N. Laukhin, A. G. Khomenko and E. B. Yagubskii, Growth of high quality single crystals of the organic superconductors beta-$(ET)_2I_3$ and beta-$(ET)_2IBr_2$, Synthetic Metals, 1989, 32, 381-388.

8. C. K. Johnson and C. R. Watson, Superstructure and modulation wave analysis for unidimensional conductor hepta(tetrathiafulvalene) pentaiodide, Journal of Chemical Physics, 1976, 64, 2271-2286.

9. U. Buontempo, A. D. Cicco, A. Filipponi, M. Nardone and P. Postorino, Determination of the I_2 bond-length distribution in liquid, solid and solution, by extended x-ray absorption fine structure spectroscopy, The Journal of Chemical Physics, 1997, 107, 5720-5726.

10. P. Atkins and T. Overton, Shriver and Atkins' Inorganic Chemistry, OUP Oxford, 2010.

11. T. C. Umland, S. Allie, T. Kuhlmann and P. Coppens, Relation between geometry and charge transfer in low-dimensional organic salts, The Journal of Physical Chemistry, 1988, 92, 6456-6460.

12. M. Y. Luo, T. Ishida, A. Kobayashi and T. Nogami, Electrical conductivities and crystal and band-electronic structures of a new phase of BEDT-TTF-bromide salt, $(BEDT\text{-}TTF)_2Br(H_2O)_3$, Synthetic Metals, 1998, 96, 97-102.

Annex 2

Publications

Articles:

"**Polycarbonate films metalized with a single component molecular conductor suited to strain and stress sensing applications**"
Elena Laukhina,Victor Lebedev, Vladimir Laukhin, Angel Pérez del Pino, Elsa B. Lopes, Ana I.S. Neves, Dulce Belo, Manuel Almeida, Jaume Veciana, Concepció Rovira,
Organic Electronics, 13 (2012) 894–898

"**All organic flexible lightweight BL-film sensor systems with wireless data transmission**"
Raphael Pfattner, Victor Lebedev, Bahareh Moradi, Eelena Laukhina, Vladimir Laukhin, Concepció Rovira and Jaume Veciana
Sensors & Transducers, 17 (2013) 128–133

"**A new $(TTF)_{11}I_8$ organic molecular conductor: from single crystals to flexible all-organic piezoresistive films**",
Victor Lebedev, Elena Laukhina, Evelyn Moreno-Calvo, Concepcio Rovira, Vladimir Laukhin, Ivan Ivanov, Sergei M. Dolotov, Valery F. Traven, Vladimir V. Chernyshev and Jaume Veciana
Journal of Materials Chemistry C, 2 (2014) 139–146

"**Silk/molecular conductor bilayer thin-films: properties and sensing functions**"
Eden Steven, Victor Lebedev, Elena Laukhina, Concepció Rovira, Vladimir Laukhin, James S. Brooks and Jaume Veciana,
Materials Horizont 1 (2014) 522–528

"**Tuning the electronic properties of piezoresistive bilayer films based on α-$(BEDT\text{-}TTF)_2I_3$**"
Victor Lebedev, Elena Laukhina, Vladimir Laukhin, Concepció Rovira and Jaume Veciana
European Journal of Inorganic Chemistry, 24 (2014) 3927–3932

Proceedings:

“Piezoresistive biocompatible membranes for flexible pressure sensors”
V. Laukhin, V. Lebedev, E. Laukhina, C. Rovira and J. Veciana
Proceedings of the 2011 16th International Solid-State Sensors, Actuators and Microsystems Conference, TRANSDUCERS'11, 2694-2697.

“Polymeric films self-metallized with organic molecular conductors”
E. Laukhina, V. Lebedev, V. Laukhin, G. Oncins, R. Pfattner, C. Rovira and J. Veciana
Proceedings of the 2011 16th International Solid-State Sensors, Actuators and Microsystems Conference, TRANSDUCERS'11, 1978-1981

“All-Organic Humidity Sensing Films with Electrical Detection Principle Suitable to Biomedical Applications”
V. Lebedev, E. Laukhina, C. Rovira, V. Laukhin, J. Veciana
Procedia Engineering, 47 (2012) 603–606

“Towards Flexible Lightweight Strain Sensors with Low Temperature Coefficient of Resistance”
V. Lebedev, E. Laukhina, V. Laukhin, C. Rovira, J. Veciana
Procedia Engineering, 47 (2012) 857–860

“**Flexible thin films based on nanostructured polymeric composites as ultra sensitive piezoresistive materials and their applications**”
E. Laukhina, R. Pfattner, V. Lebedev, V. Laukhin, C. Rovira, J. Veciana
Technical Proceedings of the 2013 NSTI Nanotechnology Conference and Expo, NSTI-Nanotech 2013, Volume 2 (2013) 80-83

“Hybrid contact lens capable of intraocular pressure monitoring in noninvasive way”
V.Laukhin, V. Lebedev, E. Laukhina, R. Martin, J. C. Pastor, R. Villa, J. Aguilo, C. Rovira and J. Veciana
Proceedings of the 2013 Transducers and Eurosensors XXVII: The 17th International Conference on Solid-State Sensors, Actuators and Microsystems, TRANSDUCERS and EUROSENSORS 2013, 1871-1874